UQAC
Université du Québec
à Chicoutimi

Investigation and Optimization of Effective Parameters for Fabrication of Novel Anti-icing Coatings containing Ionic Liquids

By

SABA GOHARSHENASMOGHADAM

Under supervision of Prof. Gelareh Momen and co-supervision of Prof. Reza Jafari

Manuscript-Based Thesis Presented to Université du Québec à Chicoutimi in Partial fulfillment of the Requirements for the Degree of Doctor of Philosophy (Ph.D.) in Engineering

BOARD OF EXAMINERS:

Professor Issouf Fofana, Department of Applied Sciences at UQAC, President of the Board

Professor Véronique Landry, Department of Wood and Forest Sciences at Université Laval, External Member of the Board

Professor Yasar Kocaefe, Department of Applied Sciences at UQAC, Internal Member of the Board

Professor Gelareh Momen, Department of Applied Sciences at UQAC, Internal Member of the Board

Professor Reza Jafari, Department of Applied Sciences at UQAC, Internal Member of the Board

Québec, Canada

RÉSUMÉ

La problématique du givrage pose différents défis dans divers industries, nécessitant un passage des surfaces anti-givre statiques passives aux technologies dynamiques anti-givre. Cette thèse de doctorat explore l'utilisation innovante des liquides ioniques (IL) et des solvants eutectiques profonds (DES) dans les surfaces dynamiques anti-givre, en réponse aux défis persistants et en repoussant les limites des solutions anti-givre actuelles.

La première phase de cette recherche explore en profondeur l'utilisation des liquides ioniques à température ambiante (RT-IL) dans les surfaces dynamiques pour les applications anti-givre. En incorporant des IL dans des revêtements à base de PDMS, l'étude établit une relation entre le comportement anti-givre et les propriétés physico-chimiques des IL. La chimie de surface des revêtements et la présence de groupes distinctifs des anions des IL à la surface des revêtements sont caractérisées par spectroscopie infrarouge à transformer de Fourier en réflexion totale atténuée (ATR-FTIR) et confirmées par spectroscopie photoélectronique X (XPS) et analyse par microscopie électronique à balayage avec analyse de dispersion en énergie des rayons X (SEM/EDX). La présence des molécules d'eau fortement liées par des liaisons hydrogène ioniques retarde significativement la nucléation de la glace en limitant la croissance de la glace en addition de la réduction la force d'adhésion de la glace, ce qui met en évidence le potentiel des IL dans les applications anti-givre. La formation d'une couche quasi-liquide auto-lubrifiante (QLL) à l'interface mène à réduire la force d'adhésion de 60% à 70% tel que confirmé par spectroscopie RMN à l'état solide. Ces résultats soulignent l'influence significative de modifications mineures de la structure chimique des IL sur leur potentiel pour les applications anti-givre.

La deuxième phase examine l'influence de l'hydrophobie de la matrice sur la mobilité des IL aux températures inférieures à zéro. Les tests de mouillabilité soulignent le rôle crucial de l'hydrophobicité des anions des IL, et la spectroscopie diélectrique distingue la mobilité ionique au sein des revêtements à basse température. L'effet de la variation de la densité de réticulation sur la mobilité ionique a été examiné en mesurant l'absorption d'eau. La mobilité accrue des ILs relargués de revêtements à des températures inférieures à zéro est confirmée par leur présence dans des solutions aqueuses puis validée par spectroscopie UV–vis, ce qui mène à une augmentation de la conductivité ionique. Les surfaces contenant des ILs montrent une réduction significative de la température de formation de la glace à -23,5 °C et une force d'adhésion de la glace extrêmement faible d'environ 15 kPa. La présence d'une couche de QLL à l'interface a confirmé par spectroscopie RMN à l'état solide. Les résultats soulignent l'importance de choisir la matrice et les IL appropriés pour des revêtements anti-givre efficaces.

La troisième phase se concentre sur l'utilisation des solvants eutectiques profonds (DES) comme analogues écologiques des IL avec des réseaux de liaisons hydrogène uniques.

Dans cette phase, des IL à base de choline avec des anions hydrophiles et hydrophobes ont été synthétisés puis leurs combinaisons synergiques avec des DES a été explorer. Le remplacement de l'éthylène glycol (EG) par le glycérol (GL) permet d'atteindre une température de formation de glace de -36 °C et une force d'adhésion de la glace de 10 kPa. La spectroscopie RMN à l'état solide confirme la présence d'une couche quasi-liquide plus épaisse sur la surface du revêtement, en améliorant la résistance à la formation de givre. Ces résultats soulignent la synergie prometteuse entre les DES et les IL pour une atténuation très efficace de la glace.

La dernière phase explore également les effets synergiques de matériaux glaciophobes sur l'amélioration les capacités anti-givre dynamiques des surfaces, en se concentrant sur le rôle hydrophobe des composants donneurs de liaisons hydrogène (HBD) dans les DESs. En se basant sur la troisième phase, un focus particulier est mis sur les DES à base de choline combinés avec des IL à base de choline synthétisés. Une caractérisation complète par ATR-FTIR, XPS et des mesures de mouillabilité révèle que le remplacement de l'éthylène glycol (EG) par le diol perfluoré (PFOL) augmente les sites de liaison hydrogène. Cela conduit à une température de formation de glace de -35 °C et une force d'adhésion de la glace de 13 kPa. De plus, la spectroscopie SS-NMR et ATR-FTIR à basse température confirment la présence d'une couche QLL à la surface, et une résistance accrue à l'accumulation de givre. L'effet plastifiant inhérent des IL et des DES augmente l'allongement à la rupture des revêtements modifiés, tandis que la résistance à la traction du revêtement à base de PFOL-DES reste inchangée par rapport à la référence. Cette phase démontre que la combinaison des DES et des IL, qui réagissent bien à la glace, surpasse leurs composants individuels, conduisant à des revêtements glaciophobes performants et durables.

Mots-clés : Liquides ioniques, Revêtement anti-givre dynamique, Adhésion de la glace, revêtement glaciophobe, Formation de la glace, Mobilité ionique, Liaison hydrogène ionique, Hydrophobicité du revêtement, Densité de réticulation, Conductivité, Comportement glaciophobe, Solvant eutectique profond, Chlorure de choline, Accepteur de liaison hydrogène, Donneur de liaison hydrogène, Éthylène glycol, Glycérol, Diol perfluoré, Liaison hydrogène, Spectroscopie ATR-FTIR à basse température, Spectroscopie RMN à l'état solide, Couche quasi-liquide.

ABSTRACT

Icing poses significant challenges across various industries, prompting a shift from static, passive anti-icing surfaces to dynamic technologies. This Ph.D. thesis investigates the innovative use of ionic liquids (ILs) and deep eutectic solvents (DESs) in dynamic anti-icing surfaces, addressing persistent challenges and advancing anti-icing solutions.

The first phase of this research focuses on the incorporation of room-temperature ionic liquids (RT-ILs) into PDMS-based coatings for dynamic anti-icing applications. By examining the relationship between the physicochemical properties of ILs and their anti-icing behavior, the study characterizes the surface chemistry of the coatings. The distinct groups of IL anions on the surface are analyzed using Attenuated Total Reflectance-Fourier transform infrared spectroscopy (ATR-FTIR) and further confirmed by X-ray photoelectron spectroscopy (XPS) and scanning electron microscopy-energy dispersive X-ray analysis (SEM/EDX). Strong ionic hydrogen-bonded water molecules effectively delay ice nucleation, limit ice growth, and reduce ice adhesion strength. Solid-state Nuclear Magnetic Resonance spectroscopy (SS-NMR) confirms a self-lubricating quasi-liquid-like layer (QLL) at the interface, which leads to a 60-70% reduction in ice adhesion strength. This phase demonstrates the significant influence of subtle chemical modifications in ILs on their anti-icing capabilities.

The second phase investigates how the hydrophobicity of the matrix influences the mobility of ILs at subzero temperatures. Wettability tests underscore the crucial role of IL anion hydrophobicity, and dielectric spectroscopy distinguishes ion mobility within coatings at low temperatures. The impact of varying crosslink density on ion mobility is examined through water absorbency tests. The higher mobility of ILs released from the coatings at subzero temperatures is confirmed by their presence in water solutions, validated via UV–vis spectroscopy, leading to increased ionic conductivity. Surfaces containing ILs demonstrate a substantial reduction in ice formation temperature to -23.5 °C and very low ice adhesion strength of approximately 15 kPa. Solid-state NMR spectroscopy provided confirmation of the existence of QLL at the interface. The findings underscore the importance of matrix selection and IL choice in optimizing anti-icing performance.

In the third phase, our focus shifts to deep eutectic solvents (DESs), eco-friendly IL analogs with unique hydrogen-bonding networks. Choline-based ILs with hydrophilic and hydrophobic anions are synthesized and combined synergistically with DESs. The substitution of ethylene glycol (EG) with glycerol (GL) results in an ice formation temperature of -36 °C and an ice adhesion strength of 10 kPa. SS-NMR spectroscopy confirms the formation of a thicker QLL on the coating surface, which enhances resistance to frost formation. This phase highlights the promising synergy between DESs and ILs in achieving superior ice mitigation.

The final phase also explores the synergistic effects of combining multiple icephobic materials to enhance the dynamic anti-icing properties of surfaces, focusing on hydrophobicity role of hydrogen-bond donor (HBD) components within DESs. Building on the third phase, choline-based DESs are combined with synthesized choline-based ILs. Comprehensive characterization using ATR-FTIR, XPS, and wettability measurements reveals that replacing ethylene glycol (EG) with Perfluorinated diol (PFOL) increases the availability of hydrogen-bonding sites. This results in an ice formation temperature of -35 °C and an ice adhesion strength of 13 kPa. SS-NMR and low-temperature ATR-FTIR spectroscopy confirm the presence of a QLL on the surface, while modified frost formation patterns demonstrate improved resistance to frost accumulation. The plasticizing effect of IL and DESs increases the elongation at break for modified coatings, while the tensile strength of the PFOL-based DES coating remains unchanged compared to the reference. This phase demonstrates that the combining DESs and ILs as ice-responsive materials outperforms their individual components, leading to durable, high-performance, and sustainable icephobic coatings.

Keywords: Ionic liquids, Dynamic anti-icing coating, Ice adhesion, Icephobic coating, Ice formation, Ion mobility, Ionic hydrogen-bond, Hydrophobicity of coating, Crosslink density, Conductivity, Anti-icing behavior, Deep eutectic solvent, Choline chloride, Hydrogen-bond acceptor, Hydrogen-bond donor, Ethylene glycol, Glycerol, Perfluorinated diol, Anti-frosting, Hydrogen-bonding, Low temperature ATR-FTIR spectroscopy, Solid-state NMR spectroscopy, Quasi liquid layer.

TABLE OF CONTENTS

RÉSUMÉ i
ABSTRACT iii
TABLE OF CONTENTS v
LIST OF FIGURES ix
LIST OF TABLES xiv
LIST OF ABBREVIATIONS xv
LIST OF SYMBOLS xix
DEDICATION xxi
ACKNOWLEDGEMENTS xxii
INTRODUCTION 1
Problem Definition 1
Overview 3
Objectives 6
Originality statement 7
Methodology 9
Thesis outline 12
CHAPTER 1 16
1. LITERATURE REVIEW 16
1.1 Introduction 16
1.2 Exploring anti-icing surfaces and surface icephobicity 19
1.3 Dynamic anti-icing surfaces 22
1.3.1 Dynamic substrates 24
1.3.2 Dynamic interfaces 27
1.3.3 Ionic liquids (ILs) 33
1.3.4 Dynamic ice 51
1.3.5 Deep eutectic solvents (DESs) 56
1.4 Combining dynamic anti-icing strategies 72
1.5 Conclusion 73

CHAPTER 2 74
2. ARTICLE 1: IN-DEPTH ANALYSIS OF THE EFFECT OF PHYSICOCHEMICAL PROPERTIES OF IONIC LIQUIDS ON ANTI-ICING BEHAVIOR OF SILICON BASED-COATINGS 74
2.1 Abstract 74
2.2 Introduction 75
2.3 Materials and methods 79
2.3.1 Materials 79
2.3.2 Methods 80
2.3.3 Surface Characterization 81
2.3.4 Anti-icing assessment 83
2.4 Results and Discussion 86
2.4.1 Surface Characterization 86
2.4.2 Wettability 92
2.4.3 Ice formation 97
2.5 Conclusion 109
CHAPTER 3 111
3. ARTICLE 2: TO BE OR NOT TO BE A HYDROPHOBIC MATRIX? THE ROLE OF COATING HYDROPHOBICITY ON ANTI-ICING BEHAVIOR AND IONS MOBILITY OF IONIC LIQUIDS 111
3.1 Abstract 111
3.2 Introduction 112
3.3 Materials and Methods 115
3.3.1 Chemical Materials 115
3.3.2 Preparation Methods 116
3.3.3 Surface Characterization 119
3.3.4 Anti-icing Properties 121
3.3.5 Assessment of ion Mobility 123
3.3.6 Water Absorption of Coatings 124
3.3.7 Pendulum Hardness 125
3.3.8 Weathering Test 125
3.3.9 Time to First Frost formation under Freeze–Thaw cycles 126
3.4 Results and Discussion 126

3.4.1 Surface Characterization 126
3.4.2 Ion Mobility 135
3.4.3 Anti-icing properties 143
3.4.4 Ice adhesion strength against icing/de-icing cycles and weathering condition 155
3.4.5 Time to First Frost Formation (TFF) under Freeze-Thaw cycles 158
3.5 Conclusion 159
CHAPTER 4 162
4. INNOVATIVE ICE MITIGATION: EXPLORING THE POTENTIAL OF CHOLINE-BASED DEEP EUTECTIC SOLVENTS AND IONIC LIQUIDS SYNERGIES 162
4.1 Introduction 162
4.2 Methodology 165
4.2.1 Materials 165
4.2.2 Synthesis of the ILs 166
4.2.3 Preparation of the DESs 166
4.2.4 Fabrication of Polyurethane coatings 167
4.2.5 ILs Characterization 169
4.2.6 DES characterization 169
4.2.7 Surface characterization 170
4.2.8 Anti-icing Properties 171
4.2.9 Mechanical characterization 174
4.3 Results and Discussion 175
4.3.1 Ionic liquids synthesis 175
4.3.2 Application of choline-based ILs in anti-icing coatings 176
4.3.3 Synergistic combination of DES and IL for anti-icing application 181
4.3.4 Influence of hydrogen-bond donor type in DES on the anti-icing efficacy of coatings 186
4.3.5 Mechanical properties and durability of DES-containing coatings 197
4.4 Conclusion 206
CHAPTER 5 208
5. ARTICLE 3: ICE-RESPONSIVE COATINGS: EVALUATING THE EFFECT OF HYDROGEN BOND DONORS ON DEEP EUTECTIC SOLVENTS/IONIC LIQUIDS ANTI-ICING EFFICIENCY 208
5.1 Abstract 208

5.2 Introduction 209
5.3 Materials and Methods 212
5.3.1 Materials 212
5.3.2 Preparation of the DESs 212
5.3.3 Fabrication of Polyurethane coatings containing ChTFSI and DESs 213
5.3.4 DES characterization 213
5.3.5 Surface characterization 214
5.3.6 Anti-icing Properties 215
5.3.7 Mechanical characterization 219
5.4 Results and Discussion 220
5.4.1 Coatings characterization 220
5.5 Conclusion 239
CHAPTER 6 242
6. Conclusion 242
CHPATER 7 247
7. Recommendations 247
APPENDIX I 251
8. SUPPORTING INFORMATION FOR ARTICLE 1 251
APPENDIX II 255
9. SUPPORTING INFORMATION FOR ARTICLE 2 255
APPENDIX III 264
10. SUPPORTING INFORMATION FOR CHAPTER 4 264
REFERENCES 271

LIST OF FIGURES

Figure 1: Research framework outlining the step-by-step approach employed in this investigation. 10
Figure 1-1: Detrimental Impacts of Ice Formation on Life and Industry [42] (Reprinted with permission). .. 17
Figure 1-2: (a) The key regions adjacent to the ice-substrate interface crucially influence the anti-icing performance of a surface and, (b) DAIS focusing on enhancing the three ice-substrate interfacial regions [18] (Reprinted with permission). 24
Figure 1-3: DAIS incorporate environmentally responsive substrates. (a) Magnetic slippery icephobic surfaces exhibit extremely low adhesion when subjected to a magnetic field [98] and (b) UV-responsive substrates demonstrate controlled lubricant release and achieve low ice adhesion strength under UV irradiation [94] (Reprinted with permission). 26
Figure 1-4: Dynamic Interface Melting in DAIS Innovations: a) Explore superhydrophobic carbon nanotube surfaces with integrated electrothermal effects, as depicted in real-time anti-icing experiments [116] , and b) Harness solar illumination with the photothermal trap to mitigate ice buildup [122] (Reprinted with permission). 32
Figure 1-5: Some chemical structures of representative cations and anions used in protic, aprotic, dicationic, polymeric, magnetic, and solvate ionic liquids. From left to right, the cations (top row) include: ammonium, pyrrolidinium, 1-methyl-3-alkylimidazolium, 1,3-bis[3-methylimidazolium-1-yl]alkane; (second row) phosphonium, pyridinium, poly(diallyldimethylammonium), metal (M^+) tetraglyme. The anions include (third row) halides, formate, nitrate, hydrogen sulfate, heptafluorobutyrate, bis(perfluoromethylsulfonyl)imide, tetrafluoroborate, (bottom row) thiocyanate, hexafluorophosphate, tris(pentafluoroethyl)trifluorophosphate, dicyanamide, poly(phosphonic acid), and tetrachloroferrate [132] (Reprinted with permission). 35
Figure 1-6: Application of ILs [150] (Reprinted with permission). 37
Figure 1-7: Illustrating diverse electrochemical applications of ILs [150] (Reprinted with permission). 38
Figure 1-8: Schematic representation of the distinctive properties of ionogels [189] (Reprinted with permission). 43
Figure 1-9: Dynamic melting of ice on ionogel surface at −20 °C. (a) A frozen droplet on the ionogel surface at 80 minutes. Green and orange dashed lines show the shape of the droplet at 110 and 140 minutes, respectively. (b) A probing needle penetrates the ice shell and into the ice-liquid mixture core of the same frozen droplet at 375 minutes. (c-e) The probing needle detaches the frozen droplet from the ionogel surface. (f) Liquid bridges are monitored during the detachment of the frozen droplet. All images share the same scale bar of 1 mm, shown in panel (g) (red bar). (g) A schematic illustrating the slush formation after ice nucleation and ionic liquid diffusion into the droplet on the ionogel surface. (h) A schematic depicting the ice growth retardation process of the droplet on the ionogel surface. The time indicated in panels (a) and (b) is the actual time of the example images [19] (Reprinted with permission). 46
Figure 1-10: Comparison of condensation-frosting on glass (a) and ionogel surfaces (b). Both samples are cooled from 25 to −20 °C at a rate of 10 °C/min and then maintained at −20 °C in a humid environment (20 °C, 60% RH). Time is recorded from the start of cooling. All images share the same scale bar of 10 μm (red bar in panel b) [19] (Reprinted with permission). 47
Figure 1-11: Demonstration of easy-sliding IGs for Droplet Mobility. (a) An 8 μL water droplet easily slides on a water-immiscible ILG composed of PMMA and [OMIm][BF_4], with the ILG containing 60 mol% [OMIm][BF_4]. (b) In contrast, a decane-immiscible ILG composed of PHEMA and [HOEtMIm][BF_4] exhibits an easy-sliding property for a decane droplet, with the ILG containing 60 mol% [HOEtMIm][BF_4]. (c) Easy-sliding properties are generated when the testing liquid is immiscible with both the ILs and polymer chains that constitute the ILG. A green checkmark indicates the corresponding ILG is easy-sliding, while a red cross

indicates the ILG cannot be synthesized. (d) Molecular structures of the polymers and ILs used for the preparation of ILGs. The tilt angles in (a) and (b) are fixed at 10° [199] (Reprinted with permission). 48
Figure 1-12: a) Schematic illustration of the fabrication process of the ionic-liquid-infused surface (ILIS), b) Icing time and ice adhesion strength on glass and the ILIS at −20 °C. c) Phase separation process of 30 wt.% TPU/[OMIM]BF_4 solution under a hot-stage microscope. The scale bars are 100 μm. And digital images of the phase separation process during natural cooling. d) Cycled de-icing test on the ILIS at −20 °C [27] (Reprinted with permission). 49
Figure 1-13: DAIS through Ice-Free Zone Programming: a) Mechanism of ice formation on rough hydrophilic, hydrophobic, and Janus surfaces [207]. b) Patterned polyelectrolyte coatings for dynamically controlling large-scale ice-free regions [209] (Reprinted with permission). 54
Figure 1-14: Choline chloride and urea mixtures at 303 K (mol % ChCl, left to right: 0, 10, 20, 33 (χ_{eut}), 40, 50, 100). The lowest observed melting point for this binary mixture occurs at a 1:2 ratio, with a melting point of 12 °C, making it a liquid at room temperature. This ratio is defined as the eutectic composition (χ_{eut}) [225] (Reprinted with permission). 56
Figure 1-15: (a) Schematic representation of the formation of a DES, illustrated using ChCl) and urea. (b) Examples of common HBA and HBD typically used [233] (Reprinted with permission). 58
Figure 1-16: Schematic illustration of a eutectic point on a binary phase diagram [225] (Reprinted with permission). 61
Figure 1-17: Bio-inspired eutectogels enabled by binary natural deep eutectic solvents (NADESs): Interfacial anti-frosting, freezing-tolerance [270] (Reprinted with permission). 69
Figure 2-1: Chemical structures of ILs. 80
Figure 2-2: Schematic of the designed set ups; (a) Push-off and (b) CAT, for measuring ice adhesion strength. 85
Figure 2-3: FT-IR spectra of reference sample lacking ILs, ILs-containing coatings, ILI and ILB. 87
Figure 2-4: XPS spectra of the prepared coatings; (a) Sylgard 184, (b) CILI, (c) CILB, including higher resolution spectra of the CILI surface for (d) C 1s and (e) F 1s. 89
Figure 2-5: The EDX mapping of the produced samples; (a) Sylgard 184, (b) CILI, and (c) CILB with the distribution of Si, F, S, and B elements over the surface. 91
Figure 2-6: The 3D profile and roughness value of the designed samples; (a) Sylgard 184, (b) CILI, (c) CILB, and (d) CILIB. 92
Figure 2-7: Wetting properties of Coatings, including (a) static and (b) dynamic water contact angles. 95
Figure 2-8: Water contact angles of coatings over time. 97
Figure 2-9: (a) Delayed ice nucleation of water and on the surface of PDMS-based samples and coatings containing ILs, (b) Schematic of the effective parameters of ILs structures on ice nucleation temperature... 100
Figure 2-10: Ice formation time on the surface of coatings. 102
Figure 2-11: Ice adhesion strength (kPa) of coatings, obtained using Push-off and Centrifugal tests. 103
Figure 2-12: ^{1}H spectra of (a) Sylgard 184+water, (b) CILI+water, and (c) CILB+water between 276 K (blue) and 253 K (yellow), obtained by SS-NMR spectroscopy. (d) Schematic of lowering ice adhesion strength in presence of ILs through formation of QLL at interface. 106
Figure 2-13: Ice adhesion strength (kPa) of coating over 10 ice/de-icing cycles, obtained by push-off. 109
Figure 3-1: FTIR spectra of the prepared coatings; (a) PU-based and (b) Silicon-based reference samples with and without ILs. 128
Figure 3-2: (a) Experimental observation and optical microscopy images of PLI and SLB coatings, and the SEM/EDX mapping of; (b) PU-based, and (c) silicon-based coatings with and without ILs. 130
Figure 3-3: Wetting properties of the stoichiometric coatings; (a) PU- and (b) Silicon-based reference samples with and without ILs in different percentages. 132
Figure 3-4: Schematic of different hydrogen-bond donor ability of ILs to water droplets. 134
Figure 3-5: The variation of conductivity with frequencies from 10^1 Hz to 10^7 Hz at different temperatures, for coatings lacking and containing 20 wt.% of ILs. 138
Figure 3-6: The measured swelling ratios of non- stoichiometric and stoichiometric samples, immersed in water over time, for (a) PU-based and (b) silicon-based coatings. 140

Figure 3-7: (a) UV-Vis spectra of remained water solution after 72 hours, (b) the measured ionic conductivity of water solutions at room temperature and -5°C, obtained by conductivity meter and schematic of effect of crosslink density on ions mobility. 142
Figure 3-8: Delayed ice formation temperature on the surface of samples; (a) PU-based and (b) Silicon-based samples lacking and containing ILs in different percentages. Images in right indicate top-down view of coated aluminum pans after placing water droplets during cooling measurements using a portable optical microscope in DSC. 144
Figure 3-9: Delayed ice formation time on the surface of samples, as well as their form of frozen droplet; PU- and Silicon-based samples lacking and containing ILs in different percentages. 146
Figure 3-10: Ice adhesion strength of the designed coatings, obtained by (a) the Push-off test, and (b) the Centrifugal test. 148
Figure 3-11: Ice adhesion strength of samples containing and lacking ILs, including (a) PU-based, and (b) Silicon-based coatings over 20 icing/de-icing cycles determined by the push-off test. 150
Figure 3-12: Schematic of proposed anti-icing mechanism of ILs. 152
Figure 3-13: ^{1}H spectra of (a) PU + water, (b) PLI-10 + water, and (c) PLB-10 + water between 276 K (blue) and 253 K (yellow) as well as T_2 relaxation data, obtained by SS-NMR spectroscopy. (d) Schematic of formation of a thicker Quasi-Liquid Layer (QLL) at the int 154
Figure 3-14: (a) The ice adhesion strength of coatings exposed 20 icing/de-icing cycles after and before QUV obtained by push-off test for non-stoichiometric and stoichiometric coatings containing 10 wt.% of ILs after QUV, and (b) 3D profile maps of coatings samples 157
Figure 3-15: Time to first frost formation of (a) PU-based and (b) silicon-based samples as well as their images after 7 freeze-thaw cycles. 159
Figure 4-1: Surface wetting properties of the PU coatings containing various percentages of choline-based ILs. 176
Figure 4-2: Ice formation temperature of water on the surface of PU coatings containing, (a) $ChNO_3$ and (b) ChTFSI. 179
Figure 4-3: (a) Ice adhesion strength (kPa) of coatings as determined through a push-off test; (b) diagram depicting the reduction of ice adhesion strength in the presence of ILs because of a QLL formed at the interface. 181
Figure 4-4: Surface wetting properties of the PU and optimized PU coatings containing ILs and DES. 182
Figure 4-5: (a) Ice formation temperature and (b) ice adhesion strength of PU and optimized PU coatings containing ILs in the presence of DES. 185
Figure 4-6: Surface wetting properties of PU coatings having ChTFSI and containing different DESs. 187
Figure 4-7: FT-IR spectrum of PU coatings containing ChTFSI with different DESs. 188
Figure 4-8: (a) Surface morphology and EDX mapping images of PU coatings containing ChTFSI with different DESs, and (b) cross sectional images of the freeze-dried coatings. 190
Figure 4-9: (a) Ice formation temperature and (b) ice adhesion strength of PU and optimized PU coatings containing ChTFSI with DESs. 192
Figure 4-10: Illustration depicting hydrogen-bonding networks within DESs that create accessible sites for potential hydrogen-bonding interactions with ILs. 193
Figure 4-11: DSC heating curves of DESs with (a) water and (b) without water. 195
Figure 4-12: ^{1}H spectra acquired via SS-NMR spectroscopy for (a) PU + water; (b) PCTFSI-10 + water; (c) PCTFSI-10-EG + water; and (d) PCTFSI-10-GL + water, spanning temperatures from 276 K (depicted in blue) to 253 K (depicted in yellow). The percentages at each temperature quantify the proportion of non-frozen water molecules present at the interface. 197
Figure 4-13: (a) Mechanical properties and (b) T_g of developed coatings containing ChTFSI and various DESs, obtained by tensile strength test. 200
Figure 4-14: (a) Ice adhesion strength and surface hardness of PU coatings exposed to 20 icing/de-icing cycles before and after QUV, as obtained by a push-off test; and (b) 3D profile maps of coatings samples before and after icing/de-icing cycles. 202
Figure 4-15: (a) The time required for frost formation on coatings during seven frost/defrosting cycles; and (b) corresponding images of the coatings during the seven cycles. 204

Figure 4-16: (a) Time required to attain to the Peltier temperature before and after the seven frost/defrost cycles; and (b) IR thermography of the samples during frost formation over time. 205
Figure 5-1: Schematic representation of the cold-based apparatus used for low-temperature ATR-FTIR spectroscopy. 218
Figure 5-2: Surface (a) chemistry and (b) wetting characteristics of the PU coatings. 221
Figure 5-3: (a–c) XPS spectra of the coatings and (d) surface morphology and cross-sectional images of the freeze-dried PIL-PFOL coating. 223
Figure 5-4: High-resolution spectra of the PIL-PFOL coating for (a) C 1s, (b) O 1s, (c) F 1s, and (d) N 1s. 225
Figure 5-5: (a) Ice formation temperature and adhesion strength of PU coatings, (b) diagram depicting the reduction of ice adhesion strength in the presence of IL/PFOL-based DES because of a QLL formed at the interface. 227
Figure 5-6: DSC heating curves analyzing the thermal properties of DESs (a) with water and (b) without water. 229
Figure 5-7: ^{1}H spectra acquired via SS-NMR spectroscopy for (a) PU + water; (b) PIL-EG + water; (c) PIL-PFOL + water; and (d) T_2 relaxation time measurements, spanning temperatures from 276 K (blue) to 253 K (yellow). 231
Figure 5-8: ATR-FTIR spectra of the PU/D2O coating recorded at different temperatures during the cooling procedure. 233
Figure 5-9: ATR-FTIR spectra of the PIL-EG/D_2O coating recorded at different temperatures during the cooling procedure. 234
Figure 5-10: ATR-FTIR spectra of the PIL-PFOL/D_2O coating recorded at different temperatures during the cooling procedure. 235
Figure 5-11: Mechanical properties of developed coatings containing various DESs, obtained by tensile strength test. 236
Figure 5-12: (a) Ice adhesion strength and surface hardness of PU coatings exposed to 20 icing/de-icing cycles before and after QUV, as obtained by a push-off test; and (b) 3D profile maps of PIL-PFOL coating samples before and after icing/de-icing cycles. 237
Figure 5-13: (a) The time required for frost formation on coatings during seven frost/defrosting cycles; and (b) corresponding images of the coatings during frost formation. 239
Figure A-I. 1:Proposed schematic reactions between ILB and base Sylgard 184 part A, including FTIR spectra of the mixture. 253
Figure A-I. 2:FT-IR spectra of reference sample lacking ILs, ILs-containing coatings, ILI and ILB. 254
Figure A-II. 1: Schematic of experimental setup for measuring freezing delay time. 256
Figure A-II. 2: Schematic of (a) the push-off test and (b) the centrifugal test. 257
Figure A-II. 3: Schematic of broadband dielectric spectroscopy setup for measuring dielectric properties and conductivity from RT to subzero temperatures. 258
Figure A-II. 4: FTIR spectra of the mixtures of LB/polyol and LB/part A Sylgard 184. 259
Figure A-II. 5: Wetting properties of the non-stoichiometric reference coatings lacking and containing 10 wt.% ILs; (a) WCAs- and (b) SAs. 260
Figure A-II. 6: The variation of dielectric constant with frequencies from 10^1 Hz to 10^7 Hz at different temperatures, for coatings lacking and containing 20 wt.% of ILs. 261
Figure A-II. 7: The variation of dielectric loss factor with frequencies from 10^1 Hz to 10^7 Hz at different temperatures, for coatings lacking and containing 20 wt.% of ILs. 262
Figure A-II. 8: Schematic of ions screening from their respective surroundings of polarized molecules of atoms. 263
Figure A-III. 1: Schematic illustration of the preparation procedure of choline-based ILs. 264
Figure A-III. 2: Schematic diagram of the experimental setup for measuring ice adhesion strength using the push-off test. 265
Figure A-III. 3: Schematic illustration of the experimental setup for evaluating anti-frosting capacity of coatings. 266
Figure A-III. 4: (a) Reaction procedure for synthesis of choline-based ILs and (b) FT-IR spectrum of ChCl, $ChNO_3$ and ChTFSI. 268

Figure A-III. 5: ^{1}H and ^{13}C NMR spectrum of (a) $ChNO_3$ and (b) ChTFSI. 269
Figure A-III. 6: Diagram illustrating the procedural methodology employed in this research. 270

LIST OF TABLES

Table 2-1: Composition of each formulation for fabrication of designed coatings. 81
Table 2-2: T_2 relaxation times of designed coatings, obtained by ^1H solid-state NMR spectroscopy. 107
Table 3-1: Composition of each formulation for fabrication of silicon-based coatings. 117
Table 3-2: Composition of each formulation for fabrication of PU-based coatings. 118
Table 3-3: Dielectric properties of coatings with and without 20 wt.% of ILs at 10^1 Hz from RT to subzero temperatures. 135
Table 4-1: Composition of each formulation for fabrication of PU-based coatings containing ILs (g). 168
Table 4-2: Composition of each formulation of PU-based coatings containing DES (g). 168
Table 4-3: Mechanical properties of developed PU coatings containing ChTFSI and various DESs. 199
Table 5-1: Composition of each formulation of PU-based coatings containing DES (g). 213
Table A-I. 1: Evaluation of reactivity of each ILs in either part of Sylgard 184. 252
Table A-II. 1: Chemical structure of the used ILs in this study. 256
Table A-II. 2: Surface hardness, roughness (Sq) and Yellowness index of specimens before and after 20 icing/de-icing cycles and QUV chamber exposure test. 263

LIST OF ABBREVIATIONS

IL	Ionic Liquid
RT-ILs	Room temperature ionic liquids
DES	Deep Eutectic Solvent
FTIR	Fourier transform infrared
ATR-FTIR	Attenuated Total Reflectance-Fourier transform infrared spectroscopy
XPS	X-ray photoelectron spectroscopy
SEM/EDX	Scanning electron microscopy-energy dispersive X-ray analysis
SS-NMR	Solid-state Nuclear Magnetic Resonance spectroscopy
QLL	Quasi-liquid like layer
EG	Ethylene glycol
GL	Glycerol
PFOL	Perfluorinated diol
DAISs	Dynamic anti-icing surfaces
SHSs	Superhydrophobic surfaces
SLIPS	Slippery liquid-infused porous surfaces
HBDs	Hydrogen-bond donors
PSLs	Phase-switching liquids
PDMS	Polydimethylsiloxane
DSC	Differential scanning calorimetry
CAT	Centrifugal adhesion test
PU	Polyurethane
ChTFSI	Choline bis(trifluoromethanesulfonyl)imide
SAIS	Static anti-icing surfaces
THF	Tetrahydrofuran
RTS-organogel	Reversible thermosecreting organogel

PTSLIPS	Phase-transformable slippery liquid-infused porous surfaces
MAGSS	Magnetic slippery surfaces
UVRS	UV-responsive substrates
LLGs	Liquid layer generators
NACI	Nanoscale crack initiators
MICI	Microscale crack initiators
MACI	Macroscale crack initiators
PVA	Polyvinyl alcohol
MWCNTs	Multiwalled carbon nanotubes
PILs	Protic ILs
AILs	Aprotic ILs
DSSCs	Dye-sensitized solar cells
SAILs	Surface-active ILs
IGs	Ionogels
PMMA	poly(methyl methacrylate)
PVDF	poly(vinylidene fluoride)
PEO	poly(ethylene oxide)
ESW	Electrochemical stability window
CSA	Critical sliding angle
TPU	Thermoplastic polyurethane
[OMIM]BF_4	1-octyl-3-methylimidazolium tetrafluoroborate
ILIS	Ionic-liquid-infused surface
PHEMA	Polyhydroxyethylmethacrylate
[HOEtMIm][BF_4]	Hydrophilic 1-ethyl-3-methylimidazolium tetrafluoroborate
PMETAC	Poly([2 (methacryloyloxy)ethyl]
OEGDMA	Oligo(ethylene glycol) dimethacrylate
$TFSI^-$	Trimethylammonium bis(trifluoromethanesulfonyl)imide
SIPNs	Semi-interpenetrating polymer networks
PIE	Polyionic elastomer

AA	Acrylic acid
AAm	Acrylamide
DMAPS	Zwitterion [2-(methacryloyloxy)ethyl]dimethyl-(3-sulfopropyl)ammonium hydroxide
AgI	Silver iodide
ASG	Along-surface growth
OSG	Off-surface growth
P(PEGMA)	Poly(poly(ethylene glycol) methyl ether methacrylate
AFPs	Antifreeze proteins
IBFs	Ice-binding faces
NIBFs	Non-ice-binding faces
GO	Graphene oxide
SCh	Cyclohexane
LIS	liquid-infused surfaces
HBAs	Hydrogen bond acceptors
DEM	Deep eutectic mixture
ChCl	Choline chloride
NADES	Natural deep eutectic solvents
THEDES	Therapeutic deep eutectic solvents
API	Active pharmaceutical ingredient
ARMMBs	Aqueous rechargeable multivalent metal-ion batteries
AZIBs	Aqueous Zn-ion batteries
VAM	Vanillin-derived monomer
CMCS	Carboxymethyl chitosan
DIWHs	Deep eutectic solvent-in-water hydrogels
Ls	Sodium lignosulfonate
PAA	Polyacrylic acid
PHEAA	Poly(N-hydroxyethyl acrylamide)
TENGs	Triboelectric nanogenerators
PDESs	Polymerizable deep eutectic solvents

WLI	White light interferometry
PSI	Phase-shifting interferometry
PCMs	Phase change materials
LiTFSI	Lithium bis(trifluoromethanesulfonyl)imide
HDI	Hexamethylene diisocynate
YI	Yellowness index
$ChNO_3$	Choline nitrate
WCA	Water contact angel
CA_t	Contact angle over time
SA	Sliding angle
CAH	Contact angle hysteresis
^{1}H-NMR	Proton nuclear magnetic resonance spectroscopy
^{13}C-NMR	Carbon nuclear magnetic resonance spectroscopy
TFF	Time to first frost formation
DFT	Density Functional Theory
IN	Ice nucleation
IGR	Ice growth recrystallization

LIST OF SYMBOLS

$\boldsymbol{\gamma_{LV}}$	Surface tension
$\boldsymbol{W_a}$	Practical work of adhesion per unit area
$\boldsymbol{v_m}$	Molecular volume
$\boldsymbol{\gamma_{SL}}$	Solid-liquid interfacial energy
$\boldsymbol{\theta_{rec}}$	Receding contact angle
$\boldsymbol{\theta_{Adv}}$	Advancing contact angle
A	Iced area
h	Planck's constant
J_0	Nucleation rate
ΔG_{act}	Activation energy barrier
r	Ice embryo
r_i^*	Critical ice embryo
k	Boltzmann's constant
m	Ice mass
$\boldsymbol{\theta_{iw}}$	Contact at ice-water interface
q	Heat flow rate
r	Beam radius
R_q	Root-mean-square deviation of line roughness
S_{ku}	Kurtosis coefficient of area roughness
S_q	Root-mean-square height of area roughness
S_{sk}	Skewness coefficient of area roughness
T	Absolute temperature
$T_{f,o}$,	Onset temperature on the freezing
T_g	Glass transition temperature
T_m	Melting temperature
m_p, $T_{m,o}$	Onset temperature on the heating
T_{ps}	Critical phase separation temperature
$T_{eutectic}$	Melting point of mixture at eutectic composition
ΔT_f	Difference in freezing points
χ_{eut}	Eutectic ratio
W	Weight of the droplet
α	Inclined angle
Δg	Diffusion activation energy
ΔT_s	Supercooling degree
ω	Angular velocity
$\boldsymbol{k}$	Thermal conductivity
$\boldsymbol{\rho}$	Density
$\boldsymbol{\tau_c}$	Ice adhesion strength
$\boldsymbol{G}$	Surface energy
$\boldsymbol{E^*}$	Bulk Young's modulus
$\boldsymbol{a}$	Total crack length
$\boldsymbol{\Lambda}$	nondimensional constant
T_2	Relaxation time of water proton

ε'	Dielectric constant
ε''	Dielectric loss
σ	Conductivity
C_0	Vacuum capacitance
Q_t	Water absorbency
m_t	Weights of the samples in the swollen state
m_0	Weights of the samples in the dry state
$[BF4]^-$	Counter ion, tetrafluoroborate
$[PF6]^-$	Counter ion, hexafluoroborate
$[DCA]^-$	Counter ion, Dicyanamide
TFSI, NTF_2^-	Counter ion, bis(trifluoronethylsolfunyl)imide
NO_3^-	Counter ion, nitrate
Wt.%	Weight percentage
Cat^+	Cation
X^-	Lewis base
Y^-	Lewis or Bronsted base
N/m	Surface Tension (γLV)
J/m^2	Work of Adhesion (Wa)
m^3/mol	Molecular Volume (vm)
K	Absolute Temperature (T)
°C or K	Glass Transition Temperature (Tg)
W/m·K	Thermal Conductivity (k)
kg/m^3	Density (ρ)
kPa	Ice Adhesion Strength (τ_c)
S/m	Conductivity (σ)

DEDICATION

This thesis is dedicated to ***my parents, [Roya and Yadollah],*** my beloved sister and brother, and my cherished nieces and nephew, whose enduring love, support, and encouragement have been the driving force behind my academic journey. Your sacrifices, guidance, and belief in me have been my greatest source of strength and motivation. This accomplishment is as much yours as it is mine, and I am profoundly grateful for everything you have done for me. Thank you for being my source of support and for always believing in my dreams.

And importantly, to ***my loving husband, Arsalan Asadi,*** my constant source of encouragement and inspiration. Without his support and love, this achievement would not have been possible.

ACKNOWLEDGEMENTS

First and foremost, I wish to extend my deepest gratitude to my research supervisor, *Prof. Gelareh Momen*. Her steadfast support, insightful guidance, and unwavering kindness have been the cornerstones of my doctoral journey. Her mentorship has been a beacon of strength and inspiration throughout this research. This dissertation stands as a testament to her dedication, and I am profoundly grateful for her encouragement, patience, and nurturing throughout this endeavor.

I am also profoundly appreciative of my co-supervisor, *Prof. Reza Jafari*, whose invaluable contributions and constant involvement were crucial in navigating the challenges I encountered. His expertise and support have been instrumental in the successful progression of my project.

My heartfelt thanks extend to the members of my committee, *Prof. Issouf Fofana, Prof. Véronic Landry and Prof. Yasar Kocaefe*, for their insightful guidance and unwavering support. Their constructive feedback and encouragement have significantly enriched my work.

I would like to express my sincere thanks to all the professionals and technicians who contributed to this project. Special gratitude goes to *Dr. Jean-Denis Brassard, Ms. Caroline Blackburn, Ms. Nathalie Gagné, and Ms. Shan Yang* at the Anti-icing Materials International Laboratory (AMIL), UQAC, for their assistance. My appreciation also goes to *Mr. Luc Chatigny* from Laboratoire Revêtements Glaciophobes et Ingénierie des Surfaces (LARGIS), *Ms. Caroline Potvin*, the laboratory assistant of the chemistry department, and Ms. Kouba Marie Lucia Yapi for their expertise in dielectric spectroscopy analyses.

Furthermore, I am grateful to the *Department of Fundamental Sciences* at UQAC for providing the facilities, equipment, and characterization tools essential for the synthesis and analysis of ionic liquids, which have significantly enhanced the outcomes of my research.

Additionally, I extend my thanks to *Prof. Hadis Zarrin* from Toronto Metropolitan University. Her support and the incredible opportunity to visit during the final months of my PhD sabbatical were invaluable. Her guidance and insights have been crucial to the success of my research.

I am deeply thankful to the *Natural Sciences and Engineering Research Council of Canada (NSERC)* for their essential financial support, which has been the backbone of this research endeavor.

Lastly, I would like to express my heartfelt thanks to my family and friends, particularly those in LARGIS: *Anahita Allahdini, Samaneh Heidarian, Mohammadreza Shamshiri, Shamim Roshan, Helya Khademsameni, Mohammadsadegh Koochaki, Mohammad Bakhtiari, Samaneh Keshavarzi and Ehsan Bakhshandeh*. Their presence and support have made this academic journey not only possible but profoundly meaningful and memorable.

INTRODUCTION

Problem Definition

Icing is widely recognized as a prevalent and hazardous natural phenomenon that impacts the performance of exposed infrastructure and equipment, leading to safety, economic, and operational challenges. It causes significant damage in sectors such as telecommunications, power transmission, wind turbines, marine vessels, heat exchangers, and transportation [1,2]. Additionally, ice and frost removal degrade components, especially in aviation, due to costly and energy-intensive repetitive icing/de-icing cycles [3,4].

One notable example of the severe impact of icing is the catastrophic blackouts that threaten electrical networks and high-voltage power lines under wet snow conditions. In Italy, wet snow experiences an annual cost of €200 million in damage to electrical networks [5]. The 2013 ice storm in eastern Canada left over 1 million people without power and resulted in insured losses amounting to approximately CAD 200 million [6]. In Oklahoma, the October 2020 ice storm damaged over 4,200 power poles and left 300,000 people without electricity [7]. Texas experienced its most costly power outage in February 2021 when severe winter storms impacted 4.5 million households and led to the deaths of more than 200 people [8]. Additionally, accreted ice in refrigeration systems disrupts airflow, leading to a roughly 20% increase in energy consumption [9]. Shipping operations in the Arctic Ocean face significant risks due to ice accretion from freezing rain, supercooled fog, and snow. This ice buildup can shift the center of gravity, destabilizing ships and offshore structures and leading

to numerous accidents in marine systems. Catastrophic frosting events cause significant damage globally each year, particularly in aviation, transportation, energy, and agriculture. For instance, frost damages crop and agricultural productivity. In 2017, the frost event in Europe caused significant crop damage, leading to €3 billion in losses. Frost and icing cause significant disruption to roads, bridges, and railways, leading to accidents and costly repairs. In 2019, it was estimated that frost-related road accidents in the U.S. resulted in more than 1,300 deaths and $4 billion in damages. These financial and mechanical challenges have heightened interest in designing and fabricating icephobic strategies and surfaces to mitigate the detrimental effects of icing [10,11].

A through on literature survey, various traditional or active methods are employed to address icing issues. These include:

1. Mechanical de-icing through external force,
2. Chemical anti-icing/de-icing using low-freezing-point agents, and
3. Thermal anti-icing/de-icing [12,13].

While these active methods are effective, they tend to be time-consuming, costly, and energy-intensive. In contrast, passive anti-icing strategies, such as the development of ice-resistant surfaces or coatings, offer a more economical and energy-efficient alternative. Although active methods are still widely utilized for certain infrastructures, incorporating passive anti-icing surfaces can provide cost-effective solutions and can also be combined with active methods to create hybrid approaches [14,15].

Over the decades, surfaces tailored for anti-icing purposes, with low ice adhesion strength to hinder ice formation, are crafted to mitigate icing issues and ease the removal of ice from exposed surfaces [14,16,17]. The design principles for anti-icing surfaces have transitioned from static models to dynamic ones, placing a greater emphasis on enhancing dynamic properties at the substrate, ice, or interface. This shift aims to ensure durability under prolonged exposure and extremely low temperatures [18]. By introducing dynamic features at the ice-substrate interface, it becomes possible to fine-tune interactions, significantly reducing ice adhesion. Addressing the growing need for sustained icing protection, ionic liquids (ILs) emerge as highly promising, especially for sub-freezing applications, by imparting dynamic properties at the interface [19].

Dynamic anti-icing surfaces (DAISs) represent a revolutionary advancement in high-tech industries, offering significant potential for use in challenging environments. Unlike traditional static coatings that maintain consistent functionality based on their formulation, DAISs integrate evolving properties that continue to mitigate interactions between ice and substrates even after ice formation occurs [18]. This research project aims to dissect the application potential of ILs in anti-icing. Accordingly, this project set out to investigate and optimize effective parameters for fabrication and development of novel anti-icing coatings containing ILs.

Overview

Over the years, extensive efforts have been dedicated to advancing passive anti-icing surfaces, such as superhydrophobic surfaces (SHSs) and slippery liquid-infused porous surfaces (SLIPS) [20,21]. Despite significant progress in creating ice-repellent coatings,

there remains a need to deepen our understanding of their underlying principles. Current anti-icing surfaces primarily adopt a static approach, modifying surface chemistry, physics, or substrate properties (e.g. surface modulus) to deter ice formation. However, factors like time, temperature variations, and external influences impact the structures and properties at the ice-substrate interface [18]. Moreover, the limited durability of SHSs and SLIPS has restricted their practical utility in combating surface icing, necessitating a shift towards enabling dynamic alterations in the chemical and physical states of the ice-substrate interface to enhance anti-icing capabilities [22–24].

This transition from static to dynamic anti-icing surfaces has stimulated research into integrating innovative agents that facilitate dynamic melting at the interface, addressing challenges posed by harsh environmental conditions [18]. Introducing dynamic properties at the ice-substrate interface allows for manipulation of interface interactions to reduce ice adhesion strength. However, developing an ideal anti-icing and anti-frosting coating still faces several challenges. ILs show promise as candidates for inducing dynamic interface melting due to their exceptionally low freezing temperatures, potentially forming a thicker interfacial liquid layer [19,25].

The exploration of ILs' anti-icing capabilities has been relatively understudied, and their application in coatings is still emerging [26]. Nonetheless, pioneering research has ignited significant efforts to manipulate dynamic interfacial properties, driving the innovation of IL-infused surfaces tailored for complex practical scenarios [19,27]. Additionally, polymer electrolytes containing ILs show great promise for energy storage, facilitating solid-state electrochemical capacitors for next-generation wearable electronics and Internet-of-Things devices. Despite this potential, developing solid electrolytes that

perform reliably at sub-zero temperatures remains a challenging yet essential task, particularly for outdoor winter applications [28].

Lately, deep eutectic solvents (DESs), a novel class of eco-friendly IL analogues, have captured significant attention due to their similar properties [29,30]. A comprehensive review of existing literature reveals a striking gap in research focusing on the anti-icing capabilities of DESs [31]. Moreover, these versatile materials have shown promise in creating conductive gels and elastomers, particularly for flexible strain sensors and Triboelectric Nanogenerators. This has sparked the interest of various scientific communities and industries, seeking solutions for challenges in outdoor and extreme environments [32–36].

Accordingly, this PhD thesis initially examines the impact of two distinct room temperature ionic liquids (RT-ILs) on ice nucleation and adhesion strength within silicon elastomer coating. The research aims to provide a detailed understanding of how the mobility and physicochemical properties of ILs affect their anti-icing performance. After a thorough analysis of IL chemistry and its influence on coating performance, key factors influencing ion mobility were explored, including the effects of IL properties and the hydrophilicity or hydrophobicity of the matrix on anti-icing effectiveness. Consequently, silicon and polyurethane coatings—both commonly used in industrial applications—were selected for a comparative and comprehensive analysis of ILs in terms of their anti-icing properties.

The findings underscore the critical role of matrix selection and IL chemistry in advancing coatings for extreme cold environments. Notably, the potential of DESs as alternative or supplementary agents for more efficient ice management is particularly

compelling. Subsequent phases focused on investigating aliphatic ILs by initiating the synthesis and characterization of choline-based ILs containing both hydrophilic and hydrophobic anions. Integration of these ILs with choline-based DESs, which offer diverse hydrogen-bond donors (HBDs), aimed to enhance the system's hydrogen-bonding donor and improve the anti-icing properties of the surfaces.

Objectives

This research mainly aimed to investigate and optimize key parameters for designing novel anti-icing coatings with ILs. By exploring the unique properties of DESs, particularly their heat capacity and hydrogen-bonding networks as phase-switching liquids (PSLs), this study aims to more effectively delay condensation-induced frosting and prevent cascade freezing.

Below are the outlined objectives in sequential order:

- Explore the chemistry and role of ILs in enhancing anti-icing properties.
- Establish a clear and rational understanding of the relationship between IL mobility, physicochemical characteristics, and their anti-icing behavior from a coating perspective.
- Investigate how matrix hydrophobicity and crosslinking density influence IL mobility and anti-icing effectiveness.
- Optimize key parameters such as IL type, concentration, and matrix composition to achieve higher IL mobility.

- ❖ Assess the anti-icing performance of the coatings under accelerated weathering conditions.
- ❖ Investigate the anti-icing properties of synthesized aliphatic ILs and evaluate the feasibility of combining DESs with these ILs to inhibit ice growth.
- ❖ Study the effect of diverse HBD component within DES systems on anti-icing properties of the coatings.
- ❖ Investigate the mechanical properties of the resulting coatings.

Originality statement

The current body of literature underscores a notable void in research concerning surface properties, specifically the anti-icing capabilities of emerging surfaces incorporating ILs. This gap has ignited significant interest within the coating realm, driven by the diverse and advantageous physical and chemical attributes inherent to ILs. However, the nascent state of anti-icing surfaces containing ILs, primarily existing in forms such as bulk materials or gels, presents a challenge. Pioneering investigations, predominantly centered on IL-based gel formulations, have spurred exploration into the dynamic properties of ice interfaces from a coating perspective. These endeavors illuminate novel pathways for designing IL-infused coatings capable of addressing challenges associated with severe environmental conditions, including extreme cold and prolonged exposure times.

To the best of current knowledge, there exists a significant gap in research concerning the application of ILs for anti-icing purposes, particularly in the systematic comparison of these ILs and the establishment of correlations between their key parameters—such as

coating hydrophilicity/hydrophobicity, IL mobility, and efficacy in sub-freezing conditions. Thus, the initial phases involve dissecting critical IL parameters and their impact on anti-icing properties. This includes establishing a coherent relationship between the chemical and physical attributes of various ILs within different matrixes through comprehensive analysis, aimed at comparing IL mobility. This approach seeks to provide a more detailed perspective for advancing ILs in the context of enhancing sustainable icephobicity in coatings.

Moreover, upon thorough review of existing literature, a prominent research gap emerges concerning the anti-icing attributes of DESs, considered a subset of ILs. Exploiting DESs to mitigate ice formation could significantly advance anti-icing technologies. A comprehensive exploration of ILs and their potential synergy with DESs presents opportunities across diverse fields, including artificial intelligence, energy storage, and the development of bioinspired surfaces endowed with exceptional anti-freezing properties. Hence the originality of this project is summarized in the following statements:

- Explore fundamental parameters for selecting ILs and matrixes to develop long-lasting anti-icing coatings.
- Conducting an exhaustive comparative analysis of ILs based on their unique physicochemical properties to determine their anti-icing efficacy.
- Conceptualization and evaluation of anti-icing capabilities in coatings exhibiting both hydrophilic and hydrophobic characteristics, with diverse IL concentrations: performing an in-depth comparative analysis of IL mobility to assess their effectiveness.

- Assessment of anti-icing characteristics in an optimized matrix, identified from previous research phases, integrating aliphatic ILs to enhance outdoor performance.

- Exploration and detailed assessment of the anti-icing efficacy of Deep Eutectic Solvents (DESs), focusing on their unique properties of HBDs component.

- Evaluating the potential for developing hybrid coatings that synergistically combine ILs and DESs to achieve superior anti-icing properties, thus addressing complex environmental challenges more effectively.

Methodology

The main goal of this research is to investigate and optimize the key parameters involved in fabricating novel anti-icing coatings containing ILs. Given the significant potential of DESs in addressing ice growth more efficiently, our study outlines a detailed methodology for designing coatings that integrate ILs and DESs in different phases, as depicted in Figure 1.

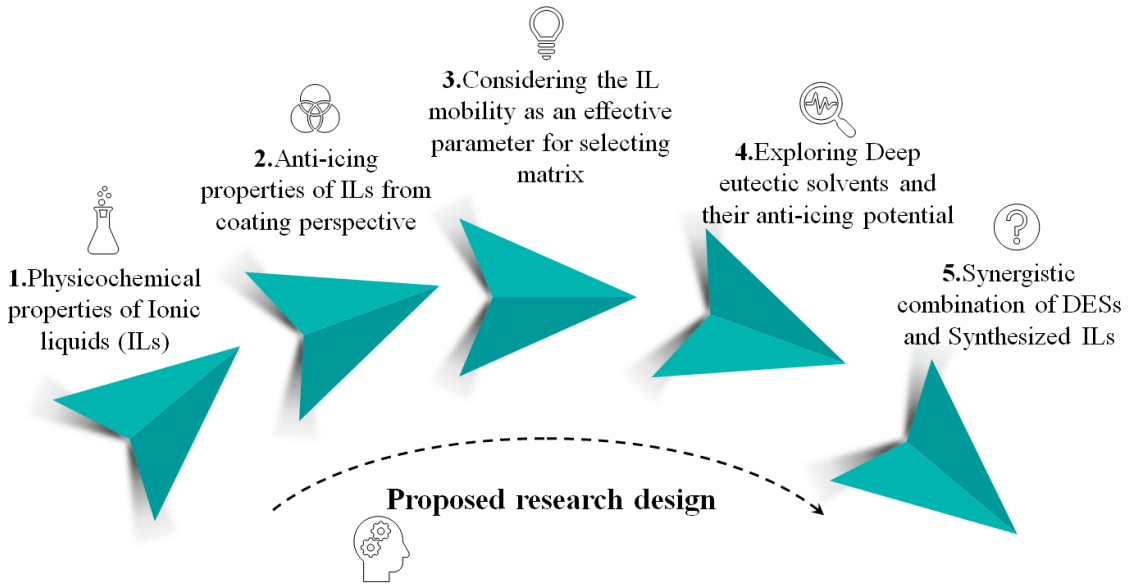

Figure 1. Research framework outlining the step-by-step approach employed in this investigation.

In the initial phase, our objective is to explore the effects of two distinct aromatic-based RT-ILs on the anti-icing properties of coatings based on Sylgard 184 silicon elastomer, a prevalent industrial choice. We aimed to establish a comprehensive understanding of how IL mobility and physicochemical properties influence their anti-icing performance. To achieve this, we formulated Polydimethylsiloxane-based (PDMS) coatings by incorporating ILs (either individually or in combination) into the Sylgard 184 base. We characterized the surface chemistry of these coatings and the presence of specific IL anion groups using techniques such as Attenuated Total Reflectance-Fourier Transform Infrared Spectroscopy (ATR-FTIR), confirmed through X-ray Photoelectron Spectroscopy (XPS) and Scanning Electron Microscopy-Energy Dispersive X-ray Analysis (SEM/EDX). Considering the critical relationship between surface wettability and ice adhesion, we thoroughly examined the coatings' wettability. We employed Differential Scanning Calorimetry (DSC), freezing delay time assessments, push-off tests, and Centrifugal Adhesion Tests (CAT) to evaluate

the performance of the two ILs concerning ice nucleation temperature, formation time, and ice adhesion strength, respectively. Additionally, we utilized a confocal laser microscopy profiler to analyze the 3D surface profiles and roughness parameters of the coatings before and after icing/de-icing cycles. Solid-state Nuclear Magnetic Resonance (SS-NMR) spectroscopy validated the presence of nonfrozen water molecules at the interface.

In the second phase, we shift our focus to exploring critical factors influencing ion mobility, particularly investigating how the physicochemical properties of ILs and the hydrophilicity/hydrophobicity of matrixes affect anti-icing performance. We selected Polyurethane (PU) and PDMS based on Sylgard 184 as representative hydrophilic and hydrophobic matrixes, respectively. We employed Dielectric Spectroscopy to evaluate the electrical conductivity of coatings at various subzero temperatures, aiming to identify ILs with optimal mobility within different matrixes crucial for achieving superior anti-icing properties. We extensively examined ion mobility, ice adhesion strength under accelerated weathering and icing/de-icing cycles, and resistance against frost formation during freeze-thaw cycles. UV-Vis Spectroscopy facilitated the analysis of IL release into water, aiding in tailoring crosslinking density, while measurements of ionic conductivity at both room temperature and -5°C provided additional validation of IL presence and mobility. Importantly, we used the same ILs from the first phase. The distinction lies in the approach: in the initial phase, we formulated PDMS-based coatings containing 10 wt.% of ILs. In contrast, the second phase expanded on these findings by exploring the impact of matrix hydrophobicity on IL mobility through the fabrication of two sets of samples: PU- and PDMS-based coatings containing ILs. Furthermore, we increased the IL concentration to observe enhanced efficacy in anti-icing performance, aiming for a more robust conclusion and comparison.

In the third and fourth phases, we investigated the anti-freezing capabilities of DESs by synthesizing and characterizing choline-based ILs containing both hydrophilic and hydrophobic anions. We integrated these ILs into an industrial coating, such as PU, building on the favorable outcomes observed in the latter stages of the second phase, particularly in enhancing anti-icing characteristics. We thoroughly examined the thermal behavior of the synthesized DESs, focusing on the interaction dynamics between choline-based DESs—featuring diverse hydrogen bond donors (HBDs)—and the previously synthesized ILs. This exploration aimed to elucidate how these interactions influence the hydrogen-bond donor capacity of the system and subsequently impact the anti-icing properties of the surfaces. Furthermore, we assessed the mechanical properties of the developed coatings to evaluate their durability against tension and various weathering conditions. This extensive approach aimed to advance our understanding of how DESs and ILs can synergistically enhance anti-icing capabilities in practical applications.

Thesis outline

The outline section offers a concise overview of the seven chapters comprising this Ph.D. thesis. Chapter one begins with a comprehensive literature review focusing on dynamic anti-icing surfaces. It introduces fundamental definitions and categorizations of these surfaces, highlighting various subcategories and their respective research contributions. The study focuses on dynamic interface melting using ILs and dynamic ice management with DESs as key methods. Specifically, existing research pertaining to anti-icing and anti-freezing surfaces incorporating ILs and DESs is critically evaluated within the context of these methodologies.

Chapter 2 explores the development of PDMS coatings incorporating two distinct RT-ILs, either individually or in combination. The chapter details a thorough surface characterization approach including wettability assessments, ATR-FTIR spectroscopy, XPS spectroscopy, and SEM/EDX analysis. The efficacy of these coatings in mitigating ice formation and adhesion is evaluated through DSC, push-off testing, and CAT analysis. SS-NMR spectroscopy validates the presence of nonfrozen water molecules at the interface, contributing to a comprehensive understanding of the coatings' anti-icing properties. The obtained results are presented in the journal article "*In-depth analysis of the effect of physicochemical properties of ionic liquids on anti-icing behavior of silicon based-coatings*" published in *Journal of Cold Regions Science and Technology* [37].

Chapter 3 of our research investigates into the influence of matrix hydrophobicity on the mobility of ILs at subzero temperatures and its subsequent impact on anti-icing capabilities. We selected two matrixes with contrasting hydrophilic and hydrophobic properties—PU and PDMS—to embed varying concentrations of ILs. Dielectric spectroscopy was employed to discern ion mobility within the coatings at low temperatures. Additionally, a comprehensive suite of techniques was used to characterize ion mobility by adjusting crosslinking density, facilitating a comparative analysis of the anti-icing properties of ILs. SS-NMR spectroscopy reaffirmed the presence of a QLL at the interface. Furthermore, the coatings' ice adhesion was evaluated under accelerated weathering, icing/de-icing cycles, and freeze–thaw conditions to assess their endurance against frost formation. The results were published with title of "*To be or not to be a hydrophobic matrix? the role of coating hydrophobicity on anti-icing behavior and ions mobility of ionic liquids*" in *Chemical Engineering Journal* [38].

In chapter 4, we conducted a comprehensive investigation on the anti-freezing properties of DESs, accomplished through the synthesis of choline-based ILs featuring both hydrophilic and hydrophobic anions. Characterization of these aliphatic ILs and a detailed examination of DESs' thermal behavior were conducted to explore how diverse hydrophilic HBDs—specifically ethylene glycol (EG) diol and glycerol (GL) triol—interacted with the synthesized ILs to enhance the system's ability to inhibit ice formation. The anti-icing efficacy of the resulting samples was comprehensively assessed from multiple perspectives, including their resistance to frost formation. Additionally, the mechanical robustness of the coatings was evaluated in terms of their ability to withstand tension and weathering conditions. SS-NMR spectroscopy was instrumental in comparing the ILs' capacity to form hydrogen-bonding networks with water molecules, thereby forming thicker QLLs at the interface. The obtained results are largely adapted from this publication with the title of ‘‘*Innovative Ice Mitigation: Exploring the Potential of Choline-Based Deep Eutectic Solvents and Ionic Liquids Synergies*’’ published by *Applied Surface Science Journal* [39].

In Chapter 5, building upon the insights gained in the previous stages, this study delves deeper into investigating the synergistic effects of combining various DESs—specifically EG-based and those incorporating hydrophobic HBDs—with 10 wt.% of a synthesized Choline-based IL, namely Choline bis(trifluoromethanesulfonyl)imide (ChTFSI), focusing on the effect of HBD hydrophobicity. Our approach in this phase involved comparing HBDs of DESs, specifically replacing a diol (EG) with another diol containing fluorinated groups, as opposed to the previous phase where we compared a diol and a triol. After conducting a comprehensive characterization of surface properties, anti-icing capabilities, and resistance to frosting, low-temperature ATR-FTIR spectroscopy was

employed to further analyze the presence of QLLs on the surface, in addition to SS-NMR spectroscopy.The results were submitted with title of "*Ice-Responsive Coatings: Evaluating the Effect of Hydrogen Bond Donors on Deep Eutectic Solvents/Ionic Liquids Anti-icing Efficiency*" in *Journal of Molecular Liquids* [40].

In Chapter 6, this Ph.D. project consolidates its primary findings into unifying conclusion.

Chapter 7 outlines recommendations derived from the results that can guide future research endeavors.

CHAPTER 1

1. LITERATURE REVIEW

1.1 Introduction

When liquid water transitions into ice, it can strongly adhere to various exposed surfaces, forming different types of ice, such as rime, glaze, wet snow, and frost. These ice formations pose significant safety, operational, and economic challenges across a broad spectrum of industries, including road, sea, and rail transportation, power transmission, telecommunications, wind turbines, pumps, and heat exchangers (Figure 1-1) [2,3,11,41]. The persistent threat of ice and its adverse effects underscore the importance of developing effective anti-icing strategies and technologies.

Figure 1-1: Detrimental Impacts of Ice Formation on Life and Industry [42] *(Reprinted with permission).*

To mitigate icing in energy systems, two principal strategies are employed: anti-icing and de-icing. Anti-icing methods are preventive, aiming to slow down ice formation, while de-icing approaches focus on removing already formed ice [43]. Both strategies can utilize active and passive methods. Active methods require external energy to eliminate ice, whereas passive methods exploit the inherent physical and chemical properties of surfaces to prevent or reduce ice accumulation. These techniques are essential for maintaining safety and efficiency across various applications. While active methods remain widely used for certain infrastructures, our focus on passive anti-icing surfaces presents a cost-effective alternative. Besides, passive surfaces can offer enhanced efficiency and versatility in ice mitigation through integrating with active techniques [44].

Significant advancements have been made in the realm of surface icephobicity in recent years [45]. The dominant viewpoint on existing anti-icing surfaces largely revolves

around the static nature of the ice-substrate interface and its adjacent areas. However, in reality, the local structures and properties of these interfaces undergo dynamic changes over time, influenced by temperature fluctuations and various external stimuli [18,24,46]. Hence, comprehending the dynamic characteristics of the icing interface is pivotal for innovating new anti-icing surfaces, capable of addressing challenges posed by severe conditions, such as ultra-low temperatures and prolonged operational durations.

Before embarking on exploration of driving on dynamic anti-icing surfaces, we thoroughly investigate the intricate science of icephobicity and explore various anti-icing surface technologies. Our attention is directed towards the latest advancements in Dynamic Anti-Icing Surfaces (DAIS), focusing sharply on critical ice-substrate interfacial regions. Here, we examine how spontaneous or stimuli-responsive changes in chemical and physical states influence ice adhesion during and after its formation.

State-of-the-art dynamic anti-icing surfaces are methodically categorized into three types: those with dynamic substrate properties, dynamic interfacial behaviors, and dynamic ice alterations. Such dynamic characteristics at ice-substrate interfaces offer promising avenues for modifying interaction and reducing ice adhesion. ILs emerge as particularly promising agents for imparting dynamic properties to these interfaces.

Simultaneously, surfaces with dynamic ice properties demonstrate capabilities in controlling ice growth, propagation, and even facilitating ice melting, thereby mitigating ice accumulation and aiding surface ice removal. DESs, recently gaining attention as eco-friendly ILs analogues, show remarkable potential in inhibiting ice growth. This chapter also explores DES components, their preparation methods, and compares their properties with ILs.

Furthermore, this chapter proceeds with survey on the anti-freezing capabilities of these technologies, integrating both proposed and existing strategies for effective ice management on surfaces.

1.2 Exploring anti-icing surfaces and surface icephobicity

Ice formation initiates as water cools to or below 0 ℃ under normal atmospheric conditions, triggering a phase transition. Within water droplets, ice nucleation commences through two distinct processes: homogeneous nucleation within the droplet itself and heterogeneous nucleation on external surfaces [47,48]. This process is driven by the spontaneous formation of durable hydrogen bonds, resulting in the creation of compact ice nuclei. These nuclei gradually evolve in shape as more stable hydrogen bonds propagate. The transformation from liquid water to solid ice reduces the system's free energy [47,49].

However, the growth of ice nuclei increases the interface free energy between the liquid phase and ice, forming a nucleation energy barrier. Heterogeneous nucleation occurs at higher temperatures compared to homogeneous nucleation, facilitated by impurities and the unique topography and chemical composition of external surfaces. These factors play a critical role in the design of anti-icing surfaces, where nucleating agents can lower the nucleation barrier to promote the formation of crucial ice nuclei [47,50].

From a thermodynamic perspective, ice formation involves three primary processes: liquid-solid freezing, vapor-solid desublimation, and vapor-liquid-solid condensation followed by freezing. In the context of developing ice-resistant surfaces and strategies, the emphasis lies on the first two mechanisms, focusing on ice formation from supercooled water

droplets at or below 0 °C and frost formation from vapor under conditions of supersaturation [47,51].

Numerous approaches have been explored to prevent surface icing, limit ice buildup, and reduce ice-surface adhesion. To mitigate the hazards posed by ice accretion, various types of passive anti-icing surfaces have been engineered. Anti-icing strategies aim to disrupt the sequential chain of events leading to ice formation, actively preventing or delaying its onset. This is achieved through engineering methods such as specialized coatings, additives, and surface treatments [52,53].

Analogous to hydrophobicity, which describes a surface's non-wetting property, "icephobicity" has been introduced in recent literature to describe anti-icing properties [16,54,55]. Based on the mechanisms underlying surface anti-icing behavior, three definitions of icephobicity have emerged [16]. Firstly, icephobicity is defined as a surface's ability to repel water droplets in cold environments, preventing water and thus ice formation [56,57]. Secondly, it can be described as a surface's ability to delay or inhibit ice nucleation and frost formation, maintaining water in its liquid phase for as long as possible [58,59]. Thirdly, icephobicity refers to a surface that exhibits low adhesion strength to ice, typically below 100 kPa [60,61]. Given that ice and frost formation are generally unavoidable in prolonged cold and harsh conditions, a more practical approach is to design surfaces that tolerate ice but have extremely low adhesion (less than 10 kPa) [62]. Strategies focused on developing materials with low ice adhesion are highly promising in the field of icephobicity [63–65].

Although both terms pertain to controlling ice on surfaces and are closely related, they highlight different aspects of surface functionality. Anti-icing focuses on preventing or delaying ice formation, employing various strategies to inhibit the initial accumulation of ice. Conversely, icephobicity emphasizes the resistance to ice adhesion, making it easier to remove ice once it forms. The distinction lies in anti-icing's proactive approach to stopping ice formation and icephobicity's reactive strategy to facilitate ice detachment [66]. These definitions, however, are not exhaustive and can be inapplicable in certain contexts, such as with superhydrophobic surfaces. In such cases, surfaces that delay ice formation do not always exhibit reduced ice adhesion within ice removal process [54,67].

Ice removal is a process of adhesive failure and/or cohesive failure. The adhesive failure of ice occurs at the ice-substrate interface, while the cohesive failure occurs in the ice itself or surface materials [68]. Therefore, ice adhesion strength is an important factor that governs the icephobic behavior of the surface. It indicates how effortlessly the ice adhered to the surface can be removed [69].

The average of intrinsic ice adhesion through atomistic attraction of water/ice molecules to a surface namely coulombic and van der Waals forces [70,71], and hydrogen bonds with hydrogen bonding donors and/or acceptors [72], can be called as macroscopic ice adhesion which can be measured through using different reported ice adhesion strength test apparatus, home-made by diverse research groups, which include centrifugal test [73], tensile test [74], horizontal shear test [75], and vertical shear test [76]. The ice adhesion strengths reported in the literature can thus be either shear strength or tensile strength.

1.3 Dynamic anti-icing surfaces

From the initial development of superhydrophobic surfaces (SHS) inspired by the lotus leaf, designed to repel water droplets and delay ice nucleation, to the recent innovation of omniphobic slippery liquid-infused porous surfaces (SLIPS) inspired by pitcher plants, advancements have continually evolved to address multifaceted anti-icing challenges [77,78].

A diverse array of anti-icing surfaces has been documented in the literature, demonstrating significant potential with practical low ice adhesion strengths ranging from 0.2 to 10 kPa. Generally, icephobic surfaces are characterized by ice adhesion strength (τ_{ice}) below 100 kPa, while passive ice removal necessitates much lower values (τ_{ice} < 10 kPa). These surfaces exhibit promising capabilities for large-scale, easily achievable ice removal [45,55,62,79].

Despite significant advancements in surface icephobicity in recent years, most anti-icing surfaces are designed with a static approach. This involves strategies such as texturing surface structures, adjusting substrate modulus, and modifying surface energy, often without accounting for the dynamic evolution of these properties over time [80,81]. A fundamental characteristic of these surfaces is the assumption that the ice-substrate contact area remains "constant" post-formation. Consequently, the primary focus of surface design is on the pre-icing state, neglecting the dynamic changes that occur after ice has formed.

For example, the anti-icing performance of SHSs, known for repelling water and delaying ice nucleation, has been extensively studied with a focus primarily on pre-icing phenomena [16]. However, once ice forms, especially through repeated icing/deicing cycles,

SHS performance deteriorates rapidly due to the easy damage of surface asperities [23,54,82,83]. Similarly, SLIPSs, which use a lubricant layer to repel immiscible materials, also concentrate on pre-icing behavior. Post-icing, the lubricant can be quickly depleted during ice removal [13,14,22]. Generally, static anti-icing surfaces (SAIS) face significant drawbacks such as ineffectiveness at extremely low temperatures, susceptibility to surface damage and degradation, and inability to adapt to environmental changes [18].

Recently, there has been a notable shift in the design principles of anti-icing surfaces. Previously static in nature, these surfaces lacked consideration for changes at the ice-substrate contact areas post-ice formation. Now, attention has turned towards enabling dynamic changes in the chemical and physical states of the ice, substrate, and their interface to enhance anti-icing performance [84,85]. These emerging surfaces are termed dynamic anti-icing surfaces (DAIS), characterized by integrated properties that mitigate ice-substrate interactions even after ice formation. Interestingly, certain effective strategies from traditional active deicing methods have been adapted in the design of DAIS. DAISs are categorized into three types: surfaces with dynamic substrate, dynamic interface, and dynamic ice, as illustrated in Figure 1-2 [18]. The subsequent sections provide detailed insights into these categories, focusing particularly on approaches involving dynamic interface and ice.

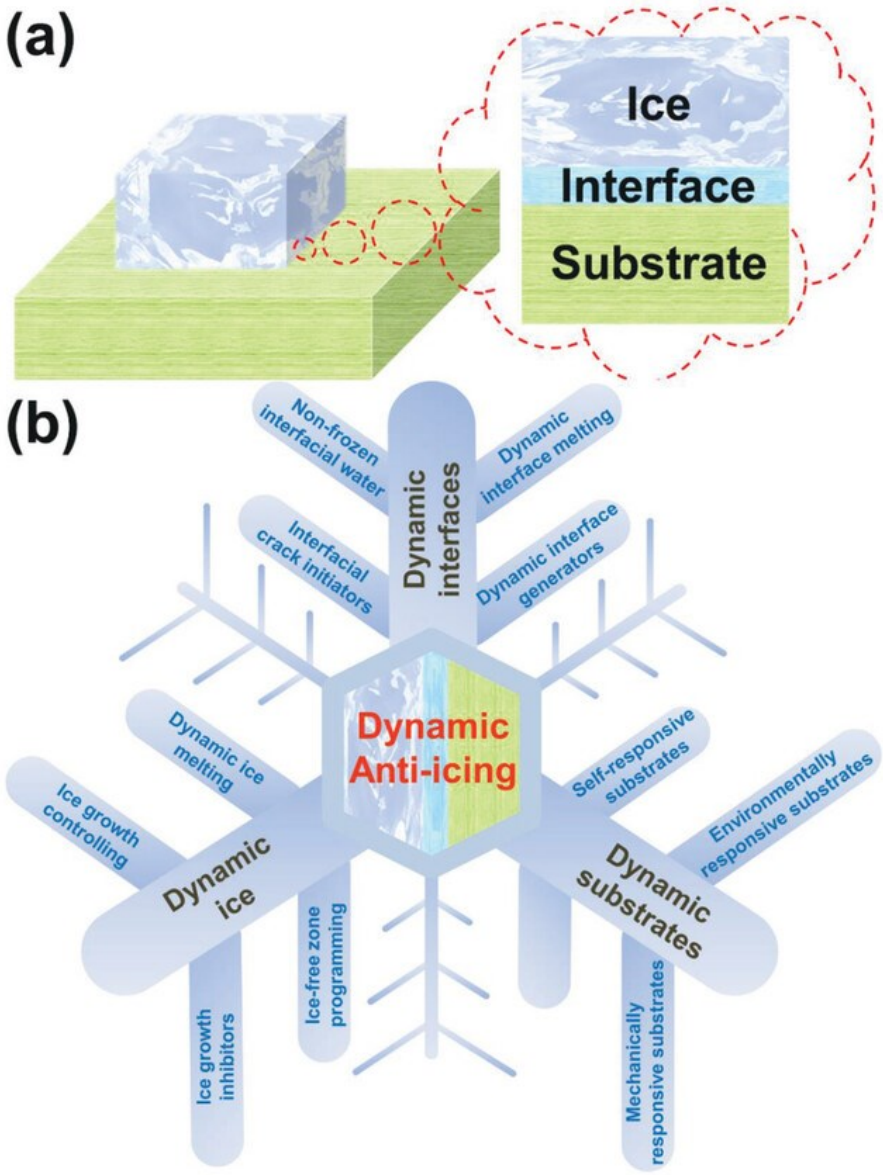

Figure 1-2: (a) The key regions adjacent to the ice-substrate interface crucially influence the anti-icing performance of a surface and, (b) DAIS focusing on enhancing the three ice-substrate interfacial regions [18] *(Reprinted with permission).*

1.3.1 Dynamic substrates

Many surfaces exhibit dynamic responses driven by internal forces, a trait commonly observed in natural organisms and systems, known as self-responsive substrates. For instance, earthworms and poison dart frogs have glands that secrete lubricants, creating a

slippery layer on their skin in response to pressure or concentration gradients [86,87]. Inspired by these mechanisms, anti-icing surfaces have been designed with embedded lubricants in substrates. One innovative approach involves phase separation, where urea and polydimethylsiloxane copolymers are dissolved with excess silicone oil in tetrahydrofuran (THF). Upon THF evaporation, a crosslinked polymer matrix forms, trapping silicone oil as internal droplets [88]. This droplet-embedded gel system is metastable and regenerable, driven by disjoining pressure from van der Waals interactions at the gel surface. Icephobic surfaces adopting this strategy have demonstrated ice adhesion strengths below 40 kPa [89], with lubricating layers regenerated after multiple wiping/regenerating cycles and maintaining long-term adhesion strengths below 70 kPa. In addition to liquid oils, solid lubricants have been employed in self-responsive substrates to facilitate the regeneration of surface lubricating layers [90,91]. Surface damage poses a significant threat to the durability and icephobicity of anti-icing surfaces, as it can increase ice adhesion through interlocking with the surface. Hence, some self-responsive substrates with self-healing capabilities have been developed for anti-icing applications [92,93] .

Anti-icing surfaces are evolving with dynamic substrates that respond to environmental triggers like temperature, magnetic fields, and light, named as environmentally-responsive substrates [92,94,95]. For instance, a reversible thermosecreting organogel (RTS-organogel) incorporated a binary liquid mixture into a PDMS network, exhibiting different properties at various temperatures and achieving very low ice adhesion strengths (less than 1 kPa) at sub-zero temperatures [96]. Traditional liquid lubricants in anti-icing surfaces often suffer from depletion and poor durability, but innovative approaches like phase-transformable slippery liquid-infused porous surfaces (PTSLIPS) address this with

temperature-responsive lubricants [92]. These advancements enhance durability, though these soft polymer matrixes remain a limitation for mechanical robustness. Magnetic fields and light have also shown promise in modulating surface properties for anti-icing applications [95,97]. Magnetic slippery surfaces (MAGSS-Figure 1-3a) utilizing ferrofluid and magnetic fields achieve exceptionally low ice adhesion strengths (≈2 Pa) with sustained performance over multiple icing/deicing cycles [98]. UV-responsive substrates (UVRS) use light-triggered changes to release embedded lubricants, demonstrating effective ice adhesion reduction under UV exposure, achieving low ice adhesion strengths (21 kPa) and maintaining long-term performance (47 kPa after 15 icing/deicing cycles, Figure 1-3b) [94].

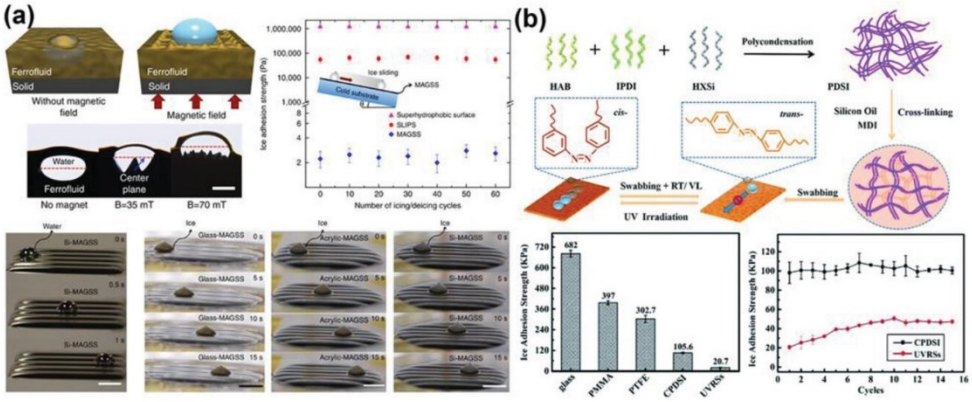

Figure 1-3: DAIS incorporate environmentally responsive substrates. (a) Magnetic slippery icephobic surfaces exhibit extremely low adhesion when subjected to a magnetic field [98] *and (b) UV-responsive substrates demonstrate controlled lubricant release and achieve low ice adhesion strength under UV irradiation* [94] *(Reprinted with permission).*

Ice removal from surfaces often involves applying stress to the ice-adhered surface. Mechanically responsive substrates achieve low ice adhesion by employing surface structures that can dynamically alter under stress. These structures include molecular configurations within base materials or geometric patterns on the surface [99,100]. An innovative approach uses slide-ring crosslinkers, termed molecular pulleys, embedded in a

PDMS base matrix to create an ultradurable icephobic coating. These crosslinkers move along polymer chains under mechanical stress and return to their original state through entropic repulsion upon stress relief. This design lowers the polymer matrix's elastic modulus for reduced ice adhesion while maintaining strong cohesion, enhancing mechanical durability. The slide-ring substrate demonstrated low ice adhesion (≈12 kPa) over 20 icing/deicing cycles and maintained strength (≈22 kPa) after 800 abrasion cycles [99]. Another development is a fish-scale-like dynamic anti-icing surface prototype inspired by the structure of fish scales. This surface utilizes stacked graphene platelets that dynamically open up under deicing forces, enabling sequential ice rupture from the surface. The design, informed by atomistic modeling and simulations, showed a significant reduction in ice adhesion strength (approximately 60%) [100].

1.3.2 Dynamic interfaces

A comprehensive understanding of the interactions between the ice-substrate interface and the intrinsic and stimuli-responsive properties of dynamic anti-icing coatings has yielded new insights into the anti-icing performance of these surfaces [18,101,102]. Incorporating dynamic properties at the ice-substrate junction offers the potential to customize interactions to minimize ice adhesion. Dynamic interface approach exploits the benefits of various strategies including, non-frozen interfacial water, dynamic interface melting, dynamic interface generators, and interfacial crack initiators to modulate the forces necessary for ice removal [17,49,62,79,103,104].

The low adhesion strength of ice to ice-skating blades is due to a pre-melted liquid layer on the ice surface at subzero temperatures [105]. This layer, formed through regelation,

pressure, or friction melting [105,106], transforms ice-substrate contact from solid-solid to solid-liquid-solid, resulting in weak interfaces with short-term van der Waals forces and hydrogen bonds. Research has highlighted the potential of this non-frozen interfacial water layer to reduce ice adhesion [107]. Current strategies focus on using highly hydrated ions to create quasi-liquid layers (QLLs) on solid surfaces, which impact water structure and inhibit ice nucleation [108]. Polyelectrolyte brushes hosting ions have been used to study their effects on ice adhesion [109]. Enhancing the lubricating effect involves increasing the QLL thickness, with covalently grafted flexible polymers on flat surfaces being an effective method [110].

Dynamic interface generators are substrates designed to dynamically create an interfacial aqueous lubricating layer, enhancing durability and ensuring low ice adhesion, even at extremely low temperatures, due to their ability to regenerate lubricants [45,55,62]. Nevertheless, the ice adhesion on substrates with interfacial non-frozen water layer can rise from approximately 27 kPa to over 400 kPa at temperatures near -60 °C [111]. In extreme environments like the Arctic, maintaining low ice adhesion is particularly challenging. A recent strategy addresses this by generating an interfacial liquid layer using ethanol instead of water, due to ethanol's low freezing point of -115 °C [104]. This approach ensures non-frozen lubricating effects in the harsh conditions. Liquid layer generators (LLGs), the first dynamic substrates capable of meeting these anti-icing requirements, rely heavily on environmental temperature. High temperatures can accelerate ethanol evaporation, potentially compromising the function of LLGs.

Interfacial cracking, as one strategy of the dynamic interface approach, can significantly reduce ice adhesion by causing stress concentration. According to classic fracture mechanics theory, the ice adhesion strength (τ_c) is determined by the Equation 1-1:

Equation 1-1

$$\tau_c = \sqrt{E^* G}/_{\pi a \Lambda}$$

where G is the surface energy, E* is the apparent bulk Young's modulus, a is the total crack length, and Λ is a nondimensional constant. Generating cracks at the ice–substrate interface is a promising method for achieving low ice adhesion. By incorporating crack initiators into surfaces, crack generation can be enhanced, leading to efficient ice adhesion reduction [62]. Three crack initiators have been identified: nanoscale crack initiators (NACI) based on surface atomistic and chemical characteristics, microscale crack initiators (MICI) based on hierarchical surface structures, and macroscale crack initiators (MACI) based on interface stiffness inhomogeneity [62]. NACI and MICI mechanisms aim to reduce ice adhesion by weakening the ice–substrate bond through surface properties like hydrophobicity and microvoid formations [71,112,113]. Despite their benefits, NACI and MICI have limitations in achieving very low ice adhesion strengths. In contrast, MACI serves as a macroscopic crack initiator that maximizes crack size at the ice–substrate interface, significantly enhancing ice removal efficiency [54,62,114]. This approach, facilitated by subsurface structures and sponge-like PDMS substrates, achieves exceptionally low initial ice adhesion strengths of ≈0.8 kPa, maintaining stability over multiple icing/deicing cycles [115]. Additionally, stress-localized surfaces, designed with phase-separated materials of varying elastic moduli, demonstrate effective ice detachment under mechanical stress,

achieving ice adhesion strengths as low as 1 kPa while ensuring robust mechanical durability [85].

To enhance the effectiveness of interfacial aqueous lubricant layers, which typically range from a few molecules to tens of nanometers in thickness [110,111] and achieve super low ice adhesion strengths, implementing the dynamic interface melting strategy could be highly beneficial [45,55,62]. This approach aims to melt interfacial ice more effectively, thereby creating thicker aqueous layers to further augment lubricant effects for practical anti-icing applications, ideally achieving ice adhesion strengths lower than approximately 10 kPa. This strategy constitutes a core mechanism of our research, and we will elaborate further on it in the subsequent section.

1.3.2.1 Dynamic interface melting

Dynamic melting of ice on substrates can be initiated by chemicals (antifreeze liquids or salts) or thermal energies (magnetic, electrothermal, photothermal), commonly used in active deicing for various applications. Unlike traditional methods that are costly and environmentally impactful, recent advancements integrate these active anti-icing agents into passive substrates with dynamic ice–substrate interfaces, offering a promising solution for ice removal [19,86,116,117].

Superhydrophobic surfaces typically exhibit high ice adhesion strength in humid environments due to their intricate surface structures [23,83,114,118,119]. To mitigate mentioned issues, antifreeze agents can be applied on superhydrophobic surfaces to create a liquid interface, effectively weakening ice adhesion. For example, a novel superhydrophobic copper mesh coated with PVACOOH-based organogel releases antifreeze agents (a mixture

of ethylene glycol and water) dynamically at subzero temperatures. This process melts neighboring ice and increases the thickness of the interfacial liquid layer over time. As a result, the ice adhesion strength on the surface decreases significantly from ≈1.3 kPa to <0.001 kPa after 5 hours, showcasing impressive ice self-removal capabilities [120].

Utilizing thermal energy to melt interfacial ice is a viable method for creating nonfrozen water lubricating layers. Thermal energy, is transferred to melt the ice at the interface, as illustrated in Figure 1-4a. Multiwalled carbon nanotubes (MWCNTs), known for their excellent thermal conductivity, were assembled into a layer-by-layer film using a vacuum-assisted technique. This resulted in superhydrophobic surfaces exhibiting exceptional water repellency and unique electrothermal properties conducive to easy ice removal. In these surfaces, substrate temperature can be precisely controlled using an external voltage without compromising superhydrophobicity. For instance, applying a 30 V voltage efficiently melted the ice at the interface, causing the ice to slide off automatically within 34 seconds [116].

Although electrothermal surfaces are effective for interfacial ice melting, they remain energy-intensive. Recently, surfaces with photothermal properties that capture solar energy for ice melting have gained significant attention [121]. A notable example is the photothermal trap, which features a trilaminar structure. This structure includes a top layer for absorbing solar radiation, a middle layer for spreading heat laterally, and an insulating layer to minimize heat dissipation. The designed surfaces efficiently convert solar energy into substrate heat. In Figure 1-4b, frozen droplets began sliding off within 19.8 seconds when the substrate was illuminated at a 30° tilt angle. Impressively, the substrate quickly developed a thin liquid layer within 0.5 seconds of initiating interfacial ice melting. Outdoor tests demonstrated

strong anti-icing performance, with frozen droplets sliding off within 30 seconds under solar illumination intensity of approximately 0.6 kW m^{-1}. With increased solar exposure, these surfaces utilizing thermal energy not only melt ice at the interface but also can melt entire ice formations [122].

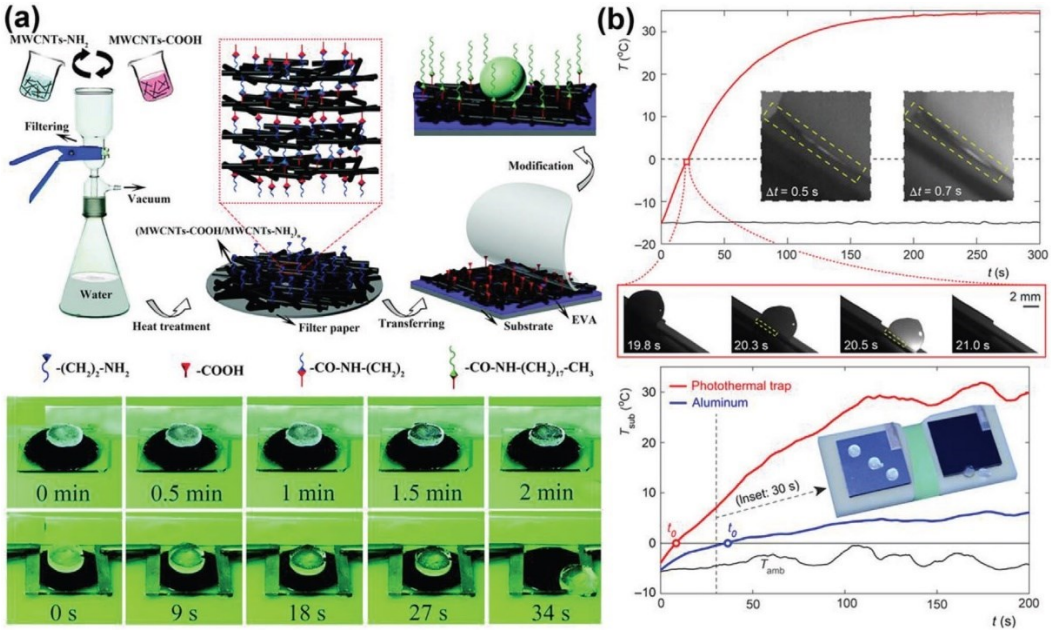

Figure 1-4:Dynamic Interface Melting in DAIS Innovations: a) Explore superhydrophobic carbon nanotube surfaces with integrated electrothermal effects, as depicted in real-time anti-icing experiments [116] *, and b) Harness solar illumination with the photothermal trap to mitigate ice buildup* [122] *(Reprinted with permission).*

Introducing dynamic characteristics at the ice-substrate interface provides a unique opportunity to tailor interactions, effectively reducing ice adhesion [17,123]. Addressing the need for durable anti-icing solutions, ILs show great potential by imparting dynamic properties to the interface, particularly in sub-freezing conditions. ILs serve as effective antifreeze agents, integrated into ionogels that span various applications from solid electrolytes to drug delivery and catalysis [124,125]. Surfaces integrating ionogels,

composed of ILs and polymers, have been creatively employed for anti-icing applications [19], with detailed discussions forthcoming in subsequent sections.

1.3.3 Ionic liquids (ILs)

ILs hold significant promise as anti-freezing agents by introducing dynamic anti-icing properties at the ice-substrate interface. The history of ILs dates back to the 1800s, with early research synthesizing the first IL, ethylammonium nitrate ($[C_2H_5NH_3][NO_3]$), which has a melting point of 12 °C, by Paul Walden in 1914. Subsequently, Prof. John Yoke from Oregon State University synthesized one of the early ILs by combining copper (I) chloride and alkyl aluminium chloride [25].

In the 1970s and 1980s, research by Osteryoung and Hussey explored chloroaluminate-based ILs in electrochemistry. Over time, scientists discovered the first generation of ionic salts that remain liquid below 100 °C. Additionally, room temperature ILs based on 1-alkyl-3-methylimidazolium cation with either tetrafluoroborate or hexafluorophosphate anions were synthesized by Wilkes and Zaworotko in 1992. Since then, an increasing number of ILs have been synthesized from a range of cations based on quaternary-onium central atoms, such as nitrogen, phosphorus, or sulfur, and various anions including trifluoromethanesulfonate, bis-(trifluoromethanesulfonyl)amide, tris-(trifluoromethanesulfonyl)methide, or perfluoroalkylphosphate [25,126–128].

Another significant contribution to air- and water-stable 1-ethyl-3-methylimidazolium-based ionic liquids in 1992 is seen by many as initiating a new phase in the development of ILs. Recently, the focus has shifted to more environmentally acceptable second- and third-generation ILs comprising biocompatible cations (e.g., cholinium salts)

and anions such as amines and amino acids. These ILs, derived from readily available renewable resources, have been used in various industrial applications and are often referred to as "liquid electrolytes," "ionic melts," "ionic fluids," "fused salts," or "liquid salts." They are also known as “Solvents of the Future” and “Designer Solvents.”

Literally, ILs are organic salts that exhibit low melting temperatures, conventionally below 100 °C. Comprising only ions, their properties are markedly different and more complex than those of molecular liquids. Today, ILs are attracting considerable attention due to their wide range of appealing physical and chemical properties [129,130].

1.3.3.1 Types, physicochemical properties and application of ILs

ILs represent a novel class of purely ionic materials that remain liquid at temperatures below 100°C. The high melting points of traditional salts, such as NaCl, are due to their efficient packing and strong ionic interactions, which form a crystal lattice. In contrast, ILs feature cations that are asymmetrically substituted with bulky groups. This asymmetry weakens the ionic interactions, preventing the formation of a crystal lattice and resulting in low melting points, making them liquid below 100°C. Room-temperature ionic liquids (RTILs), which are fluid-like at or around room temperature, are particularly notable for their wide liquid range, making them suitable for numerous advanced applications [131].

The most commonly used ILs contain cations such as imidazolium, pyridinium, phosphonium, pyrrolidinium, tetraalkylphosphonium, tetraalkylammonium, and trialkylsulfonium, which can pair with anions like tetrafluoroborate, hexafluorophosphate, trifluorotris(pentafluoroethyl)phosphate, thiocyanate, dicyanamide, ethyl sulfate, and

bis(trifluoromethylsulfonyl)amide [126]. Figure 1-5 illustrates the chemical structures of some common cations and anions.

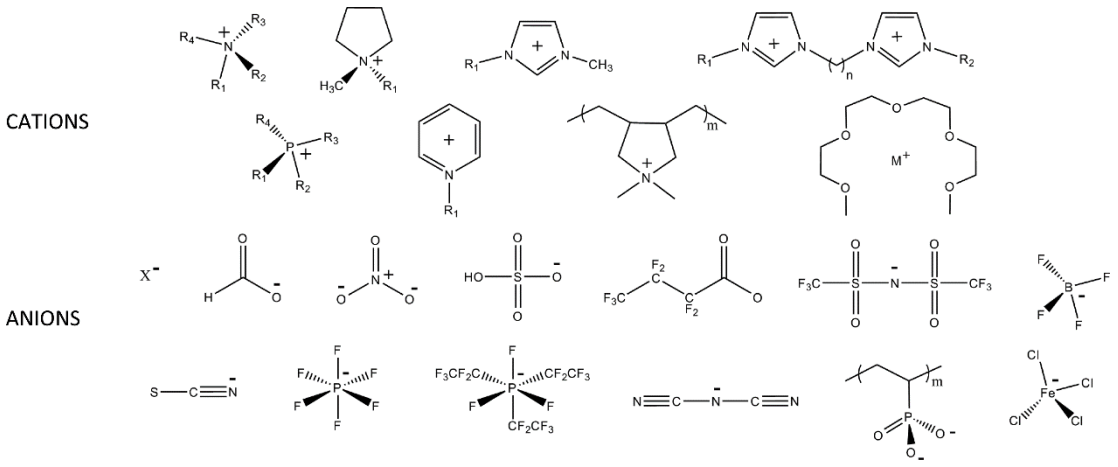

Figure 1-5: Some chemical structures of representative cations and anions used in protic, aprotic, dicationic, polymeric, magnetic, and solvate ionic liquids. From left to right, the cations (top row) include: ammonium, pyrrolidinium, 1-methyl-3-alkylimidazolium, 1,3-bis[3-methylimidazolium-1-yl] alkane; (second row) phosphonium, pyridinium, poly(diallyldimethylammonium), metal (M^+) tetraglyme. The anions include (third row) halides, formate, nitrate, hydrogen sulfate, heptafluorobutyrate, bis(perfluoromethylsulfonyl)imide, tetrafluoroborate, (bottom row) thiocyanate, hexafluorophosphate, tris(pentafluoroethyl)trifluorophosphate, dicyanamide, poly(phosphonic acid), and tetrachloroferrate [132] *(Reprinted with permission).*

ILs exhibit exceptional features, such as negligible vapor pressure, thermal stability, and low-flammability, combined with high ionic conductivity and a wide electrochemical stability window. These properties open up numerous opportunities for developing new materials and structures. Additionally, the tunability of ILs' physicochemical properties based on the choice of anion-cation pairs is a promising feature for diverse applications. The wide variation in their chemical structures significantly affects their physicochemical characteristics [126,133–136].

ILs, unlike typical solvents, present a classification challenge due to their unique structural characteristics that resemble molten salts, ionic surfactants, ionic crystals [137], and molecular liquids. The vast array of potential ILs, owing to their diverse structures, complicates their classification, as multiple labels might be suitable depending on whether the focus is on the anion, cation, or functional groups [131]. Generally, ILs are divided into two main types: protic [138] and aprotic [139], based on their ability to donate protons. Protic ILs are proton donors, while aprotic ILs are not [140]. However, this division isn't always straightforward. For instance, dicationic ILs with both protic and aprotic centers have been identified, allowing them to exhibit both properties [141].

Protic Ionic Liquids (PILs) are synthesized through a proton transfer from an equimolar combination of a Brønsted acid and a Brønsted base [138]. This simple and cost-effective preparation method results in no byproducts, making PILs attractive compared to other IL classes [142]. Despite proton transfer being a chemical equilibrium that can lead to the presence of neutral species, PILs are predominantly ionic. Most PILs exhibit “good” ionic behavior, comparable to ideal aqueous KCl solutions [141]. Due to proton transfer, PILs have H-bond donor and acceptor sites, enabling them to engage in hydrogen bonding. Although the exact mechanism of proton transfer in PILs remains unclear [143,144], this proton transfer has been linked to various properties [145].

Aprotic ILs (AILs) lack the common structural feature found in PILs. Instead, AILs encompass a diverse range of anion and cation chemical structures, with some capable of hydrogen bonding while others are not [146]. Initially, research on AILs focused on halometallate ions, but it has since expanded to include a vast array of chemical structures. AIL preparation tends to be more expensive and complex compared to PILs, often requiring

multi-step reactions. This complexity arises from the formation of ions through covalent bonding between two functional groups. Despite the increased preparation costs, AILs often result in solvents with superior thermal and electrochemical stability compared to PILs [132,147].

The extraordinary properties of ILs, including non-volatility and high ionic conductivity offer remarkable potential as safe electrolytes in advanced electrochemical devices, such as actuators, lithium batteries, electric double-layer capacitors, dye-sensitized solar cells, and fuel cells. Their negligible vapor pressure, non-volatility, and tunable solubilizing properties are of great interest for catalysis, extraction, and as replacements for organic solvents. Figure 1-6 and Figure 1-7 summarize the most important industrial and electrochemical applications of ILs [148,149].

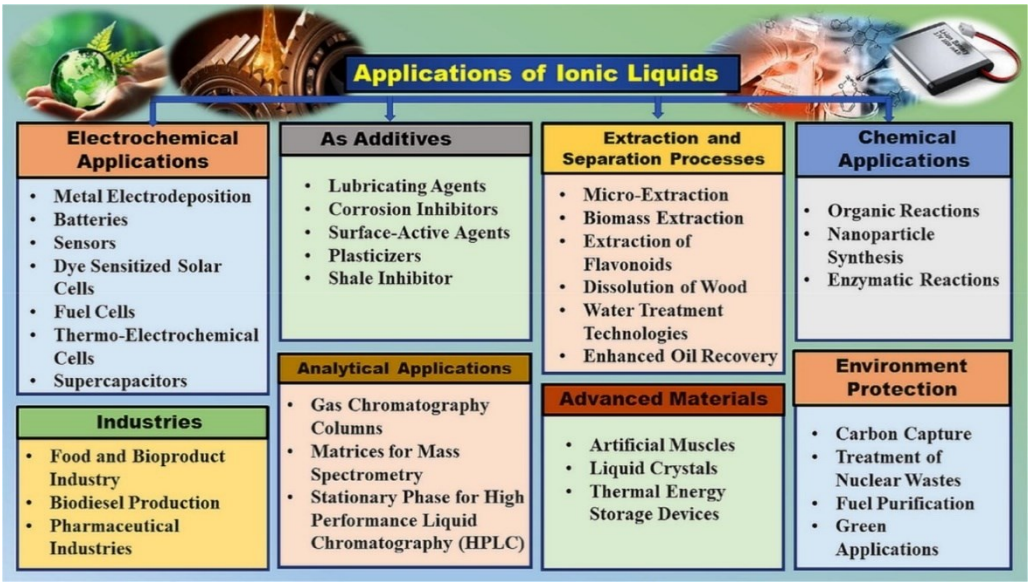

Figure 1-6: Application of ILs [150] *(Reprinted with permission).*

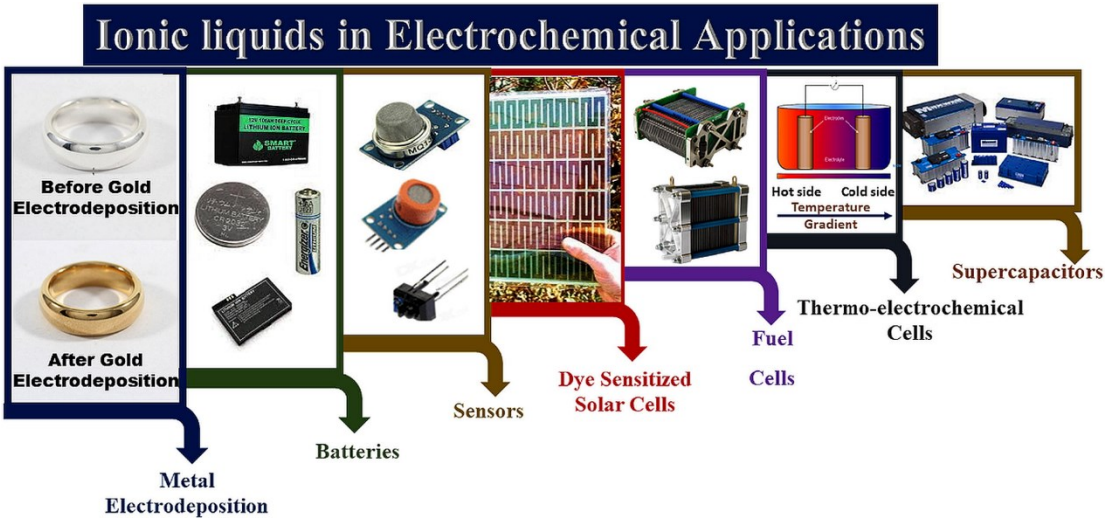

Figure 1-7: Illustrating diverse electrochemical applications of ILs [150] *(Reprinted with permission).*

ILs are increasingly valued in the automotive and aerospace industries for electrodeposition processes, providing eco-friendly protective metal coatings with improved corrosion and wear resistance [151]. They play a crucial role in developing batteries (lithium metal, lithium-oxygen, aluminum, and redox flow) due to their high ionic conductivity and electrochemical stability, enhancing battery performance and safety [152]. In dye-sensitized solar cells (DSSCs), ILs contribute to efficient light-to-electricity conversion thanks to their high conductivity, stability, and low vapor pressure, making DSSCs a promising solar energy option [153]. In supercapacitors, ILs are used as electrolytes, storing energy at the surface-electrolyte interface with greater safety and ionic conductivity compared to traditional electrolytes [154].

Their versatility extends to additives in lubricants, paints, shampoos, conditioners, fabric softeners, adhesives, and detergents, improving quality and efficiency [155,156]. ILs

also serve as effective corrosion inhibitors in desalination and petroleum industries, with specific cations providing protection against metal oxidation [157,158].

Surface-active ILs (SAILs) can function as surfactants, enhancing stabilization and emulsification processes [159]. They are used as plasticizers in materials like cellulose and polymers, improving flexibility and durability [160]. ILs enhance extraction and separation processes, offering greener alternatives for biofuel production from wood and cellulose. As catalysts, ILs improve yield, selectivity, and reaction conditions in chemical synthesis and nanoparticle stabilization [161].

ILs facilitate high conversion rates and enzyme stability in enzymatic processes and are derived from natural sources like choline and amino acids for use in food production, providing greener alternatives to conventional solvents [162,163]. They enhance drug delivery by improving drug solubility and permeability and contribute to environmental conservation by capturing hazardous gases, treating nuclear waste, and purifying fuels [164]. ILs also drive innovation in advanced materials, including artificial muscles, liquid crystals, and thermal energy storage devices, showcasing their transformative potential across various fields [165].

Overall, the diverse and innovative applications of ILs across various fields highlight their transformative potential and adaptability in addressing modern technological and environmental challenges [150].

1.3.3.2 Ionogels (IGs): classification, properties and applications

Significant efforts are being made daily to design new ILs, and many new directions will continue to be discovered [131,166,167]. However, a substantial challenge lies in

immobilizing ILs in devices while preserving their properties. The liquid state of ILs is not always suitable for certain applications. Nevertheless, they remain promising candidates for numerous applications that benefit from their tailored functionality but require the functional component to be solid.

One solution involves using ILs as absorbed films. In this approach, metal catalysts are immobilized within IL films supported on silica beads, resulting in free-flowing powders particularly suited for continuous fixed-bed reactors. This method retains the unique properties of ILs while providing the stability of a solid phase [168,169]. Another common method for IL immobilization is forming homogeneous three-dimensional networks. This two-component system, composed of IL and a solid component, is known as ionogels (IGs). IGs-based materials describe those that contain an IL confined within a gelator, which can be inorganic, organic, or a combination of both (hybrid). These resulting materials exhibit solid-like behavior while retaining the functional advantages of ILs [170,171].

Depending on the type of interaction between the IL and the gelator, ionogels can be categorized into two main types: chemical and physical gels. In physical gels, weak and reversible interactions such as hydrogen bonding and crystalline junctions dominate the cross-linked network [172]. These interactions form a network that can easily reform, providing a dynamic structure. On the other hand, chemical gels involve covalent bonding to create cross-linkages, resulting in more stable and mechanically resistant organic gels [172,173].

Polymers are extensively used as gelators to form ionogels due to their versatile skeleton design and high IL encapsulation ability [172,174]. The simplest method to prepare

ionogels is the direct mixing of an IL with a polymer network, resulting in a network that confines ILs. However, the miscibility of ILs with commercially available polymers, such as poly(methyl methacrylate) (PMMA), poly(ethylene oxide) (PEO), and etc., can limit preparation and sometimes result in low IL content in ionogels [175]. In situ gelation using monomers or polymers in the presence of an IL is an efficient strategy to form ionogels with high IL content. Techniques such as free radical polymerization, ring-opening polymerization, and thermal and UV-curing are common methods to form polymer networks that encapsulate ILs and yield ionogels [174,176,177]. These chemically cross-linked ionogels generally exhibit high mechanical strength and thermal stability, making them suitable for applications in energy and electronics materials [175,178]. Self-assembly of ABA triblock copolymers in an IL is another approach to prepare physically cross-linked ionogels [179]. Additionally, semi-crystalline homopolymers with crystalline domains can also be physically cross-linked to produce ionogels [180]. Biopolymers such as chitosan, cellulose, starch, and gelatin have also been studied as excellent gelators for ionogels [181].

Additionally, ILs can be encapsulated in inorganic ionogels using materials like silica, carbon nanotubes, and titanium dioxide. These ionogels are formed either by dispersing nanoparticles in an IL or through sol–gel reactions. Dispersing nanoparticles into ILs allows for stable suspensions without surfactants or polymeric gelators, with the formation and stability influenced by nanoparticle size, distribution, and IL properties. In sol–gel reactions, IL molecules form covalent bonds with nanoparticles [182]. The properties of these ionogels depend on the size, shape, surface area, and dispersion of inorganic particles [183,184].

Another interesting method to fabricate ionogels is using poly (ionic liquid)s. PILs are ionic polymers with IL species in their side chain or backbone. They combine the

properties of ILs and polymers, resulting in materials with superior mechanical strength, durability, processability, and structural versatility [185]. PILs can be cationic, anionic, or zwitterionic, containing cations, anions, or both on their polymer backbone. These polymers are created by combining various cations (e.g., alkylammonium, alkylphosphonium, imidazolium) and anions (e.g., halides, carboxylate, sulfonate) with diverse polymer structures (e.g., homopolymers, copolymers), leading to a wide range of PILs with applications in energy, catalysis, environmental, and biomedical fields [186]. PILs are prepared through two main strategies: direct polymerization of IL monomers and post-polymerization functionalization of non-ionic polymers. Techniques like free radical polymerization, reversible deactivation radical polymerization, ring-opening metathesis polymerization, and step-growth polymerization are employed to create homo- and co-polymers of PILs [187]. Unlike conventional cross-linked polymers, PIL-based ionogels exhibit high compatibility with ILs, preventing phase separation. Often, copolymerization of IL monomers and a cross-linker in an ionic liquid medium is used to prepare PIL-based ionogels, enhancing their application potential [188].

In terms of physicochemical properties of IGs, ionogels inherit a range of unique properties from their intrinsic ILs and gelators, including mechanical strength, viscoelastic behavior, exceptional ionic conductivity, impressive thermal and electrochemical stability, and non-volatility [189](Figure 1-8).

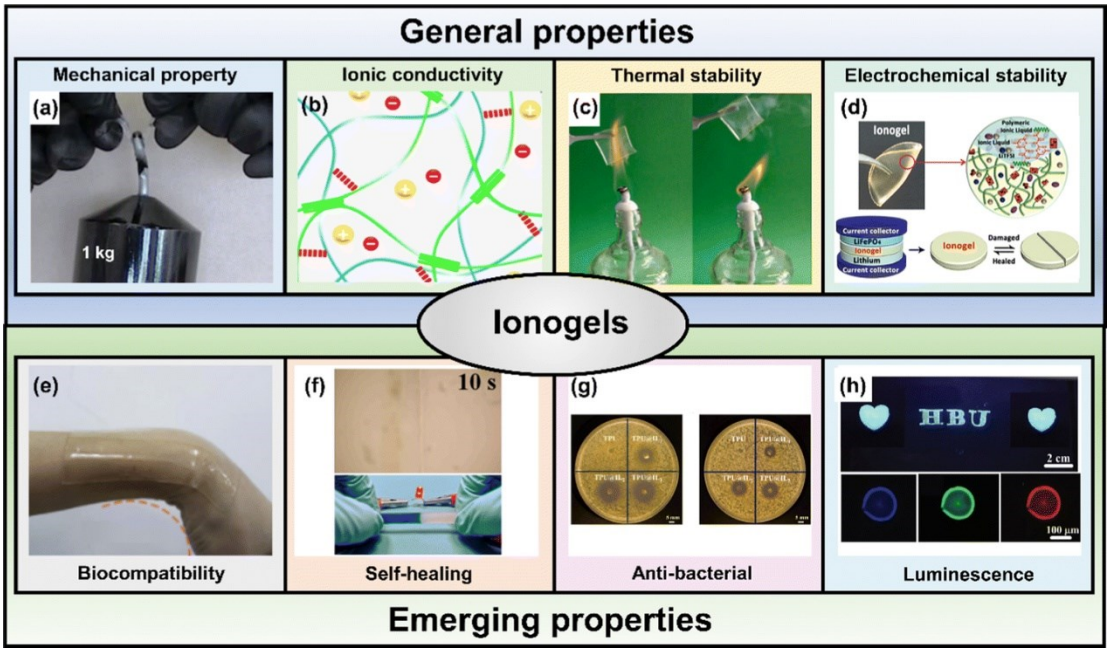

Figure 1-8: Schematic representation of the distinctive properties of ionogels [189] *(Reprinted with permission).*

The mechanical and rheological properties of ionogels are critical for various applications. Despite their many advantages, most ionogels exhibit weak mechanical properties, such as low tensile strength, fracture toughness, and tensile modulus [190]. Efforts are ongoing to improve these properties by understanding the key factors that influence them, such as the cross-link density of the ionogel host networks [191–193].

Ionic conductivity in ionogels, inherited from ILs, is a crucial characteristic influenced by several factors. Unlike ionogels containing PILs, which typically exhibit low ionic conductivity due to restricted ion movement after polymerization, ionogels composed of free ILs within polymeric or inorganic networks demonstrate relatively high ionic conductivity [194]. The chemical structure of ILs, particularly the anions with weak hydrogen bonding capabilities like $[BF_4]^-$, $[PF_6]^-$, and $[DCA]^-$, significantly impacts the ionic conductivity of ionogels [195]. Additionally, viscosity and ion size also play critical

roles; longer alkyl chains in cations increase viscosity and decrease ion mobility, thereby reducing ionic conductivity. Optimal ionogel performance thus favors ILs with low viscosity and smaller ion sizes to enhance ionic conductivity [196]. Furthermore, by varying the ILs, polymer networks, and incorporating functional fillers, ionogels can exhibit a diverse array of intriguing functional properties. These include biocompatibility, biodegradability, self-healing capabilities, shape-memory effects, luminescence, and antibacterial properties. Such versatile characteristics expand the potential applications of ionogels across various fields [189].

In the following sections, we will explore the advantages of ILs in enhancing icephobicity.

1.3.3.3 Application potential of ILs in icephobicity

Ice poses significant challenges across various human activities. Passive anti-icing strategies aim to disrupt the sequence of ice formation and accumulation. Static icephobic surfaces have been developed to prevent liquid water adherence, inhibit ice nucleation, control ice growth, restrict ice propagation, and reduce ice adhesion. However, recent academic research highlights dynamic anti-icing surfaces that can dynamically alter the chemical and physical states of the ice-substrate interface, enhancing anti-icing performance. Surfaces with dynamic interfaces are particularly intriguing for their ability to reduce ice adhesion by maintaining a premelted or liquid-like aqueous layer at the interface, effectively preventing ice formation [86,197].

The thickness of this interfacial layer, typically in the nanometer scale, plays a crucial role. Introducing dynamic interface melting agents, such as ILs, further enhances lubrication

effects by diffusing into water droplets and lowering the freezing point [106,198]. Unlike conventional ionic salts, large ILs do not get trapped within ice crystals, allowing them to create a thicker liquid interfacial layer that persists longer at subzero temperatures. ILs are commonly incorporated into IGs, particularly polymer-based IGs, which show promise in anti-icing applications despite being relatively new in development [18].

Emerging studies also explore advanced icephobic gels like hydrogels and organogels, which leverage stiffness mismatches between ice and substrate to induce interface cracks and reduce ice adhesion strength [53].

This study in first steps aims to assess how the presence of ILs influences the anti-icing performance of various top-coats, highlighting their potential in advancing icephobic technologies.

1.3.3.4 Literature survey on anti-icing surfaces containing ILs

In recent years, there has been a modest yet significant advancement in developing innovative gels and coatings incorporating ILs, aimed at maximizing their unique potential in anti-icing applications. These efforts underscore a growing interest in exploring ILs as a promising approach to enhance anti-icing performance. It is worth mentioning that the detailed exploration of these works in this area can be counted on one hand.

Zhou et al. used atomistic modeling to study the anti-icing properties of gelatin-based ionogels containing 1-butyl-3-methylimidazolium bromide as IL. They found that these ionogels can inhibit ice nucleation and slow down ice growth by reducing the freezing temperature at the interface and forming a liquid layer that helps detach ice, as demonstrated in Figure 1-9a-f. The unique ice formation dynamics on ionogel surfaces are due to the

complex interaction between ice growth and ionic liquid diffusion. When ice nucleates, latent heat is released, creating a slushy mixture of ice and liquid at 0°C. Heat is then conducted to the ionogel and convected to the air, lowering the temperature at the interfaces but maintaining a higher temperature at the ionogel interface due to the influx of ions, preventing ice growth from this interface and steering it inward. This mechanism, along with the reduced freezing point of the ILs solution, contributes to the anti-icing performance of the ionogels (Figure 1-9g,h) [19].

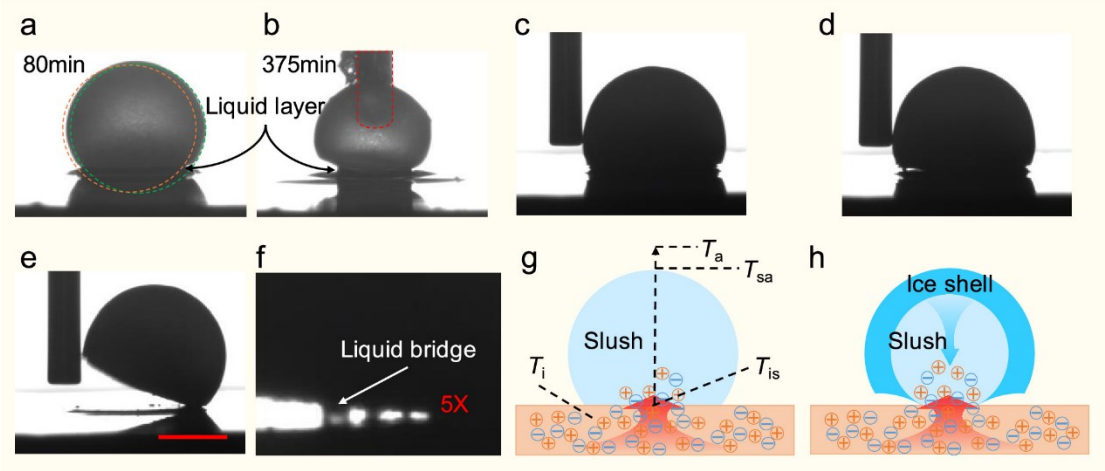

Figure 1-9: Dynamic melting of ice on ionogel surface at −20 °C. (a) A frozen droplet on the ionogel surface at 80 minutes. Green and orange dashed lines show the shape of the droplet at 110 and 140 minutes, respectively. (b) A probing needle penetrates the ice shell and into the ice-liquid mixture core of the same frozen droplet at 375 minutes. (c-e) The probing needle detaches the frozen droplet from the ionogel surface. (f) Liquid bridges are monitored during the detachment of the frozen droplet. All images share the same scale bar of 1 mm, shown in panel (g) (red bar). (g) A schematic illustrating the slush formation after ice nucleation and ionic liquid diffusion into the droplet on the ionogel surface. (h) A schematic depicting the ice growth retardation process of the droplet on the ionogel surface. The time indicated in panels (a) and (b) is the actual time of the example images [19] *(Reprinted with permission).*

According to the findings, ionogel surfaces demonstrate excellent icephobic properties due to creating a non-frozen liquid layer that inhibits ice formation and reduces

ice adhesion. In condensation-frosting experiments, ionogel surfaces showed effective anti-frost behavior (Figure 1-10) by absorbing water vapor and preventing ice solidification, confirming their potential for practical applications [19].

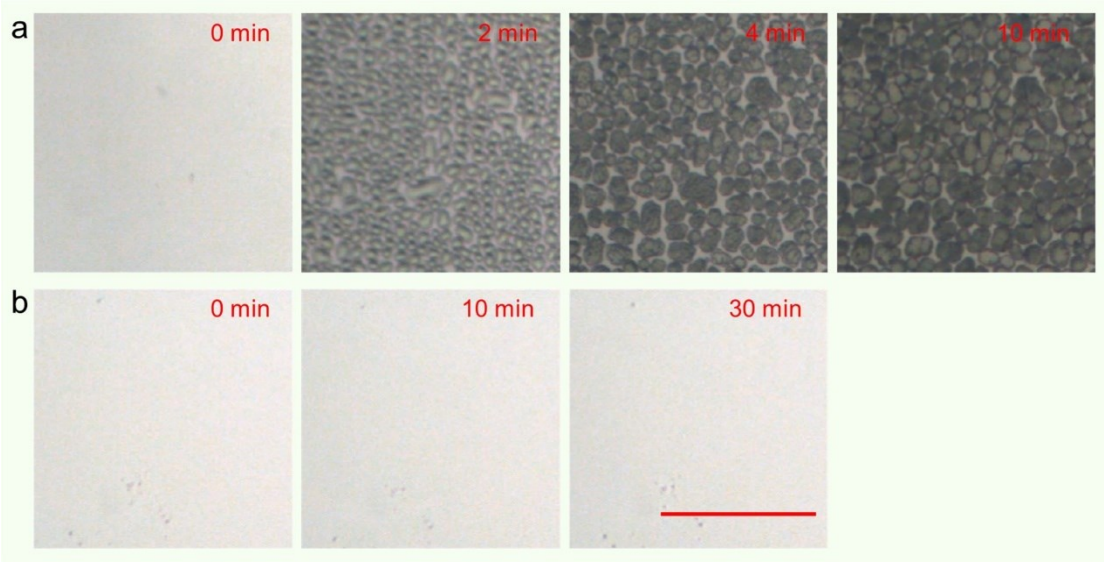

Figure 1-10: Comparison of condensation-frosting on glass (a) and ionogel surfaces (b). Both samples are cooled from 25 to −20 °C at a rate of 10 °C/min and then maintained at −20 °C in a humid environment (20 °C, 60% RH). Time is recorded from the start of cooling. All images share the same scale bar of 10 μm (red bar in panel b) [19] *(Reprinted with permission).*

In addition to interfacial slippage, a sliding angle of less than 10° is a crucial feature for facilitating the detachment and removal of ice. IGs offer promising potential to enhance the easy-sliding feature of current surfaces for long-term use. When the polymer chain and IL are miscible with each other but immiscible with water, the resulting IG exhibits easy-sliding properties for water. Figure 1-11 demonstrates the behavior of designed easy-sliding IGs for oil and water droplet mobility. According to results from Ding et al. [199], strong interactions between polymer chains and imidazolium-based ILs provide stable soft quasi-liquid surfaces with ILs trapped in the crosslinked polymer network. The anion

trifluoromethanesulfonate yields the smallest water critical sliding angle (CSA) of about 2°, whereas hexafluorophosphate shows the largest water CSA of about 18°. However, it's important to note that the anti-icing properties of these IGs were not evaluated in this study.

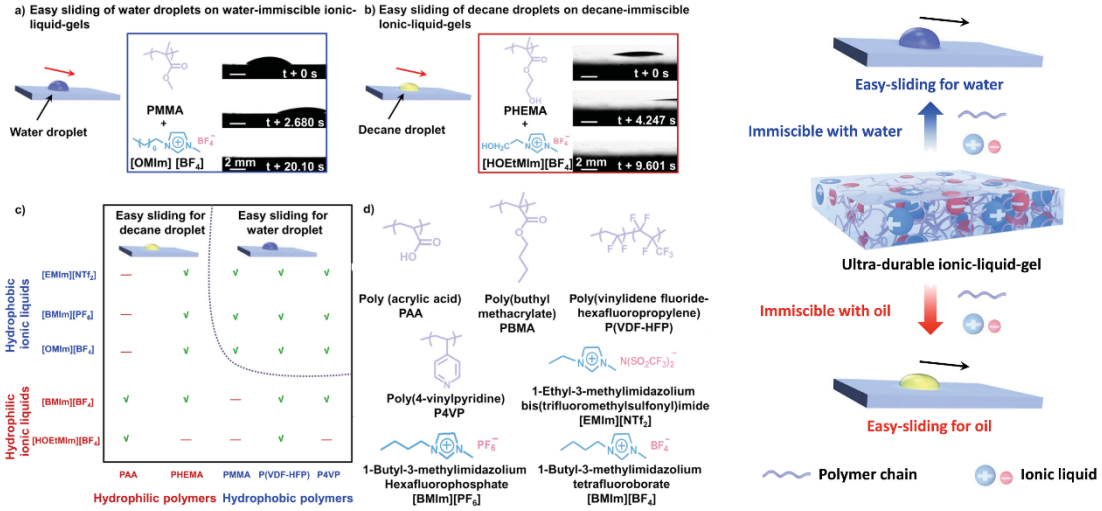

Figure 1-11: Demonstration of easy-sliding IGs for Droplet Mobility. (a) An 8 μL water droplet easily slides on a water-immiscible ILG composed of PMMA and [OMIm][BF4], with the ILG containing 60 mol% [OMIm][BF4]. (b) In contrast, a decane-immiscible ILG composed of PHEMA and [HOEtMIm][BF4] exhibits an easy-sliding property for a decane droplet, with the ILG containing 60 mol% [HOEtMIm][BF4]. (c) Easy-sliding properties are generated when the testing liquid is immiscible with both the ILs and polymer chains that constitute the ILG. A green checkmark indicates the corresponding ILG is easy-sliding, while a red cross indicates the ILG cannot be synthesized. (d) Molecular structures of the polymers and ILs used for the preparation of ILGs. The tilt angles in (a) and (b) are fixed at 10° [199] *(Reprinted with permission).*

Very recently, three significant studies have explored the potential of ILs in anti-icing applications from a coating perspective:

Wang et al. reported a novel thermoplastic polyurethane (TPU) coating infused with 1-octyl-3-methylimidazolium tetrafluoroborate ([OMIM]BF_4) through a thermally induced phase separation process, as shown in Figure 1-12. This infused coating demonstrated a low ice adhesion strength of 10.03 ± 2.62 kPa. The anti-icing mechanism, which involves the

creation of a lubricant layer through phase separation during cooling, is similar to that of superhydrophilic surfaces. Unlike the hydration layer on superhydrophilic anti-icing coatings, the ionic liquid layer can function effectively at much lower temperatures, enhancing the coating's performance in extreme cold conditions [27].

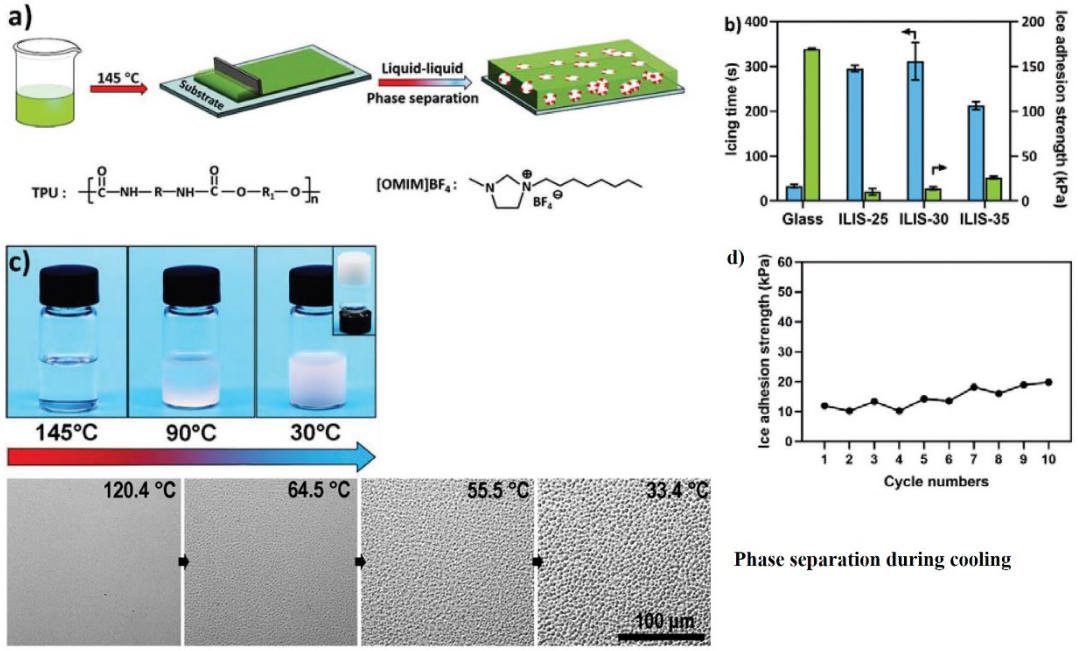

Figure 1-12: a) Schematic illustration of the fabrication process of the ionic-liquid-infused surface (ILIS), b) Icing time and ice adhesion strength on glass and the ILIS at −20 °C. c) Phase separation process of 30 wt.% TPU/[OMIM]BF_4 solution under a hot-stage microscope. The scale bars are 100 μm. And digital images of the phase separation process during natural cooling. d) Cycled de-icing test on the ILIS at −20 °C [27] *(Reprinted with permission).*

Another recent study focused on amphiphilic PIL-based surfaces designed for antifogging and anti-frosting applications, which also exhibit potential anti-icing properties. Researchers developed well-defined triblock copolymers consisting of a polydimethylsiloxane component coupled with PIL segments of poly([2 (methacryloyloxy)ethyl] trimethylammonium chloride) (PMETAC). These copolymers were

UV-cured with an oligo(ethylene glycol) dimethacrylate (OEGDMA) cross-linker. By varying the counterion (trimethylammonium bis(trifluoromethanesulfonyl)imide ($TFSI^-$)) and the content of the PIL segments and cross-linker, the resultant semi-interpenetrating polymer networks (SIPNs) achieved an ice adhesion strength as low as 13.3 ± 8.6 kPa. The study highlighted that self-lubrication due to the presence of non-freezable bound water led to the observed low ice adhesion strength, offering a new approach for exploring PIL-based icephobic coatings for practical applications [26].

Recently, Weiwei Yan and colleagues introduced an innovative solution to overcome the challenges of poor strength, weak substrate adhesion, and limited anti-icing properties by developing a thermomechanically robust polyionic elastomer (PIE) with enhanced anti-icing capabilities. This advanced PIE is composed of free ionic liquid (1-ethyl-3-methylimidazolium ethyl sulfate: EMIES) integrated into a charged three-dimensional polymer network. This network is polymerized from acrylic acid (AA), acrylamide (AAm), and the zwitterion [2-(methacryloyloxy)ethyl]dimethyl-(3-sulfopropyl)ammonium hydroxide (DMAPS) through a one-pot in situ free radical photopolymerization process. The PIE surface boasts an impressive icing delay time of up to 5400 seconds and remains frost-free after 3.5 hours of exposure to -10°C. This exceptional performance is due to the inhibitory effect on ice formation exerted by the ions from the ILs and the polyelectrolyte network. Additionally, the PIE demonstrates outstanding anti-icing durability, maintaining ice adhesion strengths below 35 kPa even after 30 icing/deicing cycles at -20°C. Its resilience is further proven through rigorous tests, including 300 cycles of sandpaper abrasion, scratching, and heat treatment at 100°C for 16 hours, where the adhesion strength remains

around 20 kPa. This highlights the material's robustness under various thermal and mechanical conditions [200].

In contrast, superhydrophobic coatings rely on low surface energy and micro-/nanostructured surfaces to repel water and delay ice formation, offering low ice adhesion but suffering from poor durability under mechanical abrasion or prolonged environmental exposure. Hydrophilic coatings, on the other hand, promote water spreading to prevent ice adhesion and are cost-effective and simple to produce, but they generally exhibit higher ice adhesion and reduced performance under freezing conditions. Conclusively, these studies illustrate the promising potential of IL-infused coatings in enhancing anti-icing properties, paving the way for more efficient and effective ice-resistant surfaces. Given the increasing demand for long-lasting anti-icing solutions, ILs show great promise for sub-freezing applications by introducing dynamic properties at the interface. However, the exploration of the anti-icing properties of different ILs has been limited, and their development as coatings remains in its early stages.

1.3.4 Dynamic ice

In outdoor settings, ice properties are dynamically changing and ice nucleation is almost unavoidable due to factors like low temperatures, prolonged icing periods, and surface contamination. Consequently, once ice begins to form, controlling its growth and propagation becomes crucial in preventing ice accumulation. This has become a significant focus in the design of anti-icing surfaces [13,201,202].

Controlling ice growth in specific patterns on surfaces offers an effective approach to achieving icephobicity, especially since complete prevention of ice formation is often

unattainable [202–204]. Further exploration of the freezing-driven ice-removal mechanism on different surfaces revealed that the key to self-dislodging of frozen droplets lies in the orientation of the freezing process. Successful self-dislodging requires the outer surface of the droplet to solidify first, forming an ice shell while the droplet-substrate contact region remains liquid. As freezing progresses inward, the expanding volume causes displacement towards the liquid interface, lifting the droplet when it solidifies. This phenomenon, observed on substrates with a range of wettability and textures, suggests a universal concept for designing ice-free surfaces through controlling asymmetric freezing dynamics [205].

Recent advancements in dynamic ice repellency involve controlling the multicrystal ice growth pattern on exposed surfaces. A novel approach utilizes silver iodide (AgI) nanoparticles as active sites for ice nucleation, ensuring simultaneous ice formation. Research indicates that ice crystals on hydrophilic surfaces (water contact angle of 14.5°) exhibit an along-surface growth (ASG) mode, while those on hydrophobic surfaces (water contact angle of 107.3°) show an off-surface growth (OSG) mode. This ASG-to-OSG transition is also seen on porous surfaces with varying water contact angles, suggesting the behavior's ubiquity across different structured surfaces. The growth mode of ice crystals had a significant impact on the contact area ($A_{contact}$) between the ice and its substrate, thereby affecting the ice adhesion strength. In the OSG mode, the contact area was approximately 10% of the projected area ($A_{project}$). In contrast, the ASG mode resulted in nearly complete ice contact with the surface, with $A_{contact}/A_{project} \approx 90\%$. During ice-removal tests, the ice formed in the OSG mode was easily dislodged by a breeze with a velocity of 5.78 m/s at −3 °C, while the ice formed in the ASG mode remained firmly attached to the surface. The unique OSG mode offers alternative methods for surface frost removal. However, further

research is required to evaluate the icephobicity of these surfaces against larger water droplets, highlighting the potential of manipulating ice growth patterns to develop more effective ice-repellent surfaces [206].

Recent studies have focused on programming ice growth across entire the surface through surface chemistry and structural design [207,208]. Surfaces created with poly(poly(ethylene glycol) methyl ether methacrylate)/PDMS (P(PEGMA)/PDMS) Janus particles exhibited controlled ice growth, resulting in ice crystals or dendrites in specific regions while keeping other areas dry and clean (Figure 1-13a) [207]. Additionally, surfaces patterned with polyelectrolyte multilayers and polyelectrolyte hydrogels achieved ice-free regions covering approximately 96% and 88% of the total surface area, respectively (Figure 1-13b) [209]. Literally, On the Janus surfaces, water condensed into a liquid film on the hydrophilic regions, forming continuous frozen films. In contrast, water droplets condensed on the hydrophobic regions, resulting in frozen droplets and ice bridges. The icing process on these surfaces followed a distinctive pattern. Initially, condensed droplets froze unevenly, with ice crystals forming primarily in the larger liquid droplets on the hydrophilic areas. These frozen droplets then influenced the surrounding regions. Meanwhile, small droplets on the hydrophobic areas clustered around the frozen droplets and evaporated. Subsequently, desublimation of vapor into ice promoted the growth of existing frozen droplets into dendrites, creating ice-free zones around the larger dendrites. This formation of ice-free zones and the reduced ice contact area contributed to the Janus surfaces exhibiting a low ice adhesion strength of 56 kPa [207,208]. This innovative approach demonstrates significant potential for enhancing ice repellency by strategically managing ice growth.

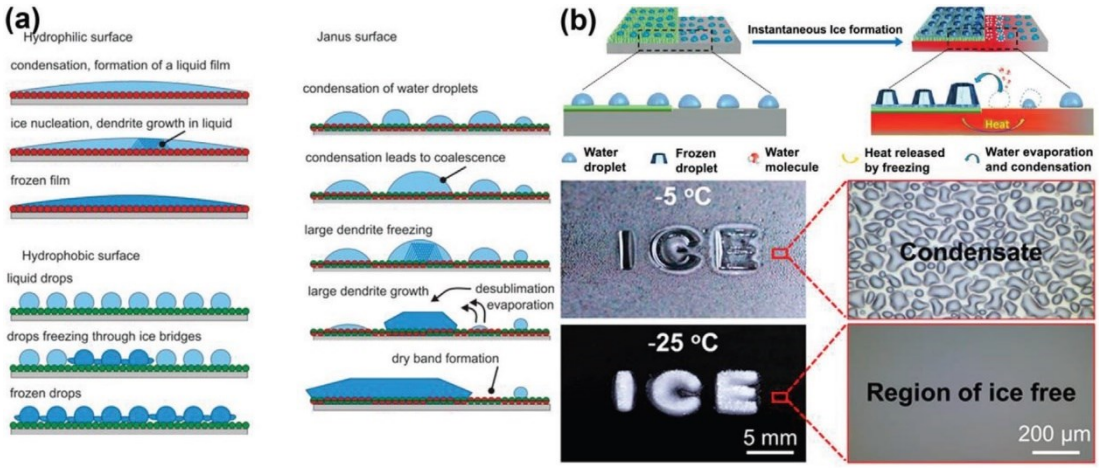

Figure 1-13: DAIS through Ice-Free Zone Programming: a) Mechanism of ice formation on rough hydrophilic, hydrophobic, and Janus surfaces [207]. *b) Patterned polyelectrolyte coatings for dynamically controlling large-scale ice-free regions* [209] *(Reprinted with permission).*

Dynamic Ice melting, one of strategies within dynamic ice approach is a crucial aspect of dynamic ice management to prevent unwanted ice accumulation. Surfaces that can dynamically melt ice are often engineered by incorporating materials with thermal properties, such as electrothermal, near-infrared photothermal, magnetothermal, and solar photothermal effects [117,210,211]. In the following section, we will explore the concept of ice growth inhibitors, another strategy of this group that that has captured our attention.

1.3.4.1 Ice growth inhibitors

Natural organisms such as insects, fish, and plants utilize antifreeze proteins (AFPs) to survive subzero temperatures, providing a vivid example of ice growth inhibition [85,212]. AFPs can suppress the freezing point and inhibit ice growth and recrystallization due to their Janus properties. These proteins have ice-binding faces (IBFs) and non-ice-binding faces (NIBFs). In solution, AFPs preferentially bind to ice crystals with IBFs, leaving the NIBFs facing liquid water, creating microcurvatures at the ice–water interface. This curvature, due to the Kelvin effect, inhibits ice growth [213]. Indeed, below equilibrium melting

temperature, ice growth is inhibited through the convex ice-water interface formation toward the water phase and, above equilibrium melting temperature, ice melting is inhibited through the concave ice-water interface formation inward to ice phase. Inspired by AFPs' ability to regulate ice growth through basal/prism plane absorption, materials such as graphene oxide (GO), oxidized quasi-carbon nitride quantum dots, and safranine molecules have been discovered to have similar properties. Although these materials have demonstrated ice growth inhibition in solutions, applying this strategy to design anti-icing surfaces is still in its early stages [214–216]. Counterions at the ice–substrate interface can also inhibit ice growth through dynamic melting [217].

Phase-switching liquids (PSLs), such as cyclohexane (SCh), have been used to inhibit ice growth due to their ability to maintain a melting temperature (T_{mp}) above the water freezing point (T_{fp}) [123,218,219]. When vapor condenses on a solidified PSL surface, the latent heat released during condensation is trapped in the droplets, increasing the temperature at the solidified cyclohexane and air interfaces to around 5°C. This increase in temperature melts the PSL in the contacted region. Comparing freezing initiation time and total freezing delay time, PSL-coated surfaces excel in inhibiting ice growth. The best sample showed sustained ice growth delay for more than 96 hours, 300 times longer than superhydrophobic surfaces. PSLs can also be infused into porous surfaces, forming SLIPS. Infused samples with 10 μm spacing microstructured surfaces dynamically inhibited frost propagation for more than 140 minutes, about seven times longer than liquid-infused surfaces (LIS). However, the reported PSL chemicals, such as benzene, are highly toxic, and safer, environmentally friendly phase-switching liquids with melting temperatures close to the

water freezing point are needed. Deep eutectic solvents as green ice-responsive materials are promising candidates for inhibiting ice growth effectively.

1.3.5 Deep eutectic solvents (DESs)

Deep Eutectic Solvents (DESs) are an emerging class of green solvents closely related to ILs and have gained significant attention over the past two decades [220]. This interest began after a study by Abbott et al. observed an unusually deep melting point depression at the eutectic composition of certain hydrogen bond donors (HBDs) and acceptors (HBAs) [221]. This phenomenon was first identified in a 1:2 mole fraction combination of powdered choline chloride ((2-hydroxyethyl)trimethylammonium chloride, ChCl) [melting point, $T_m \approx$ 302 °C] with crystalline urea [$T_m \approx 133$ °C], resulting in a liquid at room temperature [melting point of mixture at eutectic composition, $T_{eutectic} = 12$ °C] (Figure 1-14). Abbott et al. referred to this liquid as a "deep" eutectic mixture (DEM) to describe the significant melting point depression [222]. These DEMs, which melt at low enough temperatures to make novel liquids economically accessible as solutes and/or electrolytes for new and existing chemistries, have led to the widespread adoption of the term 'deep eutectic solvent' (DES) for this class of materials, highlighting their primary feature of interest [223,224].

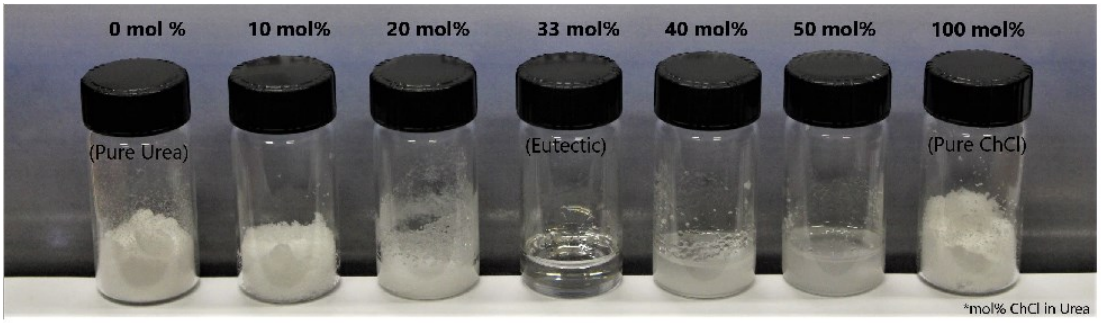

Figure 1-14: Choline chloride and urea mixtures at 303 K (mol % ChCl, left to right: 0, 10, 20, 33 (χ_{eut}), 40, 50, 100). The lowest observed melting point for this binary mixture occurs

at a 1:2 ratio, with a melting point of 12 °C, making it a liquid at room temperature. This ratio is defined as the eutectic composition (χ_{eut}) [225] *(Reprinted with permission).*

1.3.5.1 Definition and types of DESs

DESs are innovative green solvents composed of at least two components: a HBA and a HBD. These components interact to form a eutectic phase with a melting point below 100°C, lower than the melting points of the individual components. DESs are valued for their safety, low toxicity, renewability, biodegradability, and cost-effectiveness. They are often represented by the formula $Cat^+X^-_zY$, where Cat^+ is an ammonium, sulfonium, or phosphonium cation, X^- is a Lewis base (usually a halide anion), and Y is a Lewis or Bronsted base [226]. The primary interactions within DESs are hydrogen bonds, with occasional electrostatic forces and van der Waals interactions [227]. Figure 1-15a provides a schematic representation of the formation of a deep eutectic solvent.

Research shows that DESs primarily exhibit intramolecular hydrogen bonds between the HBD and the halide anion, which define their fundamental properties [228]. Recent computational studies have provided insights into the nanostructure of DESs, revealing how hydrogen bond networks between the salt and HBD contribute to melting points and viscosities [229,230]. For example, ChCl/urea mixtures demonstrate a well-established hydrogen bond network, resulting in higher melting points and viscosities, while ChCl/glycerol and ChCl/ethylene glycol mixtures show less hydrogen bond network, leading to lower melting points and viscosities. The higher viscosity of ChCl/glycerol compared to other eutectic mixtures is due to the oversaturation of HBD groups in the bulk, leading to more extensive HBD self-interaction [231].

The diversity of HBA and HBD combinations capable of forming eutectic mixtures is vast. DESs are classified into four types: Type I (quaternary salt and metal halide), Type II (quaternary salt and hydrated metal halide), Type III (quaternary salt and hydrogen bond donor), and Type IV (metal halide and hydrogen bond donor). Most studies focus on quaternary ammonium cations combined with hydrogen bond donors like amides, acids, and alcohols, particularly those involving ChCl with urea, ethylene glycol, or glycerol [226,232]. Figure 1-15b illustrates the common components of DES.

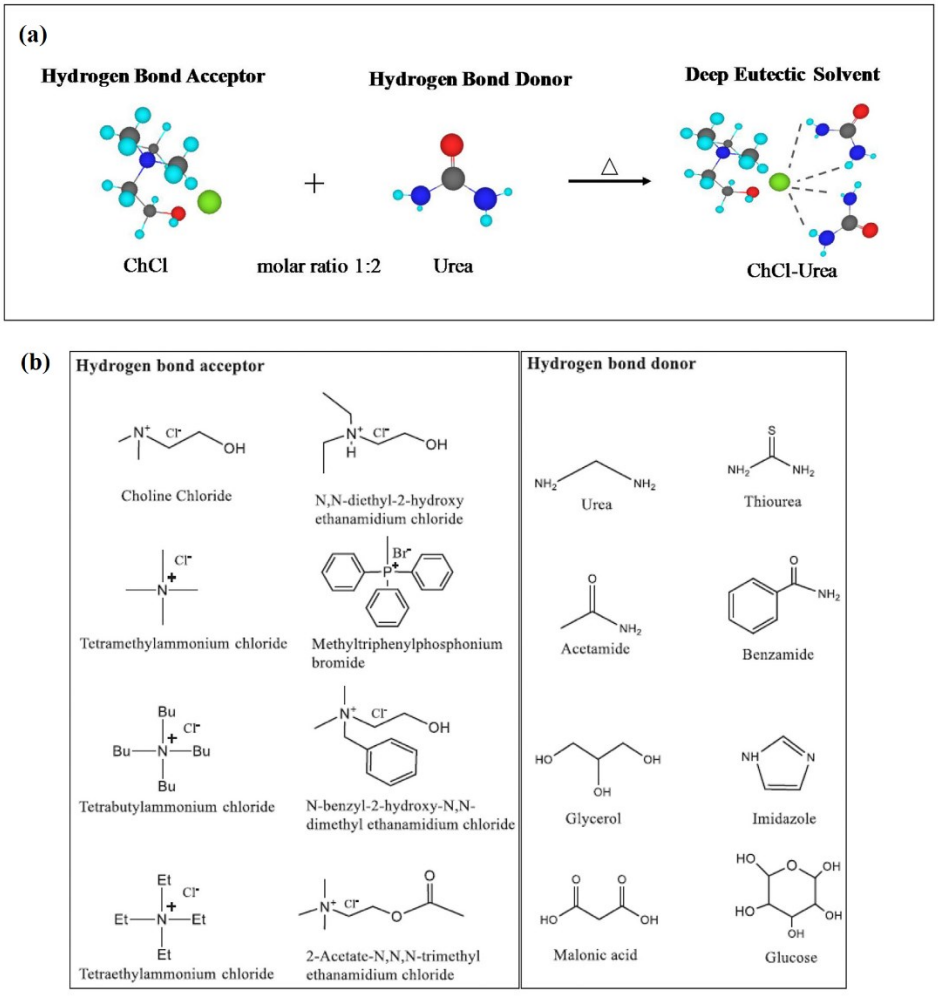

Figure 1-15: (a) Schematic representation of the formation of a DES, illustrated using ChCl) and urea. (b) Examples of common HBA and HBD typically used [233] *(Reprinted with permission).*

In 2011, Choi discovered a new class of deep eutectic solvents, termed NADES, while investigating the solubility of intracellular compounds that are insoluble in water and lipid phases [234]. There are two particular classes of DES, natural deep eutectic solvents (NADES) and therapeutic deep eutectic solvents (THEDES), which recent attention has also turned to which show promising applications due to their unique properties. NADES are mixtures of metabolites found in large quantities in cells, playing crucial roles in biological processes like cryoprotection, drought resistance, germination, and dehydration [235]. These solvents may represent a third liquid phase in living organisms, with over 30 combinations of NADES identified for solubilizing, storing, and transporting non-water-soluble metabolites. Mixtures of ChCl with various natural products, such as organic acids, alcohols, sugars, and amino acids, have resulted in the discovery of more than 100 NADES [236,237]. The potential applications of NADES in the food, cosmetic, and pharmaceutical industries have been frequently highlighted, with successful uses in extraction and separation processes [235,238].

THEDES are a specialized category of deep eutectic solvents designed for pharmaceutical applications. These systems combine an active pharmaceutical ingredient (API) with other components to form a eutectic mixture that enhances drug solubility and permeability [239]. Despite the limited structural and functional data available so far [240], THEDES hold substantial promise for advancing pharmaceutical formulations and are expected to see increased use in the near future.

1.3.5.2 Phase behavior of Deep Eutectic Solvents

The eutectic point is the defining characteristic of DESs, marking the specific composition at which the mixture achieves its lowest melting point. For example, Reline, a well-known DES, has a eutectic point at 66.7 mol % urea (HBD) and 33.3 mol % choline chloride (HBA), or a 2:1 molar ratio of HBD to HBA. However, DESs can exhibit a variety of eutectic compositions [221,241,242].

The difference in freezing points at the eutectic composition of a binary mixture, denoted as ΔT_f, indicates the strength of the interaction between the components. The greater the interaction, the larger the ΔT_f. This concept is illustrated schematically in Figure 1-16. For type I eutectics, interactions between different metal halides and the halide anion from a quaternary ammonium salt typically form similar halometallate species with comparable enthalpies of formation, suggesting ΔT_f values between 200 and 300 °C. Generally, to produce a eutectic near ambient temperature, the metal halide needs a melting point around 300 °C or lower. Hence, metal halides like $AlCl_3$ (mp = 193 °C), $FeCl_3$ (308 °C) [243], $SnCl_2$ (247 °C) , $ZnCl_2$ (290 °C) , and $GaCl_3$ (78 °C) [244] create ambient temperature eutectics. Type II eutectics aim to incorporate other metals into DES formulations, leveraging the lower melting points of metal halide hydrates compared to their anhydrous counterparts. Hydration lowers the melting point by reducing the lattice energy of metal salts [226].

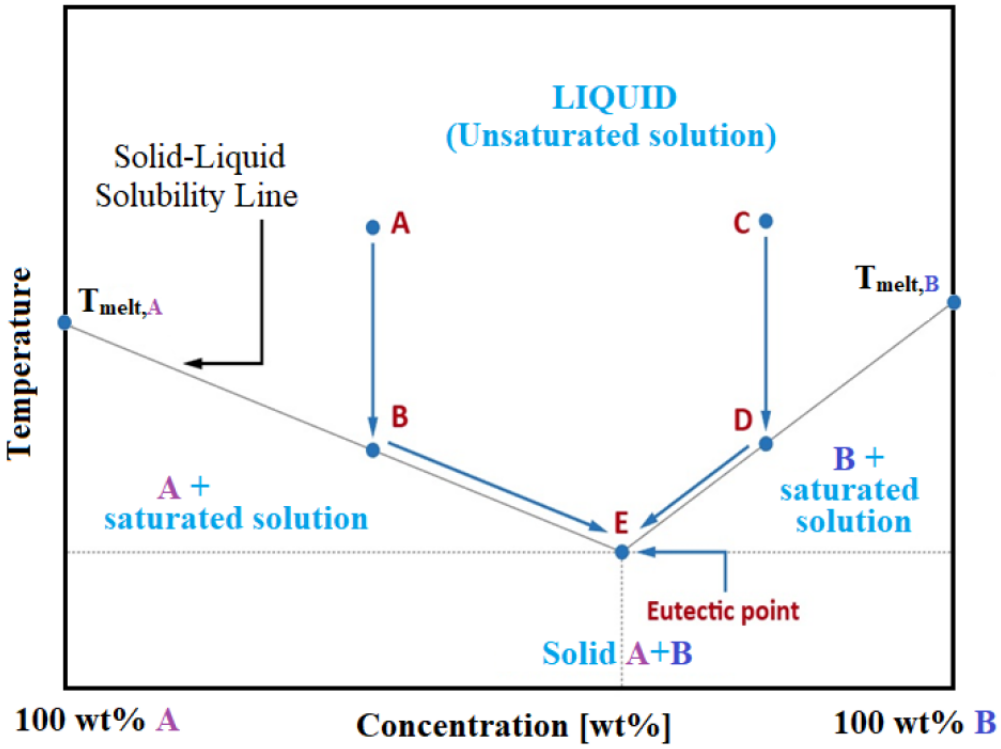

Figure 1-16: Schematic illustration of a eutectic point on a binary phase diagram [225] *(Reprinted with permission).*

Despite the significance of eutectic compositions and binary phase diagrams, specific data for individual DESs remain scarce. Obtaining these phase diagrams is crucial, as they inform researchers about the temperature and composition ranges where a liquid phase is expected, aiding in the design of DES systems for specific applications. While many studies analyze mixtures at their supposed eutectic compositions, they often lack binary phase diagrams to validate these choices [225]. The properties and dynamics of DESs vary significantly with different compositions. Therefore, exploring compositions beyond the eutectic point (χ_{eut}) could be highly beneficial [242]. This comprehensive analysis is essential for finding practical ways to utilize DESs in industrial applications, paving the way for fully realized designer solutions.

1.3.5.3 Preparation, physicochemical properties and application of DESs

While DESs and conventional ILs have distinct chemical properties, they share several appealing physical characteristics. Both serve as tunable solvents, customizable for specific chemical processes, and feature low vapor pressure, a relatively broad liquid range, and nonflammability. DESs offer notable advantages over traditional ILs, including easier preparation and availability from inexpensive, well-characterized components, facilitating large-scale processing and shipping. Despite being generally less chemically inert, DESs can be produced simply by mixing two components with moderate heating, keeping production costs lower than those of conventional ILs like imidazolium-based liquids. This simplicity and cost-effectiveness make DESs highly suitable for large-scale applications [226].

From a practical and experimental perspective, DESs are typically prepared by mixing an HBA and an HBD at an appropriate temperature, using one of two methods: (1) melting the lower melting point component first and then adding the higher melting point compound to the liquid, or (2) mixing and melting both components together when they both have high melting points. Since Abbott's pioneering work [221], where solid ChCl and urea were heated at a 1:2 molar ratio to produce a mixture that was liquid at room temperature, many DESs have been prepared using these methods [245].

To correctly design and expand the applications of DESs, a detailed understanding of their physical properties is crucial. DESs are generally characterized by low melting points, low volatility, non-flammability, low vapor pressure, dipolar nature, chemical and thermal stability, high solubility, tunability, low toxicity, and biodegradability [227]. Since these solvents are chemically tunable, their properties can be tailored to create task-specific DESs with varying physicochemical properties [226,227,246,247].

Recent systematic experimental studies have investigated the effect of cation alkyl chain length on the physical properties of DESs using mixtures of alkylammonium bromide salts with glycerol or urea [248]. The findings suggest that while the length of the cation alkyl chain has minimal impact on composition-dependent properties such as density, refractive index, and thermal conduction, it significantly influences properties affected by intermolecular forces, such as viscosity, surface tension, interfacial structure, and the melting point depression [249].

DESs with melting points below 50°C are particularly valued for their safety, low cost, and industrial applicability. The melting point of DESs is significantly influenced by the molar ratio of organic salts, alkyl chain length, hydrogen bond donors, and anions. For example, DESs formed from choline salts and urea show a decreasing melting point order of $F^- > NO_3^- > Cl^- > BF_4^-$, indicating a strong correlation with hydrogen bond strength [221].

Density is a crucial property of DESs, typically higher than water except in some hydrophobic DESs. This density is influenced by molecular organization, packing, and the presence of holes and vacancies within the liquid [232]. For instance, the urea/choline chloride system has a higher density than the urea/acetylcholine chloride system due to larger holes in the latter. The molar ratio of HBA to HBD also affects density; adding choline chloride to glycerol reduces density by increasing free volume. Additionally, longer alkyl chains in cations decrease DES density due to increased free volume from chain elongation [250]. Temperature changes significantly impact DES density, with higher temperatures leading to decreased density due to increased ionic motion and free volume [251].

Most DESs are viscous liquids at room temperature. This high viscosity is due to extensive hydrogen bonding, van der Waals forces, and electrostatic interactions between the HBD and HBA components. These interactions result in lower ionic mobility within the small void volumes of the liquid DESs. The viscosity of DESs is influenced by the chemical nature of the HBAs and HBDs, temperature, molar mass, and molar ratio [227]. Besides, DESs exhibit poor conductivity at room temperature due to their high viscosities, highlighting the strong relationship between viscosity and conductivity. The conductivity of DESs is influenced by the molar ratio of HBDs to HBAs, the alkyl chain length of the cation, and temperature [252].

Similar to the other properties, the surface tension of DESs is primarily influenced by the intermolecular interactions between HBAs and HBDs. It varies with temperature, the molar ratio of HBAs to HBDs, and the nature of these components. An increase in the alkyl chain length of the cation or the addition of organic salts tends to lower the surface tension by disrupting the hydrogen bond network [253]. DESs are primarily hydrophilic, but some are hydrophobic and immiscible with water which are useful for extraction processes due to their ability to form biphasic systems [254]. The hydrophobic nature of DESs is influenced by long alkyl chains in the HBAs, which create steric hindrance and reduce water interaction. Hydrophobic DESs generally have low densities and moderate viscosities at room temperature. Their physical properties, including viscosity, are affected by the anion size and alkyl chain length, with larger anions and longer chains increasing viscosity. Temperature increases lower the density and viscosity of hydrophobic DESs [255].

DESs have found wide-ranging applications across numerous fields due to their unique physicochemical properties. In pharmaceuticals, DESs enhance drug solubility and

permeability, leading to improved formulations. In environmental science, they are used for the extraction and recovery of valuable metals, providing a greener alternative to traditional solvents. DESs also play a significant role in green chemistry, serving as catalysts and reaction media that promote more sustainable industrial processes. In electrochemistry, DESs are utilized for electrodeposition and the synthesis of nanomaterials, while in energy storage, they are applied in the development of batteries and supercapacitors due to their high ionic conductivity and stability. Additionally, DESs are employed in biotechnology for enzyme stabilization and extraction, and in materials science for creating novel materials. Their versatility continues to drive innovation, making them indispensable in both industrial and research applications [225,226,233].

1.3.5.4 DESs vs ILs

DESs were introduced as a more accessible and environmentally friendly alternative to ILs. While some consider DESs a subclass of ILs, others view them as distinct entities [30]. DESs share many physical properties with ILs, such as a wide liquid range, low volatility, and high tunability, making them both versatile solvents. However, chemically, DESs differ from ILs in their formation and constituent materials. ILs are composed of organic heterocyclic cations and organic or inorganic anions [256], whereas DESs are combinations of HBAs and HBDs. DESs have a significant advantage in being composed of nontoxic, biocompatible, and readily available compounds, making them sustainable and environmentally safe [257]. Unlike ILs, the synthesis of DESs is straightforward, often involving simple heating or grinding methods, leading to 100% yield and efficient utilization of all starting materials without generating harmful by-products. This ease of preparation and

low cost make DESs particularly appealing for various scientific and industrial applications [256].

The structure and properties of both ILs and DESs are determined by intermolecular interactions, including Coulomb forces, hydrogen bonding, and dispersion forces. ILs are dominated by ionic interactions [258], while DESs, as eutectic mixtures, exhibit significant hydrogen bonding. Despite differences in constituent nature and dominant forces, ILs and DESs share many tunable properties, such as low melting points, density, and viscosity, which are strongly influenced by composition and temperature. High viscosity and density are practical drawbacks, though DESs can often be adjusted by adding water, albeit with caution to avoid decomposition [259]. Both ILs and DESs are highly polar, allowing them to solubilize a wide range of substances, and they exhibit low vapor pressure and wide liquid range. However, the vast number of possible combinations makes it challenging to generalize their physical properties [260]. Despite their many similarities, it is important to recognize the distinct intrinsic properties of each.

The adoption of ILs and DESs in industrial applications is hindered by several limitations, including the lack of standardized production protocols, which leads to inconsistencies in quality and properties across different batches. This challenge is particularly critical for industries such as pharmaceuticals and electronics, where precision and consistency are paramount. Additionally, there is a notable scarcity of long-term performance data regarding the durability, stability, and recyclability of ILs and DESs under operational conditions. These gaps, coupled with the need for real-world testing and extended studies, highlight the importance of addressing these challenges to unlock the full potential of ILs and DESs in diverse industrial applications.

1.3.5.5 Literature survey on anti-freezing surfaces containing DESs

Low melting points and high conductivity make DESs promising candidates for developing electrochemical systems that operate efficiently in cold environments. Recent advancements have focused on creating innovative gels incorporating DESs to maximize their potential in anti-icing applications. These efforts highlight a growing interest in exploring DESs to enhance anti-icing performance. However, similar to the literature on ILs, the detailed exploration of DESs in this context remains relatively sparse.

With the growing demand for energy storage and the need for batteries to perform in extreme weather conditions, the limitations of current batteries, especially at low temperatures, have become evident. Most batteries, particularly those using organic electrolytes, suffer from poor electrochemical properties such as low Coulombic efficiency, specific capacity, and capacity retention at low temperatures [261]. While aqueous energy storage systems offer advantages like high safety, low cost, and high stability, their high freezing points and low decomposition voltages restrict their electrochemical window, limiting their energy density and temperature range. Aqueous rechargeable multivalent metal-ion batteries (ARMMBs), especially those utilizing multivalent metals like zinc (Zn), magnesium (Mg), calcium (Ca), and aluminum (Al), have gained attention due to their high cost-efficiency, safety, environmental friendliness, and high specific capacity. However, developing ARMMBs for low-temperature operation remains challenging, particularly concerning electrolyte design. Significant progress has been made in this area, notably with aqueous Zn-ion batteries (AZIBs) [262–264]. The freezing of aqueous electrolytes at low temperatures hampers ion migration, reduces ionic conductivity, increases charge transfer resistance, and disrupts the electrode/electrolyte interface. To address these issues, anti-

freezing electrolyte strategies are critical. Among these, deep eutectic electrolytes, which have much lower freezing points than their individual components, show great promise [265]. They offer advantages such as outstanding electrochemical stability, ease of synthesis, nonflammability, low cost, and the ability to stabilize the electrolyte/electrode interface. By adjusting the solvation structure of Zn^{2+}, promoting uniform Zn nucleation, and reducing the energy barrier for Zn^{2+} de-solvation, deep eutectic electrolytes enhance the performance of AZIBs at low temperatures [266–268].

Regarding aqueous eutectic electrolytes for low temperatures, Viola et al. demonstrated that a eutectic mixture of lithium chloride and water remains liquid down to −74 °C and has high conductivity (1.83 mS/cm) at −70 °C, making it suitable for low-temperature energy storage. This electrolyte allows supercapacitors to maintain 72% of their room temperature capacitance even at −70 °C and extends the stability window to 3 V. Their gel electrolyte, combining PVA with aqueous LiCl, supports powering an LED at −70 °C, showcasing the effectiveness of aqueous eutectic electrolytes in extreme cold while using inexpensive and eco-friendly materials [269].

In the innovative study by Tian et al. [270], novel NADESs-based eutectogels were crafted with a unique sandwich-like structure, featuring two NADES@calcium alginate outer layers and a NADES@sodium alginate inner layer (Figure 1-17). This design was achieved through liquid casting and ion displacement-induced crosslinking. Static contact angle and FTIR analyses revealed that these eutectogels had highly hydrophilic surfaces (47.6°–55.7°) and were rich in hydroxy groups. Among them, the sorbitol-based DES eutectogels excelled in anti-frosting capacity, covering only 36.31% of the area with frost after 120 minutes under extreme conditions. This exceptional performance was attributed to their hydrophilic and

rough surfaces, featuring more pronounced and spikier hill-like profiles that provided a greater active area for moisture absorption. Additionally, these eutectogels demonstrated remarkable stretchability and stable mechanical strengths, even after storage at −50 °C, and maintained good flexibility at temperatures as low as −40 °C when fully moisture-absorbed. The study proposed and verified an absorption-inhibition hypothesis, where the eutectogels first absorbed ambient moisture (49% RH ~ 55% RH) and then inhibited crystallization by immobilizing the moisture within the NADESs systems (Tg: −58.6 °C ~ −50.5 °C). These findings highlight the significant potential of eutectogels for effective interfacial anti-frosting applications [270].

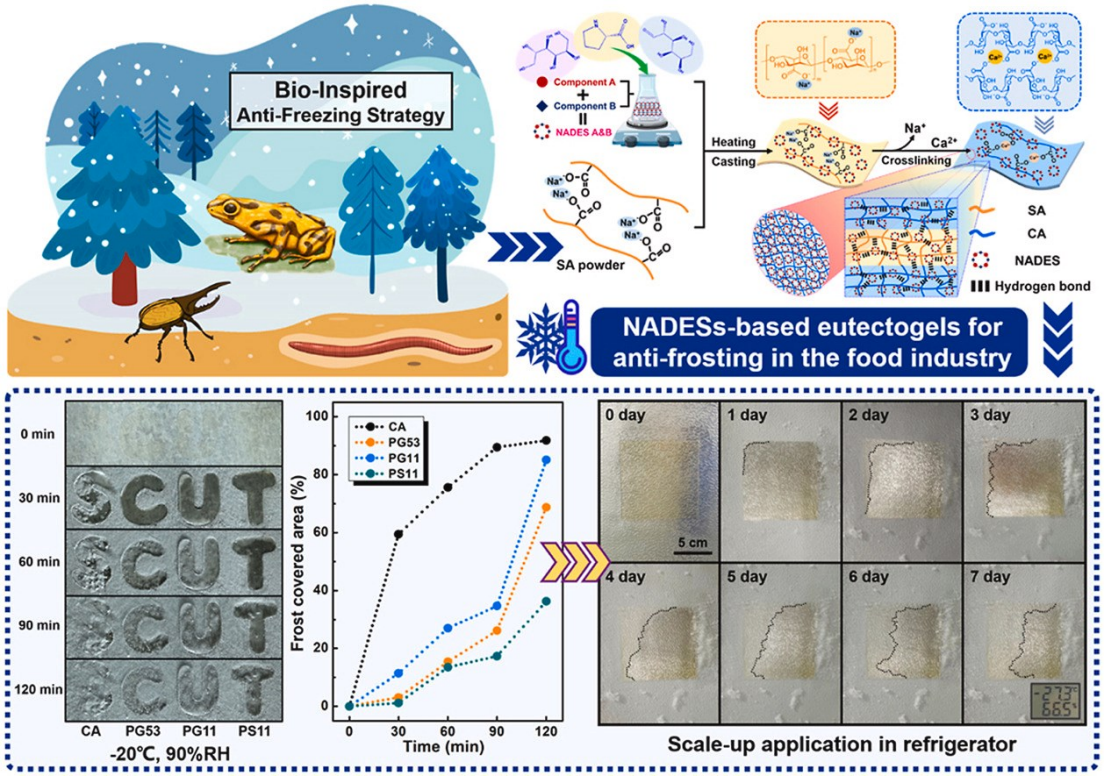

Figure 1-17: Bio-inspired eutectogels enabled by binary natural deep eutectic solvents (NADESs): Interfacial anti-frosting, freezing-tolerance [270] *(Reprinted with permission).*

Chuanwei Lu et al. [33] developed a remarkable class of self-healing, anti-freezing, and conductive elastomers featuring a dynamic dual-crosslinked network. This network was achieved by combining multiple hydrogen bonding interactions and Schiff-base chemistry. The process began with synthesizing the Poly-DES from choline chloride (ChCl), acrylic acid (AA), and a vanillin-derived monomer (VAM). This was then mixed with carboxymethyl chitosan (CMCS) to create elastomers with enhanced mechanical properties and exceptional self-healing capabilities. The hydrogen bonds between ChCl, AA, and CMCS notably reduced the glass transition temperature, resulting in excellent anti-freezing properties. These elastomers maintained their flexibility even at −50 °C. Additionally, they proved highly effective as self-healing strain sensors and wearable devices for monitoring human activities, retaining their sensing capabilities even at −25 °C and after undergoing self-healing [33].

Conductive hydrogels are gaining attention as flexible strain sensors due to their excellent biocompatibility, mechanical flexibility, and conductivity. However, their preparation is often time-consuming and their performance can be limited in extreme temperatures. Addressing these issues, a new class of "deep eutectic solvent-in-water" hydrogels (DIWHs) has been introduced by Jiao Li et al., through combining DESs with traditional hydrogels and utilize a dynamic oxidation and coordination system with sodium lignosulfonate (Ls) and Fe^{3+}. The hydrogels exhibit exceptional anti-freezing and anti-drying properties, maintaining elasticity even at −80 °C and after storage at 60 °C for 7 days [271]. Yin Yan et al. developed DES-based polyacrylic acid/polyvinyl alcohol (PAA/PVA) double network hydrogels that retain impressive flexibility and ionic conductivity even at −20 °C, as well. By using a ternary DES mixture—comprising choline chloride, glycerol, and a Lewis

acid—to pretreat lignocellulose, they created a DES solution with dissolved lignin, which served as the medium for fabricating these hydrogels. The resulting PAA/PVA hydrogels exhibited excellent mechanical strength, self-adhesion, and high electrochemical sensitivity [272]. According to Jia Yang et al., the poly(N-hydroxyethyl acrylamide) (PHEAA) supramolecular ionogel, known as PAChEG, which is based on a ChCl-based DES, shows remarkable freeze resistance even at extremely low temperatures of −40 °C. This ionogel also boasts impressive solvent retention and high sensitivity, making it an excellent candidate for use as a strain sensor capable of monitoring human movements effectively at both room temperature and in colder conditions [34].

Triboelectric nanogenerators (TENGs) are gaining prominence in energy harvesting and self-powered sensors due to their low cost, environmental friendliness, high efficiency, and flexibility. As the push for sustainability grows, biomass resources like cellulose and lignin are becoming popular for creating electrode materials. DESs have emerged as eco-friendly solvents for cellulose and have evolved into polymerizable deep eutectic solvents (PDESs), which are low-cost, low-volatility, and biodegradable. Chuanwei Lu et al. pioneered the creation of a cellulose-derived PDES-based ionic conductive elastomer that is liquid-free, recyclable, anti-freezing, and resistant to organic solvents. This innovative material features a supramolecular hydrogen-bonding network formed from ChCl, urea, cellulose, and acrylic acid, which lowers the eutectic point and enhances weather resistance, making it suitable for flexible electronics in harsh environments [35].

Despite advancements in DESs as anti-freezing eutectics, it's important to note that existing studies have primarily focused on the anti-freezing or anti-frosting resilience of these gels [273–278]. These works have not assessed their anti-icing properties or icephobicity

from a coating perspective. Thus, while these gels demonstrate resistance to freezing, their effectiveness as coatings to prevent ice formation remains unexplored.

1.4 Combining dynamic anti-icing strategies

Every icephobic coating comes with its own set of challenges, often limiting the effectiveness of each individual strategy. To overcome these limitations, integrating multiple approaches can be highly advantageous. For instance, Liu et al. [120] crafted a cutting-edge icephobic surface by combining a superhydrophobic copper mesh with a self-secreting PVA-based organogel. This dual approach not only prevented frosting at sub-zero temperatures but also ensured the gel's renewability through a simple heat-cooling treatment, achieving an impressive ice adhesion strength of just 8 Pa at −20 °C. In another innovative study, He et al. [279] combined an aqueous self-lubricating coating with macro-crack initiators at the ice-coating interface, resulting in a 51% reduction in ice adhesion compared to pure PDMS. This synergy of self-lubrication and macro-structural features showed great promise in smart anti-icing coatings [279]. Similarly, Wang et al. developed a robust icephobic surface by merging low modulus elastomers with superhydrophilicity, allowing it to repel water and ice even at -20 ˚C and 90% humidity. The combination of matrix flexibility and micro-nanostructure, including ZnO nano-hairs and PDMS microstructures, provided exceptional ice-repelling properties [280]. Combining different anti-icing strategies/or materials can significantly enhance performance, addressing the shortcomings of individual methods and pushing the boundaries of icephobic technology [14,281]. As a result, we pursued the synergistic combination of DESs and ILs to further improve effectiveness.

1.5 Conclusion

Unwanted icing has troubled humanity throughout history, and even today, we're still relying on traditional methods like mechanical scraping, energy-intensive heating, and costly chemical treatments. Despite over a decade of exploring passive anti-icing concepts, automatic ice removal technology remains elusive. Yet, exciting advances have been made in developing superlow ice adhesion surfaces that utilize natural forces for ice removal. While challenges such as durability, contamination resistance, and performance in extreme conditions persist, these innovations promise a brighter future.

This chapter highlighted the dynamic design principles of anti-icing surfaces, focusing on three categories: dynamic substrates, dynamic interfaces, and dynamic ice. Ionic liquids (ILs), known for their ability to dynamically alter interfaces, show great promise for anti-icing applications, though their development, especially in coating technologies, is still in its early stages.

On the other hand, DESs offer a promising avenue for anti-icing applications. They can act as ice growth inhibitors and provide synergistic effects, enhancing anti-icing characteristics while outperforming the individual techniques. The current research into DESs underscores their potential to meet market demands and advance dynamic anti-icing surfaces.

CHAPTER 2

2. ARTICLE 1: IN-DEPTH ANALYSIS OF THE EFFECT OF PHYSICOCHEMICAL PROPERTIES OF IONIC LIQUIDS ON ANTI-ICING BEHAVIOR OF SILICON BASED-COATINGS

Saba Goharshenas Moghadam*, Ehsan Bakhshandeh, Reza Jafari, Gelareh Momen

Department of Applied Sciences, University of Quebec in Chicoutimi (UQAC), 555, boul. de l'Université, Chicoutimi, Quebec G7H 2B1, Canada

***Corresponding author:** saba.goharshenasmoghadam1@uqac.ca

This article has been accepted in:

Journal of Cold Regions Science and Technology

2.1 Abstract

This study dissects the use of room temperature ionic liquids (RT-ILs) in a dynamic surface for anti-icing applications. Anti-icing properties of ILs-containing PDMS-based coatings fabricated by two different types of ILs, are evaluated to establish a relationship between the anti-icing behavior and physicochemical properties of the ILs. The surface chemistry of coatings and the existence of distinctive groups of the ILs anions on the surface of coatings characterized by Attenuated Total Reflectance-Fourier transform infrared (FTIR) spectroscopy (ATR-FTIR) and confirmed by using X-ray photoelectron spectroscopy (XPS) and scanning electron microscopy-energy dispersive X-ray analysis (SEM/EDX). The 3D profiles and roughness parameter of the surfaces were investigated by a confocal laser

microscopy profiler. Regarding the importance of correlation between wettability and ice adhesion, the wettability of coatings was studied. The results show a significant reduction 30-40 % in sliding angle (SA) and contact angle hysteresis (CAH) in ILs-containing coatings. Differential scanning calorimetry (DSC), freezing delay time, push-off and centrifugal adhesion tests (CAT) served to distinguish the performance of the two ILs in regard to ice nucleation temperature and formation time, and ice adhesion strength, respectively. The 60 - 70% reduction in ice adhesion strength for the IL-containing coatings, obtained by push-off test, is due to the presence of strong ionic hydrogen bounded water and the formation of self-lubricating quasi liquid layer that can function at much lower temperature. Solid-state nuclear magnetic resonance (NMR) spectroscopy has confirmed the presence of nonfrozen water molecules at the interface. Consequently, incorporating ILs into coatings provides an effective approach to delay ice nucleation, restrict ice growth recrystallization and reduce ice adhesion strength. A comparison of enhanced anti-icing performance of ILs-containing coatings highlights the significant influence of minor changes in the chemical structure of ILs on their potential for anti-icing applications.

Keywords: ionic liquids, dynamic anti-icing coating, ice adhesion, ice formation, ion mobility, ionic hydrogen bonds.

2.2 Introduction

Ionic liquids (ILs) are large organic salts characterized by their relatively low melting points, typically below 100°C [282]. Remarkably, ILs have recently emerged as potential antifreeze agents due to their dynamic interface melting properties, opening up new possibilities for diverse applications in sub-freezing conditions [18]. Contribution of intricate columbic interactions, hydrogen-bonding, and van der Waals forces between the constituent

ions of ILs, and at their interfaces with dissolved substances and surfaces manifest outstanding features including reduced flammability, low vapor pressure, superior chemical and electrochemical stability, tunable viscosity, and low corrosion susceptibility. The physicochemical properties of ILs can be tailored to specific applications by selecting appropriate combinations of cations and anions. The anion plays a significant role in determining the hydrophobic or hydrophilic nature of the IL [283,284]. The unique structural characteristics of ILs, such as their large size and low symmetry of the cation, contribute to their lower lattice energy compared to solid-state salts [285]. As a result, ILs have a lower melting point and can remain in a liquid state over a wide temperature range [132,286]. Tunability of hydrophilicity/hydrophobicity of cations and anions allows for the customization of ILs to suit specific applications. Significantly, favorable characteristics of ILs have found utility in sophisticated electrochemical and self-healing technologies such as actuators, lithium batteries, electric double-layer capacitors, dye-sensitized solar cells, and fuel cells. Efforts have been made to immobilize ILs within solid-phase materials and matrixes while preserving their unique properties [287,288]. The best option focuses on creating a three-dimensional network that permeates the IL and is in charge of giving the final material, known as an ionogel (or ion gel, IG), with solid-like behavior [289,290].

On the other hand, it is well accepted that icing is a widespread natural phenomenon in cold environments and can influence considerably human activities and exposed infrastructure. Cutting-edge advancements are currently reshaping the approach to combat the persistent challenge of surface icing [291,292]. A potential solution for replacing active systems is designing ice protective coatings as a passive strategy [22,293]. Superhydrophobic and slippery liquid-infused porous surfaces are effective passive anti-icing surfaces that

exhibit hydrophobic and ice-repelling properties. These surfaces can delay ice nucleation, hinder ice growth, and reduce ice adhesion, offering solutions at subzero temperatures [294–296]. A through on literature survey, the principles underlying the design of anti-icing surfaces have notably shifted from static to dynamic approaches, emphasizing the necessity of activating dynamic anti-icing properties at the substrate, ice, or interface [18,109,297–299]. This evolution aims to ensure enduring functionality of the surface over extended operating durations and extremely low temperatures compared to existing static anti-icing surfaces. Introducing dynamic properties at ice-substrate interfaces provide opportunities to modify interfacial interactions and thereby mitigate ice adhesion. Drawing from the available literature, this approach utilizes the benefits provided by non-frozen interfacial water, dynamic interface melting, dynamic interface generators, and interfacial crack initiators strategies to effectively reduce the requisite force for ice dislodgement. The extraordinary strategy of dynamic interface melting is of significant interest, which has gained considerable attention due to its continuous ice removal capabilities, even following the formation of ice. Ionic liquids offer an intriguing solution for introducing dynamic properties at the interface due to their fascinating characteristic of having exceptionally low melting temperatures [300,301].

In recent years, there have been both limited and notable advancements in the development of novel gels and coatings incorporating ILs, with the aim of unlocking their exceptional potential in anti-icing applications. These efforts indicate a growing interest in exploring the use of ILs as a promising avenue to improve anti-icing performance [18,300,302]. Zhou et al. employed atomistic modelling techniques to explore the anti-icing characteristics of gelatin-based IGs incorporating 1-butyl-3-methylimidazolium bromide.

Their findings revealed that properly engineered IG-based surfaces have the potential to inhibit ice nucleation (IN) and the subsequent recrystallization of ice growth (IGR). By reducing the freezing temperature at the interface and promoting the formation of a liquid layer at the interface, detachment of ice can be facilitated [19]. The ability of some anti-icing surfaces to facilitate easy sliding of water droplets or ice across the surface, even at low tilt angles represents highly desirable characteristic [92,96]. Regarding lubricating characteristics of ILs, Ding et al. demonstrated that by incorporating imidazolium-based ILs into a cross-linked polymer network, they were able to create stable soft quasi-liquid surfaces with long-lasting easy-sliding properties. The choice of ILs, particularly their anions, influenced the water sliding angle (SA), with trifluoromethansulfonate exhibiting a SA of approximately 2° and hexafluorophosphate showing a SA of approximately 18° [199]. Wang et al. recently reported on a thermoplastic polyurethane endogenous ionic liquid-infused coating using a thermally induced phase separation technique, relying on slippery liquid-infused porous surfaces. Phase separation during cooling caused the 1-octyl-3-methylimidazolium tetrafluoro-borate IL to form a lubricant layer, which reduced the ice adhesion strength [27]. Amphiphilic poly (ionic liquids)-based surfaces for anti-fogging/anti-frosting applications were also recently described by Mossayebi et al. [26].

Despite significant advancements in anti-icing surfaces, understanding the dynamic properties at the ice-substrate interface is still required to consolidate new trends and foster the developments of anti-icing applications [19,26,199,303]. In response to the increasing demand for long-lasting protection against icing, ILs by introducing dynamic properties at the interface show tremendous potential for sub-freezing applications. However, the exploration of anti-icing properties of various ILs has received limited attention, and their

development from coating perspective is still in its early stages. Researchers have been inspired by breakthrough investigations in this area to manipulate the dynamic features at the interface for designing and scrutinizing novel coatings containing ILs to meet the requirement for practical application in a complex scenario. In this study, we aim to investigate the impact of two different room temperature ILs (RT-ILs) on ice nucleation and adhesion strength in coating based on Sylgard 184 silicon elastomer, a widely used industrial coating. Our findings aim to establish a rational understanding of the relationship between IL mobility, physicochemical properties, and their anti-icing behavior. The limited attention given to evaluating the influence of diverse IL types and their physicochemical properties on their behavior in sub-freezing conditions, especially in coatings presents an intriguing avenue for comprehensive investigation, and holding great potential for customizing ILs to suit specific applications.

2.3 Materials and methods

2.3.1 Materials

Sylgard 184 silicone was used as a matrix for the developed coatings. Both the base, the polydimethylsiloxane (PDMS) elastomer and the curing agent were obtained from Dow Corning. Two ILs were used to develop the pair of IL-containing coatings. The first, 1-ethyl-3-methylimidazolium bis(trifluoromethanesulfonyl)imide (Trade name: EMIM TFSI; melting point: -15 °C; code: ILI), was obtained from TCI America™. The second, 1-butyl-3-methylimidazolium tetrafluoroborate (Trade name: BMIMBF4; melting point: -71 °C; code: ILB), was received from Sigma-Aldrich (USA). The chemical structures of both materials are also depicted in Figure 2-1. Without any additional purification, ILs were used as obtained.

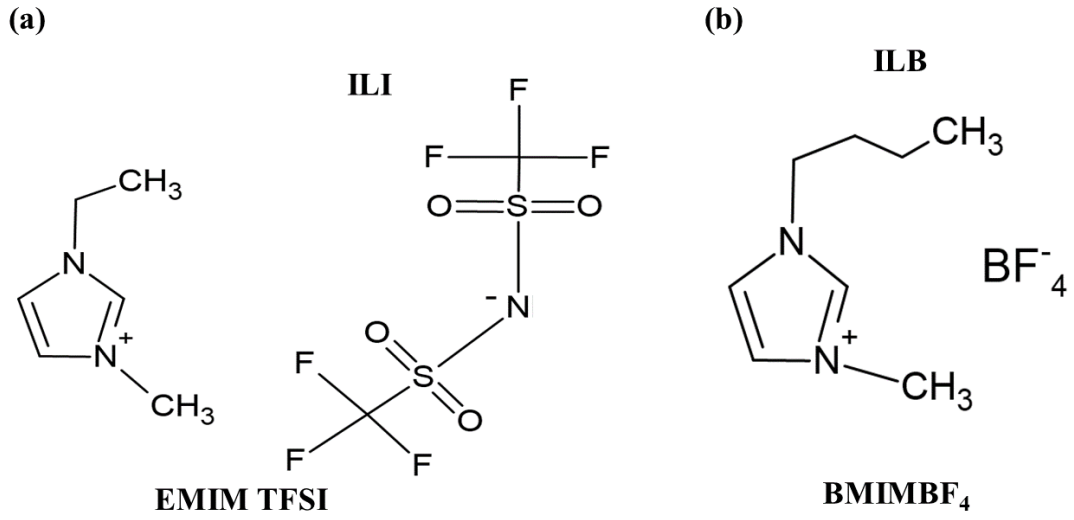

Figure 2-1: Chemical structures of ILs.

2.3.2 Methods

2.3.2.1 Preparation of IL-containing Coatings

The IL-containing coatings were prepared by adding ILs (either ILI (0.025 mol) or ILB (0.044 mol) or both) to the base Sylgard 184 at weight ratio of 1:10 (IL: Sylgard 184). In a clean beaker, the mixture was vigorously agitated for five minutes. The curing agent was then added (10%) and the full mixture was stirred for 10 min. Thereafter, each mixture underwent a 10- to 15-minute vacuum degassing process to eliminate any air bubbles. The coatings were then applied on cleaned aluminum substrates using a film applicator (Zehntner ZUA2000 universal applicator) at wet film thickness of 500 µm. The IL-containing specimens were left for about 3 h at 150 °C. According to the type of ILs that were included, the samples were given labels. CILI, CILB and CILIB are PDMS-based coatings containing 1-ethyl-3-methylimidazolium bis(trifluoromethanesulfonyl)imide (ILI), 1-butyl-3-methylimidazolium tetrafluoroborate (ILB) and equal amount of both ILs, respectively

(Table 2-1). DeFelsko's PosiTector 200 and Elektrophysik MiniTest70 coating thickness gauges were used to measure the average dry thickness of coatings, which was found to be about 210 ± 20 µm.

Table 2-1: Composition of each formulation for fabrication of designed coatings.

Samples Coding	Quantity of each component in final formulation (g)			
	Matrix (Part A)	Hardener (Part B)	ILI	ILB
Sylgard 184	100	10	-	-
CILI	100	10	10	
CILB	100	10		10
CILIB	100	10	5	5

2.3.3 Surface Characterization

The surface chemical composition of the prepared IL-containing coatings was studied using FT-IR analysis. In this study, a Cary 360 FT-IR spectrophotometer (Agilent, USA) was used in attenuated total reflection (ATR) mode to acquire the highest quality spectra. A cleaned diamond surface with isopropyl alcohol served as the testing surface of FTIR. Free films of the designed coatings were prepared to characterize ILs and their presence in PDMS matrix. The FTIR test was also performed for mixture of base Sylgard 184 and ILB to monitor possible chemical reactions. The FTIR measurements were performed with a resolution of 4 cm^{-1}, and each spectrum was recorded three times to ensure reliability.

XPS measurements, using Staib photoelectron spectroscopy (manufactured by Germany), having a non-monochromatic AlKα X-ray source (photon energy of 1486.6 eV), served to further confirm surface chemistry of the fabricated IL-containing coatings.

CasaXPS software was used for all spectrum analyses (developed by Casa Software Ltd., Telgnmouth, UK).

A KrussTM DSA100 goniometer was used to measure wettability at a temperature of 25 ± 0.5 °C. The water contact angle (WCA) was determined over time by placing a 4 µL water droplet over the surface of coatings using ADVANCE drop shape analysis software. Contact angle hysteresis (CAH) of the coated samples by needle method were also evaluated. To measure advancing angle and increase the amount of the drop, firstly the 20 µl water with rate of 1 µl/s is gently poured and then for monitoring receding angles aspirated from a needle as it is brought close to the substrate surface. Advancing and receding angles were quantified with frequency of 10 fps in 20 s and average of 10 measurements. The Kruss is also equipped to tilting table to measure sliding angles (SA) of water droplet on the surfaces. To eliminate the effects of gravity, a 35 L water droplet was placed on the samples that were affixed to a tilting platform. Up until the droplet started to slip or roll off, the stage was inclining at a 60°/min rate. The stage angle at 0.5 seconds before the droplet started to slide was used to calculate SA. WCAs, CAHs and SAs were measured according to the Tangent and Ellipse (tangent) approximation methods. It is interesting to note that the fitting methods are only the mathematical function used to describe the curvature of the drop shape.

Surface roughness and the 3D profiles of the surfaces before and after 10 icing/de-icing cycles were examined using a confocal laser microscopy profiler (with magnification of 50x, Profil3D, Filmetrics, USA). The distribution regularity of the ILs components, particularly F, S, and B on the surface of coatings were acquired by Scanning electron microscope (SEM) images (JSM-6480 LV SEM instrument manufactured by JEOL Japan)

and Energy-dispersive X-ray (EDX) elemental mappings (e-beam voltage= 15 keV). By coating the samples with a very tiny layer of gold, scanning quality was improved.

2.3.4 Anti-icing assessment

A Kruss machine equipped with a Peltier stage, capable of cooling to -20 °C, were used to measure the freezing delay times in a cold chamber. To reduce the chance of condensation, the humidity in the cold chamber was stabilized using anhydrous calcium sulphate desiccants and purging nitrogen. The length of time since a water droplet was deposited on the surface was used to measure the freezing delay time of coatings. Regarding super cooling state of water, freezing delay time of each samples was reported the average of 7 times in different points.

Using differential scanning calorimetry (DSC) with a TA instrument DSC 250 in the heating range of 40 ± 0.05 to -40 °C at a heating rate of 5 °C.min -1, the impact of ILs on the thermal behavior and ice nucleation temperature of the coatings was investigated. A 5 mg deionized water droplet was deposited into a Tzero aluminium pan for each sample. It should be noted that before that the pans were each coated with a thin layer of the designed coating. Afterwards, the lids were placed on each pan to seal them. This process was repeated three times to confirm the reproducibility.

Push-off test was utilized to measure the ice adhesion strengths of the coatings at -10 °C. Deionized water was poured into a 1-cm-diameter cylindrical column and placed on the surface of the samples. To completely freeze and create an ice cylinder, the coatings were left in a cold chamber overnight at -10.0 ± 0.2 °C. Figure 2-2a describes the working principle of home-made push-off set up. Samples were placed on the holder and vacuuming then fixed the sample onto the holder. The probe of force meter moved towards the cylindrical column

at 0.05 mm/s and applied force until the frozen cylinder separated from the sample surface. By dividing the maximum force during ice detachment by the cross-sectional area of the ice-surface interface, the ice adhesion strength was determined. Furthermore, by conducting the push-off test 10 times, the endurance of the surfaces through repeated icing/de-icing cycles was assessed. To conduct the ice centrifugal adhesion test, we prepared samples measuring 2.5 cm × 3.5 cm. The samples were covered with ice by spraying supercooled water microdroplets inside a climatic chamber set at a temperature of -8°C for approximately 35 minutes, replicating the icing conditions experienced during freezing drizzle which result in an ice accumulation of around 5.5 ± 0.5 g. The samples were firstly transferred to a cold room at temperature of -10°C ± 0.2°C, and then securely installed at the end of a beam and subjected to controlled rotation at a specific frequency, as depicted in Figure 2-2b. Subsequently, the adhesion strength was calculated by dividing the force applied by the area covered by the ice.

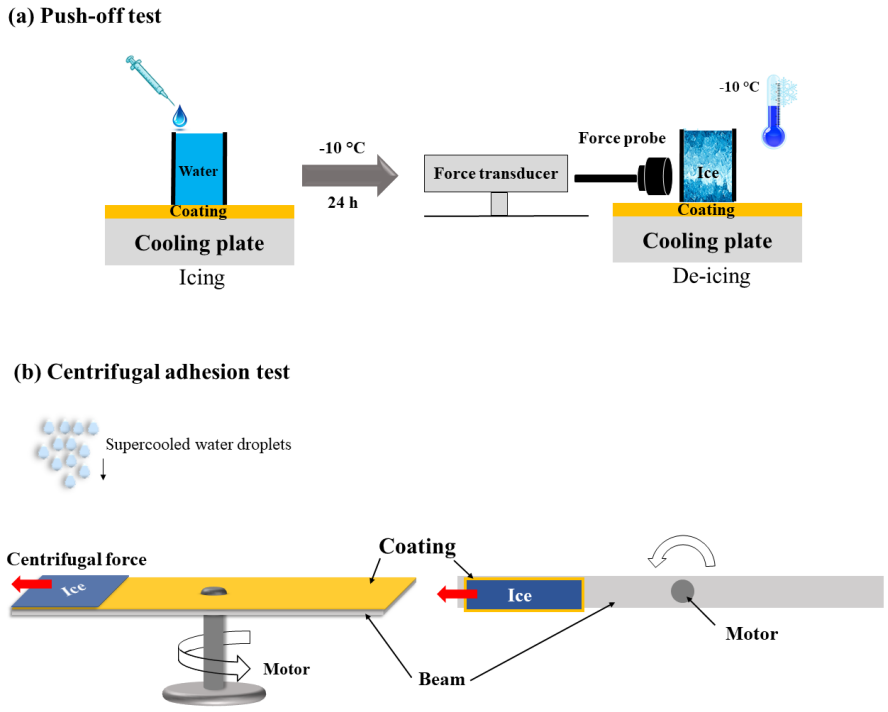

Figure 2-2: Schematic of the designed setups; (a) Push-off and (b) CAT, for measuring ice adhesion strength.

In order to verify the presence of the nonfrozen quasi-liquid layer (QLL) existing at the interface between bulk water and coatings, both lacking and containing ionic liquids (ILs), solid-state NMR spectroscopy was employed. All solid-state NMR (SS-NMR) experiments were firstly conducted at a temperature of 276 K using a 400 MHz wide-bore Bruker Avance III-HD spectrometer (Milton, Canada) operating at 400.03 MHz for ^{1}H. Subsequently, the temperature was reduced to 268 K and maintained for a duration of 3 h before acquiring additional spectra. Sequentially, spectra were collected every 3 h, with a decrement of 5 K for each subsequent temperature point, until there was no longer any liquid water detectable by NMR. To enable quantitative analysis of the ^{1}H signal in bulk water, the recycling delay was set to 5 s, ensuring complete signal relaxation. T_2 measurements and ^{1}H spectra were obtained using the Hahn echo experiment and subsequently processed using Bruker TopSpin software.

2.4 Results and Discussion

2.4.1 Surface Characterization

2.4.1.1 ATR-FTIR spectroscopy

ATR-FTIR spectroscopy was employed to characterize surface chemistry of prepared coatings containing ILs and also distinct peaks of each ILs. Figure 2-3 demonstrates FT-IR spectra of all coatings incorporating ILs and indicates characteristic peaks of ILI and ILB. As shown, the unique peaks of each ILs are identified. From FTIR spectra of ILI and ILB, peaks characteristics of imidazolium ring are symmetric and asymmetric stretching vibrations of C-N and N-H appearing at region of 1100, 1500 and 3300 cm^{-1}. In terms of their anions, sharp peaks in the range of 1000-1100, 1300 and 1350 cm^{-1} are attributed to the B-F (BF4-), C-F and S=O (TFSI) bonds, respectively [304,305]. Distinct absorption peaks at 1100 cm^{-1} and 2900 cm^{-1} related to the Si−O−Si network and the CH_3 of the PDMS-based coatings with and without ILs, respectively [99]. The comparison of the FT-IR spectra of Sylgard 184, CILI and CILB confirmed the presence of ILI and cation of ILB on the surface of the PDMS coating. It should be mentioned that all peaks were normalized according to a distinguished peak at 1100 cm^{-1} for the Si-O-Si network to eliminate concentration effect. For instance, the FT-IR spectrum of CILI reflected the existence of absorption peak at 1352 cm^{-1} for stretching vibrations of S=O group of imide in ILI and the broad absorption peak at region 3100−3400 and 1100−1200 (1190) cm^{-1} for the C−N of imidazolium ring in ILI [304]. Moreover, depicted peaks at 1170, 1576 and 3100 cm^{-1} for the stretching vibrations of C−N bonds in the imidazolium ring cation of ILB [305], confirmed the presence of ILB cation on the surface of the CILB coating. It is interesting to note that disappearing an absorption peak at range of 1000-1100 cm^{-1} [306] (1136 cm^{-1}) in the FT-IR spectrum of CILB, as mentioned

representing B−F, indicated the possible hydrolysis of the borate anion of ILB during the curing reaction of Sylgard 184 and its hardener (Appendix I, Figure A-I. 1and Figure A-I. 2) [282,307,308]. However, the absorption peak at 1300 cm^{-1} in the FT-IR spectrum of CILI can be attributed to the presence of a C−F bond of TFSI anion on the surface of the CILI coating.

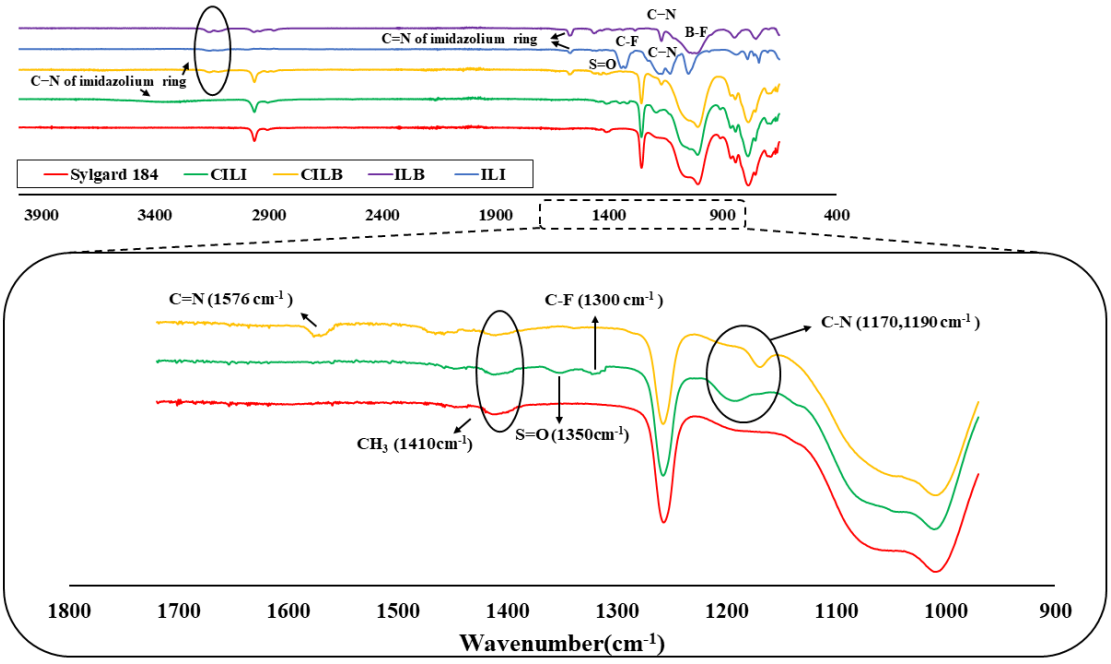

Figure 2-3: FT-IR spectra of reference sample lacking ILs, ILs-containing coatings, ILI and ILB.

2.4.1.2 XPS analysis

Given the importance of fluorinated groups on the surface and their effect on the wetting behavior of the designed coatings, XPS analysis was utilized to further evaluate of the surface chemistry and confirm the presence and absence of fluorinated groups on the surfaces of CILI and CILB, respectively (Figure 2-4a, b and c). The survey scan spectra of Sylgard 184, CILI, and CILB illustrated distinctive peaks related to Si 2s, Si 2p, C 1s, O 1s

for all coatings at their respective binding energy positions (BE). On the surface of the CILI sample, BE peaks at 690 eV were observed (Figure 2-4b). The presence of BE peaks at 690 eV representing F 1s in CILI, and its absence in the CILB coating spectra agreed with the absorption peaks obtained by ATR-FTIR spectroscopy and proposed reaction between ILB and Sylgard 184 (Appendix I, Figure A-I. 1). Due to the formation of chemical heterogeneity in terms of different surface chemistry of ILs which can be aroused from existence of fluorinated groups on the surface of CILI sample, high resolution of C 1s and F 1s are indicated in Figure 2-4d and e, respectively. According to the chemical characterization of bulk ILI and its corresponding reported value of BE, as reported by Yogendra et al.[309], illustrated that the position of BE for confined ILI in CILI differed from that of bulk IL; thus, the confinement of ILI in a silicon matrix alters the BE of the anion because of interaction with the silicon matrix. The BE of the carbon peak related to CF_3 of the bis(trifluoromethanesulfonyl)imide (TFSI) anion indicated two peaks at 291.7 and 293.5 eV (Figure 2-4d), slightly differing from the previously published BE value of CF_3 for bulk ILI at 293.0 eV [310]. The BE peak of carbon related to CF_3 was split into two peaks: the first at 293.5 eV because of the CF_3 of the TFSI anion which is near the surface, with a value equal to the reported BE of bulk ILI. The second peak is at 291.7 eV due to CF_2 of TFSI anions away from the surface [309,311]. The published BE value for bulk ILI, has a BE peak related to F 1s as a single peak at 688.8 eV [312–314]. However, more than one peak for F 1s was also produced (Figure 2-4e), which reveals that upon the confinement of ILI in PDMS, the BE of the anion is modified and confirms the presence of fluorinated groups (695 and 696.1 eV) on the surface of CILI with the percentage of 1.2 % in contrast to CILB. Therefore, the XPS results identified the presence of fluorinated groups on the surface of the CILI coating as opposed to the surface of the CILB coating further confirming the observed absorption

peaks at FTIR spectra of mixture of ILB and base Sylgard 184 owing to decomposition of BF_4^- (Figure A-I. 1).

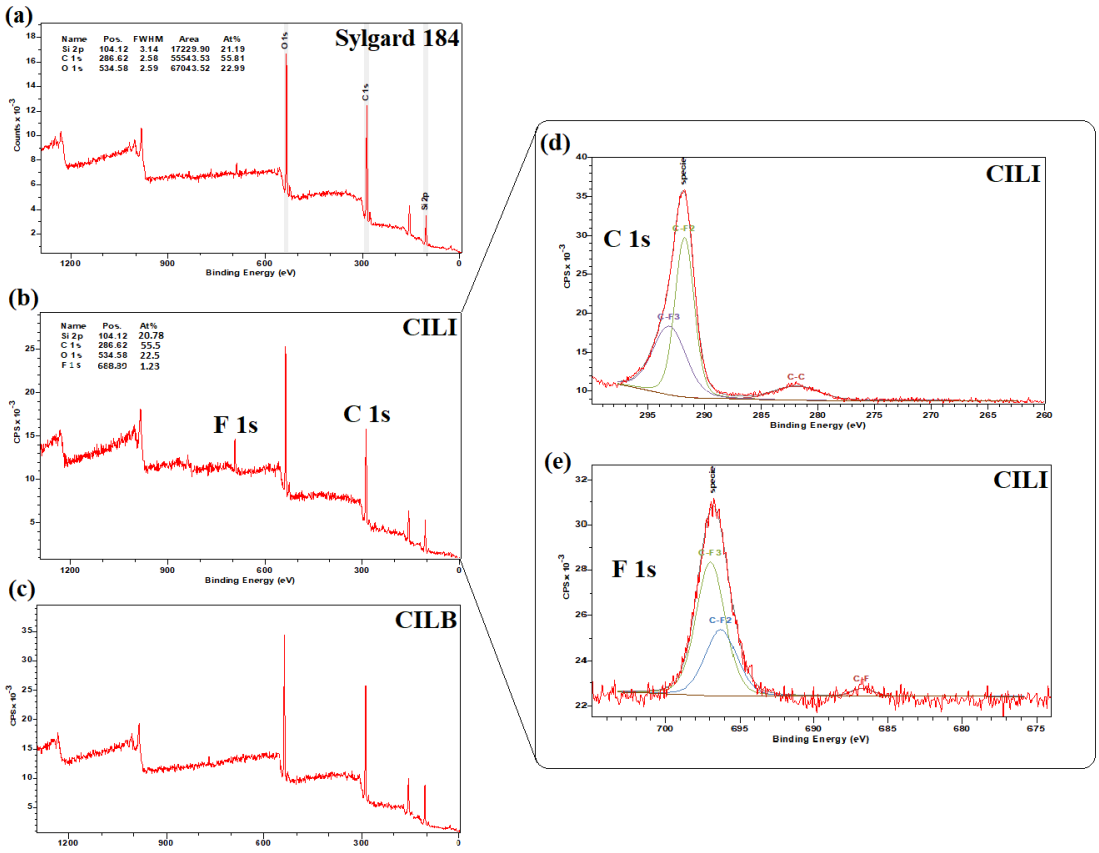

Figure 2-4: XPS spectra of the prepared coatings; (a) Sylgard 184, (b) CILI, (c) CILB, including higher resolution spectra of the CILI surface for (d) C 1s and (e) F 1s.

2.4.1.3 Surface topography

To further evaluate the presence of ILs components, either cation or anion, on the surfaces of coatings, SEM-EDX (elemental mapping mode for F, S, and B) was utilized. According to Figure 2-5a, b and c, peaks and maps of F, S components for the CILI coating and also elemental mapping of B (in the form of $B(OH)_3$, See Appendix I) for the CILB sample were further complemented the FTIR and XPS results on the surface chemistry [26].

The created heterogeneous surface allowed 3D profilometry to also shed light on the surface topography and structures. Figure 2-6(a-d) illustrates various obtained surface structures due to incorporation of ILs. As demonstrated by 3D profile maps of samples containing ILs, either ILI or ILB and the reference PDMS, the surface roughness (S_q, root mean square roughness parameter) increased from 5.68 nm ± 1.36 for the Sylgard 184 to 29.27 nm ± 5.43, 82.65 ± 6.72 and 47.27 ± 4.33 for the samples CILI, CILB and CILIB, respectively. This difference likely stems from an immiscibility between ILs and PDMS at molecular scale and migration of ILs to the surface. However, this situation did not cause any significant phase separation. It is worth mentioning that more immiscibility of ILB in Sylgard 184 compared to ILI resulted in higher S_q. Since the surface roughness of the samples containing ILs were lower than 90 nm, this structural difference could not significantly affect icephobic properties of the designed surfaces. However, surface roughness after 10 icing/de-icing cycles was measured [219].

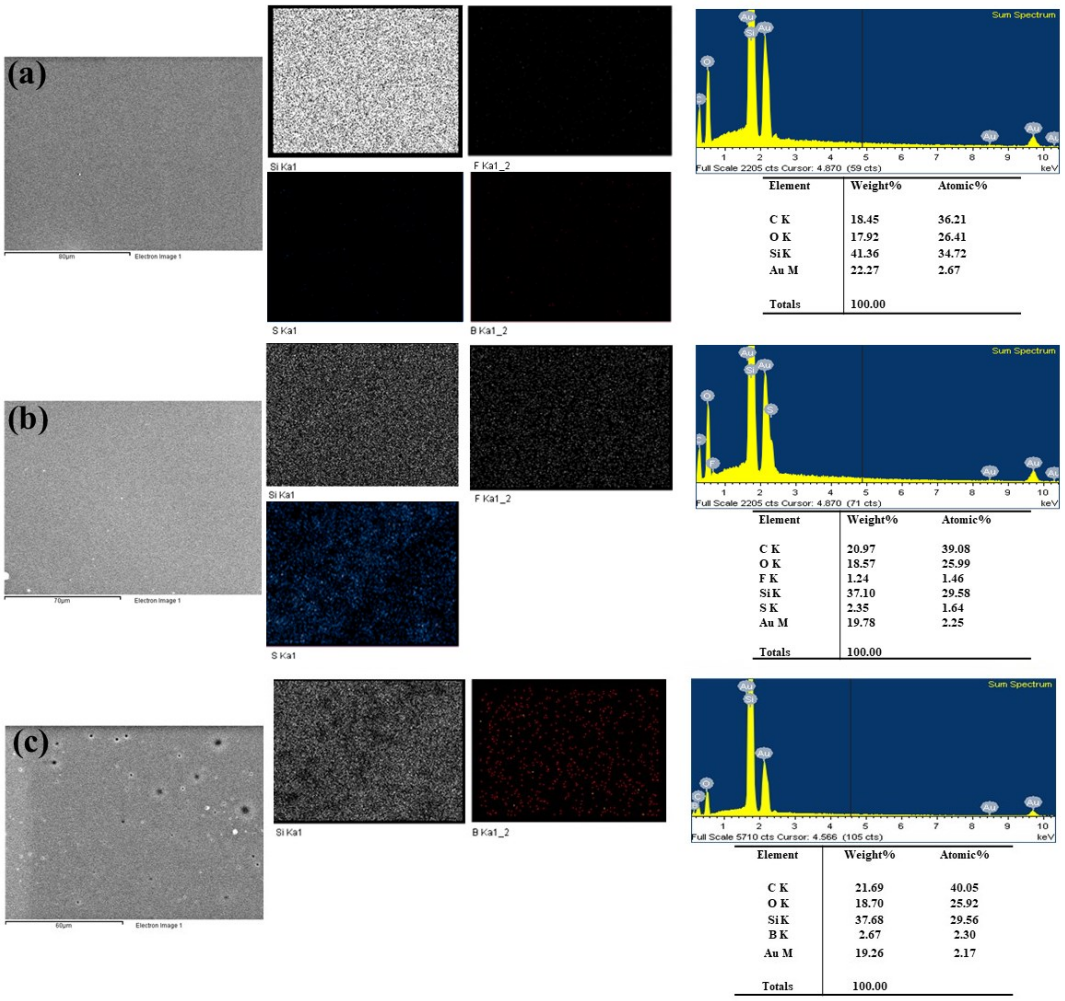

Figure 2-5: The EDX mapping of the produced samples; (a) Sylgard 184, (b) CILI, and (c) CILB with the distribution of Si, F, S, and B elements over the surface.

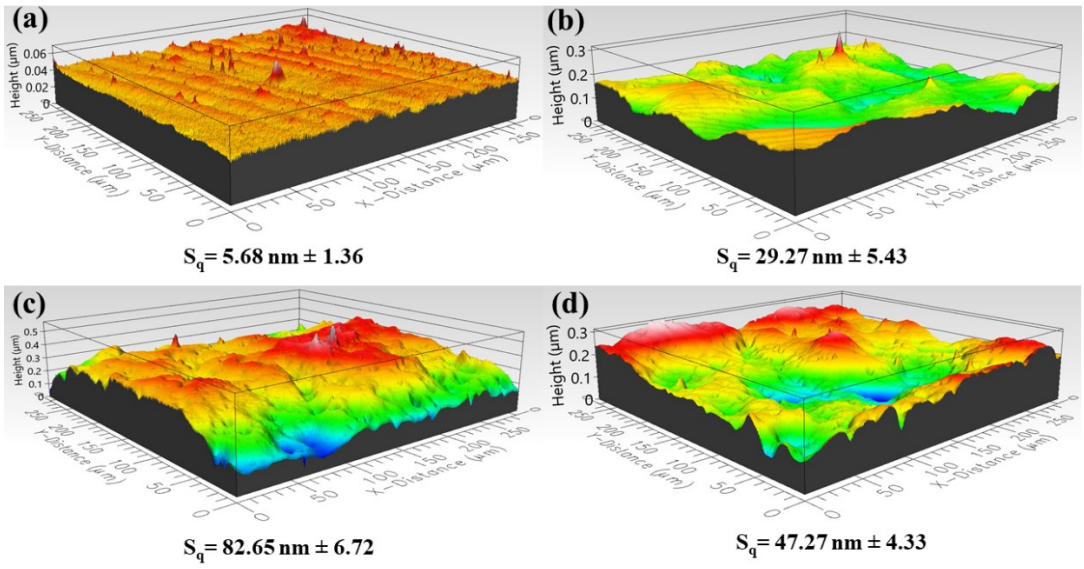

Figure 2-6: The 3D profile and roughness value of the designed samples; (a) Sylgard 184, (b) CILI, (c) CILB, and (d) CILIB.

2.4.2 Wettability

The presence of distinctive groups of ILs on the surface of coatings, confirmed through various surface characterization techniques, provided compelling evidence for the enough mobility of ILs and their migration within the Sylgard 184 matrix to the surface. This intriguing chemical heterogeneity prompted an investigation into the wetting properties of the coatings, specifically through measurements of water contact angle (WCA), contact angle hysteresis (CAH), and sliding angle (SA). The measurements presented in Figure 2-7a and Figure 2-7b offer valuable insights into the influence of ILs on the wetting behavior of individual water droplets, providing a deeper understanding of their effect on the surface properties. Based on the measurements, the average WCA values corresponding to Sylgard 184, CILI, CILB and CILIB were 116.8 °± 0.73, 110.5 °± 0.83, 110.32 °± 0.96 and 108.7 °± 1.1, respectively. However, the results show that the presence of ILs in the coating reduced slightly the WCA relative to the pure Sylgard 184. A marked decrease of the SA and CAHs,

approximately 30-40%, was observed particularly, for the CILI and CILIB relative to that of Sylgard 184. For instance, the CAH values of all IL-containing coatings ranged between 17.38 º and 26.82 º, lower values than for the blank silicon-based sample (30.37 º) due to different surface chemistry of fabricated IL-containing coatings, i.e. chemical heterogeneity. Regarding no significant change in surface roughness of the coatings, surface chemistry can be considered as the more prominent factor impacting wetting behavior. However, both surface chemistry and roughness play key roles in static and dynamic water angle measurements.

The initial WCA of the pure Sylgard 184 coating was found to be an average of 116.8°, in accordance with Young's equation for a flat and chemically homogeneous surface [315]. Because of the relatively low interfacial tension between ILs and water, IL-containing coatings were expected to have higher wettability than that of Sylgard 184. Regarding the WCA measurements, CILIB exhibited a lower WCA in comparison to the reference coating [316,317]. While no significant change was observed in the WCAs of coatings containing ILs, the changes in contact angles over time (CA_t) and CAH could shed light on the impact of physicochemical properties of ILs on the surface wettability. In the other words, reducing advancing angles of ILs-containing coatings and also CA_t better reflected higher wettability compared to reference lacking ILs. It is noteworthy underlying that lower CA_t of CILI relative to CILB can be attributed to the presence of more possible hydrogen-bonding donor sites on the CILI surface, because of its distinct anion [316,318–322].

Our finding demonstrates that, the physicochemical properties of the ILs dictated the wettability of IL-containing surfaces, in addition to different surface chemistry [316,317,323–325]. The miscibility of the ILs in water, and consequently

hydrophilicity/hydrophobicity, is significantly influenced by the choice of anion. The TFSI anion, in particular, demonstrates a clear role in this regard, as evidenced by its lower CA_t and advancing angle. Even slight changes in the anion and/or cation constituents can have noticeable effects on the solubility/miscibility characteristics of ILs with either water or within a matrix [325,326].

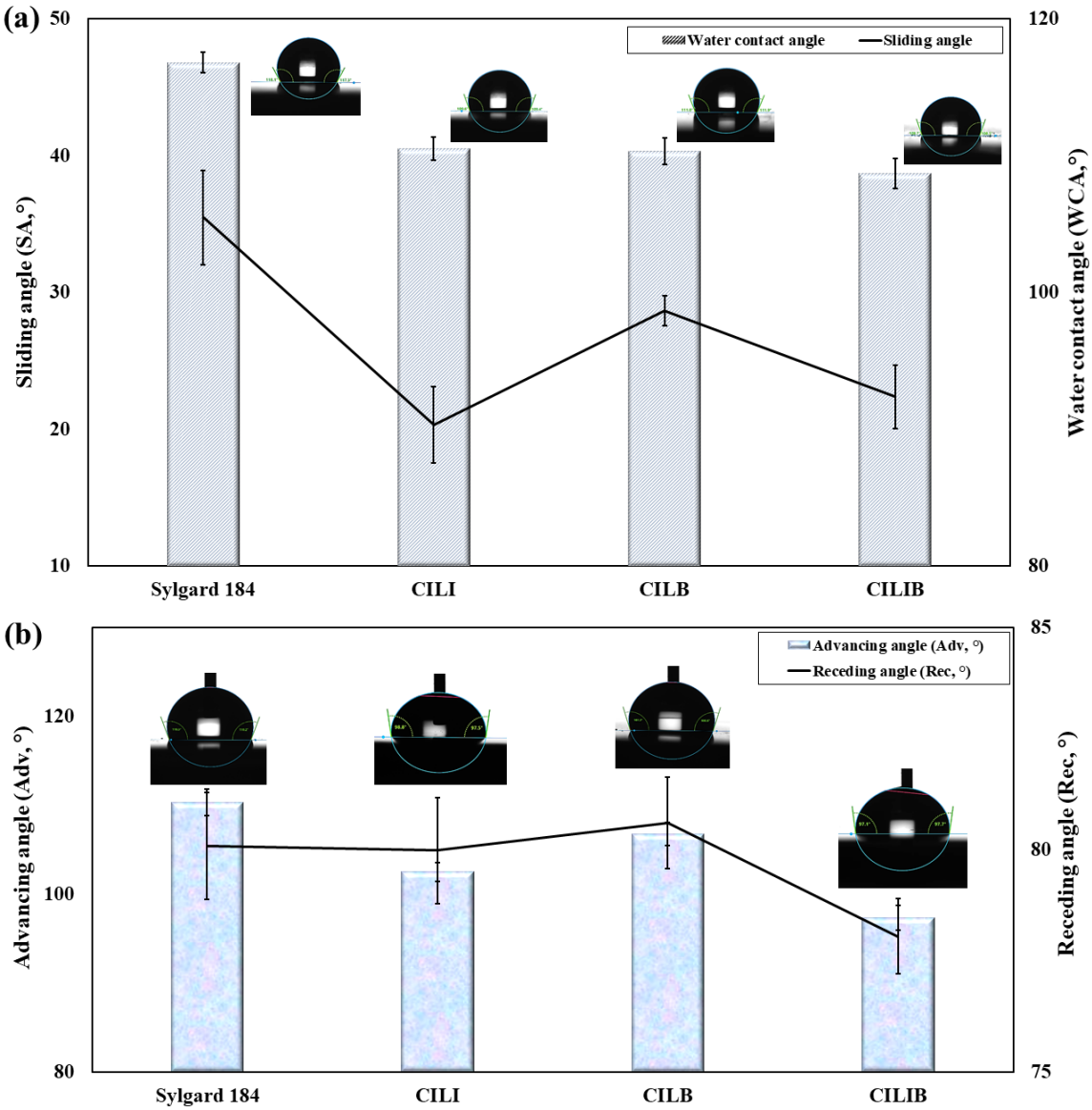

Coating samples	**Sylgard 184**	**CILI**	**CILB**	**CILIB**
Contact angle hysteresis (CAH, °)	30.37 ± 2.17	22.5 ± 2.4	26.82±2.39	17.38 ± 2.12

Figure 2-7: Wetting properties of Coatings, including (a) static and (b) dynamic water contact angles.

In addition to long-range interactions between cation/anion (Columbic forces), hydrogen-bonding as one of the important short-range interactions, plays a key role to determine ILs structuring on the surface and their physicochemical properties for anti-icing applications [323]. As there are many hydrogen bond donor and acceptor sites on the cation and anion of an IL, hydrogen-bonded network may form [327]. Thus, ILs appear to form ionic hydrogen bonding networks with water and H-bond among ILs. The TFSI as a less basic anion possess stronger hydrogen-bond donor ability. Moreover, larger and less asymmetrical structure of this anion enhances charge delocalization by sharing the net charge among several atoms and providing more able sites to create ionic hydrogen-bonds [327]. Despite the expected higher wettability of ILB with BF_4^- as a more basic anion and stronger hydrogen-bond accepting ability [325,326]. CILI with TFSI anion exhibited stronger hydrogen-bond donor ability, as indicated by CAH and CA_t [327,328]. The presence of a single cation, resulting from the decomposition of the anion on the surface of CILB, led to a reduction in the number of available hydrogen-bonding sites which explains the minimal changes to its wetting properties [323,324]. Furthermore, the lower WCA, CA_t and advancing angle in CILIB reflects the greater efficacy of ILs, in particular ILI for forming more ionic hydrogen bonds. It indicates that percentage of ILs could be an important parameter in addition to their chemistry.

A lower WCA in IL-containing coatings demonstrated ionic hydrogen bonds being formed with water molecules, as observed for fabricated superhydrophilic polyurethane ionic liquid-infused surfaces by Wang. et al. [27]. To the best of our knowledge, this phenomenon can be explained by observing the effect ILs type on surface wettability and loss of surface

hydrophobicity over time in detail. The WCA of CILI and CILIB coatings generally decreased faster than that of the reference sample (Figure 2-8). For instance, the WCAs of CILI and CILIB began (t = 0 s) at 110 ° and 108°, respectively, and attained 79 ° and 82 °, respectively, at t = 350 s. For sample CILI, despite of higher hydrophobicity of ILI, because of more able sites and the stronger ionic hydrogen bonds of ILI with water molecule at the interface caused the WCA of CILI to decrease at faster rate relative to that of CILB coating [329].

The advancing (maximum) and receding (minimum) water contact angles allowed us for a comprehensive evaluation of the surface wettability. The results, as depicted in Figure 2-7b, showed no significant variation in the receding angles of coatings containing ILs compared to the reference. Changes in advancing angle which is thought to be more sensitive to hydrophobic components of the solid surface, closely reflected the surface's tendency to either attract or repel the water [330]. Our finding reveals that incorporating ILs into Sylgard 184 decreased the advancing angles of ILs-containing coatings compared to the reference. The presence of more available sites for creating ionic hydrogen bonding can account for the lower advancing angle observed in CILI and CILIB compared to CILB [323,327,331,332].

One of the important characteristics of icephobic coatings is having SA $\leq$ 10°. Tremendous efforts have been invested to develop new surfaces and coatings to improve their easy-sliding properties [92,96,98,333]. In the recent study by Ding et al. when ILs and polymers are miscible with one another and immiscible with water, easy sliding feature to water was observed for surfaces containing ILs, thanks to the strong interactions between the polymer chains and the imidazolium-based ILs, which produced stable, soft, and quasi-liquid surfaces [199,334]. The hydrophobic nature of PDMS and fluorinated ILs ensure the required

miscibility for producing a quasi-liquid layer. The SA of the produced coatings, in presence of the ILs was generally lower. Incorporation of ILI resulted in lower reduction in SA as well as CAH of CILI coating in comparison to CILB.

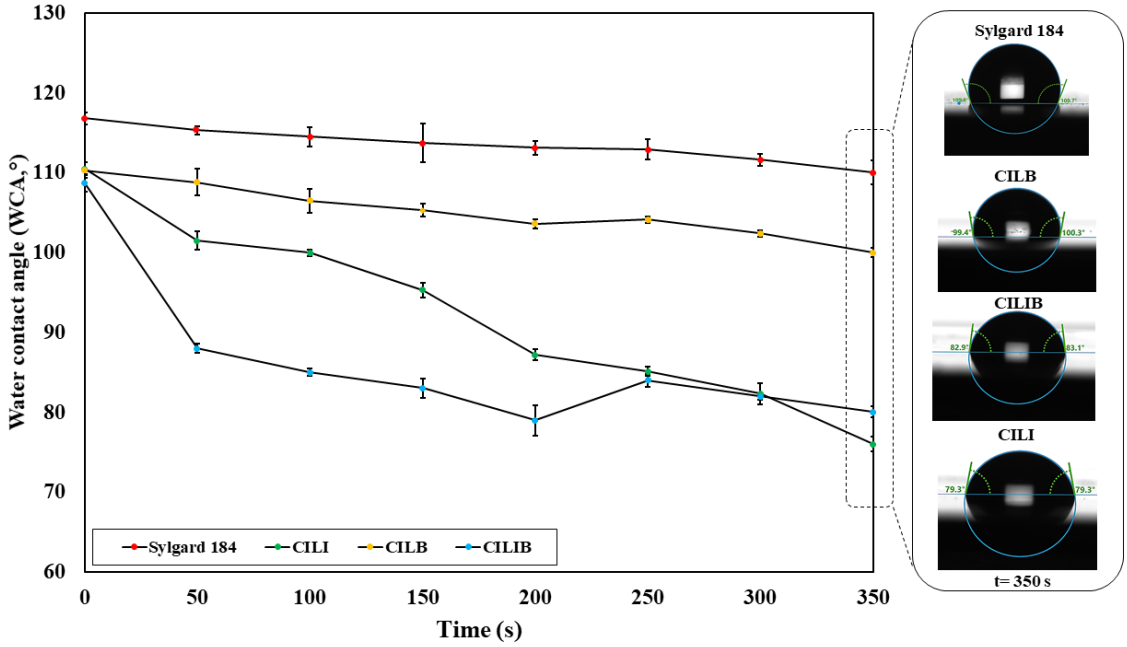

Figure 2-8: Water contact angles of coatings over time.

2.4.3 Ice formation

2.4.3.1 Ice nucleation temperature

With the aid of DSC, the impact of ILs on the ice nucleation temperature (IN_{temp}, ±0.05°C) of coatings was assessed. According to the results presented in Figure 2-9a, a significant decrease in the average IN_{temp} was observed, with a remarkable drop from -15.8 °C for Sylgard 184 to -21.8 °C for CILIB. Literally, As the sample cools below 0 °C on the PDMS surface, the water is supercooled until ice forms at -15.8 °C, which releases a significant amount of latent heat of freezing and raises the sample temperature [17]. The lower IN_{temp} of IL-containing coatings resulted from diffusing ILs into the water molecule

and depressing freezing temperature [19]. Regarding that, similar procedure was employed for water and solution of water and ILs to clearly elaborate anti-icing performance of ILs. Thus, each pan was filled with water and 10 wt.% of either ILI or ILB to assess their solubility/miscibility in water in order to further confirm the effect of ILs on dropping freezing temperature. As demonstrated in Figure 2-9a, both ILs were able to decrease IN_{temp} of water [19,302]. It should be noted that the heterogeneous nucleation temperature varies significantly when the amounts of water used in an experiment are higher than the micron-sized droplets observed in emulsions and they are supercooled because different containers are utilized and different aqueous samples have different purities. Many different experimental approaches and settings have been used to study the freezing of supercooled water [17,335,336].

The intermolecular interactions between water molecules and ILs play a crucial role in ice nucleation, in addition to the conventional melting properties exhibited by ions in solid state salts, for instance NaCl [323]. According to the literature, the H-bonds support lower melting points, lower viscosities, and fluidize the ILs through the contribution of dipole-dipole and electrostatic interactions. H-bonds in ILs primarily involve the hydrogen atoms on the imidazolium ring and the anion due to more acidic hydrogen atom at C^2–H. The geometric structure and steric configuration of ILs play a significant role in influencing the characteristics of these hydrogen bonds, which can differ from conventional H-bonds [323]. Hence, formation of these ionic hydrogen bond networks between water and ILs restricts the mobility and rearrangement of the water molecules [323,337,338]. Besides, creation of ice nuclei from bounded water requires more energy compared to non-bounded water and also higher energetic barrier for nucleation [339]. Therefore, heterogeneous ice nucleation can

inhibit and commence at lower temperature [17,335]. In addition to ionic hydrogen bond possibility, solubility/miscibility of ILs in water is another factor for determining the interaction energy of water and ILs in controlling ice nucleation [316,317,323–325]. More be able to solubilize ILB in water and its intrinsic lower freezing temperature (-71 °C) results in further reduction in IN_{temp} in water. However, similar trend was not observed for coating CILB compared to CILI [332]. The greater electronegativity and more electron withdrawing group, because of longer alkyl chain length on the imidazolium ring of ILB make the hydrogen atom more acidic at C_2-H and stronger H-bonds, resulting in decreasing IN_{temp} in water. On the other hand, when a solute is introduced, the hydrogen bond donated by the IL cation may compete with the IL anion if it has a strong affinity for accepting hydrogen bonds. Even if BF_4^- is decomposing, the presence of cation may still be able to form hydrogen bonds (Figure A-I. 1) [327]. Subsequently, ILI in Sylgard 184 performed better for depressing IN_{temp}, because of more available sites on the surface of CILI to donor hydrogen-bonds (Figure 2-9b) [327]. However, almost hydrophobic ILs are water immiscible [325,326]. It is worth mentioning that when hydrophobic ILs are introduced into an aqueous phase, a biphasic system is formed through mutual solubility which includes a top phase containing water with some dissolved ILs and a bottom phase having an IL layer with small amount of water which also enables ILI to depress IN_{temp} of CILI. According to the results, IN_{temp} can be lower than - 20 °C when both ILs are incorporated into PDMS-based coatings.

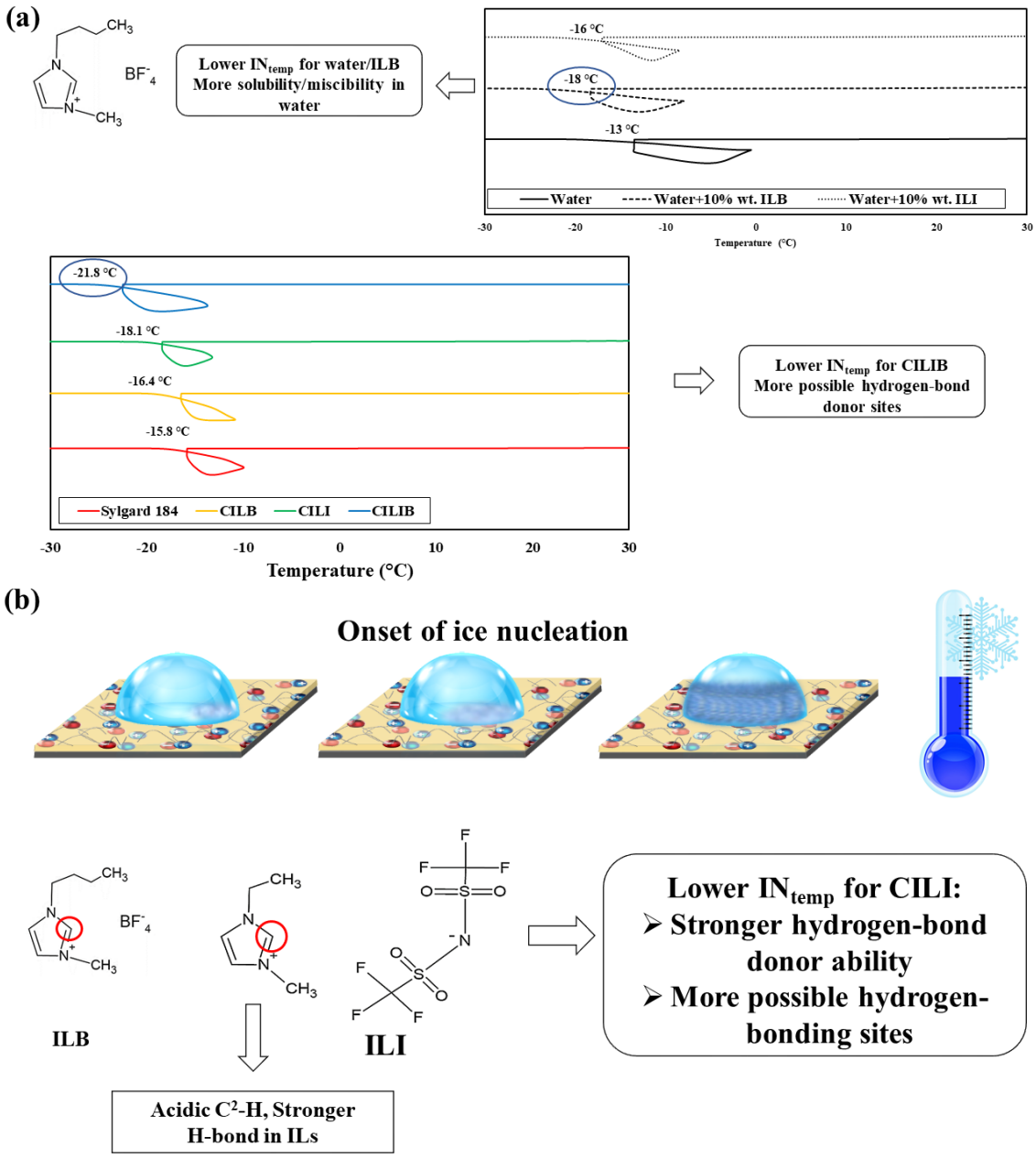

Figure 2-9: (a) Delayed ice nucleation of water and on the surface of PDMS-based samples and coatings containing ILs, (b) Schematic of the effective parameters of ILs structures on ice nucleation temperature.

2.4.3.2 Ice formation time

The freezing delay time for the designed coatings, recorded as the onset of ice nucleation was measured at -20 °C. Figure 2-10 presents the average freezing delay time as

well as the image of complete frozen of water droplets. Adding ILs into the PDMS led to a fourfold increase in freezing delay time. ILs exhibit the capability to penetrate into water droplets, effectively reducing the freezing temperature at the interface. As a result, the nucleation of ice is delayed, and once ice forms, it becomes easier to detach and remove from the surface. The foremost potential of ILs in fabrication of anti-icing surfaces comes from their large asymmetry particularly of their cations, making favorable in freezing delay time, in which these large ions can be easily expelled into the unfrozen liquid layer. The ability of ILs to lower freezing temperatures via their ionic hydrogen bond interactions with water, delay ice nucleation which can be explained by two equations, Equation 2-1and Equation 2-2 [329];

Equation 2-1

$$J \propto \frac{TK_B}{h} \exp(-\frac{\Delta G^*_{f,homo}}{TK_B} - \frac{\Delta G_{act}}{TK_B})$$

Equation 2-2

$$\Delta G^*_{f,het} = f(\cos\theta iw, {}^{r}/_{r_i^*})\Delta G^*_{f,homo}$$

An increase in ΔG_{act} causes a drop in J because the homogeneous nucleation ice nucleation rate (J) is inversely related to the freezing delay time. According to Equation 2-2, a reduction in the energy barriers required for freezing provides a thermodynamic explanation for heterogeneous freezing. The energy barriers for heterogeneous freezing, $\Delta G_{f,het}{}^*$and $\Delta G_{act,het}{}^*$, will therefore be lower than those for homogeneous nucleation. Regardless surface effect, it can be assumed that $\Delta G_{f,het}{}^* \propto \Delta G_{f,homo}{}^*$ for designed samples [17,335,340]. Moreover, according to ΔG_{act} there is an energy barrier, which is connected to the transformability and self-diffusion of water molecules at the interface and adds up to an

ice embryo. Because of the ionic hydrogen bonds that restrict the water molecules and increase viscosity, the ice nucleation rate J is decreased as a result of an increase in ΔG_{act} (Figure 2-10) [340,341]. The variations in freezing delay time among IL-containing coatings are minimal. Nevertheless, the significance of solubility, primarily influenced by the ILs' anions, becomes evident in the delay of ice nucleation temperature, as supported by the findings from DSC analysis. Regarding the icing times of gels containing ILs in the literature [19,27]. the anti-icing mechanism of the coatings was similar to that of superhydrophilic surfaces. However, compared to a hydrated layer atop a superhydrophilic anti-icing coating, the ionic liquid can operate at significantly lower temperatures.

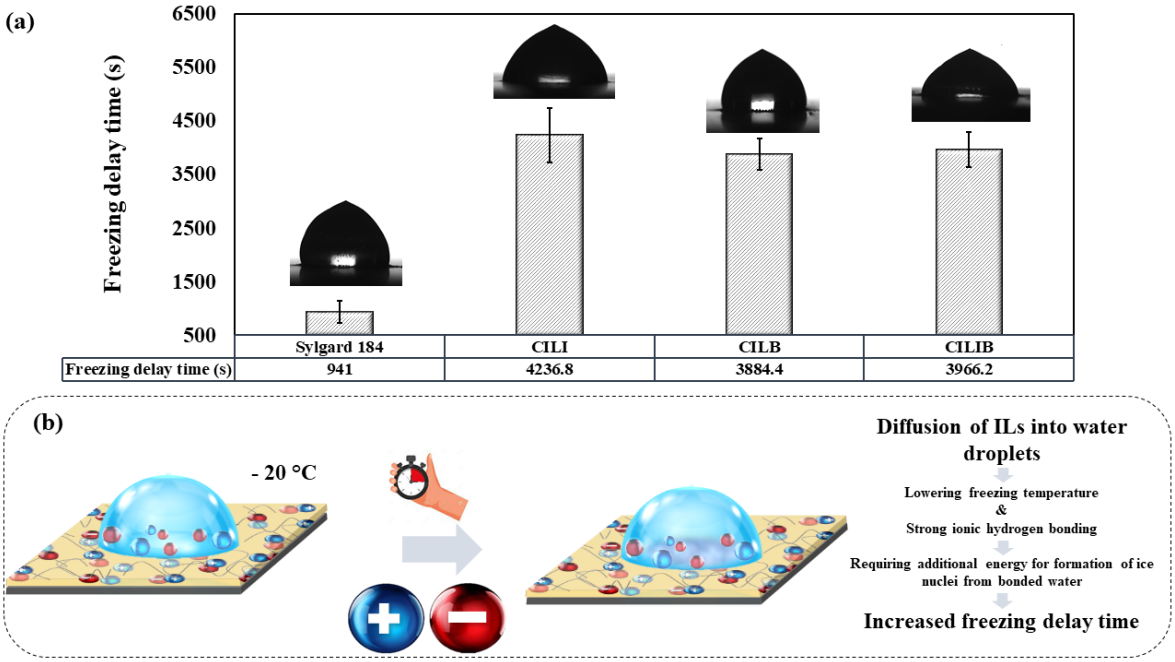

Figure 2-10: Ice formation time on the surface of coatings.

2.4.3.3 Ice adhesion strength

To assess the strength of ice adhesion, several methods can be utilized [68]. In this study, we employed two different methods, namely, push-off and centrifugal adhesion test,

which were specifically designed by our research group. The impact of ILs on the ice adhesion strength of PDMS-based coatings is revealed in Figure 2-11, showcasing a significant reduction, attaining values of < 60 kPa relative to the Sylgard 184. To be more precise, the ice adhesion strength of IL-containing coatings using push-off test was quantified to be 58.36 kPa for CILI, 81.1 kPa for CILB, and 53.98 kPa for CILIB. Despite the more severe icing conditions created by using glaze ice in the centrifugal test compared to the non-impact bulk ice used in the push-off test, it was observed that the results from both tests exhibited similar trends to a significant degree.

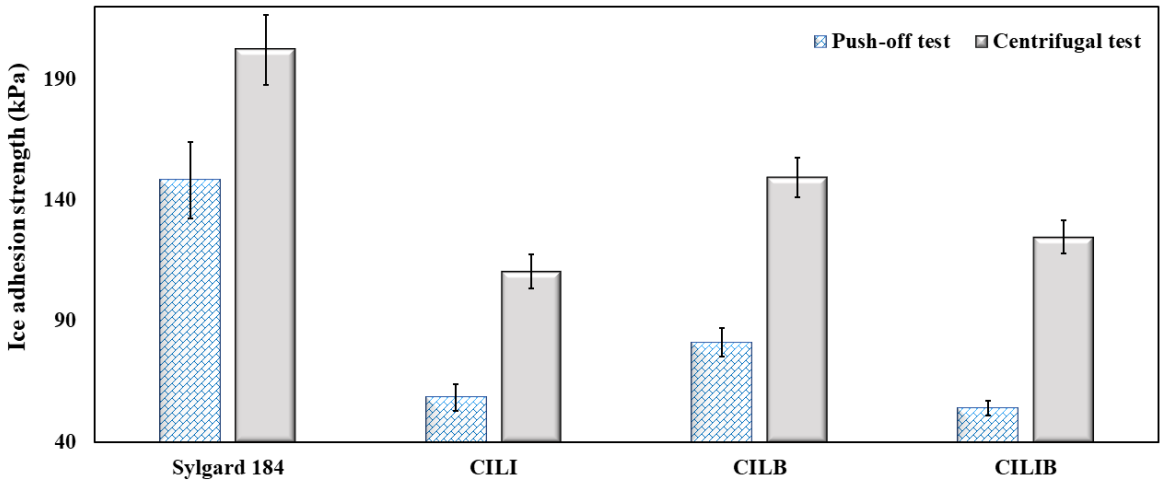

Ice adhesion strength (kPa)	Sylgard 184	CILI	CILB	CILIB
Push-off test	148.14 ± 15.71	58.36 ± 5.61	81.1 ± 6.01	53.98 ± 3.18
Centrifugal test	202 ± 14.55	110.5 ± 7.02	149.21 ± 8.23	124.72 ± 6.8

Figure 2-11: Ice adhesion strength (kPa) of coatings, obtained using Push-off and Centrifugal tests.

Understanding interfacial interactions is crucial as they directly impact the mobility and rearrangement of water molecules at the interface, thereby influencing the strength of ice adhesion. A very well-known mechanism for suppressing ice nucleation and lowering ice

adhesion strength is the formation of a quasi-liquid layer (QLL). The existence of this disordered liquid-like layer at the solid−vapor leads to weak interfaces characterized by disordered and short-term atomistic interactions involving van der Waals forces and hydrogen bonds [17,293,342]. Unlike common solid-state salts, e.g. NaCl, unique characteristics of ILs, primarily, large size and asymmetry prevent them from being trapped within ice crystals during freezing. Instead, ILs can diffuse into the water droplet, resulting in lower freezing temperatures and an extended liquid state. Furthermore, the diffused ILs are subsequently expelled by the unfrozen liquid phase, creating an interfacial liquid layer enriched with ions [19]. Ionic hydrogen bonds between water molecules and ILs also contribute to the formation of the QLL at the ice−surface interface (Figure 2-12d). When a portion of the liquid nucleates to create slushy mixture in the nucleation step, the released latent heat can be absorbed by the unfrozen liquid to raise the liquid's temperature; therefore, this self-lubrication characteristics of unfrozen liquid layer containing non-freezable bounded water at the interface reduces the ice adhesion strength [26,301,339,341,343]. The disruption of the ordered crystallized structure of ice by these large and asymmetric ILs regenerates an amorphous unfrozen interfacial layer and restricts ice growth recrystallization.

To validate the presence of the nonfrozen quasi-liquid layer (QLL) at the interface between the bulk water and coatings, particularly coatings containing ILs, we employed solid-state NMR spectroscopy. NMR proves to be an excellent method for detecting trace quantities of non-frozen water, as conventional ^{1}H NMR experiments are unable to detect solid ice due to its long T_1 and short T_2 relaxation times, whereas liquid water exhibits a readily detectable ^{1}H signal [344].

According to Figure 2-12(a-c), the ^{1}H spectra of Sylgard 184 + water, CILI + water, and CILB + water samples were initially recorded at 276 K to evaluate the properties of bulk water before the onset of freezing. All samples exhibited water ^{1}H chemical shifts of 5.05 ppm, displaying similar line shapes. Subsequently, upon lowering the temperature to subzero levels (253 K) and allowing for a 3-hour stabilization period, the water ^{1}H signal intensity of both samples notably decreased. A noteworthy observation is that the water ^{1}H chemical shifts of the coatings exhibit an increase as the temperature decreases. This behavior aligns with findings from previous investigations on supercooled water can be attributed to the strengthening of hydrogen bonds at lower temperatures, consequently affecting the shielding and deshielding of the water protons [17].

This crucial finding provides confirmation of the presence of nonfrozen water even at temperatures as low as -20 °C. This nonfrozen water layer acts as a self-lubricating interface, contributing to the low ice adhesion strength observed on IL-containing coating surfaces. It is important to note that as the temperature decreases below 0 °C, the signal intensity of the nonfrozen water (indicating the amount of nonfrozen water) rapidly diminishes for Sylgard 184. At a critical level of subcooling, the nonfrozen water will significantly decrease and may eventually freeze completely, leading to a sudden and substantial increase in ice adhesion strength on CILB. However, the presence of this signal for CILI at 253 K confirms the thicker QLL due to its stronger hydrogen-bond ability [17].

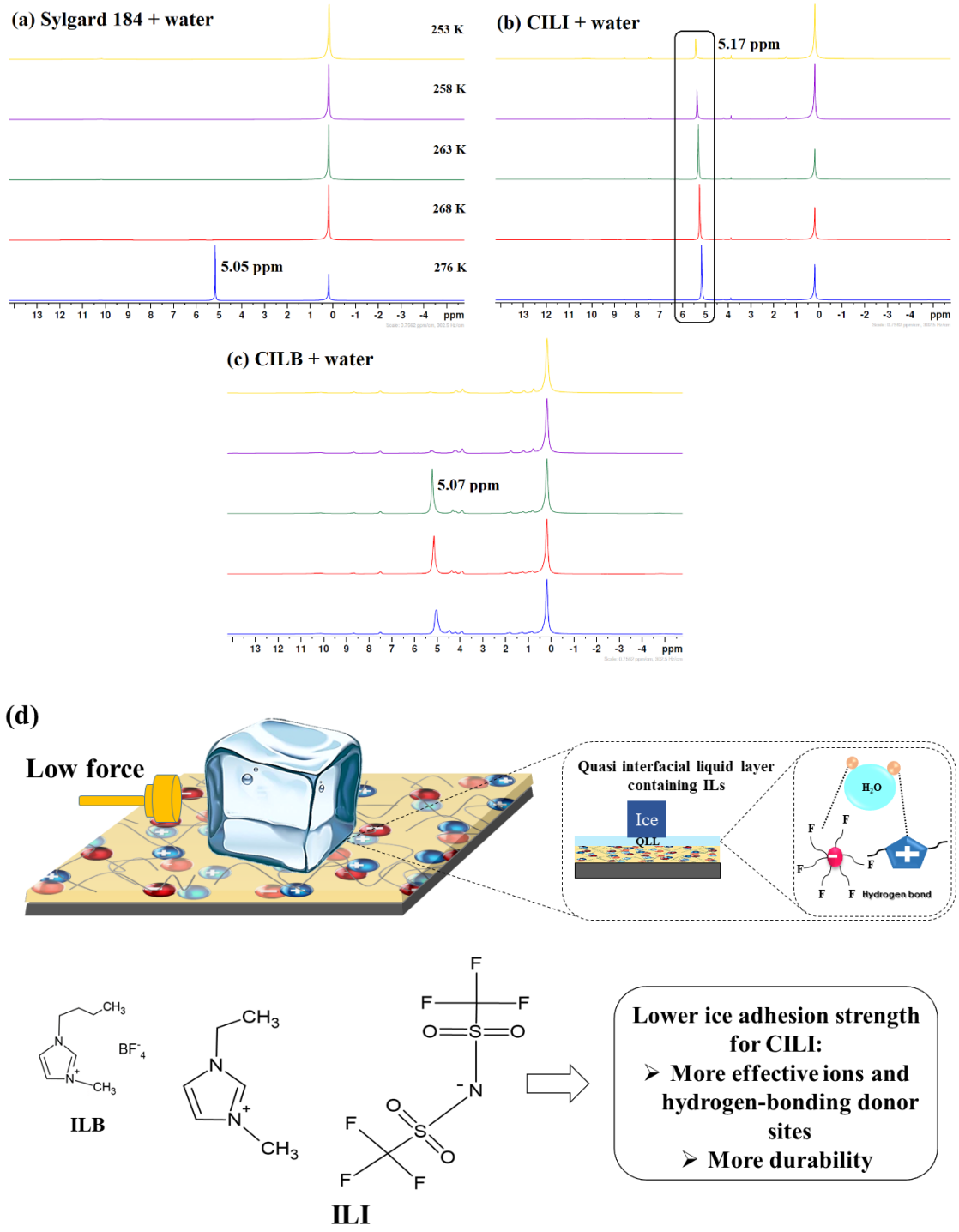

Figure 2-12: ^{1}H spectra of (a) Sylgard 184+water, (b) CILI+water, and (c) CILB+water between 276 K (blue) and 253 K (yellow), obtained by SS-NMR spectroscopy. (d) Schematic of lowering ice adhesion strength in presence of ILs through formation of QLL at interface.

As noted earlier, the water molecules bound at the interface exhibit significantly lower configurational entropy in comparison to bulk water, resulting in a substantial rise in water viscosity. This increase in viscosity can be estimated by conducting ^{1}H T_2 relaxation measurements since the T_2 relaxation time is inversely related to viscosity. Interestingly, the obtained results in Table 2-2 revealed a higher hydrogen-bond accepting capacity of ILB to local bound water at the interface up to 263 K. In addition to the existence of water ^{1}H signal at 253 K, the decrease in T_2 relaxation time for CILI further confirmed the stronger hydrogen-bond donor ability of ILI to local interfacial water.

Table 2-2: T_2 relaxation times of designed coatings, obtained by ^{1}H solid-state NMR spectroscopy.

Samples	**T_2 relaxation data (ms)**				
	276 K	268 K	263 K	258 K	253 K
Sylgard 184 + water	86	-	-	-	-
CILI + water	180	127	120	124	113
CILB + water	140	63	62	-	-

The CILIB ice adhesion again demonstrates that the quantity of ions on the surface of coatings is effective in reducing the ice adhesion. Regarding more effectiveness of BF_4^- in delaying IN_{temp} of water and conversely outperforming of CILI in anti-icing properties, the investigation of key parameters such as solubility, chemical characteristics and reactions, geometric structure of ion has allowed us to distinguish the performance of ILs at lower temperatures and gain a better understanding of the effectiveness and mobility of ILs in such conditions [325,326,332,345].

Density Functional Theory (DFT) calculations have significantly advanced our understanding of the geometric structure of typical ion-pairs in ILs, as documented in the literature [346]. The results reveal that in ILI and ILB, H-bonds are formed between the C^2-H of the cation and the N atom as well as the -SO_2 group of the TFSI anion and also F atoms of the BF_4^-. The large -SO_2 group tends to be positioned above the imidazole ring. Conversely, in ILB, the anion can reside both above and below the imidazole ring due to reduced steric hindrance. This steric configuration of ILB allows for the formation of more ion pairs and restricts mobility within the matrix [283,323,345]. Additionally, decomposition of BF_4^- through possible proposed side reactions worsen the mobility of ILB relative to that of ILI (Figure A-I. 1) [345,347–350]. Thereby, the total effective ions of ILB may decrease and limit its anti-icing performance in Sylgard 184 over the long term or after multiple icing/de-icing cycles.

To evaluate the long-term durability of our icephobic surfaces, it is necessary to subject them to numerous additional icing and deicing cycles. As illustrated in Figure 2-13, the ice adhesion values for IL-containing coatings, CILI and CILIB was less than 100 kPa over ten cycles; however, the rate of increase in ice adhesion strength for CILB was faster than observed the other coatings. Moreover, surface roughness of coatings after icing/de-icing cycles was measured. Obviously, S_q of the all coatings increased after 10 cycles of de-icing because of intrinsic low elastic modulus of Sylgard 184. Higher surface roughness of CILB samples demonstrated higher ice adhesion strength [219].

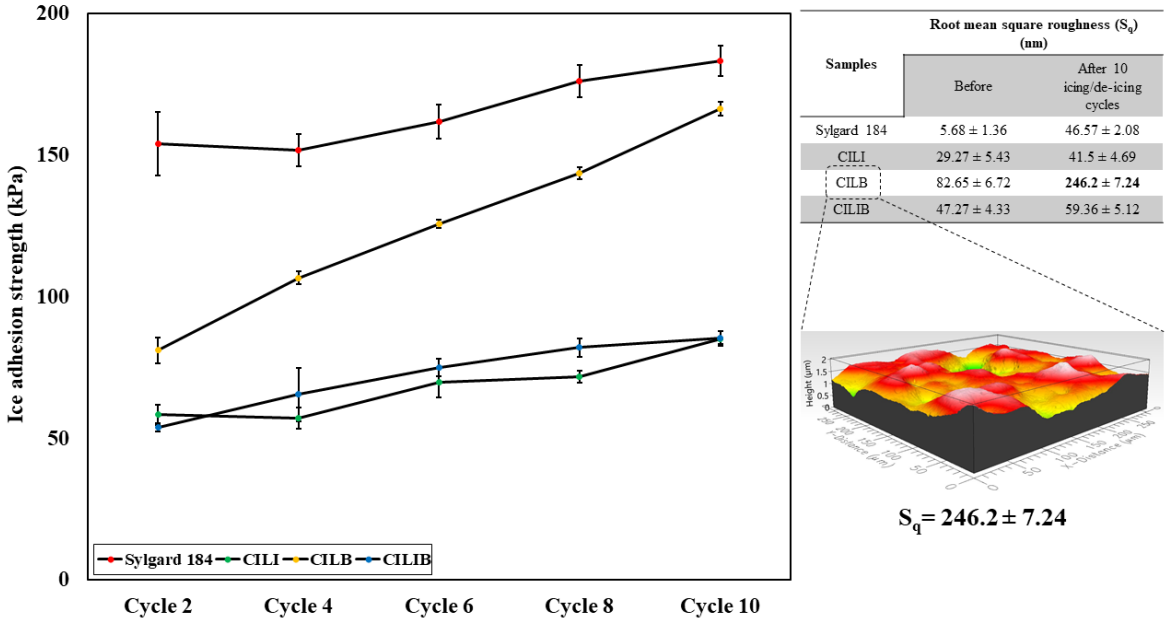

Figure 2-13: Ice adhesion strength (kPa) of coating over 10 ice/de-icing cycles, obtained by push-off.

2.5 Conclusion

Our research focuses on the development of innovative coatings that incorporate novel room temperature ionic liquids (ILs) with exceptional anti-icing properties. Through advanced analytical techniques such as ATR-FTIR, XPS, and SEM/EDX, we confirmed the presence of these ILs on the coating surfaces, enabling the formation of ionic hydrogen bonds with water molecules. Our findings also demonstrated that IL-containing coatings have the ability to lower the ice nucleation temperature, as shown by the results from DSC. By impeding ice nucleation or promoting ice melting, these coatings create an unfrozen quasi interfacial liquid layer (QLL) at low temperatures. This liquid layer, as evidenced by solid-state NMR spectroscopy, facilitates interfacial slippage and reduces ice adhesion strength, leading to enhanced anti-icing properties. Comparison of anti-icing behavior of these RT-ILs revealed that it is important to consider effect of various physicochemical characteristics of ILs, including their solubility/miscibility in water, geometric structure, mobility, on overall

performance of ILs in subzero temperatures. However, steric hinderance and intramolecular interactions affect the ILs mobility and total number of effective ions within a matrix. Hence, miscibility of ILs with matrix should be also considered, as hydrophobic ILs may exhibit different anti-icing behavior in a hydrophilic matrix. Additionally, near-surface concentration of ILs play a key role in determining the structure of QLL or their anti-icing performance which should be evaluated in details.

Acknowledgements

The authors acknowledge all support from the Natural Sciences and Engineering Research Council of Canada (NSERC) and UQAC. The authors would like to thank Caroline Potvin in the Département des Sciences Fondamentales, UQAC, for helping with the DSC test and Caroline Blackburn at the Anti-icing Materials International Laboratory (AMIL), UQAC, for helping to carry out the centrifuge test. The authors would also like to express their gratitude for Dr.Arnold Alexandre in Chemistry department of UQAM and Dr. Mohammadreza Shamshiri in conducting and helping the solid-state NMR spectroscopy.

CHAPTER 3

3. ARTICLE 2: TO BE OR NOT TO BE A HYDROPHOBIC MATRIX? THE ROLE OF COATING HYDROPHOBICITY ON ANTI-ICING BEHAVIOR AND IONS MOBILITY OF IONIC LIQUIDS

Saba Goharshenas Moghadam, Gelareh Momen*, Ehsan Bakhshandeh, Reza Jafari

Department of Applied Sciences, University of Quebec in Chicoutimi (UQAC), 555, boul. de l'Université, Chicoutimi, Quebec G7H 2B1, Canada

***Corresponding author:** Gelareh_Momen@uqac.ca

This article has been accepted in:

Chemical Engineering Journal

3.1 Abstract

The demand for anti-icing coatings to endure extremely low temperatures is substantial. Despite the innovative pioneering research on the anti-icing potential of ionic liquids (ILs), the development of such coatings is still in its infancy. Our study investigates how matrix hydrophobicity influences mobility of ILs at subzero temperatures and, consequently, their anti-icing behavior. Wettability results highlight the key role of IL anion hydrophobicity. Dielectric spectroscopy distinguishes ion mobility in the coatings at low temperatures. We also investigate how varying crosslink density affects ion mobility by

measuring the water absorbency. Higher mobility of released ILs from the coatings at subzero was confirmed by their presence in water solutions, validated with UV-vis spectroscopy, and resulted in increased ionic conductivity. Differential scanning calorimetry and experimental setups were employed to assess ice formation temperature, time, and ice adhesion strength. Notably, surfaces containing IL exhibited a remarkable reduction in ice formation temperature to -23.5 ℃ and achieved an exceptionally low ice adhesion strength (~15 kPa), attributed to the formation of a quasi-liquid layer (QLL). Solid-state NMR spectroscopy provided confirmation of the existence of QLL at the interface. Ice adhesion strength of coatings was examined against accelerated weathering, icing/de-icing cycles, as well as endurance against frost formation under freeze–thaw. Our findings underscore the significance of selecting the right matrix with regards to hydrophobicity and ILs when designing coatings for subfreezing applications.

Keywords: Ionic liquids, Hydrophobicity of coatings, Crosslink density, Ion mobility, Conductivity, Anti-icing behavior, Ice adhesion.

3.2 Introduction

Prolonged usage of infrastructure applications and devices in icy conditions and subzero temperatures can lead to critical safety concerns and significant damages [290,351,352]. Surfaces engineered for anti-icing purposes, featuring low ice adhesion strength to hinder ice growth, are designed to prevent icing problems and facilitate the removal of ice from exposed surfaces [14,18,353,354]. Organic coatings are promising and effective candidates for preventing heterogeneous ice nucleation and minimizing the adhesion force for ice removal [355–357]. Principle of designing anti-icing surfaces have recently changed from static to dynamic surfaces, putting more emphasis on empowering

dynamic anti-icing properties at substrate, ice or interface to endure in long-lasting working time and at very low temperatures [123,300,358,359].

A thorough understanding of the interactions between the ice–substrate interface on the one hand and the spontaneous and stimulus-responsive properties of dynamic anti-icing coatings on the other hand, has led to new insights into the anti-icing behavior of these surfaces [18,101,102]. Introducing dynamic properties between the ice–substrate presents an opportunity to tailor interactions for reducing ice adhesion. This approach inherits the advantages of non-frozen interfacial water, dynamic interface melting, dynamic interface generators and interfacial crack initiators to affect the force required to dislodge ice [17,49,62,79,103,104].

Dynamic interface melting, as an innovative strategy, has garnered significant attention by incorporating dynamic antifreezing–releasing capabilities into the interface to facilitate continuous ice removal even after ice has formed [76,197,360]. Ionic liquids (ILs) have been selected as relatively new antifreeze materials for melting interfaces. ILs are an intriguing new category of liquid materials with distinct property profiles. Salts known as ILs exhibit the following properties: they are entirely composed of ions, have low to very low melting points, and incredibly low vapor pressures below their thermal decomposition temperatures [150,361,362]. Their distinctive solubility and miscibility properties, versatile hydrophilicity/hydrophobicity, appealing electrical conductivity, and fascinating polarity/nucleophilicity offer a diverse range of opportunities in particular applications [356,363–365]. However, there have been may attempts to maintain distinctive features of ILs while immobilizing them in solid-phase matrixes and materials. ILs have often been

incorporated into ionogel and used in a wide spectrum of applications, including solid electrolytes, drug release, and catalysis [189,196,366,367].

The latest developments in anti-icing coatings and surfaces have sparked significant interest in incorporating ILs as innovative antifreeze agents into gels and coatings [19,26,368]. The liquid layer generated at the interface can facilitate ice detachment on such surfaces by depressing the freezing temperature. Ice and frost are suppressed when ions from the surface are diffused to water droplets, a mechanism similar to that on superhydrophilic surfaces. ILs can operate much more efficiently at a lower temperature than the hydration layer of a superhydrophilic anti-icing coating. Moreover, by providing soft quasi-liquid surfaces, ILs can extend easy sliding properties associated with surfaces [18,199,369]. In a comprehensive literature survey, a limited number of studies have been conducted to explore the anti-icing potential of ILs [26,27,37].

The higher mobility of ILs in coatings, along with their solubility/miscibility in water can facilitate ions migrate to the surface and diffuse to water droplets and, ultimately, enhance anti-icing capability of the coatings. Conversely, immobilizing ILs in various organic/inorganic matrixes can restrict ions movement depending on the type and strength of created interactions. To the best of our knowledge, the physicochemical properties of IL are key to determining whether there are ions (either cation or anion) on the surface [356]. In addition, the intrinsic characteristics of the matrix can affect ion transportation. Limited attention has been devoted to exploring the anti-icing capabilities of various ILs and, more significantly, to how different coating types impact on their anti-icing. This raises key concerns about the superior performance of specific ILs in either hydrophilic or hydrophobic coatings for anti-icing applications. Further research in this area is essential to address these

questions and develop efficient anti-icing solutions. On the one hand, polymer electrolytes incorporating ILs hold significant promise in the realm of energy storage and in enabling solid-state electrochemical capacitors to power emerging wearable electronics and Internet-of-Things devices. Nevertheless, developing solid electrolytes that can operate in sub-zero temperatures is a challenging yet critical task, especially for applications in outdoor winter environments [28]. Accordingly, this contribution attempts to scrutinize how hydrophilicity/hydrophobicity of two matrixes affect the mobility and anti-icing behavior of two ILs. The study utilized dielectric spectroscopy to assess the electrical conductivity of coatings at different subzero temperatures, aiming to pinpoint the ILs exhibiting the highest mobility within different matrixes, crucial for achieving superior anti-icing properties. The research extensively investigated ion mobility, ice adhesion strength under accelerated weathering and icing/de-icing cycles, as well as endurance against frost formation during freeze–thaw cycles. UV-Vis spectroscopy facilitated the analysis of ILs release into water, tailoring crosslinking density, while ionic conductivity measurements at both room temperature and -5°C provided additional confirmation of IL presence and mobility. This systematic exploration sheds light on how matrix hydrophobicity, crosslinking density and IL type impact the ions mobility and the coatings performance in challenging environmental conditions, which offers valuable insights for future advancements in anti-freezing technologies.

3.3 Materials and Methods

3.3.1 Chemical Materials

Silicone elastomer served as the hydrophobic matrix, while polyurethane was used as the hydrophilic matrix for the designed coatings. The Sylgard®184 silicone elastomer kit

was purchased from Dow Corning Corporation. To prepare the PU coatings, polyol resin based on acrylic copolymers (WorléeCryl® A 2445) with a 59-61% solid content and a 4.5% hydroxyl value (on solid) was supplied by Worlée industries (Germany). Aliphatic polyisocyanate resin based on hexamethylene diisocyanate (HDI) (Desmodur® N 75 BA/X) with NCO content of 16.5% ± 0.3 as a hardener was also purchased from Covestro Co. (Germany). Xylene (99%) and n-butyl acetate (99%) and n-hexane (99%) were received from Thermos Fisher Scientific as solvents. Two hydrophobic and hydrophilic ILs were used to prepare ILs-containing coatings (Table A-II. 1). The hydrophobic IL, 1-ethyl-3-methylimidazolium bis(trifluoromethanesulfonyl)imide (LI), was obtained from TCI America™. The hydrophilic IL, 1-butyl-3-methylimidazolium tetrafluoroborate (LB), was obtained from Sigma Aldrich (USA). All substances were analytical grade and used as-received without additional purification.

3.3.2 Preparation Methods

3.3.2.1 Silicon IL-containing Coatings

Various weight percentages of ILs (either LI or LB) were gently added into the base Sylgard 184 and n-hexane under stirring for 10 minutes. The curing agent was then added to the mixture at a standard ratio (1:10) and mixed thoroughly for 15 minutes. Finally, the prepared mixtures and the reference mixture without ILs were applied on cleaned substrates (aluminum and glass) by a film applicator (Zehntner ZUA2000 universal applicator) at wet film thickness of 500 μm. The coated samples were placed in the oven at 120°C for 3 hours to obtain fully cured coatings. As shown in Table 3-1, the samples were labelled by IL type and content, as SLI and SLB refers to the silicon coatings containing LI and LB, respectively.

The average dry thickness of the coatings was around 200 ± 20 µm, measured using the DeFelsko`s PosiTector 200 and the Elektrophysik MiniTest70 coating thickness gauges.

Table 3-1: Composition of each formulation for fabrication of silicon-based coatings.

Samples	Quantity of each component in final formulation (g)				
	Stoichiometric				
	Matrix (Part A)	Hardener (Part B)	LI	LB	Solvent
Sylgard 184	100	10	-	-	5
SLI-10	100	10	10	-	5
SLI-20	100	10	20	-	5
SLI-40	100	10	40	-	5
SLB-10	100	10	-	10	5
SLB-20	100	10	-	20	5
SLB-40	100	10	-	40	5
Samples	**Non-stoichiometric**				
Sylgard 184-NS	100	7.5	-	-	5
SLI-10-NS	100	7.5	10	-	5
SLB-10-NS	100	7.5	-	10	5

* Sample codes with NS coding as a symbol of non-stoichiometric coatings were designed at 10 wt.% of each IL.

3.3.2.2 Polyurethane IL-containing Coatings

PU coatings were prepared by mixing two components using a magnetic stirrer in two different ratios (stoichiometric and non-stoichiometric) of polyol and isocyanate. The different compositions prepared are shown in Table 3-2. PU coatings containing ILs were prepared by first, mixing polyol resin and polyisocyanate resin as the curing agent, stirring thoroughly in a clean beaker for 5 minutes, and then adding different percentages (wt.%) of ILs (either LI or LB) and solvent. The mixture was gently stirred again for 10 minutes. Note that the percentage of ILs was based on resin and hardener weights and their solid content.

Before applying, the viscosity of all mixtures was adjusted by adding at least 20 wt.% (based on the final mixture) of n-butyl acetate and xylene (at a weight ratio of 60:40). After stirring for 5 minutes, the prepared mixtures and the reference mixture lacking ILs were applied on clean substrates using the film applicator to a wet film thickness of 500 μm. The coatings were cured at ambient temperature for one week. The cured coatings exhibited the same thickness as their silicon-based counterparts.

Furthermore, the free-film of each coating was prepared for further testing. Additionally, non-stoichiometric coatings containing 10 wt.% of each IL were formulated, along with the process used for stoichiometric coatings involving a reduced weight ratio of the curing agent.

Table 3-2: Composition of each formulation for fabrication of PU-based coatings.

Samples	**Quantity of each component in final formulation (g)**				
	Stoichiometric				
	Matrix (Part A)	**Hardener (Part B)**	**LI**	**LB**	**Solvent**
PU	100	40	-	-	20
PLI-10	100	40	7	-	20
PLI-20	100	40	14	-	20
PLI-40	100	40	28	-	20
PLB-10	100	40	-	7	20
PLB-20	100	40	-	14	20
PLB-40	100	40	-	28	20
Samples	**Non-stoichiometric***				
PU-NS	100	30	-	-	20
PLI-10-NS	100	30	7	-	20
PLB-10-NS	100	30	-	7	20

* Sample codes with NS coding as a symbol of non-stoichiometric coatings were designed at 10 wt.% of each IL.

3.3.3 Surface Characterization

3.3.3.1 Chemistry of Surface

The chemical composition of coatings containing ILs was characterized using a Cary 630 Fourier Transform Infrared (FTIR) spectrometer (Agilent, USA) in attenuated total reflection (ATR) mode in the infrared range of 400–4000 cm^{-1}. The FTIR spectroscopy was carried out on a diamond surface cleaned with isopropyl alcohol prior to the test. The FTIR test was performed for both incorporated ILs in two matrixes to monitor potential chemical reactions and to detect ILs on the surface. The FTIR measurements were performed with a resolution of 4 cm^{-1}, and each spectrum was recorded three times to ensure reliability.

3.3.3.2 Contact Angle Measurements

Correlation between water contact angle (WCA) and ice adhesion strength manifests the atomistic interactions between water droplets and a surface. The effect of different ILs in hydrophilic and hydrophobic matrixes on wettability was assessed by quantifying wettability properties of coatings. The WCAs were measured with the sessile drop method using a Kruss™ DSA100 goniometer at a room temperature of 25°C ± 0.5°C. For the static WCA measurements, a 4-µl distilled water droplet was deposited onto the sample surface and the ADVANCE drop shape analysis software was used to quantify the WCAs. The Kruss is also equipped to a tilting table to measure sliding angles (SAs) of water droplets on the surfaces. A 35 µl water droplet (to remove the gravity effect) was placed, on the samples which were fixed on a tilting stage. The stage was inclined 60° with a speed of 60°/minute, until the droplet began to slide or roll off. SAs were measured as the stage angle at 0.5 s prior to the onset of droplet sliding.

WCAs and SAs were measured based on the Tangent and Ellipse (tangent) approximation methods. Note that the fitting approximation method is only the mathematical function used to describe the curvature of the drop shape.

3.3.3.3 Microscopy

Optical microscopy was performed using a Nikon polarizing microscope (Nikon ECLIPSE E600Pol) to observe phase separation of ILs in the developed coatings. Additionally, scanning electron microscopy (SEM) with Energy Dispersive X-Ray (EDX) analysis was utilized with a Hitachi S3500N SEM/EDX device manufactured by Oxford Instrument to further characterize F, S, N and B elements on the surface of IL-containing coatings. The samples were sputter coated with a thin platinum film before imaging.

3.3.3.4 Surface Roughness

Surface roughness was measured using an optical profilometer (Profilm3D Filmetrics®, USA) with white light interferometry (WLI) to measure surface profiles and roughness to 0.05 μm; the phase-shifting interferometry (PSI) option was added to measure smooth surfaces at the Angstrom level at 0.001 μm. All measurements were taken across a 400 μm × 300 μm region. For each sample, six randomly selected locations were assessed.

3.3.3.5 Colorimetry

Surface degradation of IL-containing coatings was characterized by color changing, defined as color measurement, after exposure to accelerated weathering conditions. The tests were performed in accordance with ASTM D 65 using a colorimeter apparatus in CILAB mode (RM 200, Lovibond LC100) illuminant D65, at a 10 ° angle. To visualize the surface

deterioration during QUV testing, the yellowness index (YI) of the sample coatings were measured before and after weathering test.

3.3.4 Anti-icing Properties

3.3.4.1 Freezing Delay Time

The freezing delay time of the samples was examined at -20°C using a Kruss™ DSA100 goniometer device equipped with a Peltier plate in a cold chamber. Figure A-II. 1 illustrates the experimental setup for the ice nucleation study. Humidity in the cold chamber was stabilized using anhydrous calcium sulfate desiccants, to minimize any condensation effect. The average of 7 measurements at various points and samples was reported as the freezing delay time.

3.3.4.2 Ice Nucleation Temperature

The effect of IL type and percentage on the ice nucleation temperature of the prepared coatings was evaluated using a TA Instrument Q250 differential scanning calorimeter (DSC) in the heating range of 40°C to - 40°C (± 0.05°C). Likewise, a precisely measured 5 mg deionized water droplet was placed on a DSC Tzero aluminum pan, covered with a thin layer of each coating (of a thickness ranging from 200 to 250 μm) prior to measurement, and then sealed with a lid. The prepared sample was initially cooled at a rate of 5 °C/minute from 40°C to -40°C. This process was repeated three times to confirm reproducibility.

3.3.4.3 Ice Adhesion Strength Measurements

The ice adhesion strength of the samples was measured in two ways: a push-off and a centrifuge test. To measure ice adhesion using the push-off test, in a cold chamber at -10°C, a thin cylindrical plastic mold, 1.5 cm in diameter, was placed on the surface and filled with

deionized water to form a cylinder of ice over 24 hours. Using a remote computer-controlled interface, the force gauge measured the shear force until the ice was detached (Figure A-II. 2**a**). Thus, adhesion stress can be calculated by determining the maximum force and the icing area. For the ice centrifuge test, the samples (2.5 cm × 3.5 cm) were ice-covered by spraying supercooled water microdroplets (approximately 300 μm) to simulate icing conditions under freezing drizzle in a climatic chamber at -8°C for about 35 minutes to obtain around 5.5 ± 0.5 g of ice. After 1 hour the iced samples were transferred to a cold room equipped with a centrifugal instrument to measure ice adhesion strength at -10°C ± 0.2°C; and the samples were installed at the end of a beam and rotated at a controlled frequency (Figure A-II. 2**b**). The force applied to the ice at the breaking point was measured and the adhesion stress was calculated by dividing the force by the icing area.

3.3.4.4 Solid-state NMR Spectroscopy

we utilized solid-state NMR spectroscopy to ascertain the existence of the nonfrozen quasi-liquid layer (QLL) at the interface between bulk water and coatings, both with and without ILs. The experiments were initially conducted at 276 K using a 400 MHz wide-bore Bruker Avance III-HD spectrometer (Milton, Canada), operating at 400.03 MHz for ^{1}H. Following this, the temperature was lowered to 268 K and held for 3 hours before acquiring additional spectra. Subsequently, spectra were collected every 3 hours, with a decrease of 5 K for each subsequent temperature point, until no liquid water was detectable by NMR. To facilitate a quantitative analysis of the ^{1}H signal in bulk water, the recycling delay was set to 5 seconds to ensure complete signal relaxation. T_2 measurements and ^{1}H spectra were obtained using the Hahn echo experiment and processed using Bruker TopSpin software.

3.3.5 Assessment of ion Mobility

Using ionic conductivity at low temperatures as a benchmark for assessing ion mobility, not only provides a true image of the presence and uniform distribution of these charge carriers, but also ensures the effectiveness of the anti-icing performance of ILs. Our contribution aims to develop a more fundamental study on how different hydrophilic and hydrophobic matrixes affect ionic conductivity and the impact of altering certain molecular characteristics (i.e. polarity) on ion transport properties, especially at extremely low temperatures to investigate their anti-icing behavior. Thus, the effect of IL type on mobility of ILs in hydrophilic and hydrophobic matrixes was assessed by measuring the conductivity of the prepared coatings at different temperatures; 25°C, 0°C, -15°C and -30°C. Accordingly, the dielectric response (ε′, ε″) of the coatings was investigated with the assistance of a Novocontrol broadband dielectric spectrometer (Microtonic Alpha-A high-performance frequency analyzer). The conductivity measurements (σ) were carried out over a wide range of frequencies. In a cell with a temperature-controlled cryosystem, the disk-shaped free-standing films of coatings with a diameter of 46 mm and thickness of approximately 125-200 μm were placed between the two stainless steel block solid electrodes, forming a plane–plane capacitor. The applied AC voltage was 3 V. Hence, ε′, ε″ and σ of all coatings was measured over the frequency range varying from 10^1 to 10^7 Hz, from RT to subzero temperature. The measurements for each coating at each temperature were conducted three times to ensure the reproducibility. Figure A-II. 3 shows a schematic of the dielectric setup for studying dielectric properties.

3.3.6 Water Absorption of Coatings

To study the effect of crosslink density and matrix type (elastic silicon / thermoset PU) on ion mobility, the first step was to measure swelling ratio of the samples at various time points. The swelling–deswelling characteristics of stoichiometric and non-stoichiometric prepared films of reference samples lacking ILs and IL-containing samples were measured through gravimetric analyses. The free-standing films were immersed in 500 mL of distilled water at room temperature for different durations (t= 1–72 h). The swollen sample was weighed after removing excess water from the films with a paper towel. The water absorbency of the film samples (Q_t; g/g) was calculated using the following Equation 3-1:

Equation 3-1

$$Q_t=(m_t-m_0)/m_0$$

where m_0 (g) and m_t (g) are the weights of the samples in the dry state and the swollen state, respectively, at a certain time. Q_t is defined as the water absorbency when swelling reached equilibrium. All experiments were performed three times, and the results were averaged.

3.3.6.1 UV-Vis Absorption of Water Solutions of Each Swelled Film

After measuring the swelling ratio of films in water and reaching equilibrium after 72 h, a Cary 5000 UV-Vis spectrophotometer in the range of 180 to 600 nm was used to assess the absorbance of each water solution in order to determine type of matrix, in which, ions have enough mobility to migrate to the surface regardless of the swelling ratio and the solubility content of each IL in water.

3.3.6.2 Measuring Ionic Conductivity of Water Solutions at RT and -5°C

Additionally, the ionic conductivity of each water solutions was determined at RT (24.8°C ± 0.3°C) and -5 °C (-4.8°C ± 0.2°C) to further verify ion mobility. A Thermo Scientific Orion Star A112 benchtop conductivity meter was utilized to determine the ionic conductivity (λ) of solutions and further verify ion mobility. It should be noted that the conductivity meter was calibrated with KCl standard solution with an ionic conductivity of 1413 $\mu S.cm^{-1}$ at 25°C. After observing the closest conductivity to that expected for KCl, the conductivity probe was rinsed with distilled water for each measurement.

3.3.7 Pendulum Hardness

Surface pendulum hardness of stoichiometric and non-stoichiometric reference coatings and IL-containing coatings as a promising representative of surface response against deformation were measured using a BYK-Gardner Byko-Swing (5867) Konig/Persoz Hardness Tester. The number of swings at 4 ° (Persoz mode) as surface hardness of the prepared coatings was analyzed based on ASTM D4366. The measurements were an average of five points.

3.3.8 Weathering Test

A QUV accelerated weathering tester was used to examine how ultraviolet light and moisture condensation affected the deterioration of the prepared coatings. The test procedure was executed using UVA-340, UVA-351 and UVB-313 fluorescent lights in accordance with ISO 11507. The test included an 8-hour test cycle with 400 hours of UV light exposure at a temperature of 60°C and an irradiance of 0.71 $W.m^{-2}$, followed by 4 hours of condensation at 50°C.

3.3.9 Time to First Frost formation under Freeze–Thaw cycles

Time to first frost formation (TFF) on the designed coatings was measured over 7 freeze–thaw cycles. TFF of samples was measured when placing on the Peltier at -20°C. The samples were then kept at room temperature to raise their temperature to 20°C, after, which were placed in the oven at 70°C for 30 minutes. TFF measurement was performed in a chamber which is equipped to the air distribution system, capable of cooling the air (0.0 °C ± 0.5 °C) and maintaining it at the specified level. Air flow shall be measured using a suitable anemometer or velometer within ±0.05 m/s. Moreover, humidity was produced using a saturated water vapor generator and recorded using a calibrated humidity sensor. The humidity generator was capable of a minimum of 80% RH when the air temperature is at 0 °C. The samples should be free of all visible contamination. After reaching test plate to desired temperature, series of either silicon-based or PU-based coatings samples were placed on the Peltier at same time to visually distinguish when the reference had been covered in frost as well as when frost formed on the surface of the ILs-containing coatings. This process was performed seven times for each series to assess ILs capacity to postpone frost formation during freeze–thaw cycles.

3.4 Results and Discussion

3.4.1 Surface Characterization

3.4.1.1 ATR-FTIR Spectroscopy

Surface chemistry and the chemical composition of the cured samples were investigated using ATR-FTIR spectroscopy. FTIR spectra of PU-based and silicon-based coatings are shown in Figure 3-1a and Figure 3-1b, respectively. As indicated, the peaks at the high wavenumber range of 3100–3400, 1400–1500, 1700 and 2800–2900 cm^{-1} are

attributed to the stretching vibration of C-N, N-H, C=O and CH_2CH_3 groups as urethane linkage existing in PU-based coating containing and lacking ILs [370]. Comparing the FTIR spectra of neat and IL-containing coatings proves the ILs structuring on the surface due to an increase in peaks intensity at 3100–3400 cm^{-1} and for the stretching vibration of C-N and N-H of the imidazolium ring. Moreover, the stretching vibration of B-F and C-N of the imidazolium ring in the FTIR spectrum of PLB coatings revealed absorption peaks at 1130 and 1170 cm^{-1}, respectively. Sharp and intense peaks at 1190, 1300 and 1350 cm^{-1} also observed in the FTIR spectrum of PLI for stretching vibration of C-N, C-F and S=O of imide [304,305]. According to Figure 3-1b, silicon-based coatings with and without ILs both exhibit distinct absorption peaks at 1100 cm^{-1} and 2900 cm^{-1} related to the Si-O-Si group and the CH_3, respectively [371]. In the FTIR spectra of SLI, the intense absorption peak at areas of 1327, 1347 and 1185 cm^{-1} are associated to S=O, C-F and C-N of the imidazolium ring in LI. The characteristic peaks at 1130 and 1400 cm^{-1} are related to B-F and N-H of imidazolium ring which also confirm the presence of LB in the SLB coating [304,305]. Due to the sensitivity of BF_4^- anion to hydrolysis and oxidization when exposing the catalyst/initiator, anion of LB may generate borax and act as a gelator for part A of Sylgard 184 and the polyol component of PU (Appendix II, Figure A-II. 4) [37,282,307]. The ATR-FTIR test was then performed for sample coatings containing 20 wt.% of each IL, either silicon-based or PU-based, as indicated in Figure 1 to characterize BF_4^- in the PLB-20 and SLB-20 coatings. It is worth mention that FTIR spectra of all coatings were normalized to minimize concentration effect, based on distinguished peaks at 1720 and 1100 cm^{-1} for the C=O and Si-O-Si linkage, for PU-based and PDMS-based coatings, respectively.

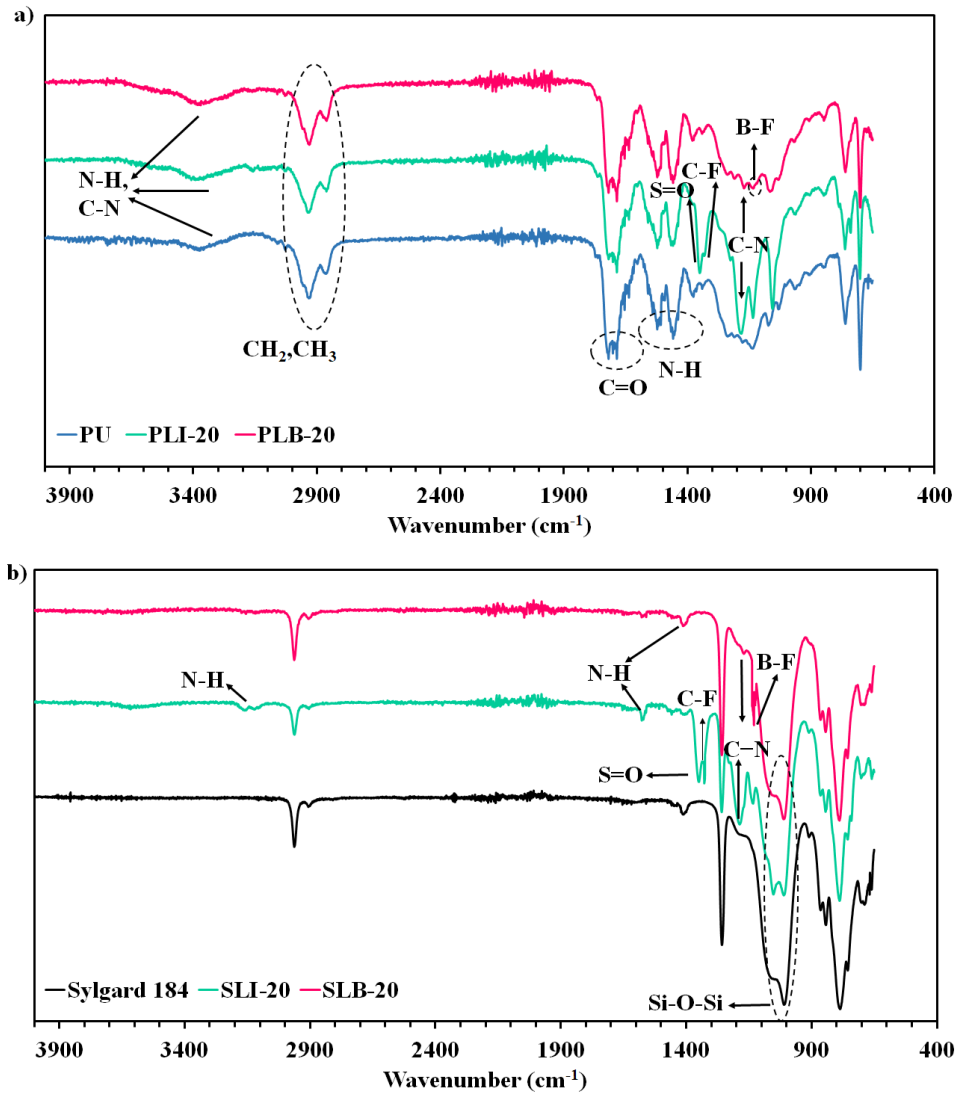

Figure 3-1: FTIR spectra of the prepared coatings; (a) PU-based and (b) Silicon-based reference samples with and without ILs.

3.4.1.2 Microstructure analysis

However, the coatings appearance did not show any visual change as shown in Figure 3-2a. Phase separation of LB in Sylgard and LI in PU was observed in optical microscopy images. The hydrophilicity/hydrophobicity difference between ILs in these two matrixes stems mostly from their anions which leads to poor compatibility between them by increasing

their contents [361,372]. As evidenced by experimental observation (Figure A-II. 4), the final PLB coating samples lost their transparency as the percentage of LB in PU rose due to the reactivity of LB in the polyol component.

To further evaluate the presence of IL components, either cation or anion, on the coatings surface, SEM-EDX (elemental mapping mode for F, S, N and B) was utilized. According to Figure 3-2b, peaks and maps of F, S components for the LI-containing coating as well as elemental mapping of B for the samples containing LB further confirmed the presence and the relatively uniform distribution of ILs anions, on the surface of designed coatings. In addition, the EDX analysis showed an increased content of components, roughly 2 wt.% for F on samples containing LI [26].

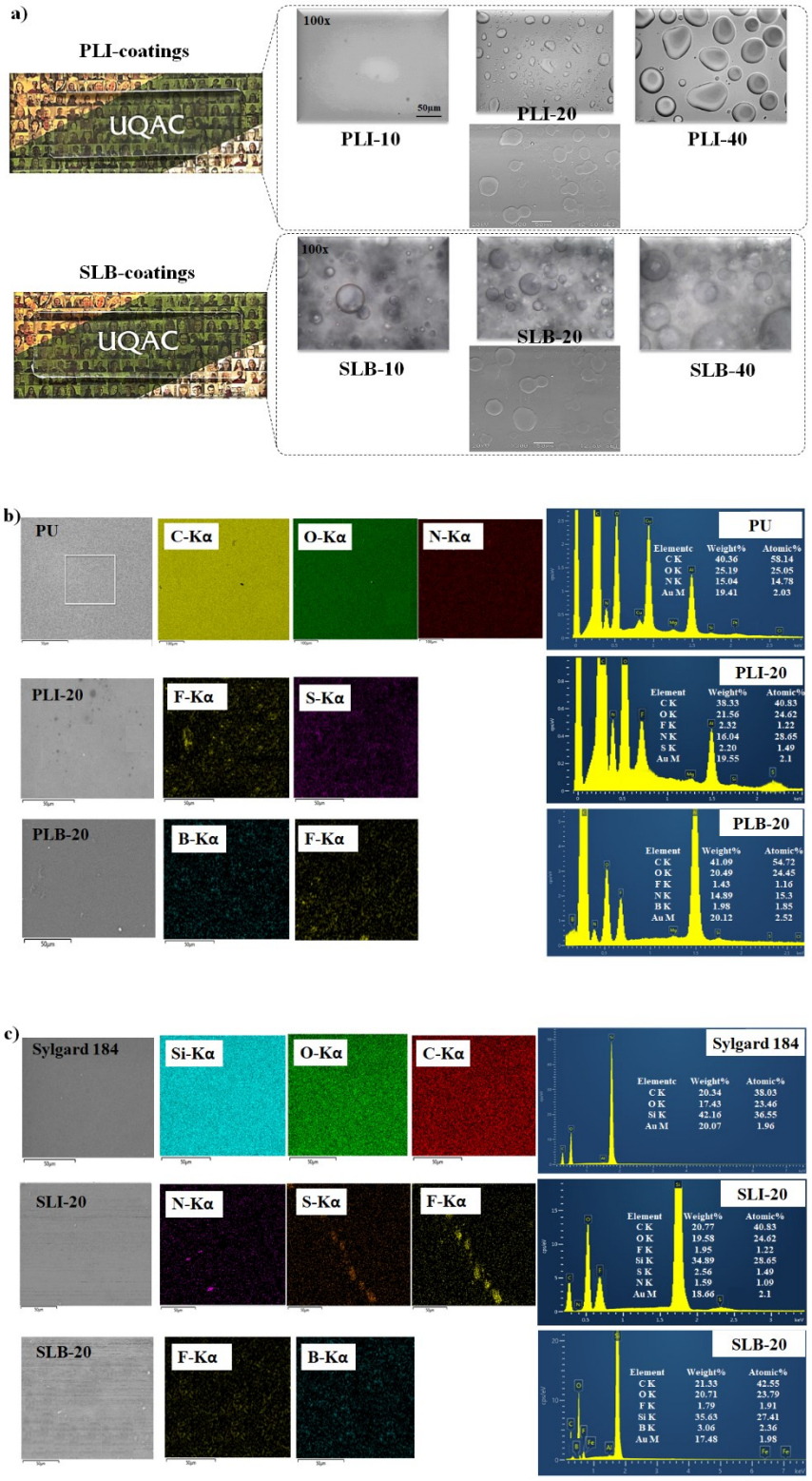

Figure 3-2: (a) Experimental observation and optical microscopy images of PLI and SLB coatings, and the SEM/EDX mapping of; (b) PU-based, and (c) silicon-based coatings with and without ILs.

3.4.1.3 Wetting behavior

A thorough understanding of the presence of ILs for anti-icing applications requires an analysis of the structure–property interactions, involving cations, anions, ILs and matrix. Exploring how ILs influence surface wettability across different matrixes offers valuable insights into the intramolecular forces governing interactions between ILs and water droplets on surfaces. Therefore, the WCA, and SA of the developed coatings were measured, as illustrated in Figure 3-3a and Figure 3-3b and in Figure A-II. 5a and Figure A-II. 5b for stoichiometric and non-stoichiometric coatings, respectively.

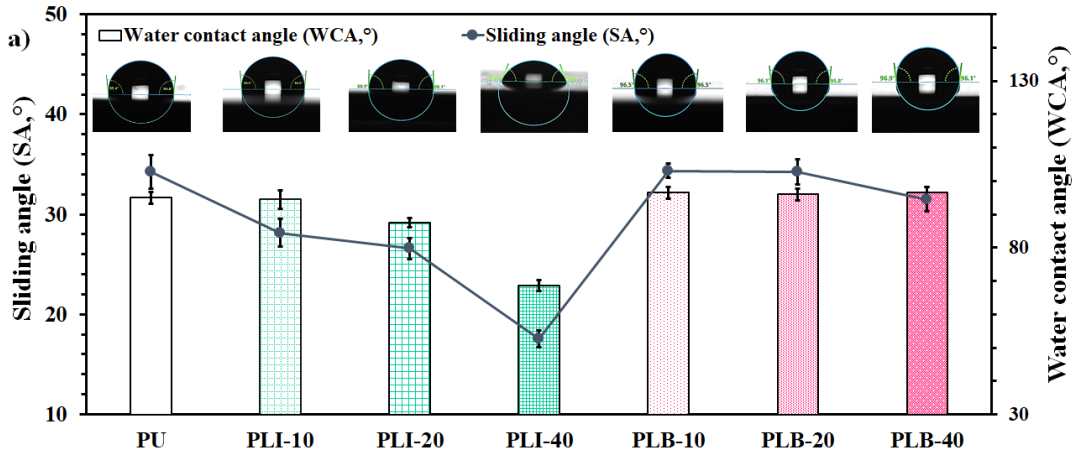

PU-based coatings	PU	PLI-10	PLI-20	PLI-40	PLB-10	PLB-20	PLB-40
WCA (°)	94.9±1.76	94.4±2.79	87.5±1.37	68.6±1.55	96.5±1.83	95.9±1.75	96.4±1.62
SA (°)	34.2 ±1.72	28.1±1.38	26.6±1.05	17.5±0.82	34.3±0.70	34.2±1.25	31.5±1.22

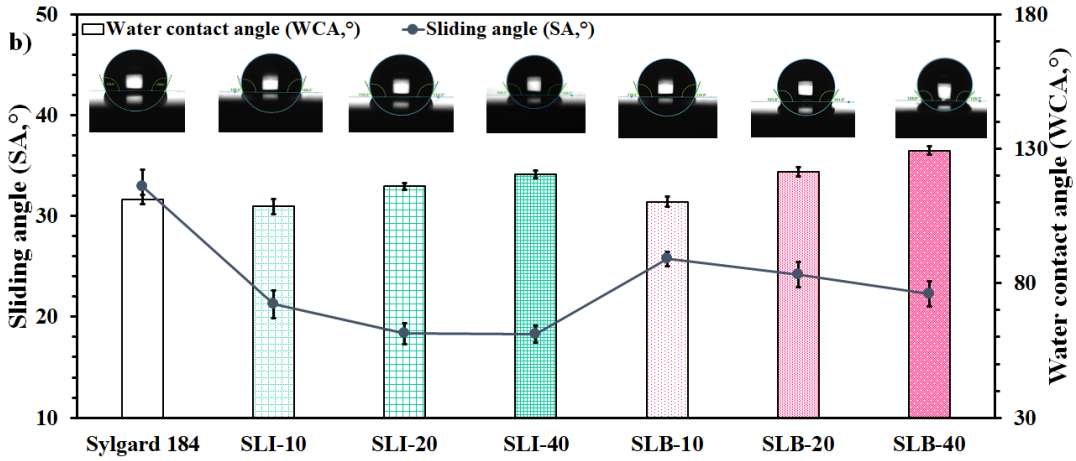

Silicon-based coatings	Sylgard 184	SLI-10	SLI-20	SLI-40	SLB-10	SLB-20	SLB-40
WCA (°)	111±2.73	108.5±3.05	115.9±2.5	120.5±2.89	110.3±1.96	121.5±1.84	129.3±2.36
SA (°)	32.9 ±1.62	21.2±1.82	18.3±1.57	18.2±1.41	25.7±1.31	24.2±1.06	22.2±1.36

Figure 3-3: Wetting properties of the stoichiometric coatings; (a) PU- and (b) Silicon-based reference samples with and without ILs in different percentages.

As the results demonstrate, a dramatic drop in the WCA was observed for PU containing LI, reaching a WCA of around 68° when its amount increased, compared to the neat coating. However, the WCA for PU containing LB in different percentages remained constant. As opposed to the PU-based coating containing LB, the average WCAs of silicon-

based coatings increased substantially from 111° ± 2.73 to 129.3° ± 2.36 for SLB-40. According to the results presented for SAs, a considerable decline of 50% in SAs of LI-containing coatings, whether PU-based or silicon-based, was also found. As indicated in Figure A-II. 5a and Figure A-II. 5, it is noteworthy mentioning that the WCA and SA of PLI-NS and SLB-NS showed a similar pattern to stoichiometric counterparts.

Regarding the Young's equation for flat and chemically uniform surface, like PU and silicon-based reference coatings [373]. to some extents different wetting behavior is determined primarily by the new surface chemistry associated with the type of IL incorporated as well as the structure of interactions between IL and matrix and between IL and water molecules. Given the relatively low interfacial tension between ILs and water, IL-containing surfaces show higher hydrophilicity than references lacking ILs. Remarkably, the wetting characteristics of ILs are predominantly dictated by the nature of the anions [316,317]. m Nevertheless, silicon-based coatings containing LB exhibited lower wettability and higher WCAs compared to counterpart coatings [132,327].

As there are many hydrogen-bond donor and acceptor sites on the cation and anion of an IL, a hydrogen-bonded network may form. According to the literature, the stronger hydrogen-bond–accepting ability of anion BF_4^- leads to more ionicity and to formation of more ion pairs [323]. Literally, the hydrogen bond that the cation donates to a newly introduced solute will be in competition with the IL anion if the anion is a strong hydrogen-bond acceptor [324,327]. While LB demonstrates higher water solubility, the enhanced hydrogen-bond-donor capability of the less basic NTf_2^- results in the creation of a more accessible and robust ionic hydrogen bond with water. Consequently, coatings containing LI exhibit lower water contact angles compared to those containing LB (Figure 3-4). Moreover,

urethane linkage of PU as a hydrophilic matrix makes the ionic hydrogen-bond stronger. The possibility of creating hydrogen-bond interactions between urethane linkages in polyurethane resins and LI appears to be higher than that of siloxane linkages, due to unique characteristics of LI [324,327]. Indeed, the hydrophobic LI in a hydrophilic matrix enhanced surface hydrophilicity as increased LI content compared to the hydrophilic LB. However, CAs of silicon-based coatings containing LI did not follow same trend because the Sylgard 184 matrix is more hydrophobic.

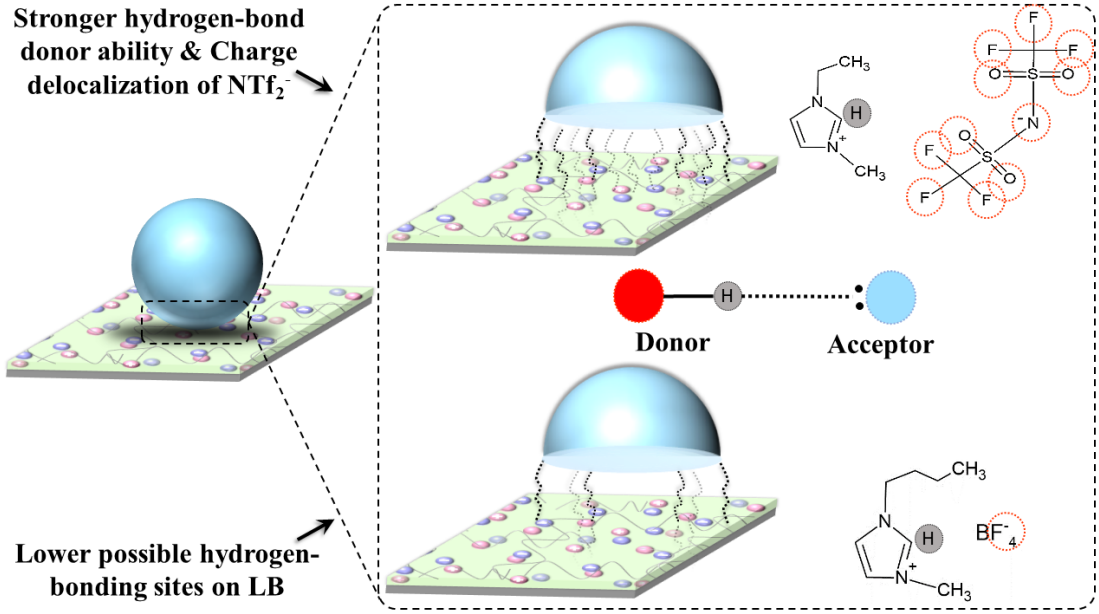

Figure 3-4: Schematic of different hydrogen-bond donor ability of ILs to water droplets.

Compared to coatings containing LB, LI- incorporating samples showed a significant decrease in SAs. The increased interaction potential between LI and PU compared to Sylgard 184, coupled with greater immiscibility with water, contributes to the enhanced easy-sliding property, evident in the significant decrease in the sliding angle at the maximum IL percentage. Additionally, phase separation of LI in the PU matrix may also strengthen its lubrication characteristics. As the IL percentage increases, the matrix type and structure–

property of the generated interactions appear to be more influential than the physiochemical characteristics of the ILs [199].

3.4.2 Ion Mobility

3.4.2.1 Dielectric Measurements of the Designed Coatings from RT to Subzero temperatures

Underscoring the pivotal role of ion mobility and its influence on their anti-icing characteristics was evaluated. This was assessed through dielectric spectroscopy, which affirmed the existence and mobility of charge carriers at various temperatures in both hydrophilic (polar) and hydrophobic (non-polar) matrixes. The dielectric spectra of PU-based and silicon-based coatings are depicted in Figure A-II. 6, Figure A-II. 7 and Table 3-3.

Table 3-3: Dielectric properties of coatings with and without 20 wt.% of ILs at 10^1 Hz from RT to subzero temperatures.

Dielectric properties at 10^1 Hz	**ε′ (±5.00E-03)**			**ε″(±5.00E-03)**		
Temperature ℃	**25**	**0**	**-30**	**25**	**0**	**-30**
PU	4.38E	4.28E	4.27E	1.06E-01	1.09E-01	9.07E-02
PLI-20	1.25E+04	8.84E+03	5.78E+03	1.02E+04	3.44E+03	1.02E+03
PLB-20	6.43E-01	6.04E-01	5.35E-01	1.95E-02	1.31E-02	4.34E-02
Sylgard 184	2.84E	2.98E	3.18E	2.40E-02	8.81E-03	9.94E-03
SLI-20	4.04E	4.02E	4.02E	3.94E-01	3.01E-01	3.51E-01
SLB-20	2.90E	2.99E	2.99E	5.58E-02	5.08E-02	4.16E-02

The term *ions* in this study refers to free charges that diffuse through materials and contribute to ionic conductivity. Factors such as free ion number density and mobility presumably contribute to increases in ionic conductivity. Identifying ion interactions with its environment of the matrix is crucial to understanding the quantity of free ions since ions with a charge are present in an amorphous solid which has tended to polarize their surroundings.

Ions undergo screening as polarized molecules or atoms rearrange around their polarized environment, forming dipoles and thereby reducing the electrostatic energy of ions (Figure A-II. 8) [374,375]. The ion must possess adequate energy to surpass the heightened potential barrier formed as it traverses the surrounding dipoles (ionic trapping). Through the activation process, ions move from one potential well to another by overcoming the energy barrier. Study of ion transport over a wide frequency range therefore provides insights into ion diffusion (σ_{DC}) and sub-diffusion (σ_{AC}) motions, particularly at subzero temperatures [323]. The varying ability of ILs to surmount the energy barrier in these two coatings under subfreezing conditions can help us distinguish their mobility and anti-icing efficacy.

The reference samples without LB and those containing LB exhibited minor disparities in dielectric constant. However, the addition of LI to Sylgard 184 or PU resulted in an increase in the ε' of SLI-20 and PLI-20 coatings in the low-frequency range, and these values remained higher at subzero temperatures, particularly for PLI. In other words, the incorporation of LI plasticizes the polymer, making it easier for electric dipoles to orient themselves and increasing the dielectric constant as a result [323,376–379]. The dipoles formed due to the presence of LI in the matrixes, clearly have far more time to orient themselves towards the external electric field, resulting in higher $\acute{\varepsilon}$ values at lower frequencies, even at very low temperatures. It is worth noting that a substantial increase in

the ε′ of PLI-10 over SLI-10 reveals the importance of matrix type. Thanks to more polarity of PU and higher number of available sites to accept/donor hydrogen-bonding between LI and PU owing to create more dipoles [379]. Thus, more uniform pathways for charge carriers may be formed, which making it easier for dipoles to align towards the external electric field and to achieve a higher dielectric constant for PU containing LI. The larger and asymmetric structure of LI results in charge delocalization and transferring charge centers to several atoms, which significantly impacts the dielectric constant of matrixes, in addition to enhanced hydrogen-bond donor ability of LI and formation of ionic hydrogen-bonds with PU (O=C-NH). In contrast, side chemical reactions of LB in either Sylgard 184 or PU can restrict the mobility of this IL and reduce quantity of free ions (Figure A-II. 4) [349].

3.4.2.2 Conductivity Measurements of the Designed Coatings from RT to subzero temperatures

Figure A-II. 7 indicates imaginary part of permittivity for PU-based and silicon-based coatings. As shown in Table 3-3, a similar trend was observed for both series samples as a function of frequency and at different temperatures. According to the results in Figure 3-5, the enhanced conductivity observed in LI-containing coatings compared to their counterparts affirms the superior mobility of LI at subzero temperatures. However, the conductivity of silicon-based coatings containing LI increased by 1.19E+01 at RT. Adding LI into PU lead to a conductivity increase of 10^6 times (about 3.32E+06).

Correlation of ε″ and σ_{DC} can be explained by using Equation 3-2:

Equation 3-2

$$\varepsilon'' = \sigma_{DC} (\omega C_0)$$

where σ_{DC} is the dc conductance and C_0 is the vacuum capacitance for the unfilled cell in which the electrode plate spacing is equal to the sample thickness [353,374,377–380]. This may exhibit that the conduction process (i.e., conductivity) is temperature-dependent and influenced by the nature of restructuring, possibly arising from structural diffusion. The reduced conductivity at very low temperatures (-15℃ or -30℃) illustrates that conductivity depends on temperature. Reduced conductivity for PLI-20 from 3.92E-05 at RT to 6.78E-08 S/cm at -30℃ may illustrate stable and higher mobility as well as more stable anti-icing performance of LI in PU under subfreezing conditions.

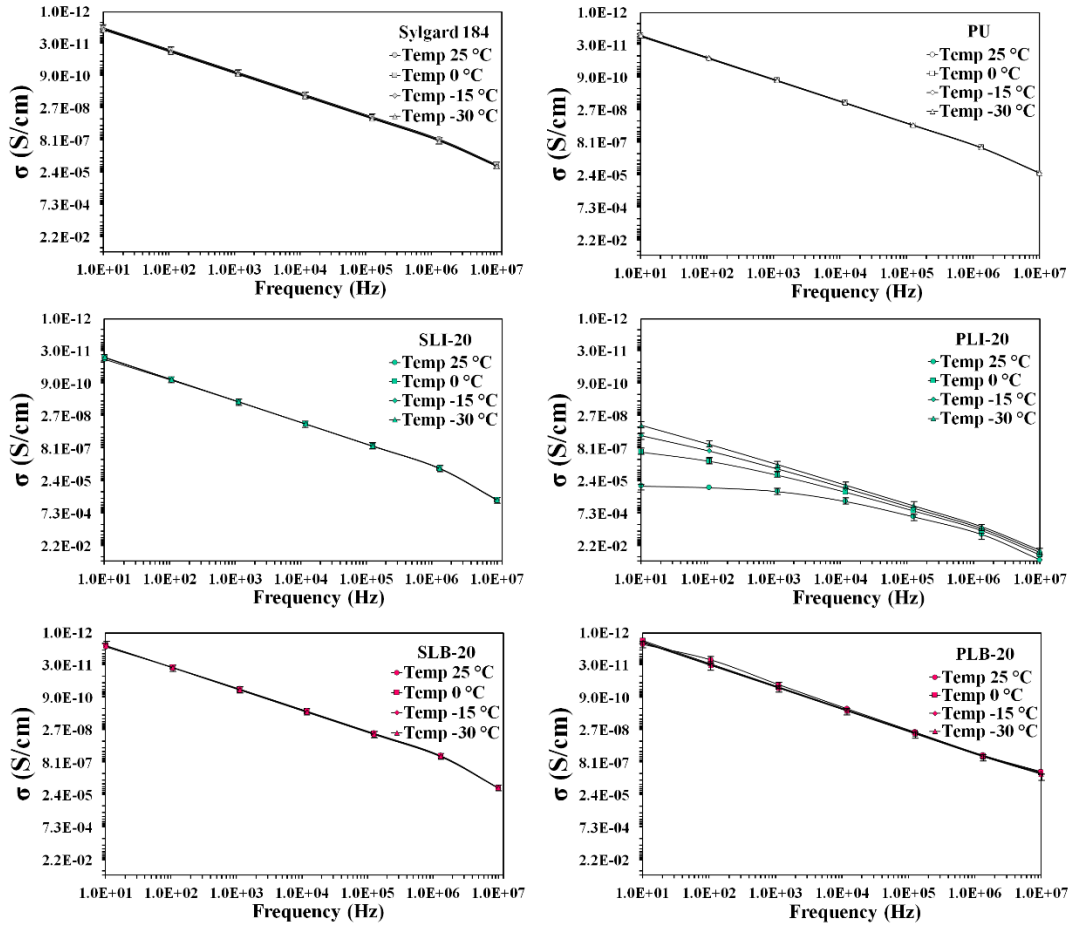

Figure 3-5: The variation of conductivity with frequencies from 10^1 Hz to 10^7 Hz at different temperatures, for coatings lacking and containing 20 wt.% of ILs.

3.4.2.3 Study on the ILs Released from the Surface into Water

Ion mobility and transportation may be influenced not only by the chemistry of the matrix but also by its crosslink density. Non-stoichiometric silicon-based and PU-based coatings with a minimum percentage of ILs of 10 wt.% as well as stoichiometric counterparts were formulated. Following a 72-hour swelling period in water, UV-Vis spectroscopy was utilized to assess the release of ILs into the water, considering their diverse solubility and interactions with the matrix. Additionally, the ionic conductivity of the solutions was examined at both room temperature (RT) and -5°C to discern the ionic mobility of each IL.

As can be seen in Figure 3-6a and Figure 3-6b, coatings having low crosslink density clearly showed a higher water absorption rate than their stoichiometric counterparts. LB-containing samples swelled more than free films containing LI in both series likely due to side chemical reactions. Figure 3-7a indicates UV-Vis spectra of solutions containing ILs released into water. Since LB is more soluble/miscible in water, more UV absorbance is expected to be found for LB. In contrast, LI-containing water solutions, particularly for PLI, had the maximum UV absorbance for imidazolium rings and alkyl side chains at a wide range of 190 to 330 nm, which supports the presence and higher mobility of LI [381–383].

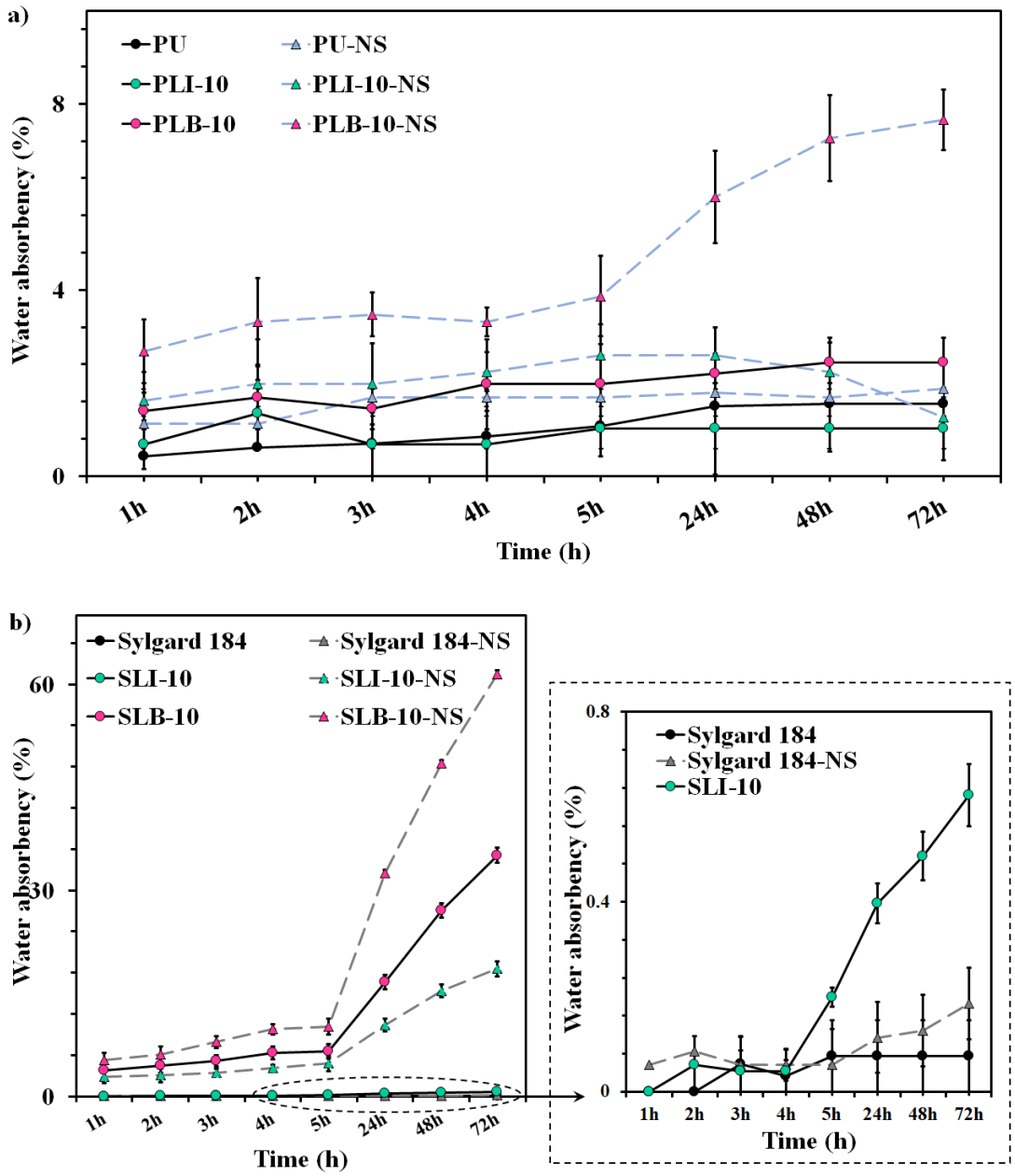

Figure 3-6: The measured swelling ratios of non- stoichiometric and stoichiometric samples, immersed in water over time, for (a) PU-based and (b) silicon-based coatings.

According to Figure 3-7b, our findings indicate that water solutions of all swelled films show a superior ionic conductivity at RT and -5°C than high grade deionized water with a stated ionic conductivity of roughly 0.05 $\mu S.cm^{-1}$. Further, solutions containing LI for PU-based swelled films showed significantly higher ionic conductivity at either RT or -5°C.

It is worth underlying that pure LI has higher ionic conductivity (6.6 $mS.cm^{-1}$) than LB (3.5 $mS.cm^{-1}$), as measured by a conductivity meter at RT.

Considering that both coatings exhibit comparable ion permeability, the observed disparities in their response to an electric field may be attributed to additional underlying factors or mechanisms within the coatings. Furthermore, an examination of the UV absorbance of released IL into water from swollen coatings suggests varying degrees of depletion from the surface, indicating potential variations in the interaction among the coatings, water, and the surrounding environment. The evaluation of ionic conductivity, which reflects a material's ability to conduct ions, suggests that LI within the PU matrix might exhibit enhanced mobility. These results underscore the influence of matrix hydrophobicity, crosslinking density, and IL type on ion mobility and coating performance under demanding environmental conditions, and more significantly, offering new perspective for future advancements in anti-freezing technologies.

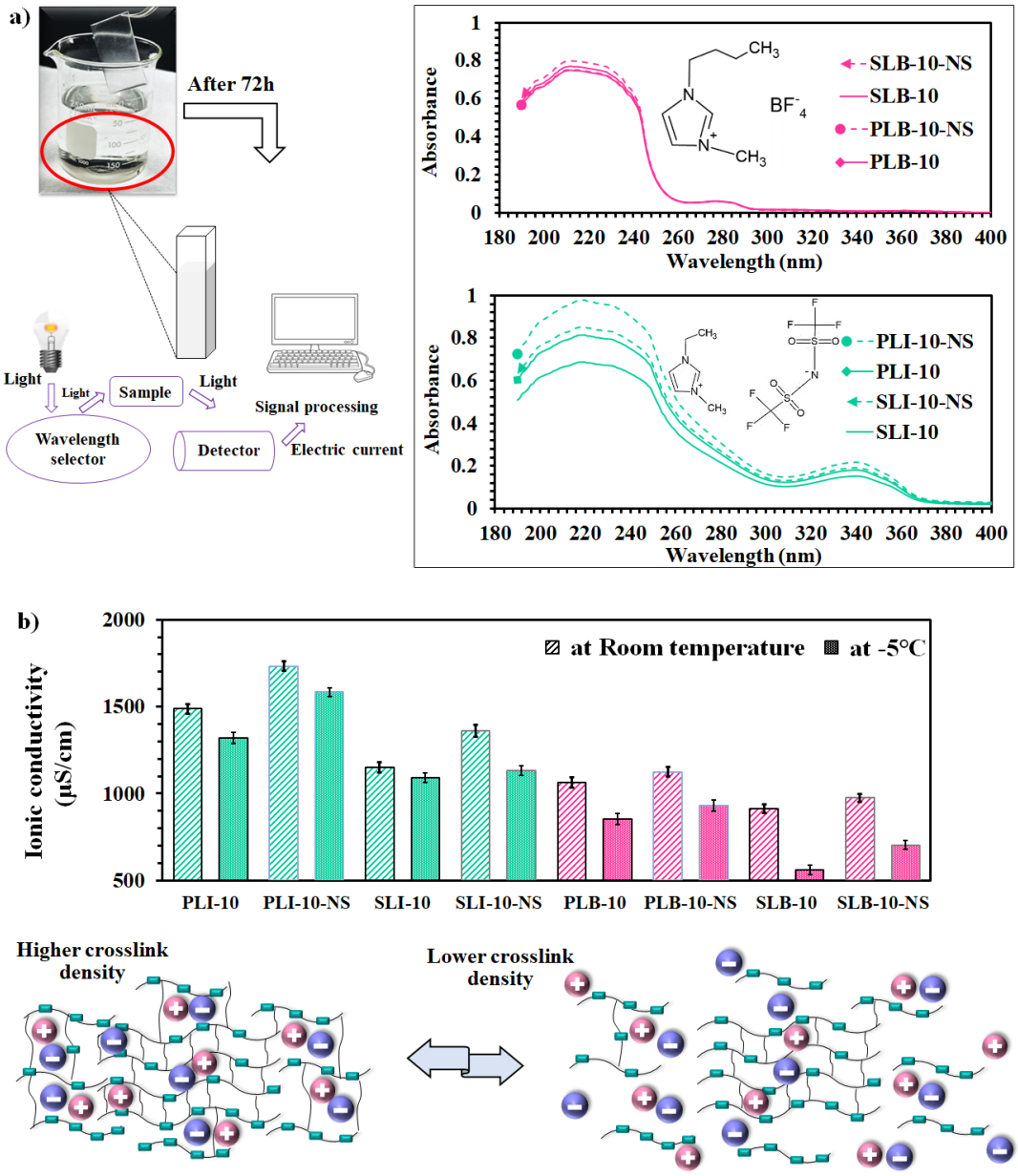

Figure 3-7: (a) UV-Vis spectra of remained water solution after 72 hours, (b) the measured ionic conductivity of water solutions at room temperature and -5°C, obtained by conductivity meter and schematic of effect of crosslink density on ions mobility.

3.4.3 Anti-icing properties

3.4.3.1 3.3.1. Ice Formation Temperature and Time

A differential scanning calorimetry (DSC) analysis was conducted to determine the impact of IL presence and concentration on ice formation temperature (IF-temp) in both silicon-based and PU-based coatings. Incorporating ILs into both coatings decreased IF-temp, as can be seen in Figure 3-8a and Figure 3-8b. For instance, a sharp drop in the IF-temp of Sylgard 184 containing LB was found from -15.3°C to -21.8°C, for samples Sylgard 184, and SLB-40, respectively. Similarly, adding ILs to PU-based coatings reduced the ice formation temperature of samples, whether containing LI or LB. The diffusion of ILs into water molecules and the subsequent depression of the freezing point of water contributed to the lower IF-temp observed in coatings containing ILs [19].

The combination of ionic hydrogen bonds, dipole–dipole, and electrostatic interactions imparts unique characteristics to ILs, such as lower melting points, lower viscosities, lubrication and etc. This offers an excellent opportunity for manifold anti-icing mechanisms simultaneously [323]. Mobility and rearrangement of the water molecules are also constrained by the creation of ionic hydrogen-bond networks between water and ILs. As demonstrated, incorporating LI in PU remarkably decreased the IF-temp of PU-based coatings, from -15.8°C for the PU to -23.5°C for the PLI-40 sample, when in comparison with LB, even though LB is more water soluble [324,325] and more miscible in PU (less hydrophobicity). The stronger hydrogen-donor ability of LI leads to the formation of a stronger ionic hydrogen-bond with water, particularly in PU given its hydrophilic chemistry, which in turn leads to greater polarity and more potential hydrogen-bond sites 55]. Bonded water has a higher energetic barrier for nucleation and requires more energy to form ice nuclei

than non-bonded molecules [329,340]. Heterogeneous ice nucleation can thus be inhibited and start at lower temperatures. Hence, it seems that the type and characteristics of the matrix play a more substantial role than the physicochemical properties of ILs when increasing the IL percentage.

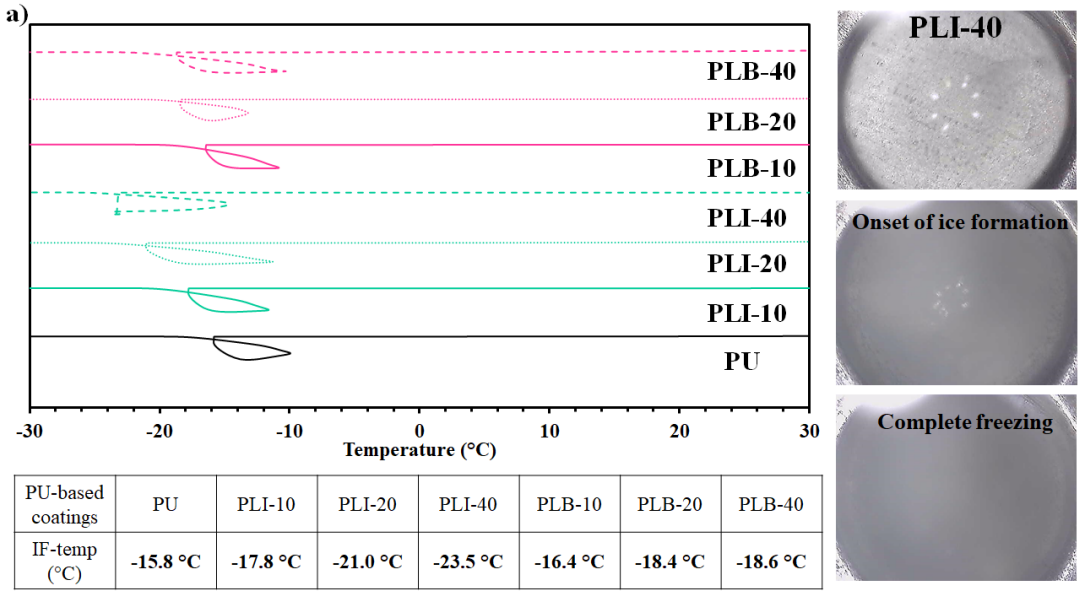

PU-based coatings	PU	PLI-10	PLI-20	PLI-40	PLB-10	PLB-20	PLB-40
IF-temp (°C)	**-15.8 °C**	**-17.8 °C**	**-21.0 °C**	**-23.5 °C**	**-16.4 °C**	**-18.4 °C**	**-18.6 °C**

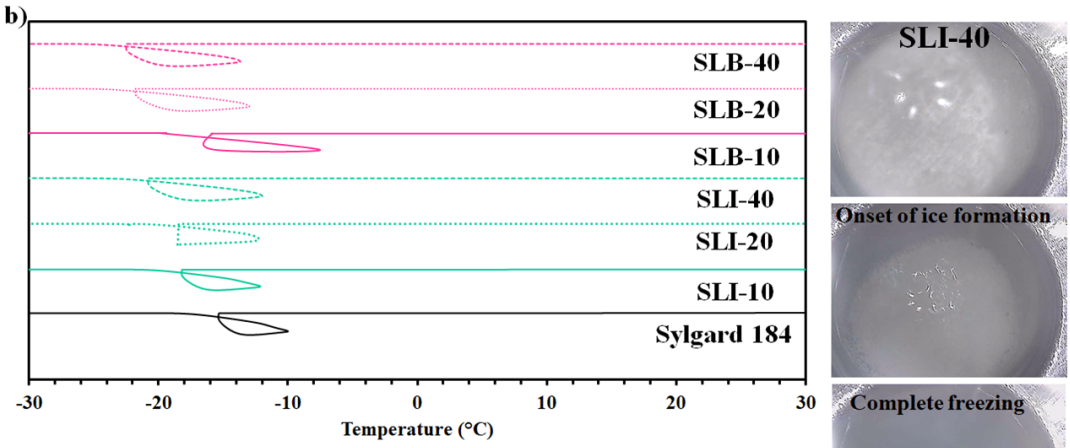

Silicon-based coatings	Sylgard 184	SLI-10	SLI-20	SLI-40	SLB-10	SLB-20	SLB-40
IF-temp (°C)	**-15.3 °C**	**-18.1 °C**	**-18.3 °C**	**-21.0 °C**	**-16.8 °C**	**-21.0 °C**	**-21.8 °C**

Figure 3-8: Delayed ice formation temperature on the surface of samples; (a) PU-based and (b) Silicon-based samples lacking and containing ILs in different percentages. Images

in right indicate top-down view of coated aluminum pans after placing water droplets during cooling measurements using a portable optical microscope in DSC.

A rise of 1°C in supercooling degrees can result in a notable reduction of the ice nucleation rate, potentially by an order of magnitude ranging from 2 to 3 [340,384]. A clear increase in the average freezing-delay times was observed due to the ILs diffusion, a lower freezing temperature and a slower ice formation time (Figure 3-9). It is interesting to note that addition of more ionic liquid (LI) to Sylgard 184 or PU samples significantly prolonged the time taken for the coatings to completely freeze, extending beyond the initial two-hour timeframe. The observation of longer ice formation times in samples containing ILs aligns with the results obtained through DSC measurements, specifically the IF-temp, and corroborates findings from the ion mobility study.

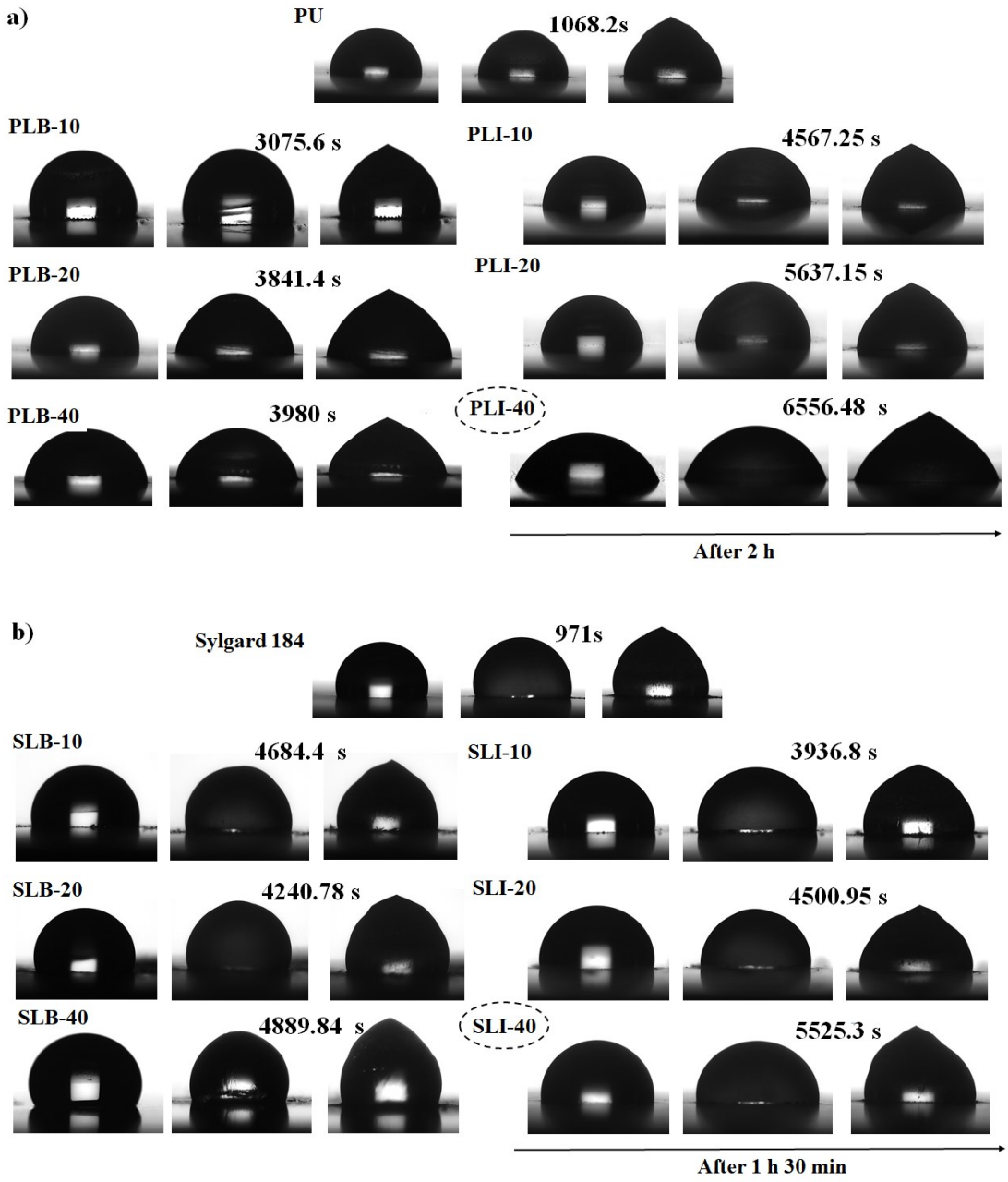

Figure 3-9: Delayed ice formation time on the surface of samples, as well as their form of frozen droplet; PU- and Silicon-based samples lacking and containing ILs in different percentages.

3.4.3.2 Ice adhesion strength

The push-off and centrifugal adhesion tests allowed us to delve into the subtle impact of introducing ILs on the ice adhesion strength of two distinct matrix types. The results

clearly show that the ice adhesion strength of both matrixes significantly declined when ILs were incorporated into the coatings. As illustrated in Figure 3-10a, the average ice adhesion strength diminished roughly from 160 to 20 kPa for silicon-based coatings and from 280 to15 kPa, for PU-based coatings when ILs were present. Likewise, the abrupt decline in ice adhesion strength of samples containing LI can be attributed to the higher number of available sites on the surface and stronger hydrogen-bond donor ability of LI (Video 1) [327]. It was also observed that PU-based coatings containing LI, including PLI-40 and PLI-10-NS, possess lower ice adhesion strength due to stronger hydrogen bonds formed by the matrix and the immiscibility of LI due to phase separation [27]. These findings support the greater effectiveness of LI in lowering the freezing temperature and postponing the time at which ice forms on the surface, particularly for PLI coatings. Moreover, it appears that the lower crosslink density of non-stoichiometric coatings facilitates chain movements and leads to more mobile ions. The lower surface elastic modulus and higher ion mobility (i.e., higher ionic conductivity for solutions containing released ILs) in non-stoichiometric coatings containing ILs contributed to a more significant mismatch in surface elastic modulus between ice and substrate, resulting in visibly lower ice adhesion strength compared to their stoichiometric counterparts [68]. It's noteworthy to emphasize that, among coatings with IL content at 10%, 20%, and 40%, the non-stoichiometric samples containing 10% ILs were specifically selected for a more detailed examination of how crosslink density influences ice adhesion strength.

Furthermore, according to the obtained adhesion strength of glaze ice, all graphs mostly followed the same trends as those shown for PLI samples with the push-off test (Figure 3-10b). The higher ice adhesion strength of coatings containing LB demonstrated

that whether in Sylgard 184 or PU, LB was not enough capable to completely detach ice on the surface.

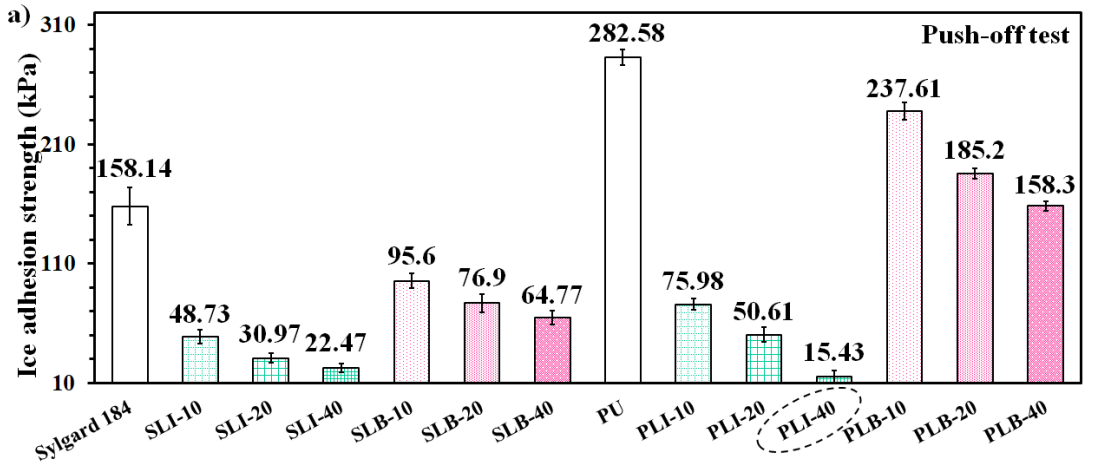

Ice adhesion strength (Kpa)	Sylgard 184	SLI-10	SLB-10	PU	PLI-10	PLB-10
Stochiometric	158.14±15.71	48.73±5.6	95.6±6.01	282.58±6.54	75.98±4.83	237.61±7.34
Non-stochiometric	140.89 ±7.26	41.59±3.52	76.28±3.81	220.27±8.57	38.93±5.73	153.08±5.49

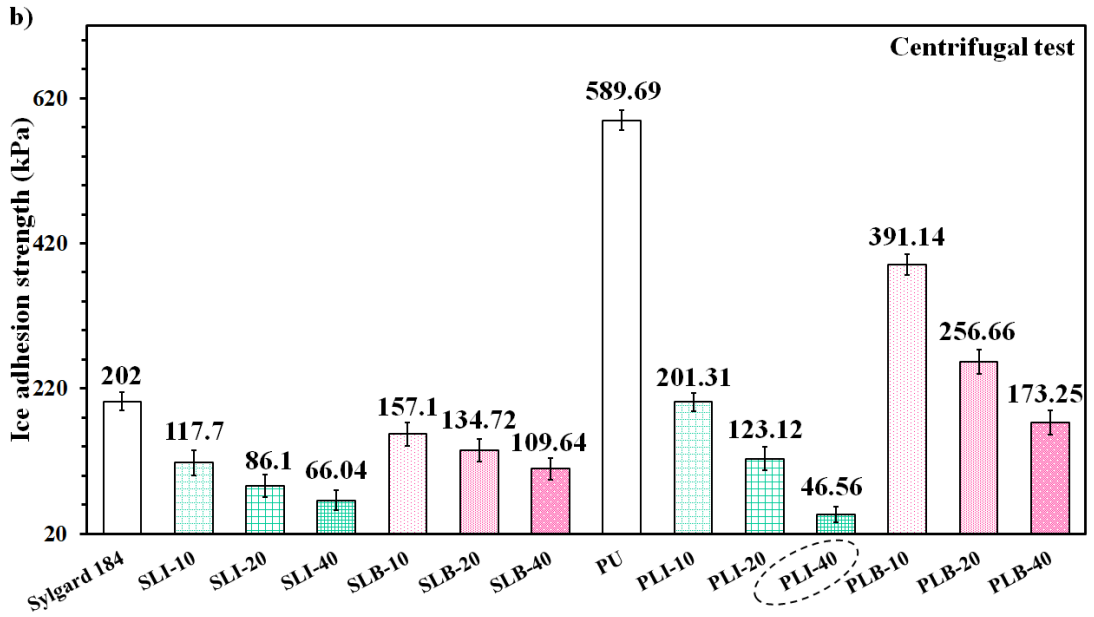

Figure 3-10: Ice adhesion strength of the designed coatings, obtained by (a) the Push-off test, and (b) the Centrifugal test.

Moreover, the ice adhesion strength of the coatings was assessed after 20 icing/de-icing cycles in the push-off test for both coatings when ILs are used, given that PU-based coatings are known to have excellent mechanical and weathering resistance. As can be seen in Figure 3-11, over the course of 20 icing/de-icing cycles, values for the ice adhesion strength of PU-based coatings did not vary significantly. During more than 20 icing/de-icing cycles, coatings SLI and PLI consistently exhibited ice adhesion values below 100 kPa. Notably, coatings containing LB demonstrated a faster increase in ice adhesion strength compared to other coatings over the same cycles [37].

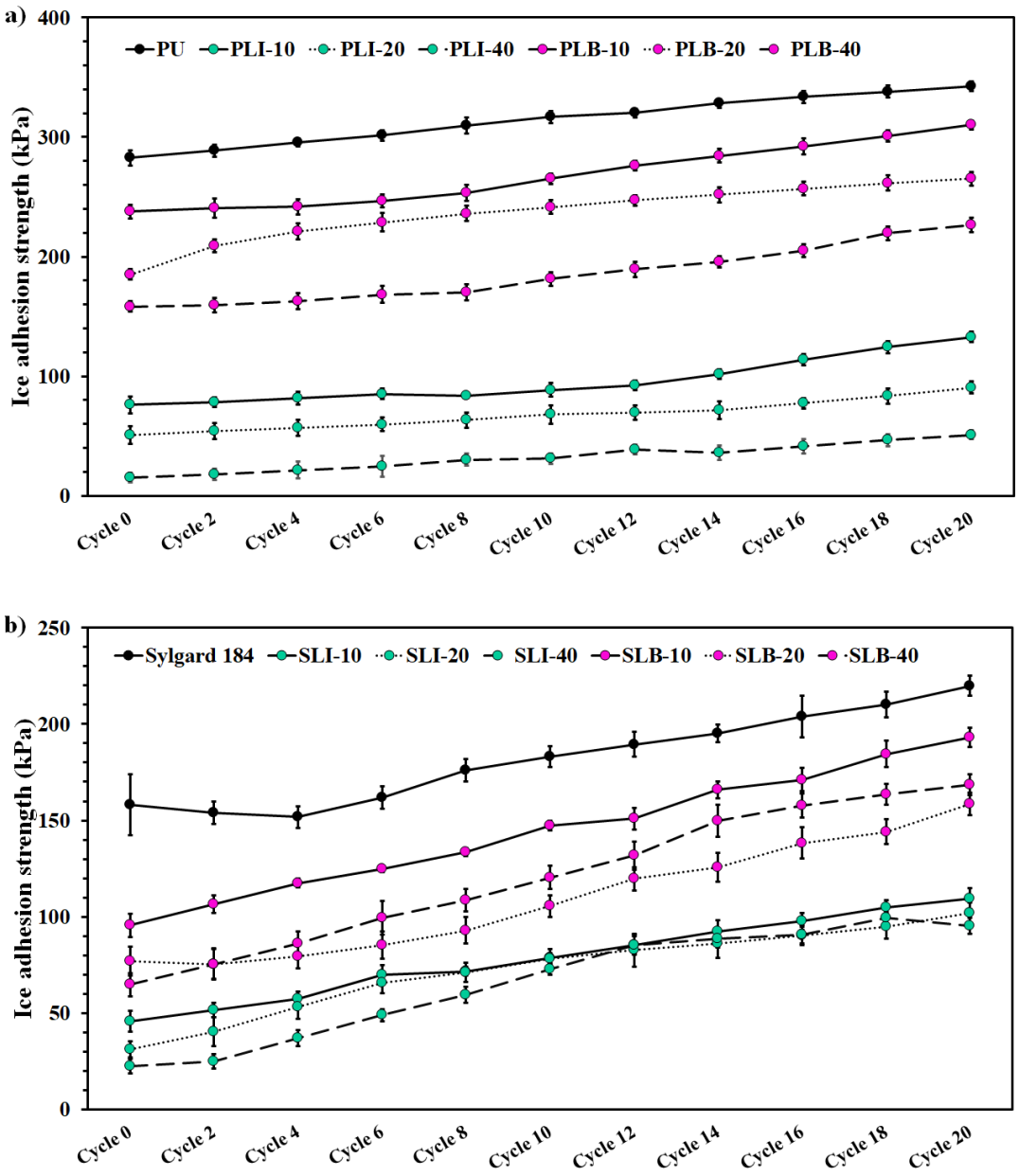

Figure 3-11: Ice adhesion strength of samples containing and lacking ILs, including (a) PU-based, and (b) Silicon-based coatings over 20 icing/de-icing cycles determined by the push-off test.

Figure 3-12 illustrates the proposed anti-icing mechanism of ILs. Weak interfaces characterized by disordered and short-term atomistic interactions, including van der Waals forces and hydrogen bonds, result from the presence of a disordered liquid-like layer at the

solid-vapor interface [17,293,342]. Manipulating interactions between water droplets and the interface surface through the formation of a quasi-liquid layer (QLL) leads to a reduction in ice adhesion strength [385]. The formation an ionic hydrogen-bond network at the interface between ILs and the water molecules may generate a QLL that may exhibit remarkable efficiency even at lower temperatures [37]. This is because ILs cannot be captured by ice crystals during freezing due to their size and asymmetry, unlike conventional antifreezing solid-state salts. Thanks to lower freezing temperatures caused by the diffusion of ILs into the water droplet, thus maintaining the water droplet in a liquid state for an extended period. Diffused ILs might also be rejected by the unfrozen liquid phase, replenishing the unfrozen interfacial liquid layer with a heightened ion concentration. During rapid freezing, a fraction of the liquid at the interface nucleates into a slushy mixture, and the temperature of the liquid layer rises due to the release of latent heat during the nucleation stage. On the other hand, large and asymmetric ILs can disturb the ordered crystalline structure of ice, then can regenerate the amorphous unfrozen interfacial layer and prevent further ice propagation and recrystallization, which in turn lowers ice adhesion strength [19,37]. Regarding the results determined by either push-off or centrifugal tests, remarkable abrupt of ice adhesion strength of PLI coatings indicated that the type of matrix and its interactions with IL enhance the ability of the LI within a hydrophilic matrix to donate more hydrogen to water, which further reduce the ice adhesion.

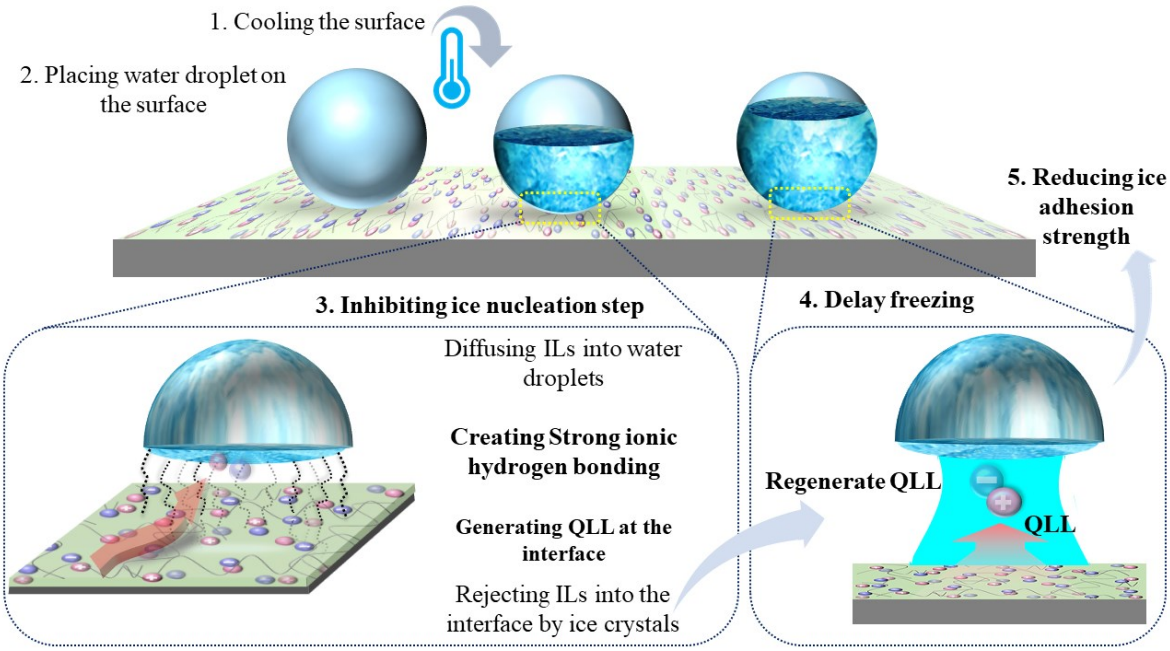

Figure 3-12: Schematic of proposed anti-icing mechanism of ILs.

Contrary to expectations based on higher water solubility, smaller anion size, lower steric hindrance, and lower freezing point of LB, observing an unexpected trend in its ice adhesion strength indicated that the matrix, alongside IL chemical structure, size, and concentration, emerged as a significant factor in ion mobility and migration to the surface. The dielectric findings, showing higher conductivity of PLI than SLI and the reference counterpart in subzero temperatures, correlates with the observed anti-icing behavior of LI, underscoring the crucial role of matrix type in influencing performance characteristics.

We utilized solid-state NMR spectroscopy to dissect the existence of the nonfrozen QLL at the interface between bulk water and coatings beneath low ice adhesion strength of especially PU-based containing and lacking ILs. Solid-state NMR spectroscopy serves as a highly effective method for identifying trace amounts of non-frozen water. Conventional ^{1}H NMR experiments face challenges in detecting solid ice due to its long T_1 and short T_2

relaxation times. In contrast, liquid water exhibits a readily detectable ^{1}H signal using this method [344]. The ^{1}H spectra of PU + water, PLI-10 + water, and PLB-10 + water samples were initially recorded at 276 K to assess the characteristics of bulk water before freezing commenced, as illustrated in Figure 3-13(a-c).

The water ^{1}H chemical shifts were approximately 5.0 ppm, with consistent line shapes observed in all samples. The strength of the water ^{1}H signal in PU and PLB samples fell significantly following further cooling to subzero temperatures (253 K) and allowing for a 3-hour stabilization period. The rise in water ^{1}H chemical shifts of the coatings as temperature drops is a remarkable observation. This behavior can be associated to the strengthening of hydrogen bonds at lower temperatures, which affects the shielding and deshielding of water protons [17]. The identified nonfrozen water layer at temperatures as low as -20 °C functions as a self-lubricating interface, contributing significantly to the observed low ice adhesion strength on coating surfaces containing ILs. As the temperature drops below 0 °C, the signal strength of nonfrozen water, an indicator of the quantity of nonfrozen water, rapidly diminishes for PU. Nonfrozen water may significantly drop and finally freeze entirely at a crucial subcooling threshold, causing a quick and large rise in ice adhesion strength on PLB as well. The persistence of this signal for PLI at 253 K, on the other hand, encourages the presence of a thicker QLL owing to its greater hydrogen-bonding capacity (Figure 3-13d) [17,37].

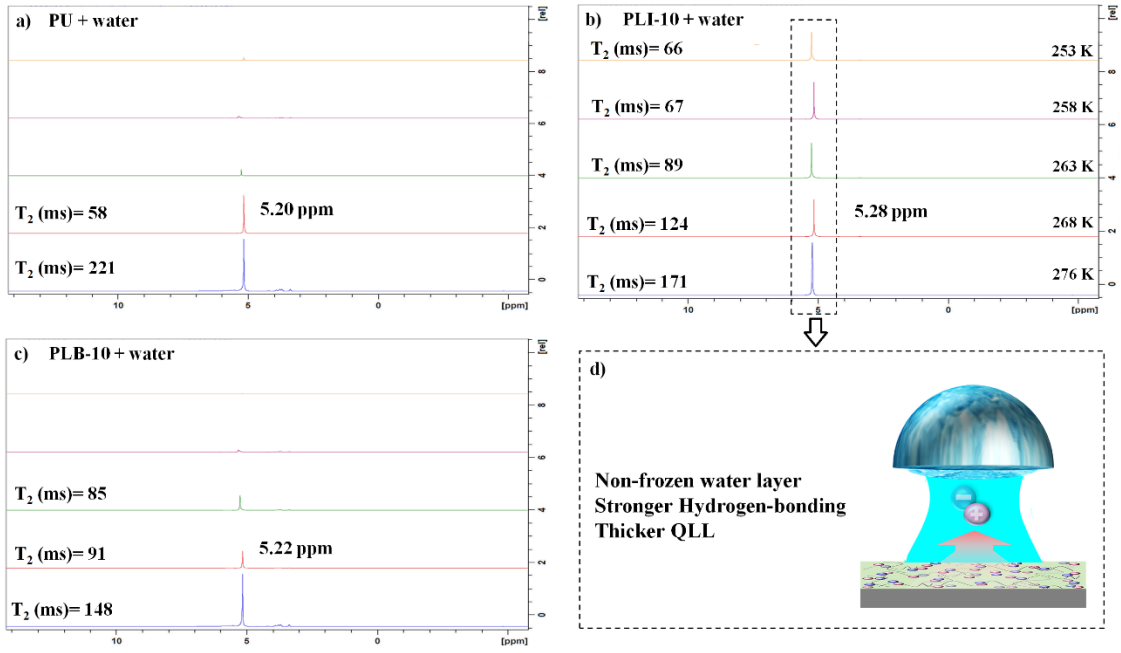

Figure 3-13: ^{1}H spectra of (a) PU + water, (b) PLI-10 + water, and (c) PLB-10 + water between 276 K (blue) and 253 K (yellow) as well as T_2 relaxation data, obtained by SS-NMR spectroscopy. (d) Schematic of formation of a thicker Quasi-Liquid Layer (QLL) at the int

Given that water molecules bonded near the interface possess much lower configurational entropy than bulk water, resulting in a large rise in water viscosity. Measuring ^{1}H T_2 relaxation time, which is inversely linked to viscosity, can quantify the increasing in viscosity. Notably, the results obtained in Figure 3-13 revealed a higher hydrogen-bond accepting capacity of LB for locally bound water at the interface, particularly up to 263 K. Furthermore, in conjunction with the presence of the water ^{1}H signal up to 253 K, the more decrease in T_2 relaxation time for PLI further affirms the stronger hydrogen-bond donor ability of ILI to local interfacial water. On the other hand, S.G. Moghadam et al. conducted solid-state NMR spectroscopy on silicon-based coatings incorporating ILs. When compared to the ^{1}H NMR spectra of PU-based coatings, the existence of the water ^{1}H signal for PU at

268 K and the lower T_2 relaxation time of PLI from 276 K to 253 K confirm the stronger hydrogen-bonding donor ability of LI within PU than Sylgard 184 [37].

3.4.4 Ice adhesion strength against icing/de-icing cycles and weathering condition

Where coatings are applied in outdoors and aromatic ILs are present, the weathering resistance of surfaces can also be negatively impacted by UV radiation and humidity. Here, we assessed how accelerated weathering conditions affect the ice adhesion strength of stoichiometric and non-stoichiometric surfaces after 20 icing/de-icing cycles. As shown in Figure 3-14a and Figure 3-14b, it can be stated that PU-based coatings offered more resistance capability to accelerated UV light and high humidity, representing about 1.5 years of real outdoor conditions. Non-stoichiometric coatings with lower crosslink density and reduced surface hardness exhibited lower ice adhesion strength, as indicated in the table of Figure 3-14a. However, PU coating (hard surface) exhibited higher ice adhesion strength compared to Sylgard 184 coating (soft surface) because of their nature [68,386]. It's important to highlight that the ice adhesion strength and surface roughness of silicon coatings increased more rapidly than PU-based coatings following de-icing cycles, attributable to the weaker mechanical properties of silicon coatings. For example, the ice adhesion strength of SLB coating reached to the reference Sylgard 184.

Hence, it is unsurprising that the yellowness index of IL-containing coatings increased due to aromatic structure of the two ILs, as shown in Table A-II. 2. Moreover, the surface topography and structures of the heterogeneous fabricated surfaces could also be revealed by 3D profilometry. The surface roughness (S_q, root mean square roughness parameter), as shown by 3D profile maps of samples containing ILs, (LI or LB) increased over the PDMS and PU reference coatings. It is of interest that the S_q of all silicon coatings

increased further after 20 de-icing cycles given intrinsic low modulus elastic of Sylgard 184. The higher surface roughness of SLB samples evidentiate higher ice adhesion strength. Additionally, because of their lower crosslink density, non-stoichiometric samples of either silicon-based or PU-based coatings showed less surface hardness. Due to the intrinsic elasticity of silicon-based coatings, Sylgard 184 samples lacking and containing ILs had lower hardness as compared to PU-based samples. The inherent plastization properties of ILs resulted in reduced surface hardness for both sets of samples incorporating ILs, in contrast to the reference samples without ILs (Table A-II. 2) [387,388].

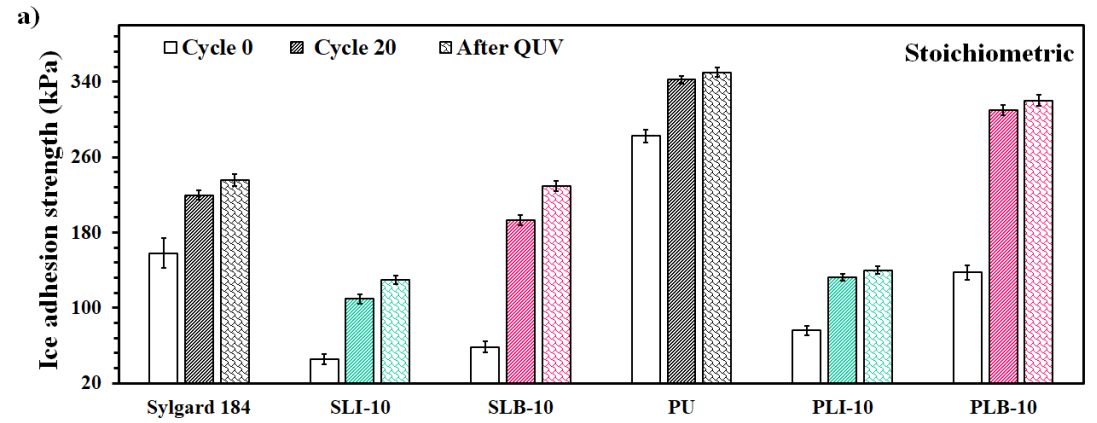

Ice adhesion strength (Kpa)	Non-Stoichiometric					
	Sylgard 184-NS	**SLI-10-NS**	**SLB-10-NS**	**PU-NS**	**PLI-10-NS**	**PLB-10-NS**
Cycle 0	140.89 ±7.26	41.59±3.52	76.28±3.81	220.27±8.57	38.93±5.73	153.08±5.49
Cycle 20	189.63 ±4.12	92.13±6.3	168.32±5.25	290.45±4.13	62.3±3.59	290.56±5.09
After QUV	199.23 ±4.3	105.63±5.352	209.04±5.5	330.71±5.05	98.36±3.9	300.12±5. 9

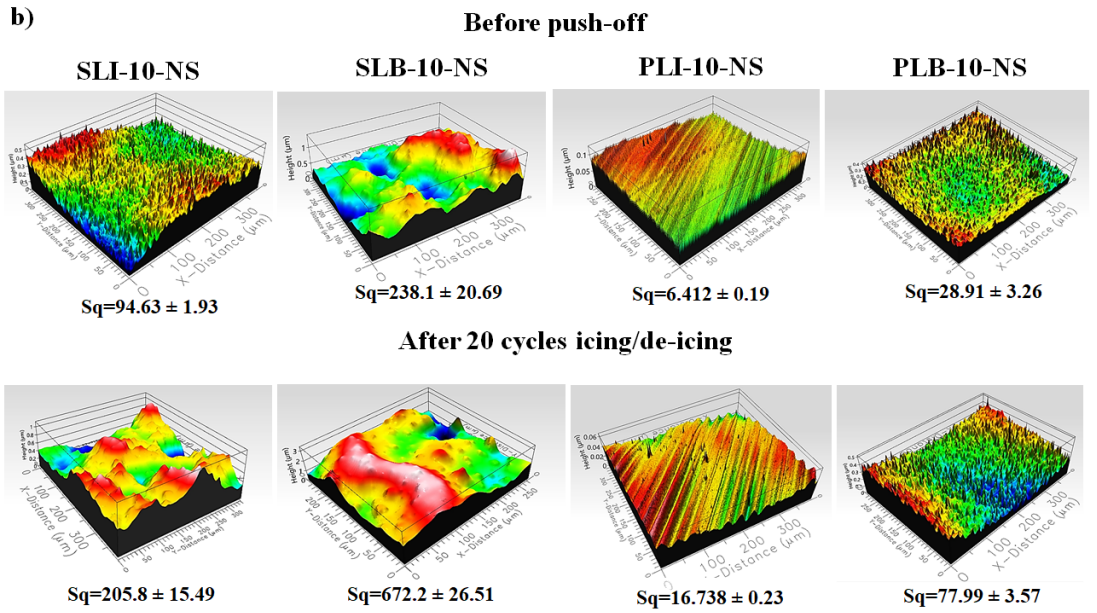

Figure 3-14: (a) The ice adhesion strength of coatings exposed 20 icing/de-icing cycles after and before QUV obtained by push-off test for non-stoichiometric and stoichiometric coatings containing 10 wt.% of ILs after QUV, and (b) 3D profile maps of coatings samples

3.4.5 Time to First Frost Formation (TFF) under Freeze-Thaw cycles

The longevity of non-stoichiometric and stoichiometric coatings with and without ILs was evaluated against frost formation under freeze–thaw. The time to first frost formation (TFF) of samples was measured after 7 freeze–thaw cycles at freezing temperature of -20°C. As illustrated in Figure 3-15a and Figure 3-15b, upon reaching the desired temperature at the test plate (t=0), visual differentiation of silicon-based or PU-based coating samples became apparent. This distinction occurred simultaneously with the reference being covered in frost, as well as when frost formed on the surface of coatings containing LB. Notably, coatings containing LI demonstrated effective frost formation delay even after undergoing seven repeated freeze-thaw cycles. Figure 3-15a also shows that non-stoichiometric and stoichiometric of PLI-10 samples had the highest TFF and greater endurance against frost formation, than the other coatings [19].

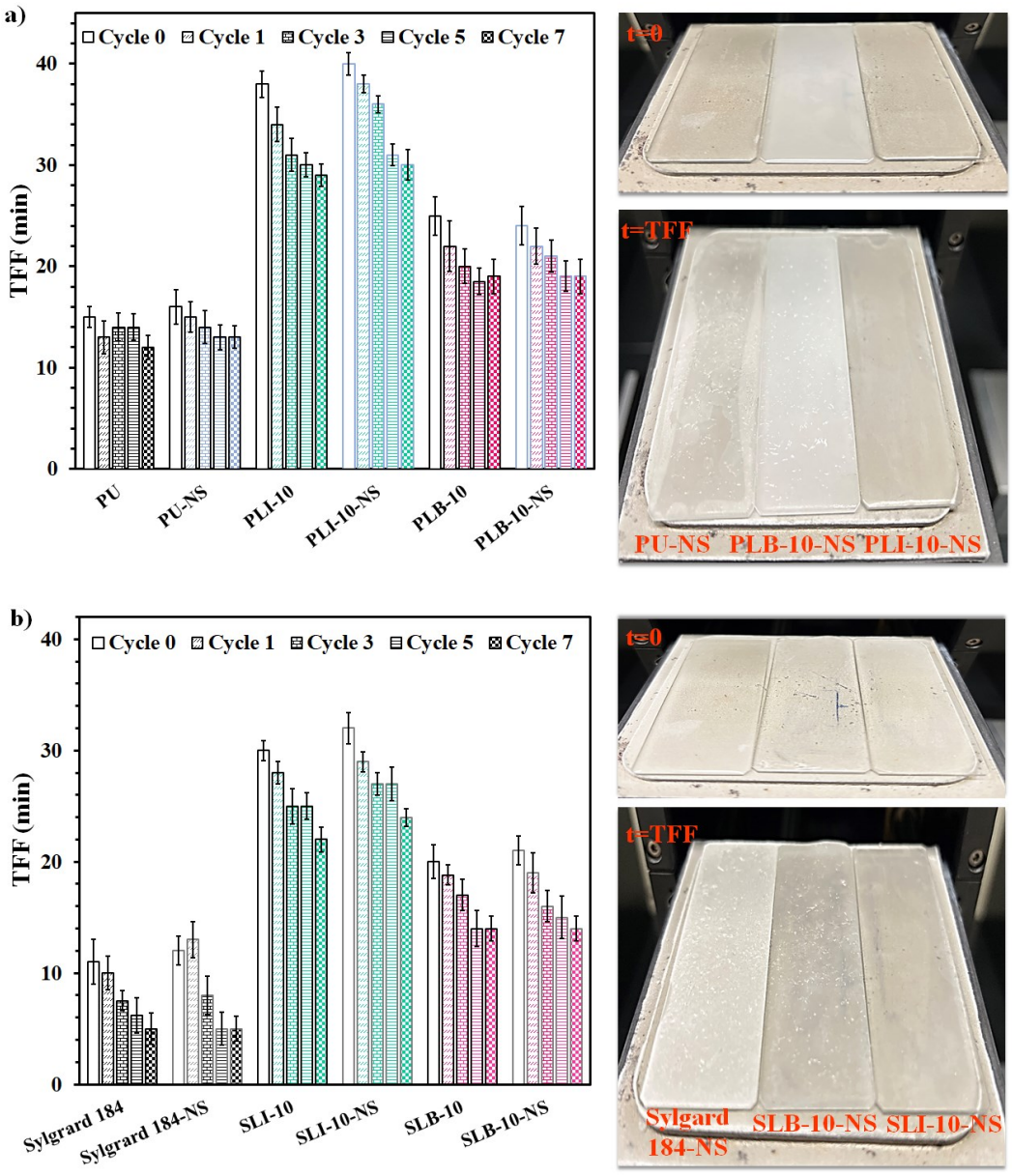

Figure 3-15: Time to first frost formation of (a) PU-based and (b) silicon-based samples as well as their images after 7 freeze-thaw cycles.

3.5 Conclusion

This study investigated key factors influencing ion mobility, particularly exploring the impact of IL physiochemical properties and matrix hydrophilicity/hydrophobicity. PU and Sylgard 184 were chosen as hydrophilic and hydrophobic matrixes, respectively. PLI

and SLB coatings exhibited lower and higher water contact angles, indicating anion influence on surface wettability. PLI's surface experienced a remarkable drop in ice formation temperature to -23.5 °C, and very low ice adhesion strength of 15 kPa, due to creation of stronger ionic hydrogen-bond network and thicker QLL within PU matrix, as revealed by solid-state NMR spectroscopy. As IL molecules disperse between polymer chains on the surface, greater distances are created between polymer chains, which in turn generates IL conduction pathways. As regards the dielectric spectroscopy findings, more stable conductivity at low temperatures yielded accurate picture of ion mobility and uniform distribution of these charge carriers which may guarantee stable anti-icing performance. In particular, the PLI coating showed the most stable anti-icing behavior. Comprehensive analysis of ILs released from non-stoichiometric coatings, UV absorbance, and ionic conductivity provided evidence for superior mobility of LI compared to LB. Over icing/de-icing cycles and exposure to weathering and freeze-thaw cycles, LI-containing coatings stabilized their ice adhesion strength, particularly PU-based coatings. These findings highlight the pivotal role of matrix and IL selection in advancing coatings for extreme cold conditions. Future research could explore aliphatic-based ILs and enhance mechanical durability in icing conditions.

Acknowledgements

The authors acknowledge all support from the Natural Sciences and Engineering Research Council of Canada (NSERC) and Université du Québec à Chicoutimi (UQAC). The authors also wish to thank Caroline Blackburn in Laboratoire International des Matériaux Antigivre (LIMA-UQAC), for helping with the ice centrifugal test. The authors

would also like to express their gratitude for Professor Ramzi Zarrougui in Chemistry department of UQAC in conducting and helping ionic conductivity measurements.

CHAPTER 4

4. INNOVATIVE ICE MITIGATION: EXPLORING THE POTENTIAL OF CHOLINE-BASED DEEP EUTECTIC SOLVENTS AND IONIC LIQUIDS SYNERGIES

4.1 Introduction

The development of effective anti-icing coatings that perform well in extremely low temperatures is an ongoing challenge, especially for applications in harsh environments. Among emerging solutions, deep eutectic solvents (DESs)—a subset of ionic liquid (IL) analogues—have gained considerable interest due to their unique and adaptable properties. Despite extensive exploration of DESs in various applications, their potential in anti-icing technology remains largely unexplored. This research focuses on the promising attributes of choline-based DESs, which offer significant potential for anti-icing through their intrinsic hydrogen-bonding properties and structural versatility.

Choline-based DESs are formulated by pairing hydrogen bond acceptors (HBAs) with various hydrogen bond donors (HBDs), resulting in solvents that are low in toxicity, highly thermally stable, and biodegradable. These characteristics make DESs environmentally friendly alternatives to conventional solvents, distinguished by desirable

physical properties such as density, viscosity, surface tension, and conductivity [389]. This combination of properties, governed by the specific nature of the HBAs and HBDs, allows DESs to exhibit favorable characteristics, including non-flammability, thermal stability, and biodegradability. These properties, coupled with their affordability and ease of preparation, make DESs ideal candidates for applications across several fields, from selective separations to conductive gels and electrochemical systems designed for cold environments [390]. The exceptional nature of DES properties presents numerous avenues of exploration to enhance existing processes and discover novel applications for these solvents.

DESs were originally developed as an environmentally friendly subset of ionic liquid analogues. While ILs and DESs share some similarities, they also exhibit unique characteristics that highlight their fundamental differences [30,31,391–393]. DESs, distinguished by their unique attributes, are composed through the complex interaction between hydrogen bond acceptors (HBAs) and hydrogen bond donors (HBDs). This hydrogen-bond network creates a supermolecular structure with melting and freezing points lower than those of the individual components [226,257]. DESs are capable of reducing lattice energy due to intermolecular forces, such as hydrogen bonds and ion-dipole interactions, within the complex ions formed during their assembly [228,394]. For instance, a choline-based DES made by combining choline chloride and urea in a 1:2 molar ratio achieves a melting point of 12 °C, significantly lower than the individual melting points of 302 °C and 133 °C, respectively [31]. The versatility of DESs extends across multiple research fields due to their affordability and simple preparation. DESs have shown outstanding sustainability as media for various separation processes, displaying a high degree of selectivity. For instance, DESs have proven effective—often outperforming ILs—in

separating aromatic and aliphatic compounds in hydrocarbon mixtures, as well as in dissolving metals and oxides [395,396]. Their low melting points and high conductivity make them promising for applications in developing electrochemical systems designed to operate efficiently in cold environments. The robust electrochemical stability of DESs suggests a potential use as safe electrolytes in electrochemical devices such as batteries [266]. Furthermore, DESs show utility in fabricating conductive gels and elastomers, especially for flexible strain sensors [33,34,270–272,397], and Triboelectric Nanogenerators [35]. This versatility has attracted the interest of various scientific communities and industries for use in outdoor and harsh environments [269,398–400].

Drawing inspiration from the design of ice-skating blades, a pre-melted layer on the surface effectively reduces ice adhesion strength and prevents ice buildup [18,53,104,401–404]. Both hydrogen-bonding and hydrophobic groups play a critical role in modulating the dynamics of this interfacial water [197,405–407]. Short-term atomistic interactions in DESs and ILs, combined with hydrogen bonding, enable a range of applications, including artificial intelligence, energy storage, and bioinspired anti-freezing surfaces [36,273–278].

However, a knowledge gap still exists regarding the anti-icing properties of DESs [32]. Additionally, there is a limited body of work exploring the anti-icing capabilities of ILs [37], particularly choline-based ILs. Here, we explore the anti-freezing capabilities of DESs by synthesizing and characterizing choline-based ILs that have both hydrophilic and hydrophobic anions. These ILs are then incorporated into an industrial coating, and the optimal IL-containing coatings are selected for the addition of DES. Through examining the thermal behavior of DESs, our focus shifted on the combination of choline-based DESs (which contain diverse hydrogen-bond donors), with the synthesized ILs. We aimed to assess

how this combination impacts the system's hydrogen-bond donor capacity. We also evaluate the mechanical properties of the coatings in terms of their resilience against tension and weathering conditions. Our goal is to determine how these compositional modifications influence the anti-icing properties of the coatings.

4.2 Methodology

4.2.1 Materials

For the synthesis of choline-based ILs, we acquired choline chloride (ChCl, ⩾98%) and ammonium nitrate (99.99%) from Sigma Aldrich (USA), and lithium bis(trifluoromethanesulfonyl)imide (LiTFSI) (99.99%) was obtained from Goldbio (USA). The polyol resin used for preparing polyurethane (PU) coatings produced using acrylic copolymers (WorléeCryl® A 2445), with a solid content of 59%–61%, and a 4.5% hydroxyl (on solid), was supplied by Worlée Industries (Germany). Covestro Co. (Germany) provided the aliphatic polyisocyanate resin composed of hexamethylene diisocyanate (HDI) (Desmodur® N 75 BA/X), with an NCO content of 16.5% ± 0.3%, serving as the hardener. Solvents, including xylene (99%), n-butyl acetate (99%), isopropanol (99%), and dichloromethane (99%), were purchased from Thermos Fisher Scientific (USA). For the DES preparation, pure ethylene glycol (99.9%, EG) and glycerol (99.9%, GL) were obtained from Sigma Aldrich (USA) and Thermo Fisher Scientific (USA), respectively. All substances were of analytical grade and used as received without additional purification.

4.2.2 Synthesis of the ILs

4.2.2.1 Choline nitrate ($ChNO_3$)

To prepare $ChNO_3$, we dissolved 100.0 mmol of ammonium nitrate (NH_4NO_3) and 13.62 mmol of choline chloride (ChCl) in 100.0 ml of dry isopropanol, achieving a 1:1 molar ratio. The mixture was heated to 60°C under reflux for 120 minutes with continuous stirring, forming a white precipitate of ammonium chloride (NH_4Cl) as a reaction indicator. After completion, the precipitate was filtered, washed with isopropanol, and the solvent was removed using a rotary evaporator. The residue was purified with activated carbon and underwent three evaporation cycles, achieving a conversion rate of over 85%.

4.2.2.2 Choline bis(trifluoromethanesulfonyl)imide (ChTFSI)

To synthesize ChTFSI, 0.143 mmol of choline chloride (ChCl) was dissolved in 100 ml of deionized water, followed by the addition of 0.143 mmol of lithium bis(trifluoromethanesulfonyl)imide (LiTFSI), maintaining a 1:1 molar ratio. The mixture was stirred at room temperature for 4 hours, achieving over 85% conversion to ChTFSI. The reaction mixture was then extracted with 20 ml of dichloromethane (DCM), and the DCM layer containing ChTFSI was separated, washed with deionized water to remove residual ions, and dried using a rotary evaporator at 35 °C. The product was further purified by filtering it through anhydrous sodium sulfate (Na_2SO_4) three times to ensure high purity. Figure A-III. 1a and Figure A-III. 1b present the IL synthesis procedure.

4.2.3 Preparation of the DESs

Choline chloride (ChCl) was first dried in a vacuum oven set to 50°C overnight under reduced pressure to eliminate any residual water and moisture. This drying process is crucial

to ensure that the ChCl is free from impurities and moisture. To synthesize the DESs, ChCl was combined with ethylene glycol (EG) or glycerol (GL) in a 1:2 molar ratio. The components were then mixed thoroughly and heated to 80°C while stirring continuously. This heating and stirring process was maintained until the mixture turned into a homogeneous, clear, colorless liquid, indicating that the DES had formed successfully. Once the DES was fully synthesized, it was transferred to a vacuum desiccator. The desiccator helped to further remove any remaining moisture and protect the DES from atmospheric humidity, ensuring its stability for future use.

4.2.4 Fabrication of Polyurethane coatings

4.2.4.1 IL-containing polyurethane coatings

Polyurethane (PU) coatings were prepared by incorporating synthesized ionic liquids (ILs), either $ChNO_3$ or ChTFSI, into a polyurethane resin system. Polyol and polyisocyanate resins were first mixed in a 100:40 weight ratio for uniformity. The ILs were then added in varying weight percentages along with solvents (n-butyl acetate and xylene in a 60:40 ratio, totaling 20 wt.% of the mixture) to adjust viscosity. After blending, the coatings were applied to substrates with a wet film thickness of 500 μm and cured at room temperature for seven days. The final dry thickness was 200 ± 20 μm, confirmed with precision thickness gauges. Free-film samples were also prepared on non-stick surfaces for further testing.

Each sample was labeled according to the type and concentration of the IL used, as outlined in Table 4-1.

Table 4-1: Composition of each formulation for fabrication of PU-based coatings containing ILs (g).

Samples	Polyol (g)	Polyisocyanate (g)	$ChNO_3$(g)	ChTFSI (g)	Solvent (g)
PU	100	40	-	-	20
PCNO3-10	100	40	7	-	20
PCNO3-20	100	40	14	-	20
PCNO3-40	100	40	28	-	20
PCTFSI-10	100	40	-	7	20
PCTFSI-20	100	40	-	14	20
PCTFSI-40	100	40	-	28	20

4.2.4.2 Polyurethane coatings containing IL and DES

PU coatings containing both ILs and DESs were prepared using a modified protocol. First, DESs were synthesized and combined with an optimized percentage of ILs. This IL-DES mixture was stirred for 10 minutes to ensure homogeneity. Separately, polyol and polyisocyanate resins were mixed to form the PU resin. The IL-DES blend, constituting 10 wt.% of the final formulation, was added to the PU resin and mixed thoroughly with a homogenizer at 500 rpm for 10 minutes. To adjust viscosity for application, 10 wt.% of n-butyl acetate and xylene (60:40 ratio) was added. The coatings were applied to substrates, labeled according to the type of hydrogen bond donor (HBD) in the DES, to facilitate identification and comparison during testing, as detailed in Table 4-2. This labeling allowed for easy identification and comparison of the different coating formulations during subsequent tests and analyses.

Table 4-2: Composition of each formulation of PU-based coatings containing DES (g).

Samples	Polyol (g)	Polyisocyanate (g)	$ChNO_3$ (g)	ChTFSI (g)	Solvent (g)	EG-DES (g)	GL-DES (g)
PU-EG	100	40	-	-	10	10	-
PCNO3-20-EG	100	40	14	-	10	10	-
PCTFSI-10-EG	100	40	-	7	10	10	-

PCTFSI-10-GL	100	40	-	7	10	-	10

4.2.5 ILs Characterization

4.2.5.1 Nuclear Magnetic Resonance (NMR) spectroscopy

The NMR spectra of both synthesized ILs were recorded using a Bruker Avance 400 spectrometer (400.13 MHz for 1H and 100.61 MHz for 13C, Bruker, Milton, ON, Canada) equipped with a 5 mm quadruple nuclear probe (QNP). All spectra were acquired in CDCl3 and chemical shifts were reported in ppm (δ) relative to TMS. The ^{1}H and ^{13}C spectra were obtained using the Hahn echo experiment and processed using Bruker TopSpin software.

4.2.5.2 Fourier Transform Infrared (FTIR) spectrometer

The FTIR spectra of the synthesized ILs were recorded and analyzed using a Fourier Transform Infrared (FTIR) spectrometer (PerkinElmer, Spectrum Two, USA) in attenuated total reflection (ATR) mode across the infrared range of 400–4000 cm^{-1}.

4.2.6 DES characterization

The thermal behavior of each eutectic mixture was assessed with differential scanning calorimetry (DSC, ± 0.05 ℃) via a TA Instrument Q250 differential scanning calorimeter (DSC Q250, TA Instruments, New Castle, DE, USA). A sample of each mixture was weighed into an aluminum pan and then hermetically sealed. Each sample was initially cooled to −90 °C and heated to 40 °C at 2.5 °C/min, with a 10 min hold at each extreme. As the rate of heating/cooling can influence observed phase behavior, we selected 2.5 °C/min as a suitable intermediate rate that would capture the thermal behavior most relevant to possible applications. Each cool/heat cycle was repeated three times. Data were evaluated using TA

software to extract thermal transition information including the temperature of freezing, melting, and glass transitions. Because of kinetic effects such as supercooling, the thermal behavior is reported on the basis of the heating cycles. The glass transition is reported as the onset of melting of the glass phase, and the melting point is reported as the onset of the highest observed temperature melting point.

4.2.7 Surface characterization

4.2.7.1 Surface chemistry

The chemical composition of the IL- and DES-containing coatings was characterized using a FTIR spectrometer (PerkinElmer, Spectrum Two, USA) in ATR mode across the infrared range of 400–4000 cm^{-1}. The FTIR spectroscopy was conducted on a diamond surface that was thoroughly cleaned with isopropyl alcohol prior to the start of the test. The FTIR measurements were performed with a resolution of 4 cm^{-1}, and each spectrum was recorded three times to ensure reliability.

4.2.7.2 Contact angle measurements

The interplay between water contact angle (WCA) and ice adhesion strength reflects the intricate atomistic interactions governing the relationship between water droplets and a surface. To explore the impact of various ILs on wettability, we conducted a comprehensive analysis of the coatings' wettability properties. WCA was measured using the sessile drop method with a Kruss™ DSA100 goniometer (KRÜSS Scientific, Hamburg, Germany), maintaining a room temperature of 25 ± 0.5 °C. For static WCA measurements, a 4 µL distilled water droplet was delicately deposited onto the sample surface, and the ADVANCE drop shape analysis software facilitated the quantification of WCA. Additionally, the Kruss

apparatus, equipped with a tilting table, was used to assess the sliding angles (SAs) of water droplets on the surfaces. A 35 μL water droplet was positioned on the samples affixed to a tilting stage. The stage was inclined to 60°, tilting at 60°/min, until the droplet initiated sliding or rolling off. SAs were calculated as the stage angle 0.5 s before the onset of droplet sliding. Both WCA and SA were determined using the tangent and ellipse (tangent) approximation methods, where the fitting approximation method serves as the mathematical function to describe the curvature of the drop shape.

4.2.7.3 Microscopy

To characterize the coating microstructure, we conducted scanning electron microscopy (SEM; JSM-6480 LV SEM, JEOL Japan). This analysis focused specifically on coatings containing DES. Additionally, SEM with Energy Dispersive X-Ray (EDX) analysis was utilized to further characterize F, and N elements on the surface of coatings. Prior to imaging, the samples underwent sputter coating with a thin platinum film.

4.2.7.4 Surface roughness

Surface roughness was assessed using an optical profilometer (Profilm3D Filmetrics®, USA), which integrated white light interferometry (WLI) to measure surface profiles and roughness with a precision of 0.05 μm. Additionally, we used the phase-shifting interferometry (PSI) option to measure smooth surfaces at the Angstrom level with a precision of 0.001 μm. These measurements covered an area of 400 × 300 μm, and six randomly selected locations were scrutinized for each sample.

4.2.8 Anti-icing Properties

4.2.8.1 Ice formation temperature

The impact of IL and DES types, as well as their respective proportions, on the ice formation temperature of the formulated coatings was assessed utilizing a TA Instrument Q250 DSC (DSC Q250, TA Instruments, New Castle, DE, USA) within a heating range from 40 to −40 °C (± 0.05 °C). For this procedure, a 5 mg droplet of deionized water was positioned on a DSC Tzero aluminum pan covered by a thin layer of each coating (thickness 200–250 μm) and then sealed with a lid. The prepared sample was initially cooled at a rate of 5 ℃/min from 40 to −40° C, and this process was repeated three times.

4.2.8.2 Ice adhesion strength

The ice adhesion strength of the samples was assessed through a push-off test (Figure A-III. 2). In this test, conducted in a cold chamber at −10 °C, a 1.5 cm diameter cylindrical plastic mold was positioned on the surface and filled with deionized water, allowing an ice cylinder to form over 24 h. To measure the force required to detach the ice cylinders from the coating surface, a digital force gauge (FG-3005, Shimpo Instruments, Lynbrook, NY, USA) was utilized. Using a remote computer-controlled interface, the force gauge recorded the shear force until the ice detached from the surface. The force meter probe moved toward the cylindrical column at a rate of 0.05 mm/s and applied a force until the frozen cylinder separated from the sample surface. Consequently, the adhesion stress was computed by dividing the maximum force by the area subjected to icing.

4.2.8.3 Solid-state NMR spectroscopy

Solid-state NMR spectroscopy confirmed the presence of the nonfrozen quasi-liquid layer (QLL) at the bulk water–coating interface, particularly in samples containing DESs. To prepare the SS-NMR samples, thin films were meticulously cut into small fragments,

approximately 1 mm in length. Around 70 mg of these fragments were loaded into rotors, each of which was then filled with 35 mg of deionized water. The rotors were sealed and weighed before and after each experimental run to monitor and ensure there was no loss of water due to dehydration. The water content was further analyzed by recording a ^{1}H NMR spectrum at room temperature before and after each series of experiments. Spectra were obtained using a Bruker Avance III HD spectrometer with a magnetic field strength of 9.4 T, corresponding to a ^{1}H Larmor frequency of 400.1 MHz, following the procedure described by Chen et al. [17]. A double resonance 4 mm Magic-Angle Spinning probe was employed, with the rotors spinning at 4 kHz. Each spectrum was acquired using a single 2.9 μs 90° pulse (with a radiofrequency field of 85 kHz), a spectral width of 8 kHz (20 ppm), an acquisition time of 1 s, and a recycle delay of 5 s. T_2 transverse relaxation times were measured using a rotor-synchronized Hahn echo sequence with interpulse delays ranging from 500 μs to 1 s. For single pulse spectra, 64 scans were performed, and for T_2 measurements, 32 scans were used. T_2 values were derived by fitting the echo intensities to a single exponential decay model whenever the bound water peak intensity was adequate. The amount of free water was quantified at each temperature by integrating the free water peak (around 5.1 ppm) and normalizing it against the integral of the PDMS CH_3 peak (0.18 ppm). Temperature calibration was performed before the experiments at the specified spinning frequency, and samples were allowed to equilibrate for 3 hours at each temperature. Temperature stability during experiments was maintained within ±0.1 °C. T_2 measurements and ^{1}H spectra were obtained using the Hahn echo experiment and processed with Bruker TopSpin software.

4.2.8.4 Anti-frosting capacity

The anti-frosting capabilities of the formulated DES-containing coatings were investigated using a cold chamber equipped with a programmable temperature and humidity device featuring an IR system (see Figure A-III. 3). The coatings were directly adhered to the Peltier (cooling stage) set at −20 °C. Anti-frosting performance was assessed in a chamber equipped with an air distribution system, capable of cooling the air to 0.0 ± 0.5 °C and maintaining this temperature. Airflow was measured using a suitable anemometer or velometer (±0.05 m/s). Humidity was generated through a saturated water vapor generator and monitored by a calibrated humidity sensor. The humidity generator was designed to achieve a minimum of 80% RH when the air temperature reached 0 °C. Prior to testing, the samples were ensured to be free of all visible contamination. Once the test plate reached the desired temperature, coating samples were positioned onto the Peltier stage, and digital images were captured every 15 min to visually assess their anti-frosting capacity. This procedure was repeated seven times for each series to evaluate their ability to delay frost formation. To determine the surface temperature of the samples, we utilized a FLIR T1030sc camera equipped with a 50 μm close-up lens, which was connected to a standard 28° IR lens to enhance optical zoom capabilities. This camera facilitated precise measurement of surface temperature, with each pixel serving as an individual thermal recorder, ensuring detailed analysis. Additionally, an Optris PIX infrared camera (Germany) was employed to continuously monitor sample temperatures during the test.

4.2.9 Mechanical characterization

4.2.9.1 Tensile strength

The tensile test was conducted at room temperature using a TA.XTPlus 100 (TA.TX Plus100C, Stable Micro System, Godalming, UK) machine with a 5 kg load cell. The free

films used for the measurements were 10 ± 0.5 mm long, 1 ± 0.1 mm wide, and 2 mm thick. Five free films were prepared for each coating, and they were subjected to testing at a speed of 50 mm/min.

4.2.9.2 Weathering test

A QUV-accelerated weathering tester was used to investigate the impact of UV light and moisture condensation on the degradation of the formulated coatings and the subsequent ice adhesion strength after icing/de-icing cycles. The testing procedure used UVA-340, UVA-351, and UVB-313 fluorescent lights in compliance with ISO 11507 standards. The test comprised an 8 h cycle with 400 h of UV light exposure at a temperature of 60 °C and an irradiance of 0.71 $W \cdot m^{-2}$ (UVA-365 radiation meter from LUTRON Co., Taiwan), followed by 4 h of condensation at 50 °C.

4.2.9.3 Pendulum hardness

The surface pendulum hardness of DES-containing coatings was assessed as a representative indicator of surface response to deformation, both before and after exposure to QUV. A BYK-Gardner Byko-Swing (5867) Konig/Persoz hardness tester (byko-swing Persoz, Byk-Gardner, Columbia, MD, USA) was used for these measurements. The number of swings at 4° (Persoz mode), representing the surface hardness of the formulated coatings, was analyzed in accordance with ASTM D4366 standards. The reported measurements represent an average of five data points.

4.3 Results and Discussion

4.3.1 Ionic liquids synthesis

4.3.1.1 FT-IR & NMR spectroscopy

FT-IR spectroscopy was employed to investigate the synthesis of ILs, confirming the results through spectroscopic analysis. Comprehensive details of the findings are provided in the supplementary information, demonstrated in Figure A-III. 4a and Figure A-III. 4b. Additionally, ^{1}H NMR spectroscopy was utilized for chemical structure analysis of each component, facilitating the identification of specific protons within the molecules. Both the ^{1}H and ^{13}C-NMR spectra of the ILs are presented in Figure A-III. 5a and Figure A-III. 5b for reference.

4.3.2 Application of choline-based ILs in anti-icing coatings

4.3.2.1 Surface wetting properties

The WCA and SA were determined for PU coatings integrating $ChNO_3$ and ChTFSI (Figure 4-1 and Table 4-3). Evaluating the IL influence on surface wettability within the coating yields important insights into the forces operating within the IL–coating and IL–water droplet interactions.

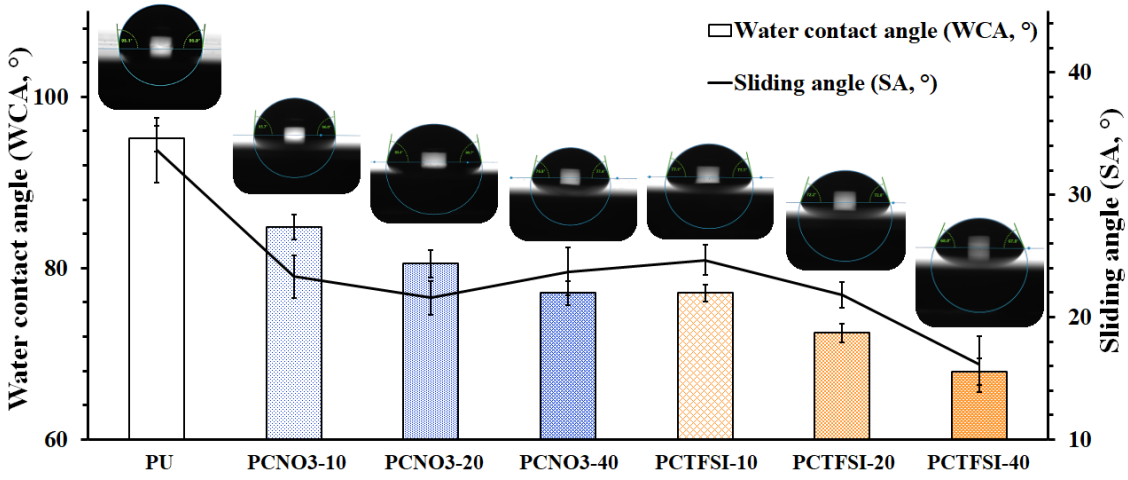

Figure 4-1: Surface wetting properties of the PU coatings containing various percentages of choline-based ILs.

Table 4-3: Water contact and Sliding angles of PU-based coatings containing ILs.

PU-based coatings	PU	PCNO3-10	PCNO3-20	PCNO3-40	PCTFSI-10	PCTFSI-20	PCTFSI-40
WCA (°)	95 ± 1.5	85 ±1	80 ± 2	77 ± 1	77 ± 1	72 ±1	68 ± 1
SA (°)	34 ± 3	23 ± 2	21 ± 1	24 ± 2	25 ± 1	22 ±1	16 ±2

A pronounced reduction in the WCA was noted in PU formulations containing either $ChNO_3$ or ChTFSI, with WCAs approximately reaching 77° and 68°, respectively, as the quantities of both ILs increased. Nevertheless, the average WCA for PU incorporating ChTFSI at varying concentrations was consistently lower than that of the $PCNO_3$ coatings. A notable reduction of 50% in SAs was observed for ChTFSI-containing PU coatings, reaching a value of 16° for PCTFSI-40.

Surface chemistry affected the wettability on the developed surfaces, influenced by the specific type of IL integration, the interactions between the IL–coating and IL–water molecules, and the comparatively low interfacial tension between the ILs and water [317]. The wetting characteristics of ILs are primarily governed by the nature of the anions [323,327]. ChTFSI-containing PU coatings had greater wettability, evidenced by lower WCAs than the $ChNO_3$-containing coatings. The presence of hydrogen-bond donor and acceptor sites on both the cations and anions within an IL allows hydrogen-bonded networks to form. $ChNO_3$ is distinguished by higher water solubility and its hydrophilic anion, whereas the less basic and hydrophobic TFSI possesses an augmented hydrogen bond–donor capacity through its cation, because of charge delocalization and steric configuration [37,327]. This heightened capacity produces a more accessible and robust ionic hydrogen bond with water. Therefore, ChTFSI-incorporated coatings demonstrate lower WCAs than $ChNO_3$-incorporated coatings.

4.3.2.2 Anti-icing properties

DSC assessed the ice formation temperature on the surface of the PU coatings. The introduction of ILs into the coating markedly reduced the ice formation temperature (Figure 4-2a and Figure 4-2b). Specifically, the ice formation temperature of PU coatings decreased by more than 3 °C, cooling from –16.01 (PU) to –19.02 (PCNO3-20) and –19.72 °C (PCTFSI-10). Thus, the diffusion of IL into water molecules and the formation of ionic hydrogen bonding decreased the freezing point of water [19]. The heightened hydrogen-donor capability of ChTFSI produced a more robust ionic hydrogen bond with water, particularly at a concentration of 10 wt. %, further lowering the ice formation temperature. The presence of bonded water introduces a higher energetic barrier for nucleation, necessitating greater energy to form ice nuclei than for non-bonded molecules. Consequently, heterogeneous ice nucleation is inhibited, and initiation occurs at lower temperatures [340].

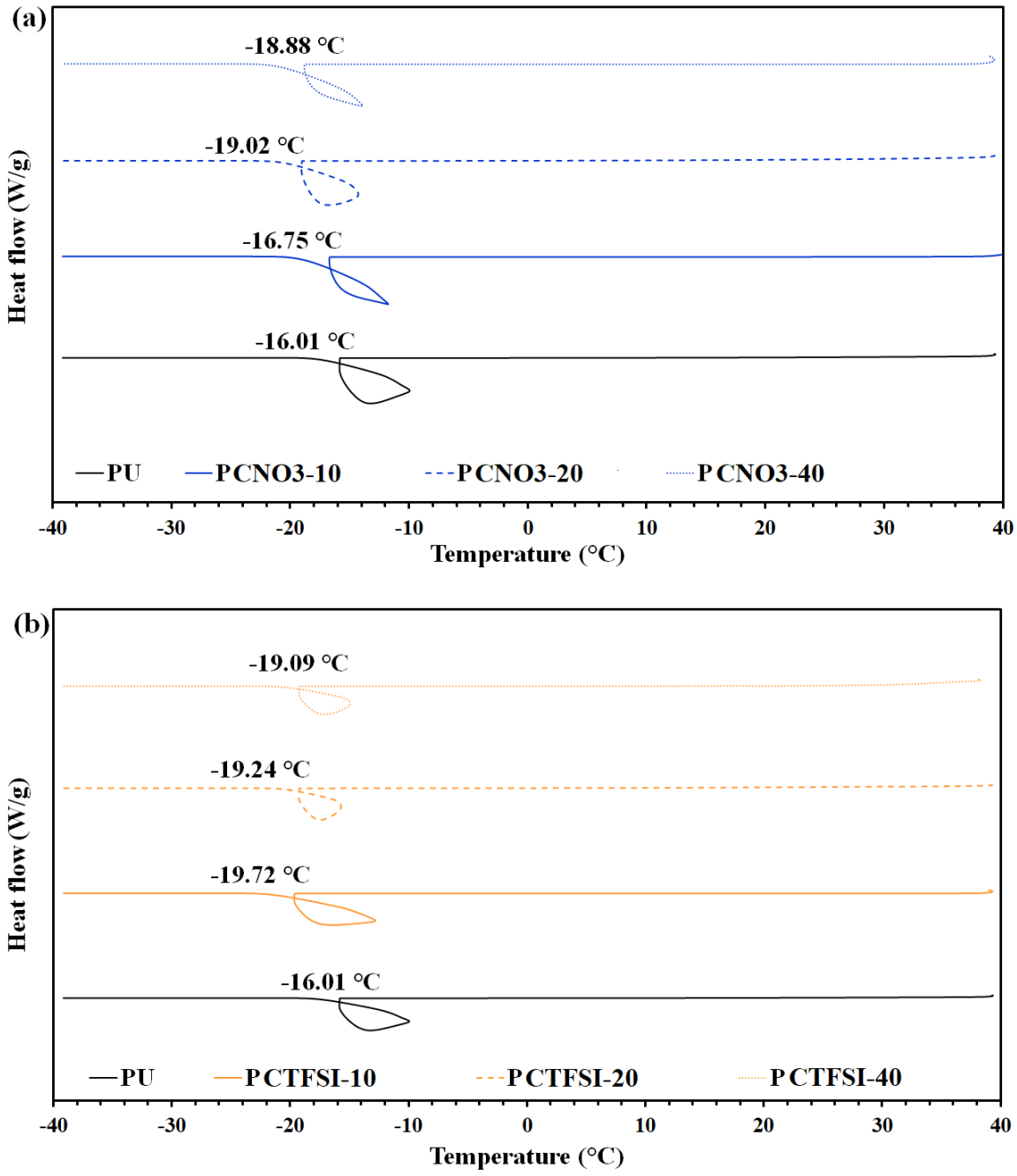

Figure 4-2: Ice formation temperature of water on the surface of PU coatings containing, (a) $ChNO_3$ and (b) ChTFSI.

A low or super low ice adhesion strength for engineered surfaces is a characteristic of an icephobic surface. The ice adhesion strength of PU coatings, tested using the push-off test, was lower for IL-containing coatings. Ice adhesion strength decreased substantially from

310 (PU) to 112 kPa (40 wt. % $ChNO_3$) and 79 kPa (10 wt. % ChTFSI) (Figure 4-3a). Weak interfaces, produced by manipulating the short-term atomistic interactions between water and the surface, create a disordered QLL and in turn reduces ice adhesion strength [17,342,385]. The diffusion of ILs into water droplets lowers the freezing temperatures, thereby maintaining the droplets in a liquid state for a longer duration. In freezing conditions, ILs, characterized by their size and asymmetry, resist being incorporated into ice crystals, which distinguishes them from traditional anti-freezing solid-state salts. Freezing may lead to the rejection of ILs into the unfrozen liquid phase, producing an elevated ion concentration in the layer. During rapid freezing, a portion of the liquid at the interface nucleates into a slushy mixture, causing the temperature of the liquid layer to increase because of latent heat release during nucleation. Conversely, disrupting the ordered crystalline structure of ice and regenerating an amorphous unfrozen interfacial layer hinder further ice propagation and recrystallization, ultimately reducing ice adhesion strength (Figure 4-3b) [19,37]. The lower ice adhesion strength in samples containing ChTFSI aligns with the DSC measurements, confirming the superior hydrogen-bond donor ability of TFSI [323,327].

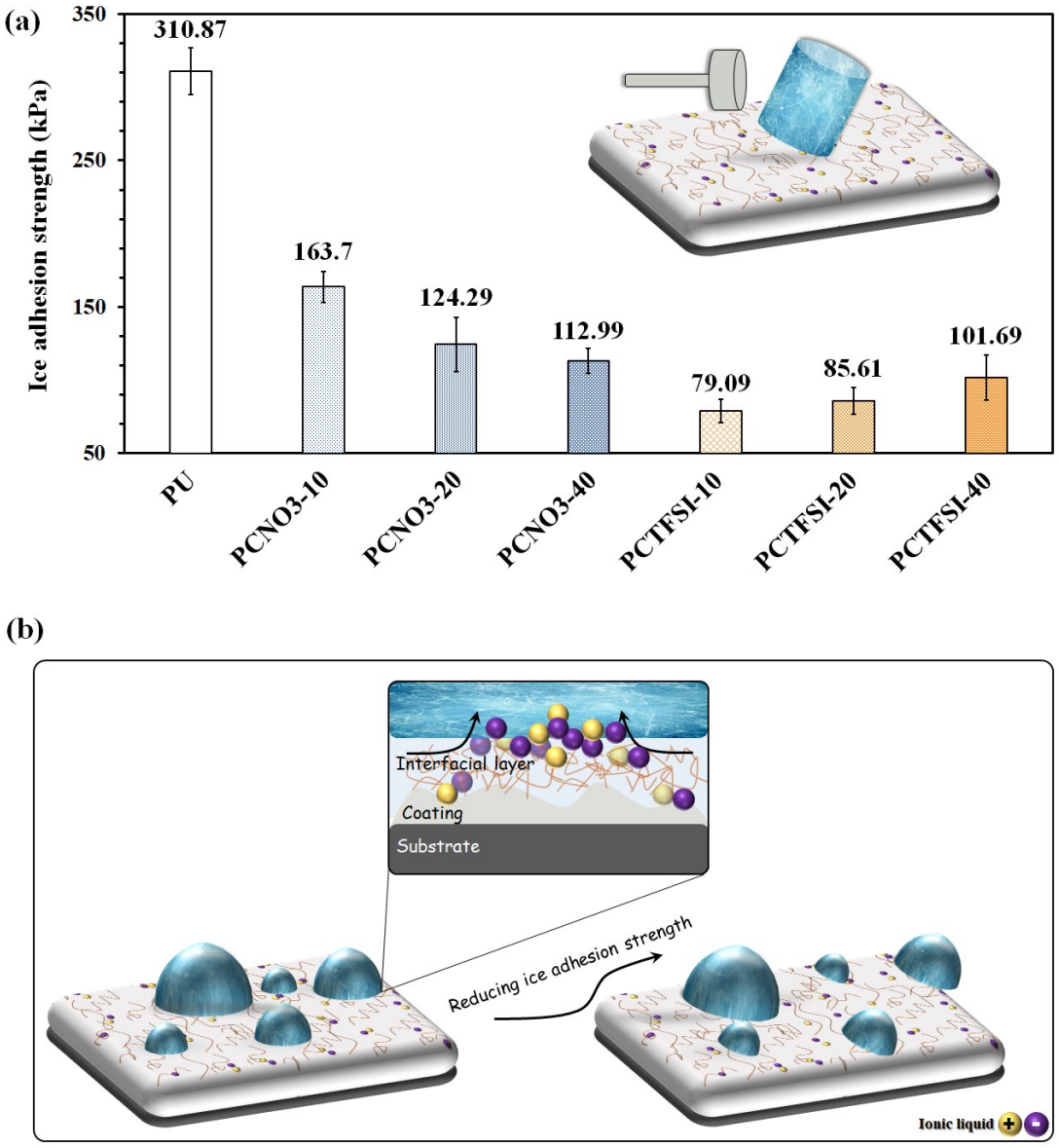

Figure 4-3: (a) Ice adhesion strength (kPa) of coatings as determined through a push-off test; (b) diagram depicting the reduction of ice adhesion strength in the presence of ILs because of a QLL formed at the interface.

4.3.3 Synergistic combination of DES and IL for anti-icing application

The notable hydrogen bond network formed within the DES system may provide a valuable reservoir of hydrogen-bonding donor capability to water, particularly when combined with ILs [398]. The active involvement of hydrogen bonding on the surface plays

a vital role in regulating the dynamics of interfacial water, leading to the inhibition of ice growth and the prevention of ice formation [197,408]. We therefore investigated the surface and anti-icing properties of the developed coatings, selecting IL-containing samples to study the effect of DESs on their performance at subzero temperatures (Figure A-III. 6).

4.3.3.1 Surface wetting properties of optimized IL-containing coatings with DES

We first investigated how the hydrogen-bonding network in the IL–DES system influences the wetting behavior of individual water droplets on the coatings (Figure 4-4 and Table 4-4). The WCA for PU, PCNO3-20, and PCTFSI-10 in the presence of EG-DES were 85° ± 1°, 73° ± 3°, and 58° ± 2°, respectively. The inclusion of DES in the coating slightly lowered the WCA compared to pure PU. A significant decrease in SA and WCA was observed for PCTFSI-10 in the presence of DES compared to those of PU and PCTFSI-10 without DES.

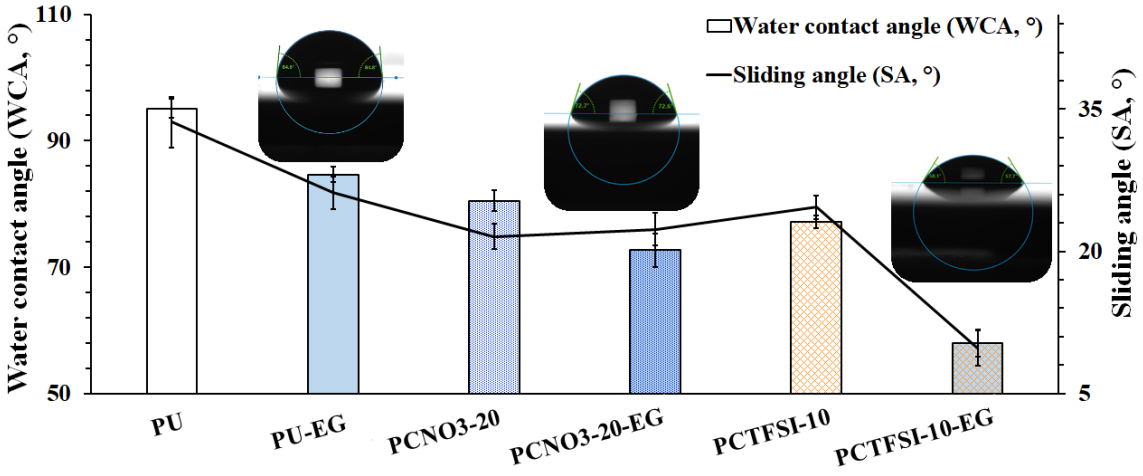

Figure 4-4: Surface wetting properties of the PU and optimized PU coatings containing ILs and DES.

Table 4-4: Water contact and Sliding angles of PU and optimized PU coatings containing ILs and DES.

PU-based coatings	PU	PU-EG	PCNO3-20	PCNO3-20-EG	PCTFSI-10	PCTFSI-10-EG
WCA (°)	95 ± 1	85 ±b1	80 ± 2	73 ± 3	77 ± 1	58 ±2
SA (°)	34 ± 3	26 ± 2	21 ± 1	22 ± 2	25 ± 1	10 ± 2

Hydrogen bonding is a potent electrostatic force governing the formation of the supramolecular structure of eutectic solvents in DESs. The strength, direction, short length, and tunability of hydrogen bonds regulate the assembly of ions and molecules [409]. Typically, DESs exhibit three types of hydrogen bonds, namely neutral, ionic, and doubly ionic hydrogen bonds, which arise from the presence of neutral, positive, and negative components within the network. ChCl, serving as an H-bond acceptor—Cl^- is capable of forming four H-bonds—can combine with H-bond donor species (such as ethylene glycol). These components link through intermolecular hydrogen bonds, resulting in the formation of a 3D supramolecular network [410].

Molecular simulations suggest that the behavior of hydrogen bond donor species alters how the assemblies are organized in the eutectic mixture [411]. Thus, the presence of other non-covalent interactions, such as hydrogen bonding and London forces within supramolecular structures, intensifies solvation effects [228], resembling the DES–IL combination [410]. The higher electronegativity of Cl^- and the existence of (O-H···O) interactions in DESs provide additional binding sites to form hydrogen bonds. This electrostatic force of attraction, comprising both intramolecular and intermolecular hydrogen bonding, significantly influences the freezing points of various eutectic mixtures through charge delocalization [410]. Despite the hydrophilic nature of NO_3^-, ChTFSI with the larger

and less asymmetric TFSI—serving as a less basic anion—exhibits a stronger hydrogen-bond donor ability. The lower WCA of the PCTFSI-10 coating with DES demonstrates a new deep eutectic mixture with a higher number of sites available for forming ionic hydrogen bonds with water molecules and lower surface tension [253,317].

4.3.3.2 Anti-icing properties of optimized IL-containing coatings with DES

Incorporating EG-based DES into the coating substantially lowers the ice formation temperature (Figure 4-5a and Table 4-5). For example, $PCNO_3$-20 had its ice formation temperature lowered from −19.02 to −21.07 °C when DES was added. This lower freezing point of water is attributed to a heightened hydrogen-bonding network being established in the presence of DES.

Furthermore, the superior hydrogen-donor capability of ChTFSI produces a more robust ionic hydrogen bond with water, as evidenced by an extraordinary reduction in the ice formation temperature from −19.72 to −25.68 °C for PCTFSI-10 without and with DES, respectively. These findings emphasize the substantial impact of the hydrogen-bonding network within the IL–DES system on reducing the ice formation temperature [340].

Table 4-5: Ice formation temperature of PU and optimized PU coatings containing ILs in the presence of DES.

PU-based coatings	PU	PU-EG	PCNO3-20	PCNO3-20-EG	PCTFSI-10	PCTFSI-10-EG
Ice formation temperature (°C)	-16.01±0.09	-18.45±0.28	-19.02±0.45	-21.07±0.55	-19.72±0.08	-25.68±0.32

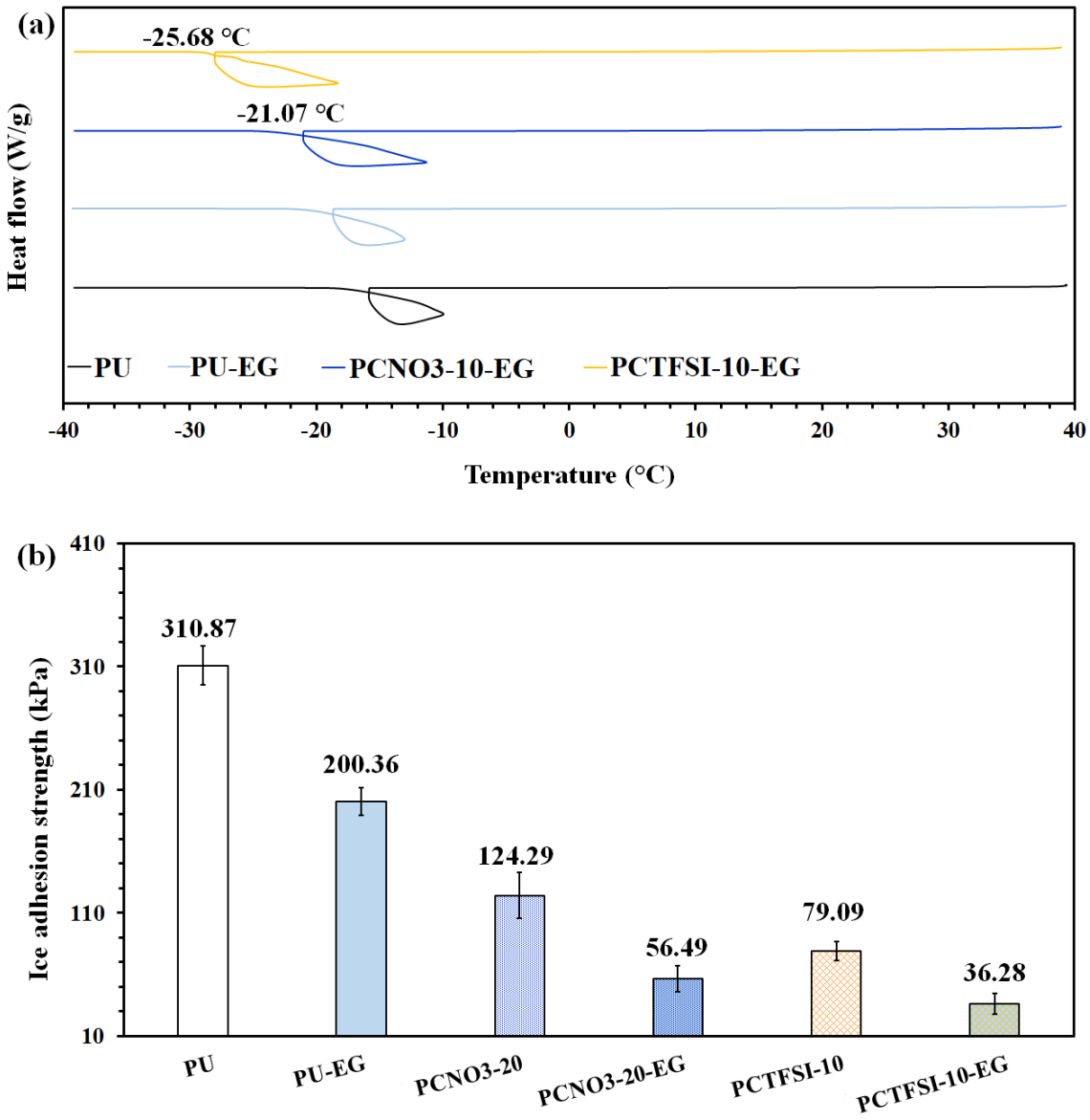

Figure 4-5: (a) Ice formation temperature and (b) ice adhesion strength of PU and optimized PU coatings containing ILs in the presence of DES.

Including DES significantly reduces the ice adhesion strength of the coating, as well (Figure 4-5b). For example, the ice adhesion strength plummets from 310 to 56 kPa for the PCNO3 coating that incorporates DES. The PCTFSI coating with DES has an ice adhesion strength of only 36 kPa. This transformative effect highlights the powerful influence of DES in greatly reducing ice adhesion on these coatings.

Incorporating DES is crucial for establishing a hydrogen-bonding network, which leads to the formation of a substantial QLL and a decrease in ice adhesion strength. This intricate hydrogen-bonding, facilitated by DES, organizes the creation of a notably thicker QLL at the interface [197,228,410]. Thus, DES modifies the interfacial characteristics and produces coatings that have a much lower ice adhesion strength.

4.3.4 Influence of hydrogen-bond donor type in DES on the anti-icing efficacy of coatings

We used a prevalent ChCl-based DES as the HBA, coupled with an EG serving as the HBD and integrated them with synthesized choline-based ILs to produce a coating. The PCTFSI-10-EG coating had an ice formation temperature of approximately –25 °C and an impressive ice adhesion strength of 36 kPa. To further explore the pivotal role of the HBD in enhancing surface properties, we introduced glycerol (GL)—an adept hydrogen bond donor with three hydroxyl groups. We selected the PCTFSI-10 coating, capitalizing on the robust hydrogen bond donor capability of ChTFSI and its overall exceptional results in the presence of EG-based DES. This targeted selection aimed to unravel the subtle effects of HBD variations on the effectiveness of the coating in subzero conditions.

4.3.4.1 Surface wetting properties of PCTFSI-10 coating with various DESs

The choice of hydrogen-bond donor in DESs not only affects the internal structuring of the hydrogen-bonding network within the individual components but also plays a crucial role in shaping the hydrogen-bond network within the DES–IL system [412,413]. Consequently, this choice significantly influences the donation capacity of the system to water. Thus, by changing the HBD type in the DES from ethylene glycol to glycerol, WCA measurements for PCTFSI-10 decreased markedly from approximately 77° to 52° (Figure

4-6 and Table 4-6). The three hydroxyl groups on glycerol significantly influenced the surface wetting properties. The presence of glycerol facilitated the creation of efficient sites for establishing a hydrogen-bonding network with Cl^- and subsequently with ChTFSI, contributing to the formation of a new deep eutectic mixture.

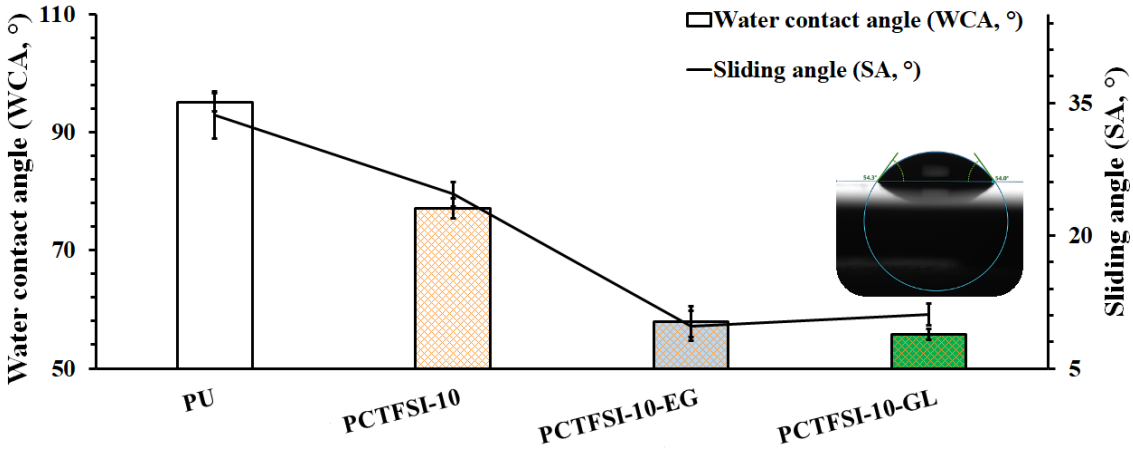

Figure 4-6: Surface wetting properties of PU coatings having ChTFSI and containing different DESs.

Table 4-6: Water contact and Sliding angles of PU and optimized PCTFSI coatings containing DES.

PU-based coatings	PU	PCTFSI-10	PCTFSI-10-EG	PCTFSI-10-GL
WCA (°)	95 ± 1	77 ± 1	58 ± 2	55 ± 2
SA (°)	34 ± 3	25 ± 1	10 ± 2	11 ± 1

4.3.4.2 Surface chemistry of PCTFSI-10 coatings with various DESs

The FTIR spectra were acquired for pristine PU and PCTFSI-10 with and without DESs (Figure 4-7). The vibrational peaks corresponding to the O–H group in the 3200–3500 cm^{-1} range for the coatings were altered when the DES was included [390]. The presence of

characteristic peaks associated with hydrogen bonding was evident in both samples containing DESs, providing strong support for the occurrence of hydrogen bonding interactions. In particular, we noted a well-defined peak in the 3300–3600 cm^{-1} range for the glycerol-based DES. This observation indicates the existence of a comparatively robust hydrogen bonding association between this DES and the IL on the surface, in contrast to the ethylene glycol-based DES [414].

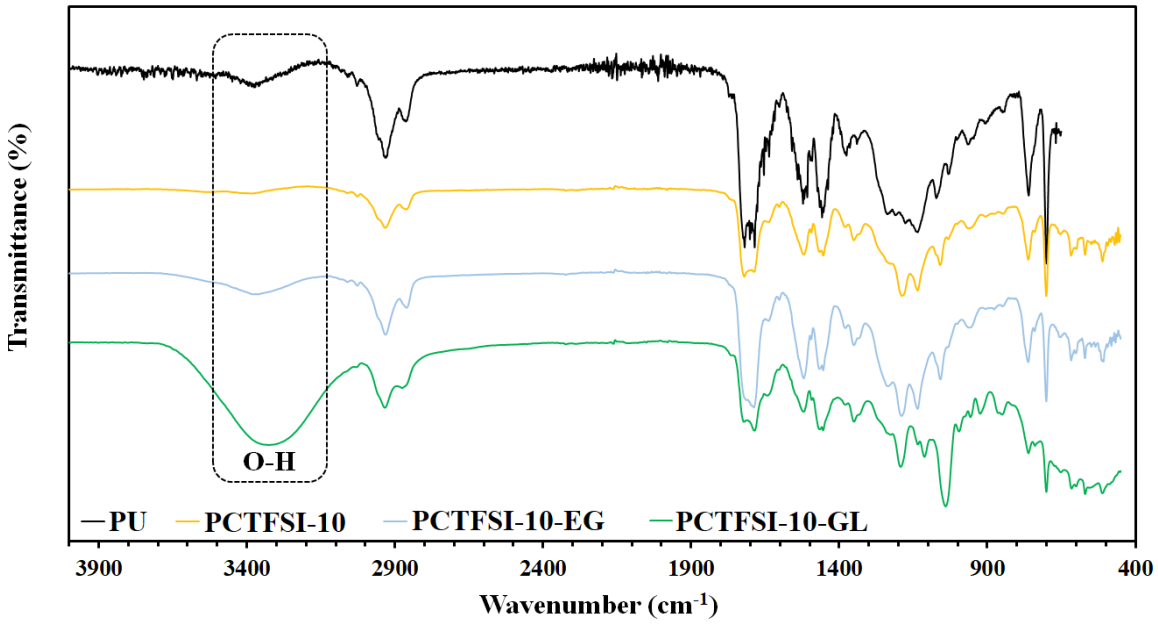

Figure 4-7: FT-IR spectrum of PU coatings containing ChTFSI with different DESs.

4.3.4.3 Surface morphology of PCTFSI-10 coatings with various DESs

SEM imaging served to examine the surface morphology of coatings, both with and without DESs (Figure 4-8). The PCTFSI coatings containing DESs exhibited a more heterogeneous and likely porous structure. To validate these visual observations, we evaluated cross-sections of freeze-dried coatings via SEM. The micrographs confirmed that both DES-containing coatings had a porous and 3D structure. In contrast, the PU and

PCTFSI-10 coatings were considerably more homogeneous, with PU presenting a clearer and more uniform structure characterized by sharp and brittle edges. PCTFSI-10 coatings, however, exhibited slightly brittle edges because of the plasticizing nature of ILs. The distinctive morphology of the DES-containing coatings can be attributed to the development of hydrogen bonds between DES, IL, and the matrix, which form a 3D network structure characterized by randomly distributed pores [415]. Mapping the F and N components of the coating revealed the presence and relatively uniform distribution of the ChTFSI anion and DES on the surface. Moreover, EDX analysis indicated a higher concentration of these components, with F content increasing by approximately 2 wt.% in samples.

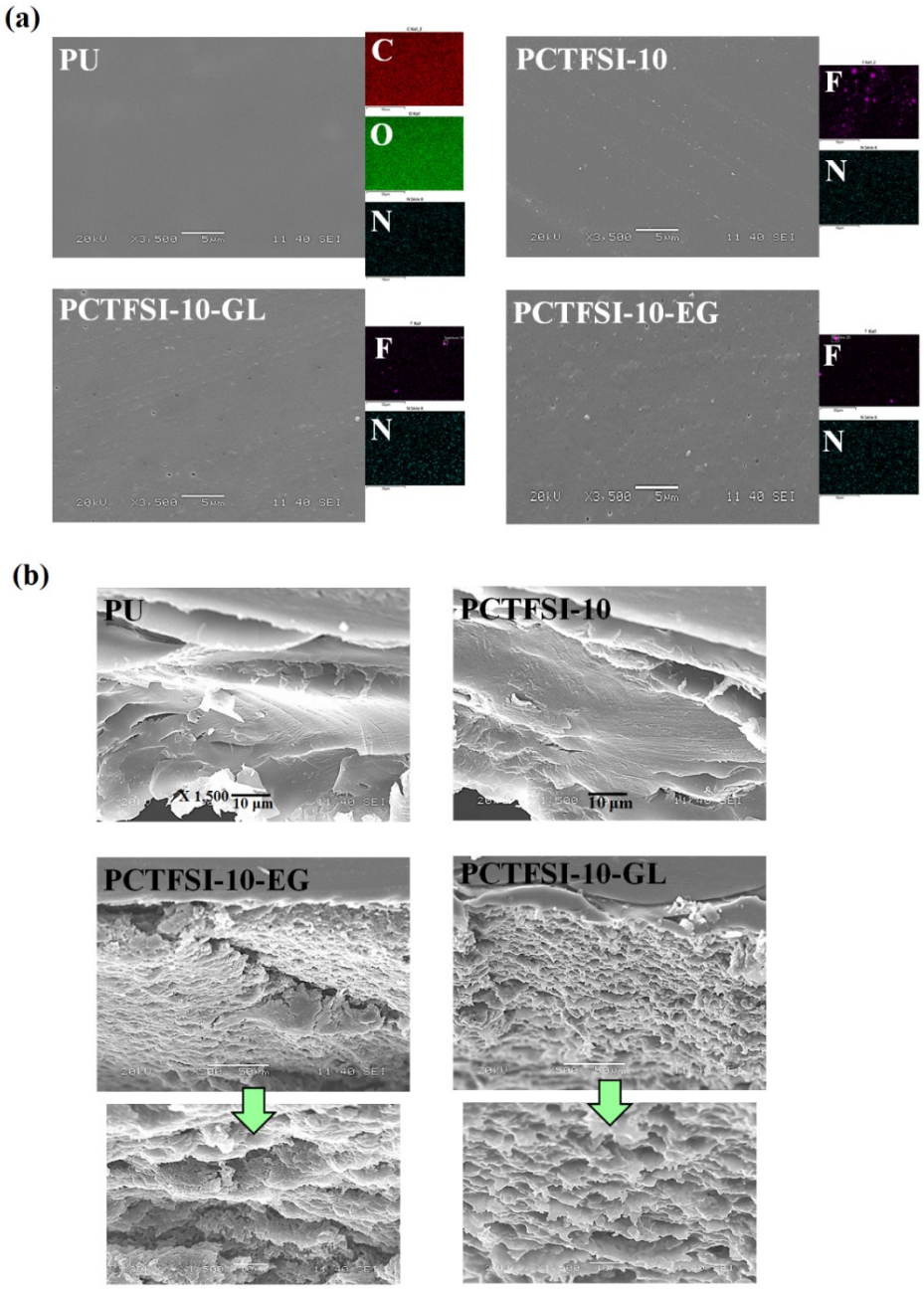

Figure 4-8: (a) Surface morphology and EDX mapping images of PU coatings containing ChTFSI with different DESs, and (b) cross sectional images of the freeze-dried coatings.

4.3.4.4 Anti-icing properties of PU coatings containing ChTFSI with various DESs

We observed a substantial decrease in ice formation temperature (−36 °C) solely by changing the HBD component and opting for glycerol, as depicted in Figure 4-9a. This

marked decrease in temperature reflects the heightened hydrogen-bonding network within GL-based DES. Moreover, push-off testing of the PCTFSI coatings containing glycerol-based DES demonstrated a low ice adhesion strength of ≈ 10 kPa (Figure 4-9b and Table 4-7). These intriguing observations underscore an extraordinary depression in the freezing point of water and highlight the superior performance of this coating in reducing ice adhesion, thanks to the establishment of a spectacularly heightened hydrogen-bonding network within GL-based DES [410].

When comparing the PCTFSI coatings containing EG-based and GL-based DES, the substantial impact of glycerol's three hydroxyl groups in increasing hydrogen bond formation with water becomes evident. Simulations of quantum mechanical molecular dynamics have investigated the structures and interactions of DESs [416] to explain differences in the physicochemical properties of DESs. These simulations demonstrate that the structure of the bulk HBD is mostly preserved for hydroxyl-based HBDs, such as GL- or EG-based DESs.

Table 4-7: Ice formation temperature of PU and optimized PCTFSI coatings in the presence of DES.

PU-based coatings	**PU**	**PCTFSI-10**	**PCTFSI-10-EG**	**PCTFSI-10-GL**
Ice formation temperature (°C)	-16.01±0.09	-19.72±0.08	-25.68±0.32	-36.52±1.58

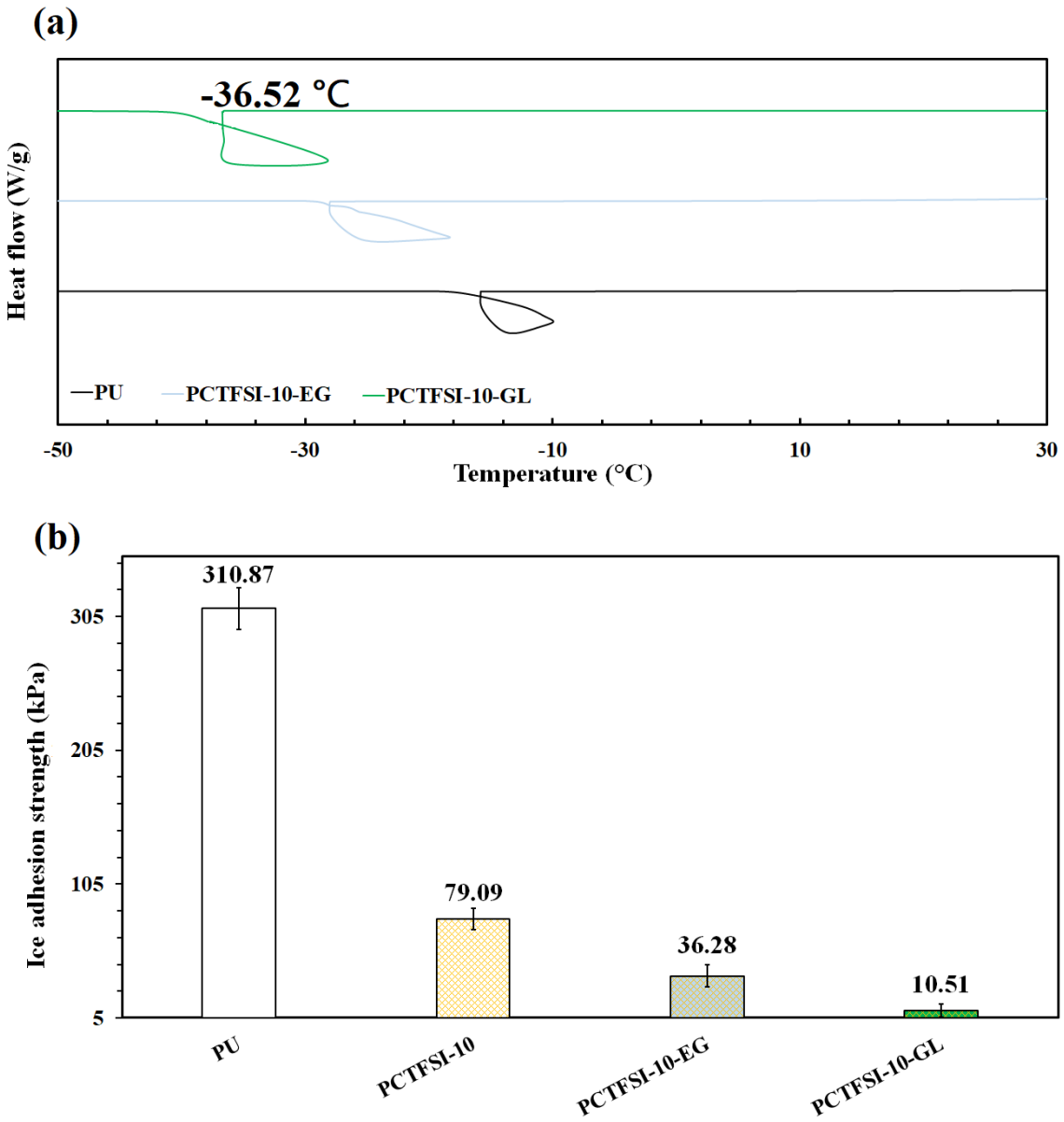

Figure 4-9: (a) Ice formation temperature and (b) ice adhesion strength of PU and optimized PU coatings containing ChTFSI with DESs.

The literature reveals compelling evidence that the hydrogen bonding established between the HBD hydroxyl hydrogen atom and the chloride anion (i.e., H_{EGOH}-C^{-} and H_{GLOH}-Cl^{-}) of both DESs is highly similar. Both DESs exhibit nearly linear bonding arrangements for the O-H-Cl hydrogen bond angles, which can be attributed to the conformational flexibility of the HBD [417]. The extent and nature of HBD–Cl^{-} hydrogen

bonding are similar for both of these DESs, as well as the number of HBD–Cl^- hydrogen bonds (per HBD molecule) for both ChCl:EG and ChCl:GL, in accordance with the radial distribution functions (RDF). Given the HBD:Cl^- molar ratio of 2:1, all H_{EGOH} hydrogens effectively coordinate with Cl^- in ChCl:EG. In contrast, only two-thirds of the H_{GLOH} hydrogens in ChCl:Gly actively engage in hydrogen bonding with Cl^- under the same 2:1 molar ratio. This phenomenon occurs because of the oversaturation of hydrogen bond donor sites facilitated by glycerol. This excess creates more glycerol–glycerol hydrogen bonding within this DES [229]. Specifically, those H_{GLOH} atoms that are unable to interact with Cl^- offer a greater number of potential and accessible sites for creating hydrogen bonding network with IL and water (Figure 4-10). This observation explains the remarkable effectiveness of the GL-based DES–IL system in reducing both the ice formation temperature and adhesion strength of PCTFSI.

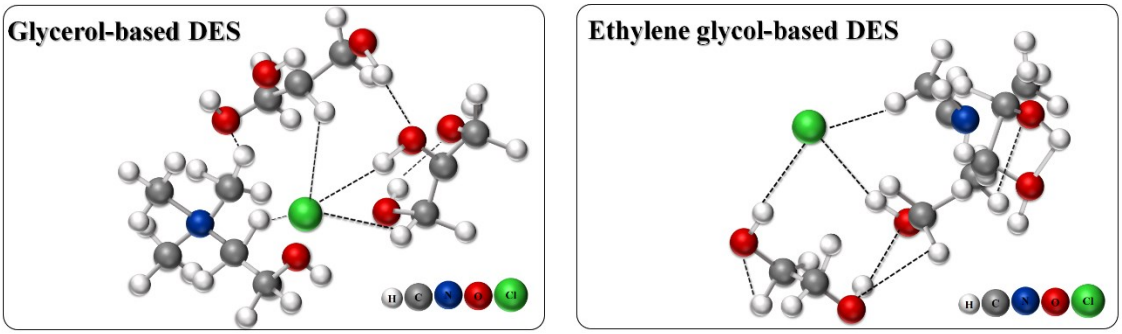

Figure 4-10: Illustration depicting hydrogen-bonding networks within DESs that create accessible sites for potential hydrogen-bonding interactions with ILs.

Notably, the DSC heating curves, which showcase the melting temperature of frozen water, with and without DES, offer a basis for further examining the distinct capabilities of both DESs in inducing the melting of ice [418]. Both DES heating curves in Figure 4-11a show a marked decrease in the temperature of melting onset from −0.93 °C (frozen pure

water) to −23.11 and −30.97 °C, for water/EG-based and water/GL-based DES, respectively (Table 4-8). This shift reflects the presence of an exceptional hydrogen-bonding network with water, particularly in the case of the GL-based DES and water mixture.

High heat capacity is another prominent characteristic of DESs [392,419]. We elucidated the thermal properties of DESs through DSC heating and cooling curves (Figure 4-11b). The dry eutectic mixtures exhibited freezing/melting behaviors at ultra-slow scan rates of 2.5 °C/min. Multiple thermal events have been noted for these mixtures, attributed to eutectic melting and dissolution of the excess component. However, the thermal behavior of choline-based DESs can vary because of numerous factors, such as; ratio and amount of water [420]. DESs can exhibit a similar behavior to that of phase change materials (PCMs), particularly in regard to their high latent heat of fusion and melting temperature within the desired operating range [421,422]. Given this and our observations, DESs hold promise for applications requiring functionality at low temperatures.

Table 4-8: Melting temperature of water and water solutions in the presence of DES.

Samples	**Water**	**Water+(1)Ch:(2)EG**	**Water+(1)Ch:(2)GL**
Onset of Melting (°C)	-0.93±0.06	-23.11±0.25	-30.97±0.51

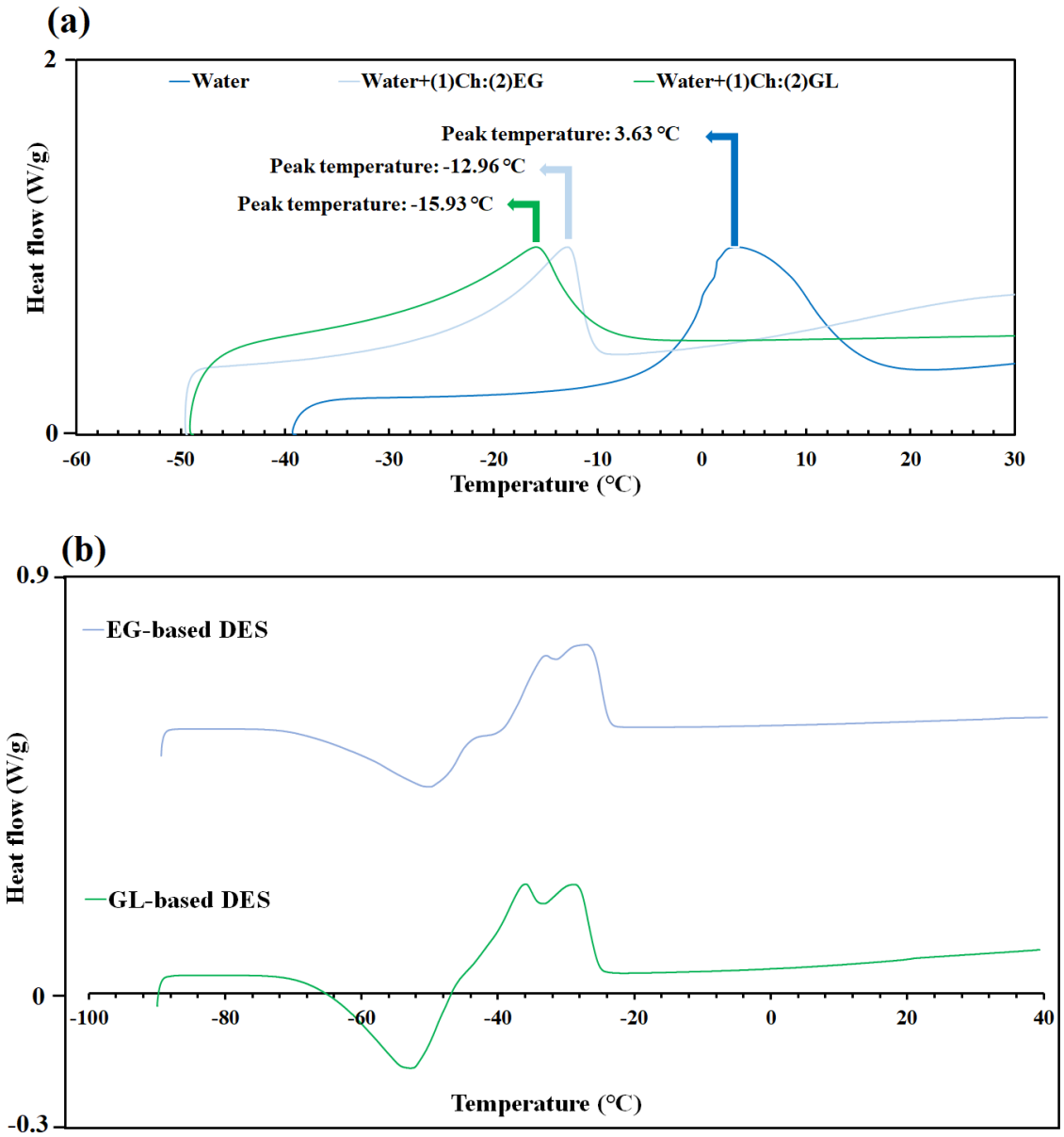

Figure 4-11: DSC heating curves of DESs with (a) water and (b) without water.

4.3.4.5 Characterization of QLL between the ice and surface of PCTFSI coatings in the presence of different DESs

Solid-state NMR spectroscopy characterized the nonfrozen QLL at the bulk water–coating interface (Figure 4-12a–d). Initially recorded at 276 K, the ^{1}H spectra served to assess the characteristics of bulk water before the onset of freezing for the samples: PU + water, PCTFSI-10 + water, in both the absence and presence of EG and GL-based DESs + water

samples. The water ^{1}H chemical shifts were consistent, approximately 5.0 ppm in all samples. After further cooling to subzero temperatures (253 K) and a 3 h stabilization period, the strength of the water ^{1}H signal was notably reduced for the PU and PCTFSI-10 samples. As the temperature decreased, the higher water ^{1}H chemical shifts within the coatings, particularly in DES-containing samples was observed. This behavior can be attributed to the reinforcement of hydrogen bonds at lower temperatures, influencing the shielding and de-shielding of water protons [17].

As the temperature descends below 0 °C, the signal strength corresponding to nonfrozen water, indicative of the quantity of nonfrozen water, rapidly decreases for both PU and PCTFSI-10. However, the persistence of this signal at 253 K for PCTFSI-10 containing DESs, specifically GL-based DESs, suggests the presence of a thicker QLL because of the enhanced hydrogen-bonding capacity of GL. The higher percentages of detected nonfrozen water layer at temperatures as low as −20 °C serves as a self-lubricating interface, making a substantial contribution to the observed low ice adhesion strength [342]. The ^{1}H T_2 relaxation time, inversely linked to viscosity, provides a quantitative assessment of this viscosity increase, as water molecules near the interface exhibit a substantially lower configurational entropy than bulk water, resulting in a notable increase in water viscosity [37,38]. The persistence of the water ^{1}H signal down to 253 K for coatings containing GL-based DES and a more pronounced decrease in T_2 relaxation time for this coating affirm the superior hydrogen-bond donor ability of the GL-based DES–IL system to local interfacial water compared to coatings containing EG-based DES.

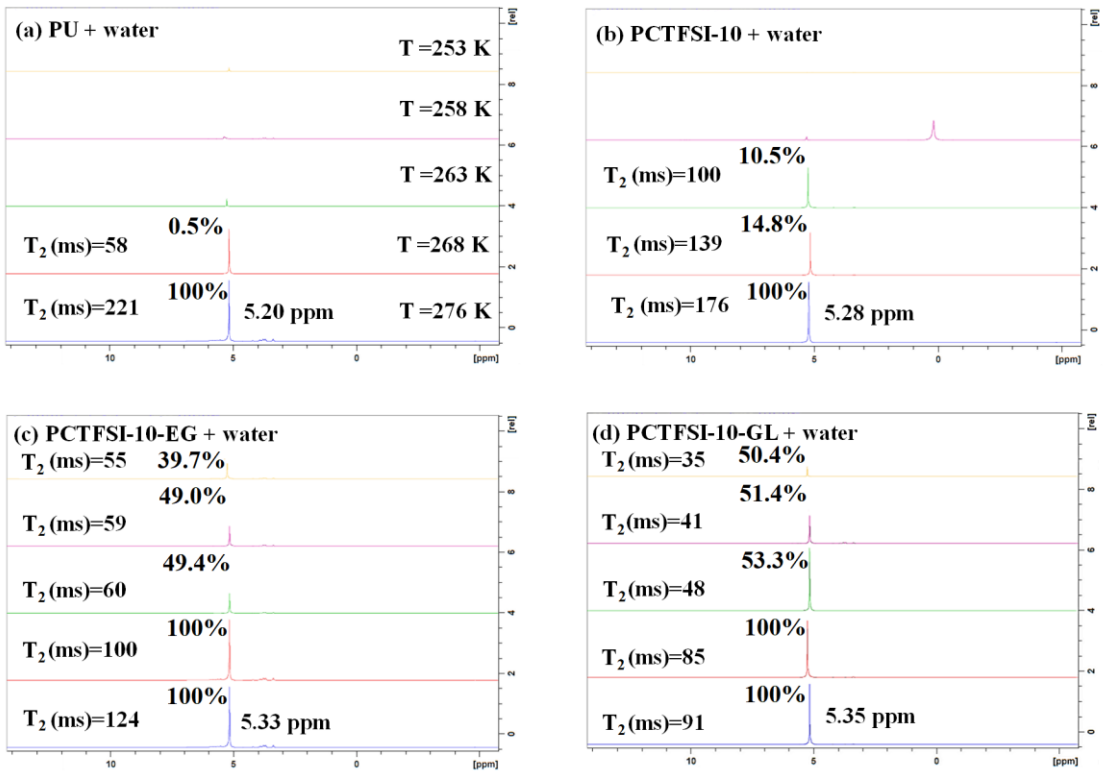

Figure 4-12: ^{1}H spectra acquired via SS-NMR spectroscopy for (a) PU + water; (b) PCTFSI-10 + water; (c) PCTFSI-10-EG + water; and (d) PCTFSI-10-GL + water, spanning temperatures from 276 K (depicted in blue) to 253 K (depicted in yellow). The percentages at each temperature quantify the proportion of non-frozen water molecules present at the interface.

4.3.5 Mechanical properties and durability of DES-containing coatings

4.3.5.1 Tensile strength

The mechanical properties of coatings are largely associated with the distribution and density of intermolecular and intramolecular interactions in the network. When comparing the mechanical properties of the various coatings (Table 4-9), we noted a decrease in tensile strength and an increase in elongation-at-break when ChTFSI was added to PU, particularly for DES-containing coatings (Figure 4-13a). These changes reflect the presence of the IL, which typically has a plasticizing effect on polymer films and enhances chain mobility. A

similar effect can be observed in the DES-containing samples, attributed to the role of both ILs and DESs as plasticizers [423]. Although PCTFSI has a lower tensile strength, the lower elongation-at-break than those of PCTFSI containing DESs is attributed to the hydrophobic nature of the TFSI anion and the migration of the ILs from the matrix [424]. Moreover, the tensile strength of PCTFSI-10-GL was greater than that of coatings containing EG-based DES. This behavior may stem from partial crosslinking through hydrogen bonding, which forms bridges between PU chains and limits their mobility because of more hydroxyl groups on GL [425].

The brittle behavior of the PU coating became elastic after adding of ILs and DESs into the matrix. The glass transition (Tg) value of a coating reflects the presence of hydrogen bonding within the system and the manifestations of molecular interactions at both the atomic and bulk scales. As illustrated in Figure 4-13b, the Tg of the coatings shifted to lower temperatures, from 56 ℃ for PU to 37, −28, and −31 ℃ for PCTFSI-10, PCTFSI-10-GL, and PCTFSI-10-EG, respectively. The intrinsic plasticizing effect of ILs and DESs, along with the more rubber-like behavior observed in the tensile tests, is reflected in the slight reduction in Tg for PCTFSI-10 and the further decrease in Tg for PCTFSI-10 containing DESs [426].

Table 4-9: Mechanical properties of developed PU coatings containing ChTFSI and various DESs.

PU coatings	Tensile strength (MPa)	Elongation (%)
PU	8.1 ± 0.43	4.7 ± 0.09
PCTFSI-10	7.05 ± 0.68	23.85 ± 0.4
PCTFSI-10-GL	6.85 ± 0.55	38.02 ± 0.29
PCTFSI-10-EG	6.5 ± 0.32	55.44 ± 0.47

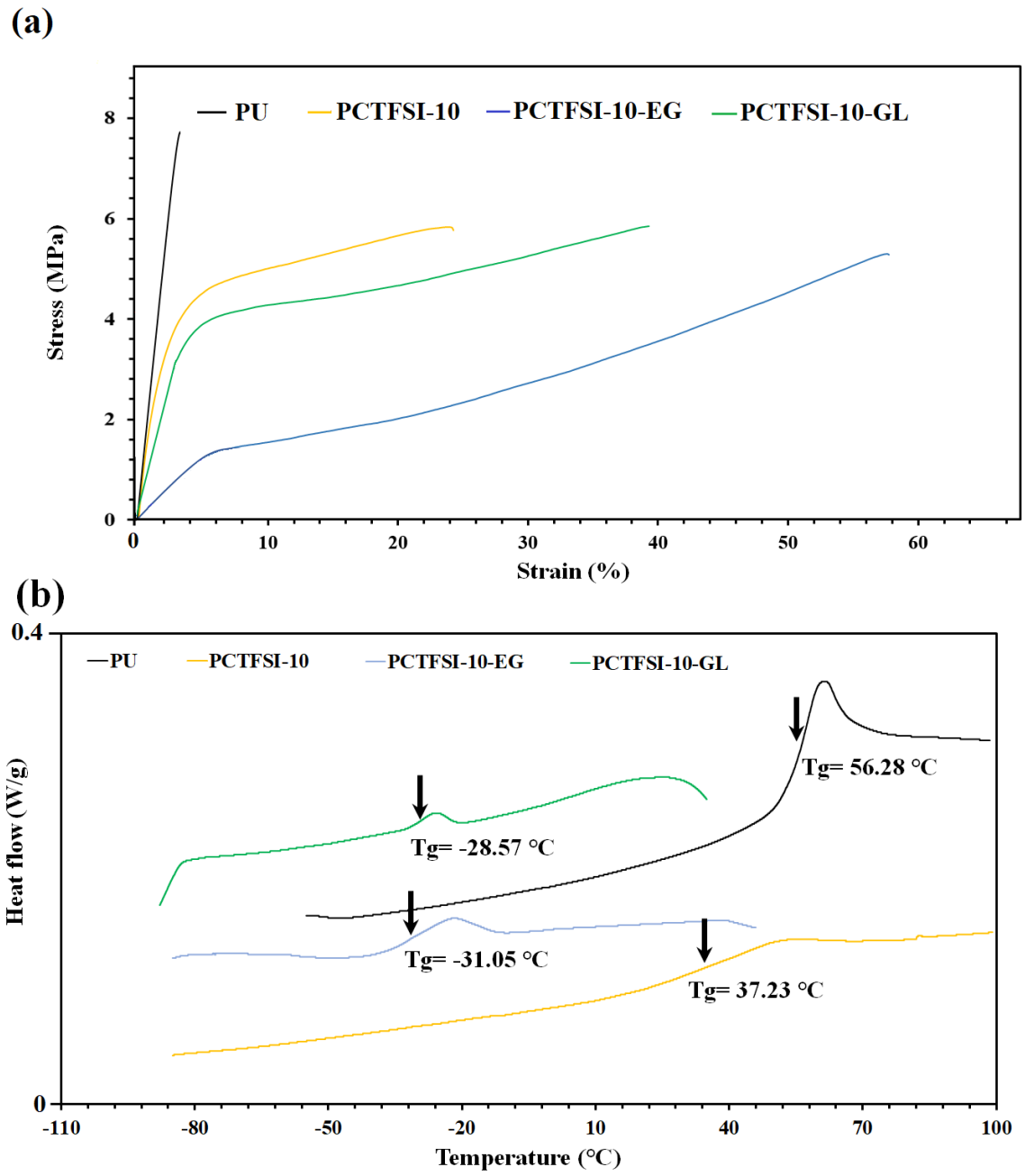

Figure 4-13: (a) Mechanical properties and (b) T_g of developed coatings containing ChTFSI and various DESs, obtained by tensile strength test.

The coating containing GL-based DES exhibited a stronger hydrogen-bonding network, leading to higher Tg values compared to the coating containing EG-based DES [427]. As coatings have higher chain mobility at Tg and a higher intensity of hydrogen

bonding at this temperature, the subzero Tg of DES-containing coatings indicates an exceptionally enhanced functionality for anti-icing applications [428].

Furthermore, within these surfaces, the integrated uncross-linked polymeric chains enhanced mobility at the ice–substrate interface. This altered boundary condition facilitated interfacial slippage, reducing ice adhesion [45]. The increased mobility of polymeric chains at the "nonzero slip" interface imparted the coating with ultra-low ice adhesion strength. In finely tuned samples of such surfaces, both the deformation-incompatibility anti-icing mechanism and interfacial slippage helped lower the ice adhesion strength [429].

4.3.5.2 Ice adhesion strength over icing/de-icing cycles and against accelerated weathering conditions

We used a push-off test to determine the ice adhesion strength of the coatings over 20 icing/de-icing cycles. Over these cycles, the ice adhesion strength of PU-based coatings did not vary significantly (Figure 4-14). The PCTFSI-10 DES-containing coating consistently had an ice adhesion strength below 100 kPa.

We then assessed how accelerated weathering conditions affect the ice adhesion strength of coatings after 20 icing/de-icing cycles. In general, the coatings showed greater resistance to accelerated UV light and high humidity (Figure 4-14a). The 3D profilometry of the fabricated surfaces indicated that the DES-containing samples had greater surface roughness (Sq, root mean square roughness parameter) than the PU reference coatings. Moreover, the DES-containing coatings had higher Sq values after the de-icing cycles because of the surfaces' rubber-like behavior and low modulus elasticity. The inherent plasticization effect of ILs and DESs reduced the surface hardness (Table 4-10) of both sets of samples incorporating DESs, in contrast to the reference samples.

Table 4-10: Surface hardness of developed PU coatings containing ChTFSI and various DESs, upon UV exposure.

PU coating	Surface hardness (4° persoz)			
	PU	PCTFSI-10	PCTFSI-10-EG	PCTFSI-10-GL
Before QUV	133 ± 3	140 ± 4	98 ± 4	102 ± 3
After QUV	126 ± 2	130 ± 5	90 ± 4	92 ± 3

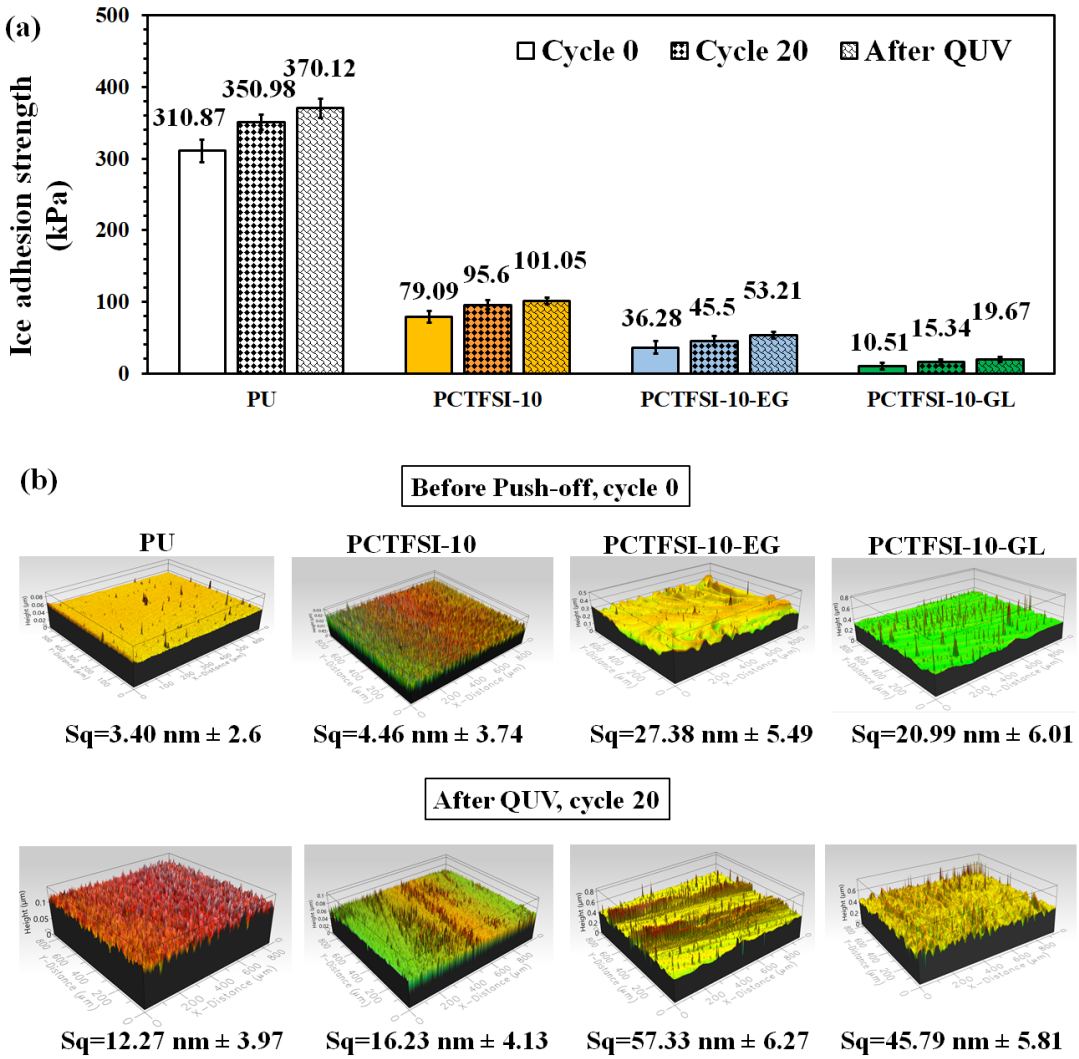

Figure 4-14: (a) Ice adhesion strength and surface hardness of PU coatings exposed to 20 icing/de-icing cycles before and after QUV, as obtained by a push-off test; and (b) 3D profile maps of coatings samples before and after icing/de-icing cycles.

4.3.5.3 Anti-frosting ability of PU coatings containing ChTFSI with various DESs

We subjected the PCTFSI-10 coatings, with and without DESs, to seven freeze–thaw cycles with freezing at −20 °C in each cycle. We observed a noticeable change in the visual appearance of PU coatings immediately upon reaching the designated temperature on the test plate (Figure 4-15a). The DES-containing coatings had a markedly delayed frost formation over the seven cycles. Among all the coatings, the PCTFSI-10-GL sample produced the longest frosting delay and greatest resistance to frost formation (Figure 4-15b). Moreover, the frost formation pattern for the DES-containing PCTFSI-10 coatings adopted a more pointed and localized pattern of frost formation. We also observed the emergence of a bridge-like structure on the PU surface during frost formation. These observations highlight the remarkable effectiveness of DESs, especially PCTFSI-10-GL, in increasing surface resistance to frost formation, which represents a significant advancement in coating technologies [270].

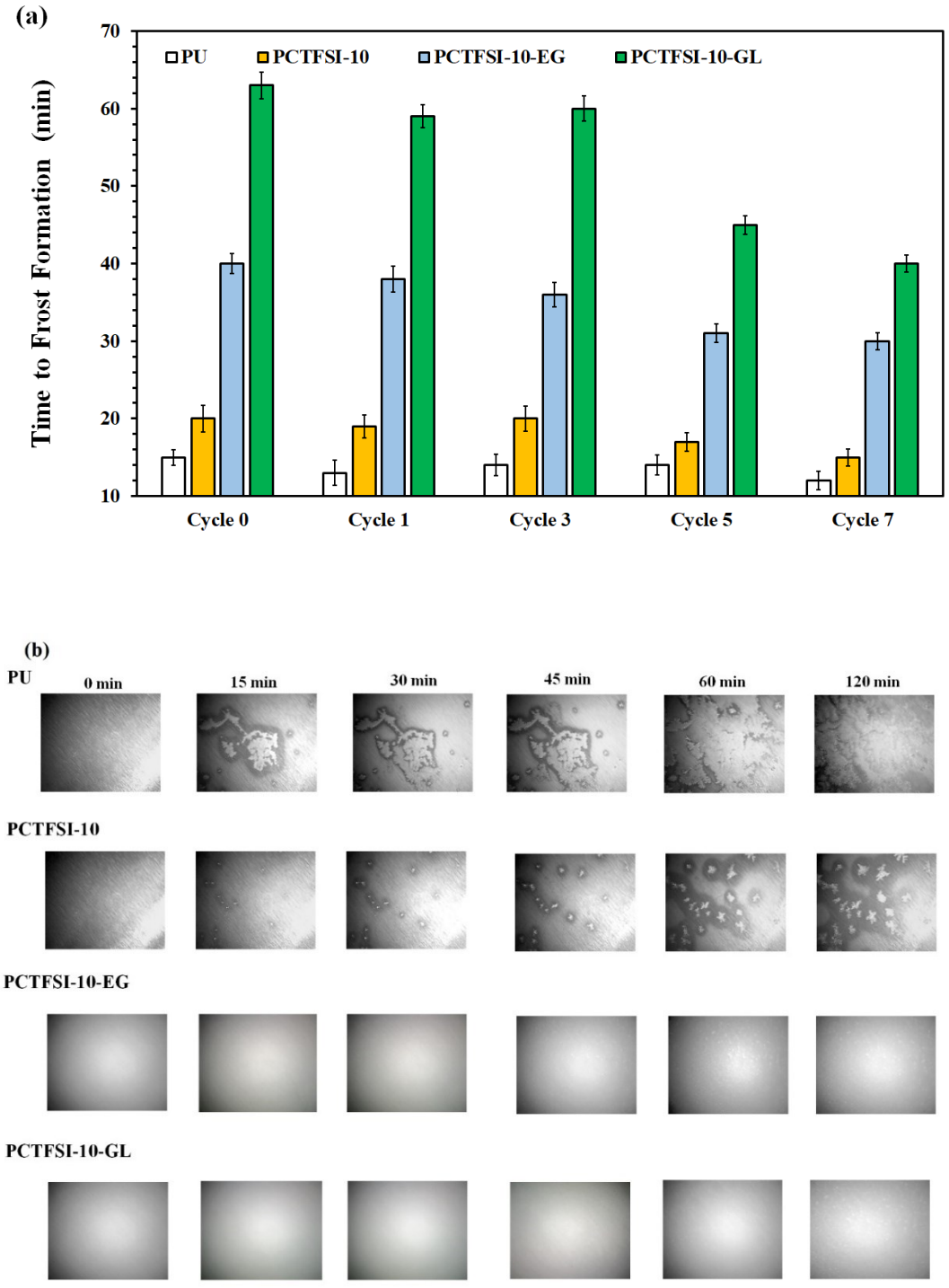

Figure 4-15: (a) The time required for frost formation on coatings during seven frost/defrosting cycles; and (b) corresponding images of the coatings during the seven cycles.

The DES-containing coatings, particularly those with GL-based DES, required much more time to reach the Peltier temperature (Figure 4-16a). Infrared (IR) thermography recorded the temperature variations of this sample during frost formation (Figure 4-16b). As the Peltier temperature approached approximately –18 °C (averaged across areas 3 and 5), the surface temperature of the PCTFSI-10-GL coating on the Peltier platform gradually decreased (average of areas 1, 2, and 4). This phenomenon can be attributed to the various phase changes occurring within the DES at subzero temperatures.

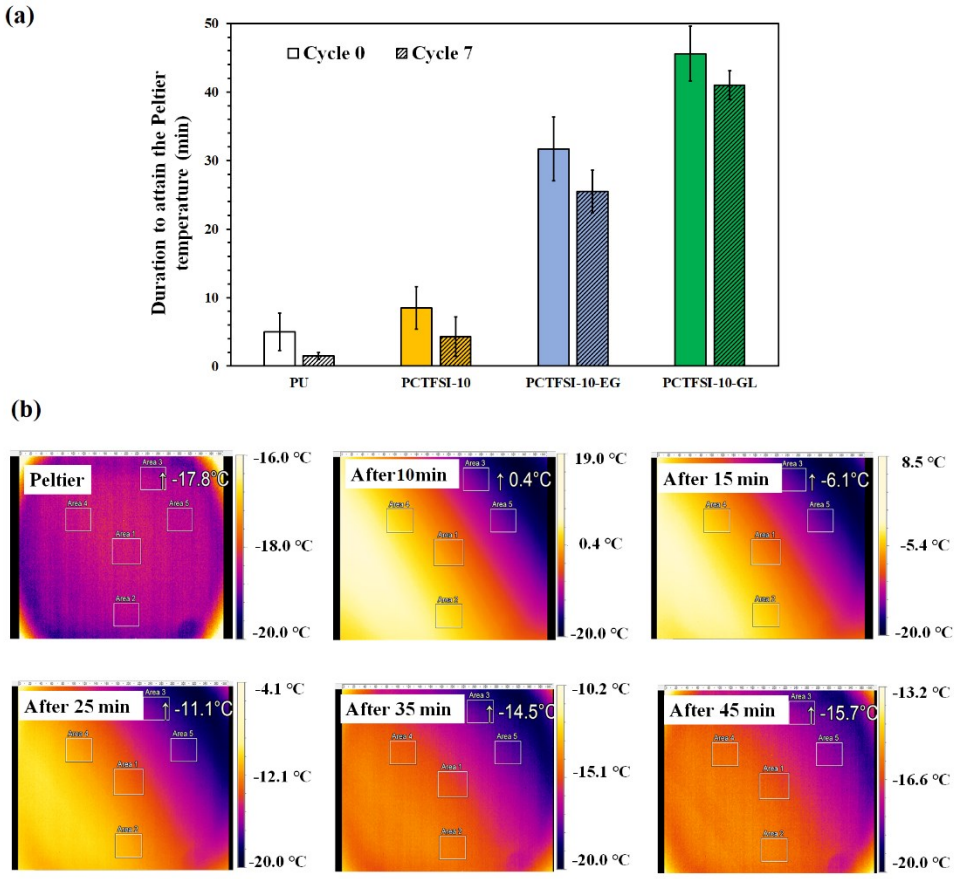

Figure 4-16: (a) Time required to attain to the Peltier temperature before and after the seven frost/defrost cycles; and (b) IR thermography of the samples during frost formation over time.

4.4 Conclusion

This study explored the anti-icing potential of deep eutectic solvents (DESs), focusing specifically on the impact of the hydrogen-bond donor (HBD) component in DESs on the hydrogen-bond donor capacity of ionic liquids (ILs). Choline nitrate and choline TFSI were synthesized as ILs. For icephobic applications, PCNO3-20 and PCTFSI-10 were selected as optimized coatings for further evaluation in combination with DESs. Incorporating ethylene glycol (EG)-based DESs with these optimized coatings enhanced the ice formation temperature, reaching −21 °C for PCNO3-20 and −25 °C for PCTFSI-10. The results underscore the critical role of hydrogen bonding in achieving strong anti-icing properties. By modifying the HBD component of the DESs from EG to glycerol (GL), the coatings achieved exceptionally low ice formation temperatures (−36 °C) and ice adhesion strength (10 kPa). This improvement is attributed to a thicker quasi-liquid layer (QLL) acting as a self-lubricating interface, confirmed by solid-state NMR spectroscopy. Compared to previous studies [17,37,38,342], the DES-containing coatings exhibited lower ^{1}H T_2 relaxation times, which correlate with a thicker QLL. The GL-based DES–IL system offers a greater number of accessible sites for hydrogen bonding with water, leading to minimal ice formation temperatures and reduced ice adhesion strength, especially in the PCTFSI coating. Additionally, differential scanning calorimetry (DSC) showed that this hydrogen-bonding network lowers the melting onset temperature, with values of −0.93 °C for pure water and −30.97 °C for water/GL-based DES, outperforming zwitterionic coatings reported in previous studies [418]. These findings highlight the synergistic effect of combined DESs and ILs in enhancing anti-icing efficacy. The inherent plasticizing effect of ILs and DESs, along with increased rubber-like behavior in tensile strength, lowered the glass transition temperature (Tg) of PCTFSI-10 and, even more significantly, of PCTFSI-10 containing

DESs. Unlike previous studies that reported Tg values above 0 °C in the presence of certain DESs, our coatings demonstrated significantly subzero Tg values [425,427]. Since coatings experience enhanced chain mobility and intensified hydrogen bonding at Tg, a subzero Tg for DES-containing coatings indicates superior anti-icing functionality. This enhanced functionality is further evidenced by the coatings' robust anti-frosting capacity. Consistent with findings by Y. Tian et al. [270] on the anti-frosting ability of certain natural DESs, our study observed only 10% frost coverage on the GL-containing coating after 120 minutes, substantially lower than the 36% frost coverage reported in their study.

CHAPTER 5

5. ARTICLE 3: ICE-RESPONSIVE COATINGS: EVALUATING THE EFFECT OF HYDROGEN BOND DONORS ON DEEP EUTECTIC SOLVENTS/IONIC LIQUIDS ANTI-ICING EFFICIENCY

Saba Goharshenas Moghadam[1], Gelareh Momen[1]*, Reza Jafari[1]

[1] Department of Applied Sciences, University of Quebec in Chicoutimi (UQAC), 555, boul. de l'Université, Chicoutimi, Quebec G7H 2B1, Canada

*corresponding author: Gelareh_Momen@uqac.ca

This article has been submitted in:

Journal of Molecular Liquids

5.1 Abstract

Although there has been pioneering research on the anti-icing properties of Ionic liquids (ILs) and Deep Eutectic Solvents (DESs), coatings based on these materials are still in the early stages of development. Given the limited understanding of DESs in anti-icing applications, we investigated the role of hydrogen bond donors (HBDs) within DESs, focusing on their hydrophilicity and hydrophobicity. After conducting a comprehensive study using advanced characterization techniques, including ATR-FTIR, X-ray photoelectron spectroscopy (XPS), and wettability measurements, our findings demonstrate that DESs can be effectively introduced as ice-responsive components on a surface,

significantly improving their anti-icing performance. Our comparative analysis showed that the introduction of hydrophobic HBDs into DES-based coatings reduced ice adhesion strength to 13 kPa, while maintaining an ice formation temperature of −35 °C. Despite plasticizing characteristic of DESs, notably, the mechanical properties, including tensile strength, remained consistent with the neat coating, though with enhanced elongation at break. Solid-state NMR spectroscopy revealed the formation of a thicker quasi-liquid layer (QLL) on the surface of coatings containing hydrophobic HBDs, which was further confirmed by low-temperature ATR-FTIR analysis. Moreover, these coatings exhibited modified frost formation patterns, leading to increased resistance to frost buildup over multiple cycles. Ice adhesion strength of coatings was examined against accelerated weathering, icing/de-icing cycles, as well. This study presents a novel approach for designing sustainable, high-performance icephobic coatings, emphasizing the potential of DESs as effective ice-responsive components in achieving superior anti-icing and anti-frosting capabilities.

Keywords: Deep eutectic solvent, Ethylene glycol, Perfluorinated diol, Anti-frosting, Hydrogen-bonding, Low temperature ATR, Quasi liquid layer.

5.2 Introduction

Ice accumulation and frost on solid surfaces cause serious issues in both industrial and everyday settings [430]. Much research has focused on icing, and various anti-icing approaches have been developed [431,432]. While traditional energy-based anti-icing methods are effective, they are costly and inefficient. As a result, passive anti-icing strategies, including coatings and materials, have gained attention for their simplicity, energy efficiency, and cost-effectiveness [290,433].

Multiple intermolecular forces and mechanical interlocking collectively contribute to the adhesion between ice and a coating [385]. Given the critical role of the ice–substrate interface, the focus of much recent research involves inducing dynamic changes in the physicochemical properties of this interface [18,38]. Although a nonfreezing water layer at the ice–solid interface had been identified as early as 2000 [434–436], only recently has it been determined that adjusting the configuration of hydrophobic/hydrophilic and charged functional groups on surfaces can regulate interfacial water, thereby suppressing ice nucleation, growth, and adhesion [402,405–407,437]. Even with a significantly reduced ice adhesion strength achieved by current state-of-the-art surfaces, persistent challenges, e.g., coating damage and lubricant depletion during ice removal, limit their practical applicability [101,358,359]. Hence, there is a pressing need to develop sustainable icephobic properties within durable coatings.

An anti-freezing liquid layer on surfaces at extremely low temperatures can be produced through the interactions between the ice and ice-responsive components [18,76]. Surfaces containing ice-responsive agents prevent ice formation and reduce ice adhesion through these interactions. The ice-responsive materials includes anti-freezing chemicals, proteins, organics, solid-state salts, and both polyionic and ionic liquids (ILs) [53,302,438,439]. Despite the promise of ILs for tackling icing issues, few studies have explored their anti-icing potential [19,26,27,37,38]. Deep eutectic solvents (DESs) have recently emerged as a potential anti-icing agent and have attracted interest because of their similarity to ILs [389]. Their rapid advancement across a wide range of applications highlights their versatility, attributed to characteristics such as non-flammability, low toxicity, affordability, non-volatility, thermal stability, sustainability, recyclability, and

biodegradability. Nonetheless, the exploration of the anti-icing properties of DESs remains surprisingly limited [32,269,398–400]. Innovatively combining various anti-icing strategies and materials could unlock new possibilities for enhancing icephobic performance while mitigating current challenges. These combined methods must work synergistically to maximize their effectiveness and sustainability [39,281,440].

Our research focuses on investigating how the hydrophobicity of the HBDs within DESs influences the hydrogen-bond network and enhances the anti-icing effectiveness and durability of an industrial coating. Given the significant knowledge gap in leveraging DESs for anti-icing applications [39]. this study aims to fill this void by closely comparing the roles of hydrophobic versus hydrophilic HBDs. We examine how these ice-responsive components interact with our synthesized IL to enhance the interfacial water, thereby delaying ice nucleation, adhesion and frost accumulation. Using advanced solid-state nuclear magnetic resonance (SS-NMR), we aim to provide definitive evidence of the quasi-liquid layer (QLL) formation on the coating's surface, which is crucial for preventing ice adhesion. Furthermore, low-temperature ATR-FTIR spectroscopy is employed to investigate the coating-water interface, enabling us to elucidate the molecular interactions, especially the role of hydrogen bonding in modulating the surface's resistance to ice formation. The in-depth comparative analysis of both hydrophilic and hydrophobic HBD components within DESs offers a promising approach and valuable insights for enhancing coating performance in extreme environments, paving the way for more efficient and sustainable solutions for ice mitigation.

5.3 Materials and Methods

5.3.1 Materials

The polyol resin used for formulating the PU coatings, synthesized from acrylic copolymers (WorléeCryl® A 2445), had a 59%–61% solid content and a 4.5% hydroxyl content (based on solids). This specialized resin was supplied by Worlée Industries, Germany. Covestro Co. (Germany) provided the aliphatic polyisocyanate resin composed of hexamethylene diisocyanate (HDI) (Desmodur® N 75 BA/X), with an NCO content of 16.5% ± 0.3% to serve as the hardener. Solvents, including xylene (99%), n-butyl acetate (99%), isopropanol (99%), and dichloromethane (99%), were purchased from Thermos Fisher Scientific. For the DES preparation, pure ethylene glycol (99.9%, EG) and 1H,1H,8H,8H-perfluorooctane-1,8-Diol (98%, PFOL) as HBDs were obtained from Sigma Aldrich (USA) and INDOFINE Chemical Company, Inc. (USA), respectively. We acquired choline chloride (ChCl, $\geqslant$98%) from Sigma Aldrich (USA) as a hydrogen-bond acceptor (HBA). All substances were of analytical grade and used as received without additional purification.

5.3.2 Preparation of the DESs

Choline chloride (ChCl) was dehydrated in a vacuum oven at 50 °C overnight to thoroughly remove any traces of water and moisture. DESs based on EG and PFOL were synthesized by mixing ChCl with EG and PFOL, respectively, in a 1:2 molar ratio. The mixtures were heated and continuously stirred at 80 °C until a uniform, colorless liquid was achieved. The synthesized DESs (EG-DES, PFOL-DES) were then stored in a vacuum desiccator for subsequent use.

5.3.3 Fabrication of Polyurethane coatings containing ChTFSI and DESs

Choline bis(trifluoromethanesulfonyl)imide (ChTFSI), synthesized in our previous work, was used to prepare PU coatings containing a combination of ChTFSI and DESs. The details for IL characterization were reported elsewhere [39]. Firstly, 10 wt.% of IL was added to the respective DES and stirred thoroughly for 10 min in a clean beaker. Alongside, a mixture of polyol and polyisocyanate resin was stirred in another beaker for 5 min. The DES + IL mixture (totally 10 wt.%) was then incorporated into the PU mixture and homogenized at 500 rpm for 10 min. To achieve the desired viscosity, we added 10 wt.% (based on the final mixture) of n-butyl acetate and xylene, maintaining a weight ratio of 60:40. The prepared PU coatings, blended with IL-DES mixtures, were applied to substrates using conventional film applicator. The samples were cured in ambient temperature for one week and labeled according to the HBD type for those coatings containing DES (Table 5-1).

Table 5-1: Composition of each formulation of PU-based coatings containing DES (g).

Sample	Polyol (g)	Polyisocyanate (g)	IL (g)	Solvent (g)	EG-DES (g)	PFOL-DES (g)
PU	100	40	-	20	-	-
PIL-EG	100	40	7	10	10	-
PIL-PFOL	100	40	7	10	-	10

5.3.4 DES characterization

The thermal behavior of each eutectic mixture was evaluated using differential scanning calorimetry (DSC) (DSC Q250, TA Instruments, New Castle, DE, USA) with a TA Instrument Q250 differential scanning calorimeter. Each sample was weighed into an aluminum pan, which was then hermetically sealed. The samples were initially cooled to −90 °C and then heated to 40 °C at a rate of 2.5 °C/min, with a 10 min hold at each temperature endpoint. Given that the heating and cooling rate can influence the observed phase behavior,

we selected 2.5 °C/min as an optimal intermediate rate to capture the thermal behavior relevant to potential applications. Each cooling and heating cycle was repeated three times. The data were analyzed using TA software to extract the thermal transition information.

5.3.5 Surface characterization

5.3.5.1 Surface chemistry

The chemical composition of the coatings was characterized using an FTIR spectrometer (PerkinElmer, Spectrum Two, USA) in ATR mode across the infrared range of 400–4000 cm^{-1}. FTIR spectroscopy was conducted on a diamond surface that was thoroughly cleaned with isopropyl alcohol prior to the start of the test. The FTIR measurements were performed with a resolution of 4 cm^{-1}, and each spectrum was recorded three times to ensure reliability.

Additionally, x-ray photoelectron spectroscopy (XPS) was used to investigate the surface chemical composition of the prepared coatings. This analysis was conducted using a PHI 5600-ci spectrometer (Physical Electronics, Chanhassen, MN, USA). We analyzed a 0.5 mm^2 area with a standard achromatic Al x-ray source, emitting at a maximum energy of 1486.6 eV. Spectra were collected at a 45° incidence angle relative to the normal surface. High-resolution spectra were acquired using a standard magnesium x-ray source without neutralization.

5.3.5.2 Contact angle measurements

Water contact angle (WCA) was measured using the sessile drop method with a Kruss™ DSA100 goniometer (KRÜSS Scientific, Hamburg, Germany), maintaining a room temperature of 25 ± 0.5 °C. For static WCA measurements, a 4 μL distilled water droplet

was delicately deposited onto the sample surface, and the ADVANCE drop shape analysis software facilitated the quantification of WCA. Additionally, the Kruss apparatus, equipped with a tilting table, was used to assess the sliding angles (SAs) of water droplets on the surfaces. A 35 μL water droplet was positioned on the samples affixed to a tilting stage. The stage was inclined to 60°, tilting at 60°/min, until the droplet initiated sliding or rolling off. SAs were calculated as the stage angle 0.5 s before the onset of droplet sliding.

5.3.5.3 Microscopy

To characterize the coating microstructure, we conducted scanning electron microscopy (SEM; JSM-6480 LV SEM, JEOL Japan). This analysis focused specifically on coatings containing DES. Prior to imaging, the samples underwent sputter coating with a thin platinum film.

5.3.5.4 Surface roughness

Surface roughness was assessed using an optical profilometer (Profilm3D Filmetrics®, San Diego, CA, USA), which integrated white light interferometry (WLI) to measure surface profiles and roughness at a precision of 0.05 μm. Additionally, we used the phase-shifting interferometry (PSI) option to measure smooth surfaces at the Angstrom level with a precision of 0.001 μm. These measurements covered an area of 400 × 300 μm, and six randomly selected locations were scrutinized for each sample.

5.3.6 Anti-icing Properties

5.3.6.1 Ice formation temperature

The effect of DES types on the ice formation temperature of the formulated coatings was assessed utilizing a TA Instrument Q250 DSC (DSC Q250, TA Instruments, New Castle,

DE, USA) within a heating range of 40 to −40 °C (±0.05 °C). For this procedure, a 5 mg droplet of deionized water was positioned on a DSC Tzero aluminum pan covered by a thin layer of each coating (thickness 200–250 μm) and then sealed with a lid. The prepared sample was initially cooled at a rate of 5 °C/min from 40 to −40 °C, and this process was repeated three times.

5.3.6.2 Ice adhesion strength

The ice adhesion strength of the samples was assessed through a push-off test. In this test, conducted in a cold chamber at −10 °C, a 1.5 cm diameter cylindrical plastic mold was positioned on the coating surface and filled with deionized water, allowing an ice cylinder to form over 24 h. A digital force gauge (FG-3005, Shimpo Instruments, Lynbrook, NY, USA) was used to measure the force required to detach the ice cylinders from the coating surface. We used a remote computer-controlled interface to manipulate the force gauge, which recorded the shear force until the ice detached from the surface. The force meter probe moved toward the cylindrical column at a rate of 0.05 mm/s and applied a force until the frozen cylinder separated from the sample surface. Consequently, the adhesion stress was computed by dividing the maximum force by the area subjected to icing.

5.3.6.3 Solid-state NMR spectroscopy

Solid-state NMR spectroscopy was used to show the presence of the nonfrozen QLL at the bulk water–coating interface, particularly in samples containing DESs. Initial experiments were conducted at 276 K using a 400 MHz wide-bore Bruker Avance III-HD spectrometer (Milton, Canada), operating at 400.03 MHz for ^{1}H. The temperature was then lowered to 268 K and maintained for 3 h before acquiring additional spectra. Spectra were

collected every 3 h, with a decrease of 5 K for each subsequent test until no liquid water was detectable by NMR. To facilitate a quantitative analysis of the ^{1}H signal in bulk water, we set the recycling delay to 5 s to ensure complete signal relaxation. T_2 measurements and ^{1}H spectra were obtained using the Hahn echo experiment, and the data were processed with Bruker TopSpin software.

5.3.6.4 Low temperature ATR-FTIR spectroscopy

ATR-FTIR spectroscopy (Spectrum II, Perkin Elmer, Waltham, MA, USA) was used to investigate the coating–water interface at low temperatures and to examine the presence of QLL on the coatings' surfaces. A cold-base apparatus (Figure 5-1) was used to regulate the temperature of the coatings on the ATR prism during spectroscopy. The temperature controller sensor (accuracy = 0.1 °C) was positioned at the interface of the coating and prism to ensure precise measurement and control of the interface temperature. Given the interference expected by overlapping the absorption bands of the amine groups of the coatings with the hydroxyl groups of water, deuterium oxide (D_2O, 99.9%, CDN ISOTOPES INC., Pointe-Claire, QC, Canada) was substituted for water during spectroscopic analysis. The O-D stretching band of deuterium oxide at 2467 cm^{-1} does not interfere with any of the coatings and notably shifts to 2355 cm^{-1} upon freezing. The substitution of water with D_2O has minimal impact on the experimental results, as the freezing behavior of D_2O closely resembles that of H_2O because of their similar physical and chemical properties. Free films of the coating samples (200 ± 10 μm thickness) were immersed in D_2O for 6 h before FTIR analysis. The FTIR data were recorded continuously (every 6 s) from +25 °C to −40 °C at a rate of 1 °C/min using PerkinElmer's SpectrumTM TimeBase software (Application Version: 10.7.2.1630), within the infrared range of 4000–400 cm^{-1}.

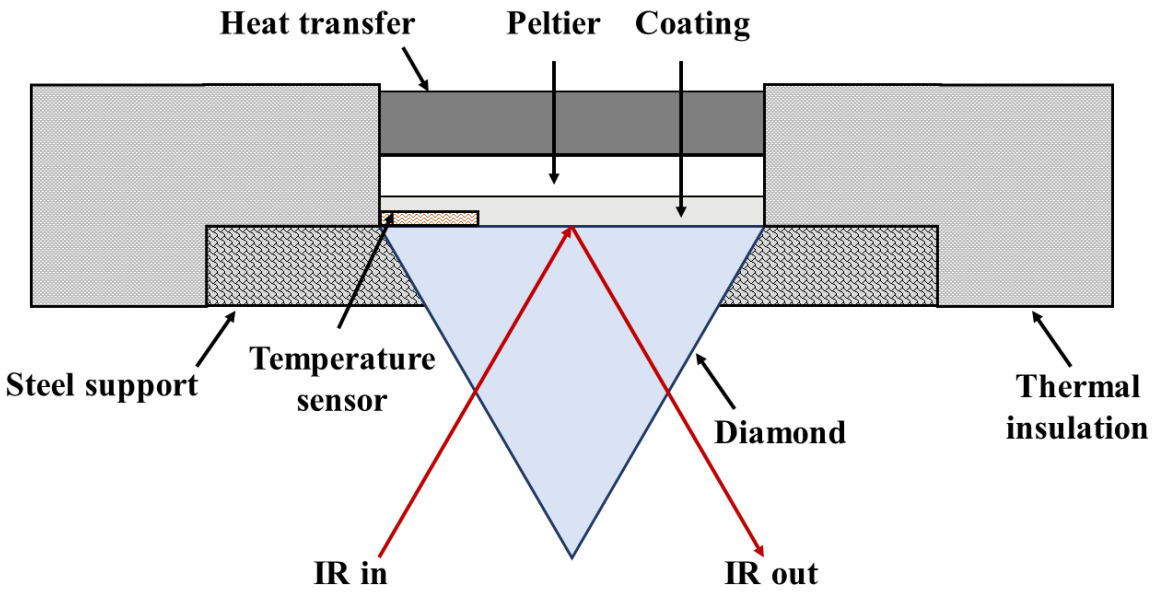

Figure 5-1: Schematic representation of the cold-based apparatus used for low-temperature ATR-FTIR spectroscopy.

5.3.6.5 Anti-frosting properties

The anti-frosting properties of the DES-containing coatings were tested in a cold chamber with programmable temperature and humidity controls. Coatings were applied to a Peltier cooling stage set at −20 °C. The chamber was cooled to 0.0 ± 0.5 °C with precise airflow, measured by an anemometer or velometer (±0.05 m/s). Humidity was created using a saturated water vapor generator and monitored by a calibrated sensor, achieving between 80% and 98% relative humidity at 0 °C. Before testing, all samples were thoroughly cleaned to remove visible contaminants. Once the test plate reached the desired temperature, the coated samples were placed on the Peltier stage. This process was repeated seven times for each sample to evaluate their effectiveness in delaying frost formation.

5.3.7 Mechanical characterization

5.3.7.1 Tensile strength

The tensile test was conducted at room temperature using a TA.XTPlus 100 machine (TA.TX Plus100C, Stable Micro System, Godalming, UK) with a 5 kg load cell. The free films used for the measurements were 10 ± 0.5 mm long, 1 ± 0.1 mm wide, and 2 mm thick. Five free films were prepared for each coating, and they were subjected to testing at a speed of 50 mm/min.

5.3.7.2 Weathering test

A QUV-accelerated weathering tester was used to investigate the effect of UV light and moisture condensation on the degradation of the formulated coatings and the subsequent ice adhesion strength after icing/de-icing cycles. The testing procedure used UVA-340, UVA-351, and UVB-313 fluorescent lights in compliance with ISO 11507 standards. The test comprised an 8 h cycle with 400 h of UV light exposure (UVA-365 radiation meter from LUTRON Co., Taiwan) at a temperature of 60 °C and an irradiance of 0.71 $W \cdot m^{-2}$, followed by 4 h of condensation at 50 °C.

5.3.7.3 Pendulum hardness

The surface pendulum hardness of DES-containing coatings was assessed as a representative indicator of surface response to deformation, both before and after exposure to QUV. A BYK-Gardner Byko-Swing (5867) Konig/Persoz hardness tester (byko-swing Persoz, Byk-Gardner, Columbia, MD, USA) was used for these measurements. The number of swings at 4° (Persoz mode), representing the surface hardness of the formulated coatings,

was analyzed in accordance with ASTM D4366 standards. The reported measurements represent an average of five data points.

5.4 Results and Discussion

5.4.1 Coatings characterization

5.4.1.1 Surface properties

Our objective was to uncover how various HBDs within the IL-DES system influences the interaction of water droplets with the coatings through hydrogen-bonding. To achieve this, we began by examining the surface chemistry of the polyurethane coatings incorporating the IL and two different DESs using FTIR spectroscopy (Figure 5-2a). Following this, we assessed the coatings' wetting behavior by measuring the WCA and the SA (Figure 5-2b).

(a)

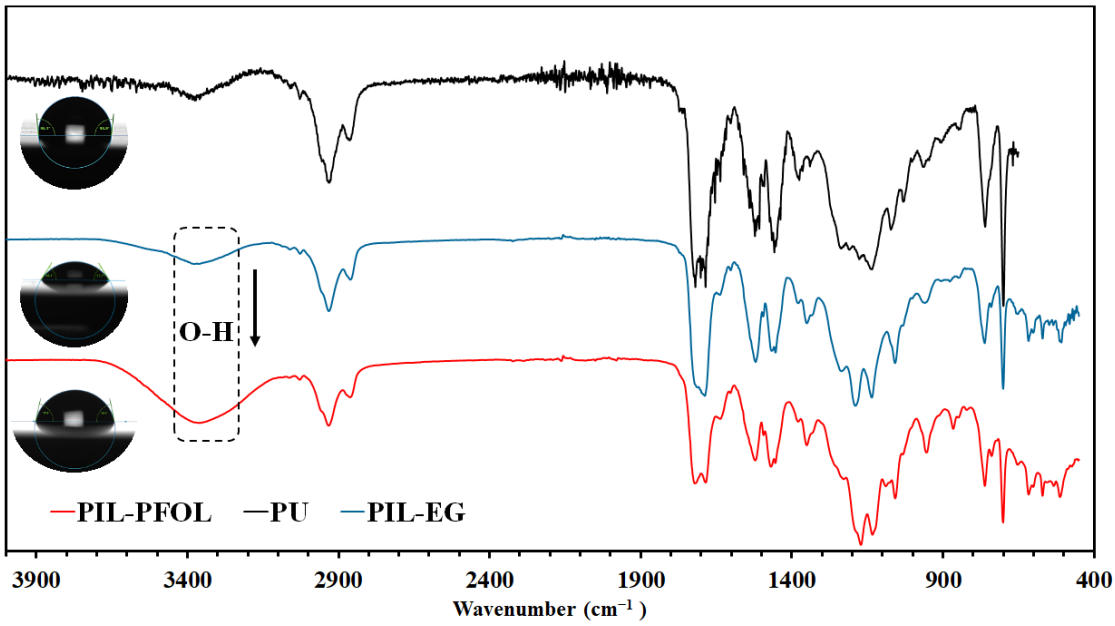

(b)

PU-based coatings	PU	PIL-EG	PIL-PFOL
WCA (°)	95 ± 1.5	57 ± 2.1	78 ± 2.5
SA (°)	33 ± 2.6	9.5 ± 1.8	12 ± 2.5

Figure 5-2: Surface (a) chemistry and (b) wetting characteristics of the PU coatings.

As indicated in Figure 5-2a, the vibrational peaks corresponding to the O–H group in the 3300–3400 cm^{-1} range for the coatings were presented upon the inclusion of the DES [390]. This distinctive peak was clearly observed in the samples containing DESs, underscoring the potential of hydrogen-bonding interactions. Notably, the pronounced peak in this range for the PFOL-based DES may suggest a relatively stronger hydrogen-bonding interaction between the PFOL-based DES and the IL on the surface, relative to the EG-based DES [414]. Thus, it was not unexpected that we observed a significant decrease in the WCA

in PU formulations incorporating either PFOL or EG-based DES. The WCAs were 78° ± 2.5 and 57° ± 2.1, respectively. Additionally, the SA of the coatings containing DESs decreased by more than 50% relative to the PU, for instance PIL-EG with the SA reaching a value of 9.5° ± 1.8.

Given the significant influence of fluorinated groups on the wetting behavior of the coatings, we ran XPS to detail the surface chemistry of the PU, PIL-EG, and PIL-PFOL coatings (Figure 5-3 and Figure 5-4). The spectra of PU coatings with and without IL/DESs presented distinct peaks that corresponded to C 1s, O 1s, F 1s, and N 1s at their respective binding energy positions (BE) (Figure 5-3a–c). Notably, the PIL-PFOL sample had BE peaks at 689.60 eV, representing F 1s, which correlated with the higher WCA observed for this coating than for the one containing EG-based DES (Figure 5-3c).

To investigate surface morphology, SEM imaging was conducted on the PIL-PFOL coating (Figure 5-3d), which exhibited a heterogeneous and likely porous structure. Cross-sectional micrographs of the freeze-dried coating confirmed its porous and 3D structure, consistent with findings from our previous research on coatings with DESs [39]. The unique morphology of the PIL-PFOL coating is attributed to the formation of a 3D network structure with randomly distributed pores, resulting from the development of hydrogen bonds between the DES, IL, and the matrix [415].

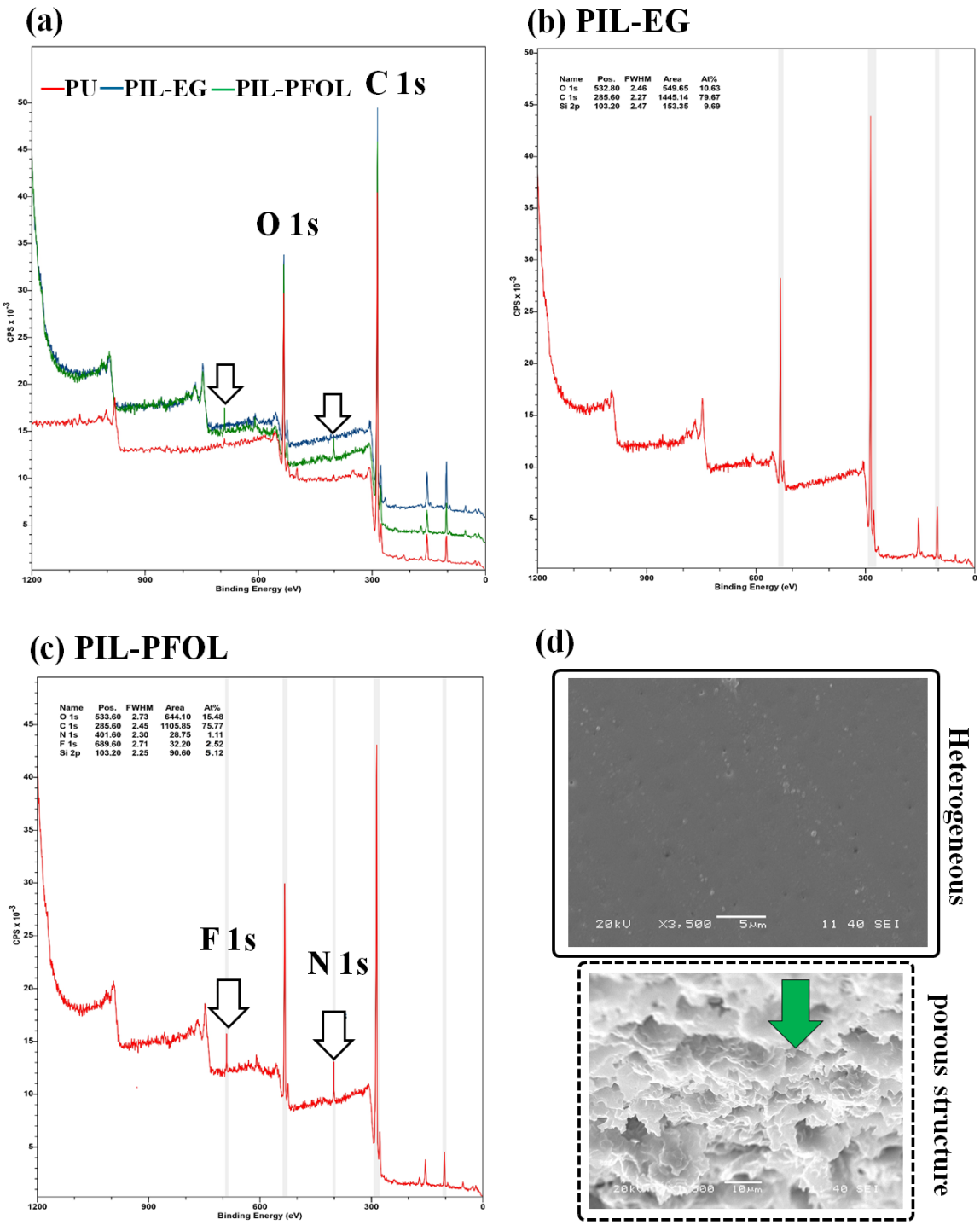

Figure 5-3: (a–c) XPS spectra of the coatings and (d) surface morphology and cross-sectional images of the freeze-dried PIL-PFOL coating.

High-resolution XPS spectra of PIL-PFOL for C 1s, O 1s, F 1s, and N 1s are shown in Figure 5-4a-d. According to the curve fitting of C 1s, the BE of the carbon peak displayed four distinct peaks at 285.4, 286.8, 287.9, and 290.2 eV, corresponding to different carbon components within the coating [441]. The BE peak at 290.2 eV (Figure 5-4a) is attributed to the C-F bond on the surface of PIL-PFOL. For this sample, the F 1s spectrum likely split into four distinct peaks, each potentially associated with fluorine-containing components. This indicates that approximately 3.5% of the signal might be attributed to both the IL and the HBD in DES (Figure 5-4c). Furthermore, curve fitting for the N 1s and O 1s spectra each exhibited multiple peaks (Figure 5-4b, d), suggesting that IL/DES incorporated into PU results in C-OH groups related to ChCl or HBD (PFOL). According to observed C-F and O-H moieties at distinctive BEs, these groups might be responsible for forming hydrogen bonds on the surface of PIL-PFOL [442].

Choline chloride (ChCl), functioning as a HBA, can form hydrogen bonds with HBDs such as PFOL and EG, to create a 3D supramolecular network [410]. Molecular simulations reveal that HBDs influence the structural organization within the eutectic mixture [411]. The presence of non-covalent interactions, such as hydrogen bonding and London dispersion forces, enhances solvation effects [228], similar to those seen in DES–IL combinations [410]. This is further affected by the high electronegativity of components in DESs, which introduces additional hydrogen-bond sites, thereby influencing the freezing points of the mixtures through charge delocalization.

The IL with larger, less asymmetric anions display stronger hydrogen-bond donor capabilities, which produces competitive hydrogen-bonding between the IL and DES [37,410]. The lower WCAs of these surfaces indicate the formation of a new deep eutectic

mixture with abundant sites for ionic hydrogen bonding with water molecules. Conversely, coatings having higher fluorine content, such as those with the PFOL-based DES, showed greater hydrophobicity and higher WCAs than coatings containing EG-based DES [37,253].

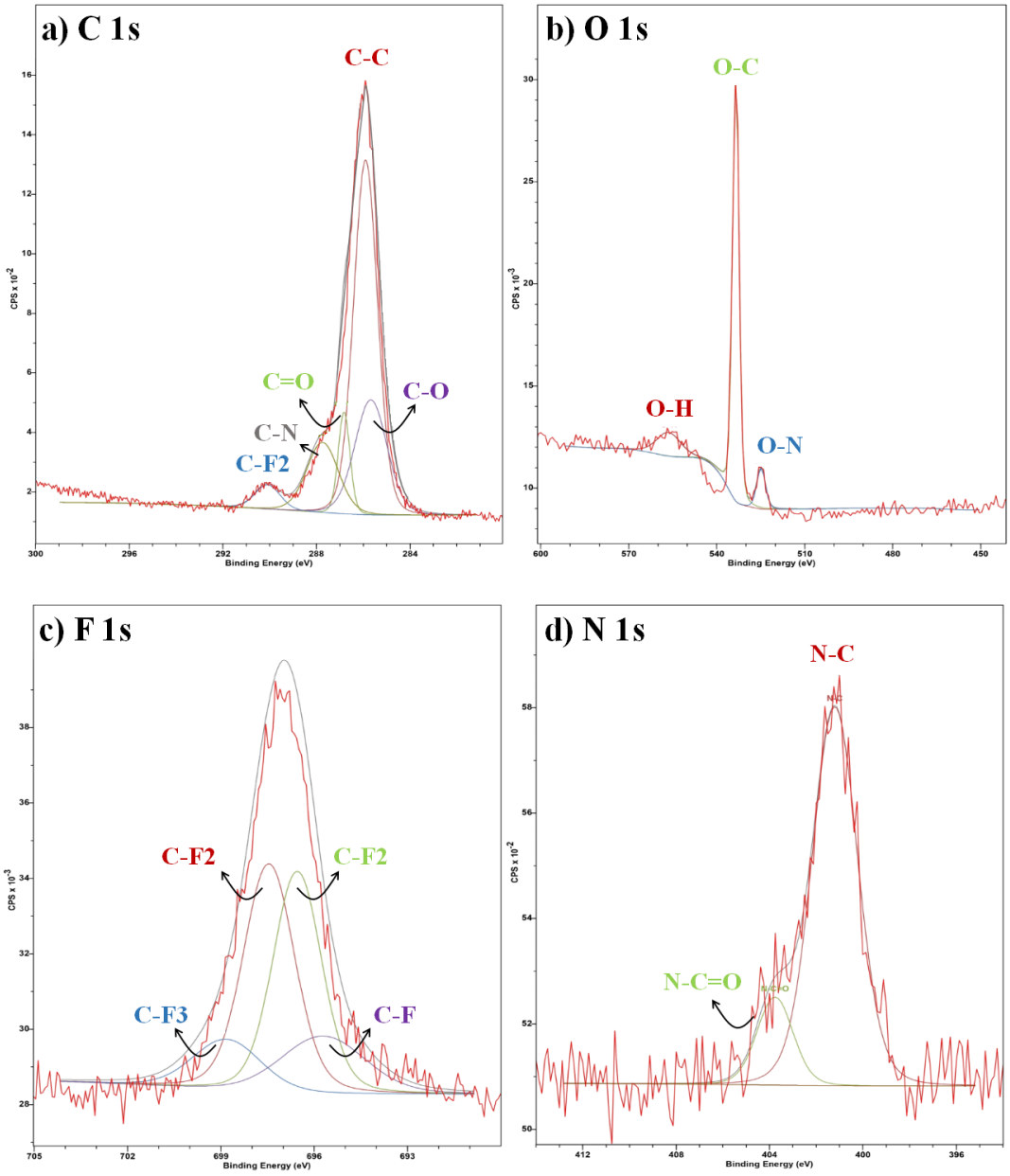

Figure 5-4: High-resolution spectra of the PIL-PFOL coating for (a) C 1s, (b) O 1s, (c) F 1s, and (d) N 1s.

5.4.1.2 Anti-icing properties

We ran DSC to determine the ice formation temperature on the surface of the PU coatings. The potential of forming hydrogen-bonding networks on the surface of the PIL coatings, particularly PFOL-based DES drived us to examine the effect of hydrophobicity of HBDs in DESs on both ice formation temperature and adhesion strength. We recorded a significant decrease in ice formation temperature (−35 °C) simply by substituting the HBD component with PFOL (Figure 5-5a). This considerable decrease in temperature indicates an intensified hydrogen-bonding network within the PFOL-based DES. Moreover, push-off testing of the coatings with PFOL-based DES demonstrated a low ice adhesion strength of approximately 13 kPa (see the table in Figure 5-5a). The coating's marked decrease in the freezing point of water and exceptional ice adhesion reduction result from the significantly enhanced hydrogen-bonding network within this DES relative to the EG type and the resulting thicker QLL (Figure 5-5b) [410].

When we compare the PIL coatings containing EG- and PFOL-based DES, the substantial influence of PFOL in enhancing hydrogen-bond formation with water becomes apparent. Given that the bulk structure of HBDs is largely maintained for hydroxyl-based HBDs such as PFOL-, glycerol-, and EG-based DESs [416], the results suggest that PFOL had improved anti-icing properties relative to EG (Figure 5-5b).

(a)

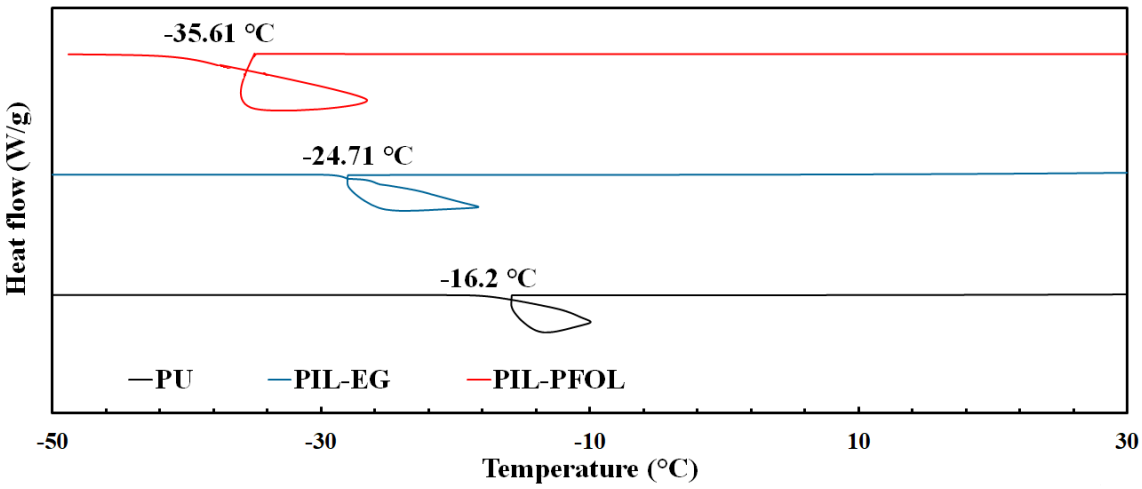

PU-based coatings	PU	PIL-EG	PIL-PFOL
Ice adhesion strength (kPa)	320.5 ± 12.4	39.4 ± 4.65	13.7 ± 7.13

(b)

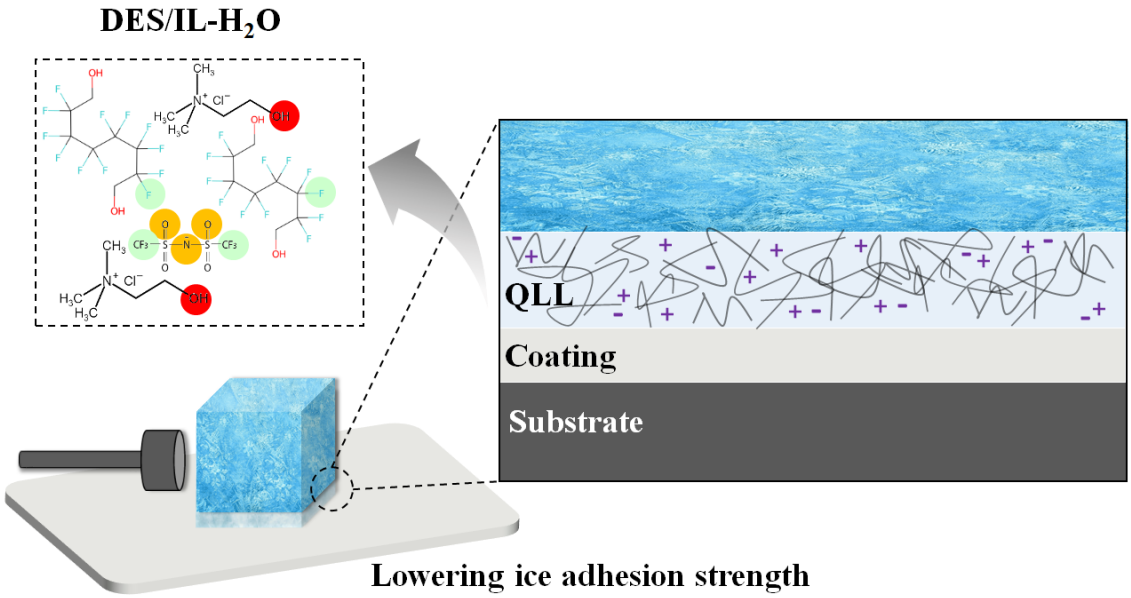

Figure 5-5: (a) Ice formation temperature and adhesion strength of PU coatings, (b) diagram depicting the reduction of ice adhesion strength in the presence of IL/PFOL-based DES because of a QLL formed at the interface.

The DSC heating curves that depict the melting temperature of frozen water, both with and without DES, provide a foundation for investigating the unique capabilities of DESs in facilitating ice melting [418]. The heating curves of DESs (Figure 5-6a) show that the melting onset temperature decreased markedly from −0.89 °C (frozen water) to −22.85 °C and −30.80 °C for the water/EG-based and water/PFOL-based DESs, respectively. This large shift stems from the formation of an exceptional hydrogen-bonding network with water, which was especially evident in the PFOL-based DES and water mixture. Another key feature of DESs is their high heat capacity [392,419]. The thermal properties of DESs were elucidated through DSC heating and cooling curves (Figure 5-6b and Figure 5-6c). These curves showed the behavior of dry eutectic mixtures at slow scan rates of 2.5°C/min, indicating multiple thermal events because of eutectic melting and the dissolution of the excess component. The thermal behavior of choline-based DESs can vary because of their ratio and amount of water present [420]. Interestingly, DESs can show similar characteristics to phase change materials, particularly in terms of their high latent heat of fusion and melting temperature within the desired operating range [421,422]. DESs therefore offer significant potential for applications that require performance at low temperatures.

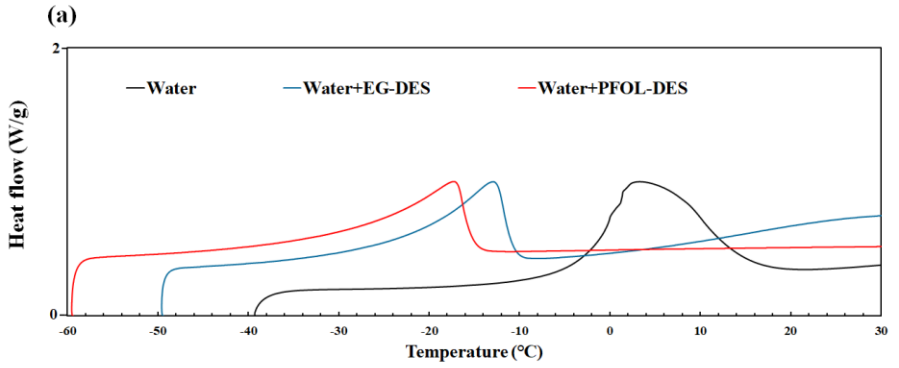

Samples	Water	Water + EG-DES	Water + PFOL-DES
Onset of Melting (°C)	-0.89 ± 0.12	-22.85 ± 0.49	-30.80 ± 0.58
Peak temperature (°C)	3.59 ± 0.19	-13.09 ± 0.41	-17.29 ± 0.37

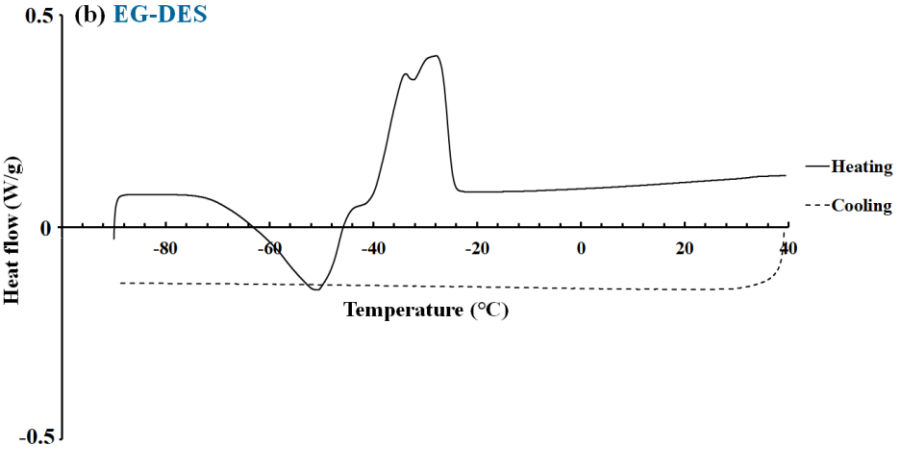

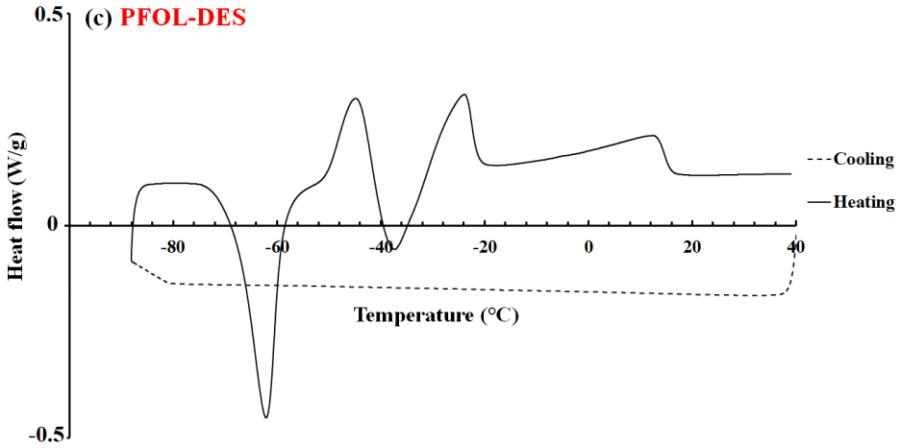

Figure 5-6: DSC heating curves analyzing the thermal properties of DESs (a) with water and (b) without water.

5.4.1.3 QLL characterization

DESs promote intricate molecular arrangements. These patterns enhance the QLL at the interface by creating an extensive hydrogen-bonding network to produce coatings with significantly lower ice adhesion strength; this finding highlights a potentially major advancement in anti-icing technologies [197,228,410].

We ran Solid-state NMR (Figure 5-7) and low-temperature ATR-FTIR spectroscopy (Figure 5-8, Figure 5-9 and Figure 5-10) to characterize the nonfrozen QLL at the bulk water–coating interface. Initially run at 276 K, the ^{1}H spectra assessed the bulk water characteristics (with water ^{1}H chemical shifts around 5.0 ppm) before the freezing onset for the PU + water, PIL-EG + water, and PIL-PFOL + water samples. Upon further cooling to subzero temperatures (253 K) and after a 3 h stabilization period, the water ^{1}H signal strength significantly diminished in the PU sample. As temperature decreased, larger water ^{1}H chemical shifts were particularly evident in the DES-containing coatings. These shifts stem from the enhanced hydrogen-bond formation at lower temperatures, which affects the shielding and deshielding of water protons [17].

As the temperature fell below 0 °C, the signal strength for nonfrozen water in PU coatings decreased, indicating less nonfrozen water. However, in coatings with PFOL-based DES, this signal persists at 253 K, suggesting a thicker quasi-liquid layer because of enhanced hydrogen bonding. This layer, present at temperatures as low as −20 °C, acts as a self-lubricating interface to significantly reduce ice adhesion strength [342].

The ^{1}H T_2 relaxation time, inversely related to viscosity, quantitatively highlights the viscosity increase near the interface, where water molecules have a significantly lower

configurational entropy than in bulk water; thus, viscosity increases [37,38]. Notably, the persistence of the water ^{1}H signal at temperatures down to 253 K in coatings with PFOL-based DES, coupled with a more pronounced decrease in T_2 relaxation time, underscores the superior hydrogen-bond donor capacity of the PFOL-based DES/IL combination.

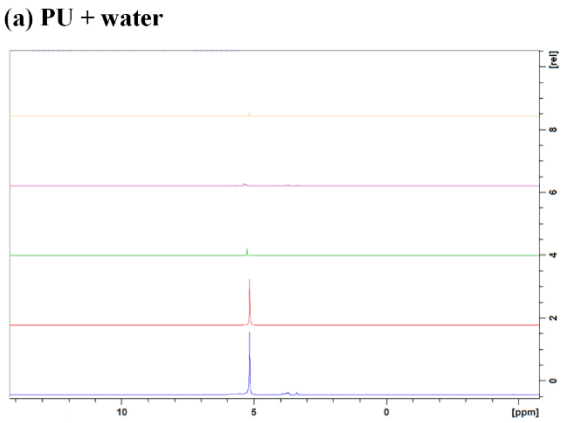

(d) T_2 Relaxation time measurement

PU-based coatings	T_2 Relaxation time (ms)				
	Temperature (K)				
	276	268	263	258	253
PU	221	58	-	-	-
PIL-EG	124	100	60	59	-
PIL-PFOL	94	81	51	44	33

Figure 5-7: ^{1}H spectra acquired via SS-NMR spectroscopy for (a) PU + water; (b) PIL-EG + water; (c) PIL-PFOL + water; and (d) T_2 relaxation time measurements, spanning temperatures from 276 K (blue) to 253 K (yellow).

The evanescent wave of the reflected IR beam served as a precise method to probe functional groups located near the ATR crystal–sample interface. We selected this approach because of the temperature-dependent behavior of the OH stretching absorbance band of H2O (3307 cm^{-1}), which shifts to a lower frequency (3162 cm^{-1}) and becomes sharper upon freezing, making it challenging to distinguish from other peaks. D_2O, chosen for the

favorable freezing properties of the O-D stretching absorbance band, was used [443]. Figure 5-8, Figure 5-9 and Figure 5-10 illustrate the ATR-FTIR spectra of the PU/D_2O, PIL-EG/D_2O, and PIL-PFOL/D_2O coatings at different temperatures during the cooling process. In Figure 5-8a and Figure 5-8b, for the PU coating, the O-D stretching band of liquid D_2O at 25 °C appeared at 2489 cm^{-1}, similar to bulk D_2O but with a slight shift because of interactions with the coating. Upon freezing at −10 °C, this peak shifted to 2220 cm^{-1}, indicative of the solid-state O-D stretching band, accompanied by a gradual decrease in intensity at 2489 cm^{-1} and an increase at 2220 cm^{-1}. The presence of the liquid O-D stretching band within the temperature range of the D_2O melting point (3.8 °C to −10 °C) [444] indicates the presence of absorbed D_2O as a QLL in the supercooled state. The respective position and intensity of the peaks exhibited minimal change from −10 °C to −20 °C, indicating that the QLL freezes at temperatures below −10 °C in pure PU. This temperature dependence is also evident in Figure 5-9a-d.

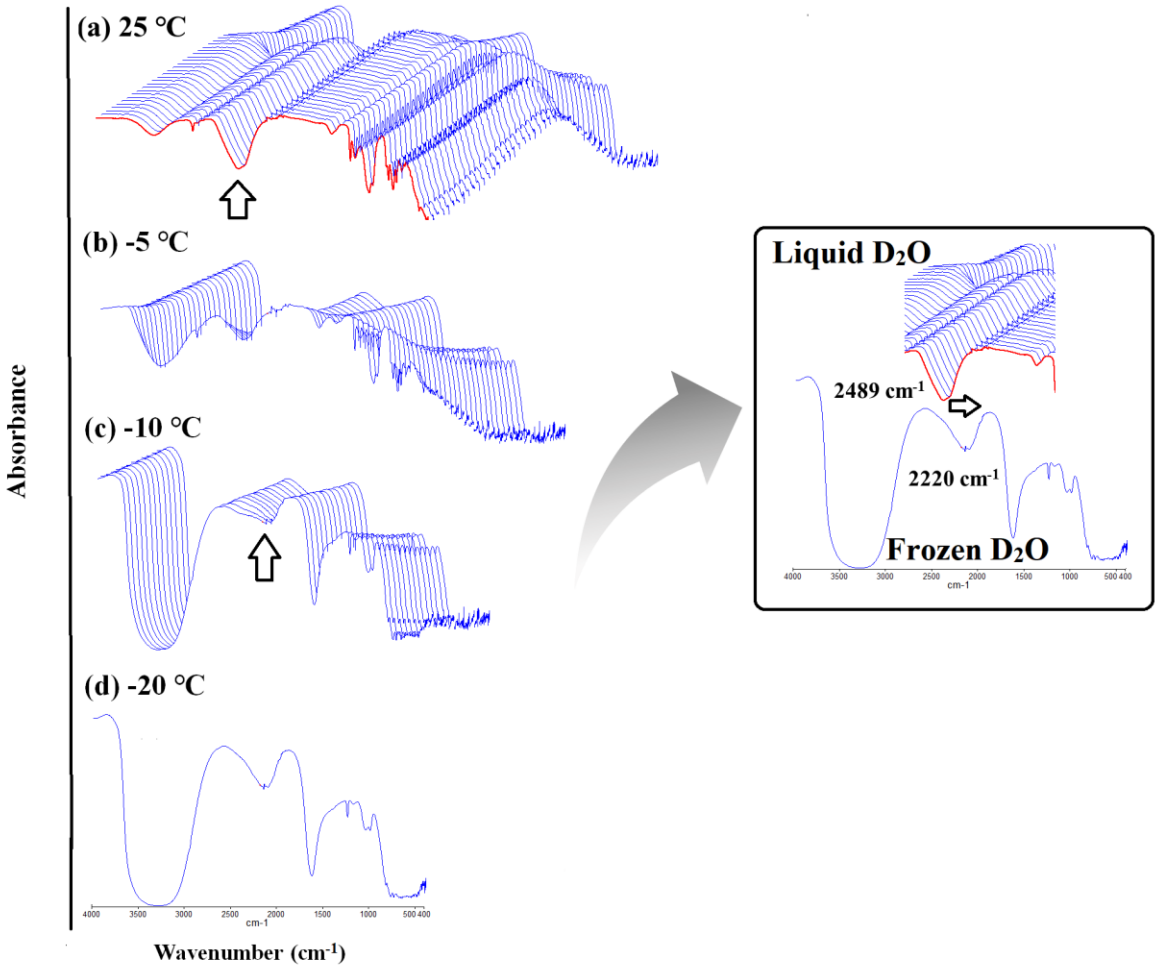

Figure 5-8: ATR-FTIR spectra of the PU/D_2O coating recorded at different temperatures during the cooling procedure.

The O-D stretching band of D_2O in the PIL-EG coating underwent a notable shift from 2495 to 2000 cm^{-1} during the phase change observed between −20 °C and −25 °C. The spectra remained consistent at temperatures below −24 °C. This static nature indicated the freezing of surface-absorbed D_2O, which was facilitated by the robust hydrogen-bonding network within the IL/EG-based DES and water. Interestingly, in the PIL-PFOL coatings, the O-D stretching band of D_2O exhibited an extraordinary shift from 2487 to 1990 cm^{-1} between −34 °C and −36 °C and then remained relatively constant at temperatures below −34 °C (Figure 5-10a-e). This pattern demonstrates that the freezing of the interfacial

absorbed D_2O because of the exceptionally strong hydrogen-bonding network within the IL/PFOL-based DES and water, surpassing that of the EG-containing coatings.

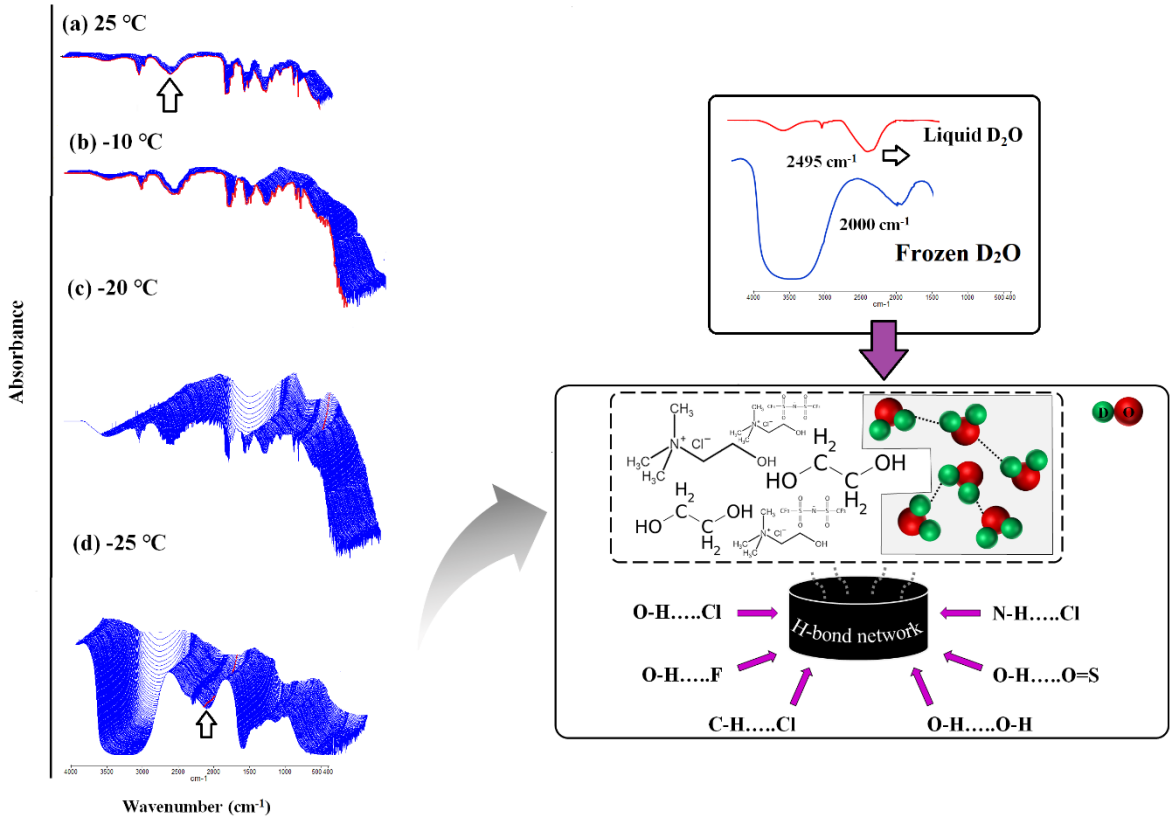

Figure 5-9: ATR-FTIR spectra of the PIL-EG/D_2O coating recorded at different temperatures during the cooling procedure.

The difference in the temperature at which the peak shift occurs in the O-D stretching band between the unmodified and modified PU coatings, marking the phase change of D_2O, can be explained by the presence and increased thickness of the QLL on the surface of the PIL-PFOL coating, along with its interactions with the coating material. These interactions of the QLL likely inhibit the formation and growth of ice crystals at the interface by disrupting the orderly arrangement of water molecules required for ice formation.

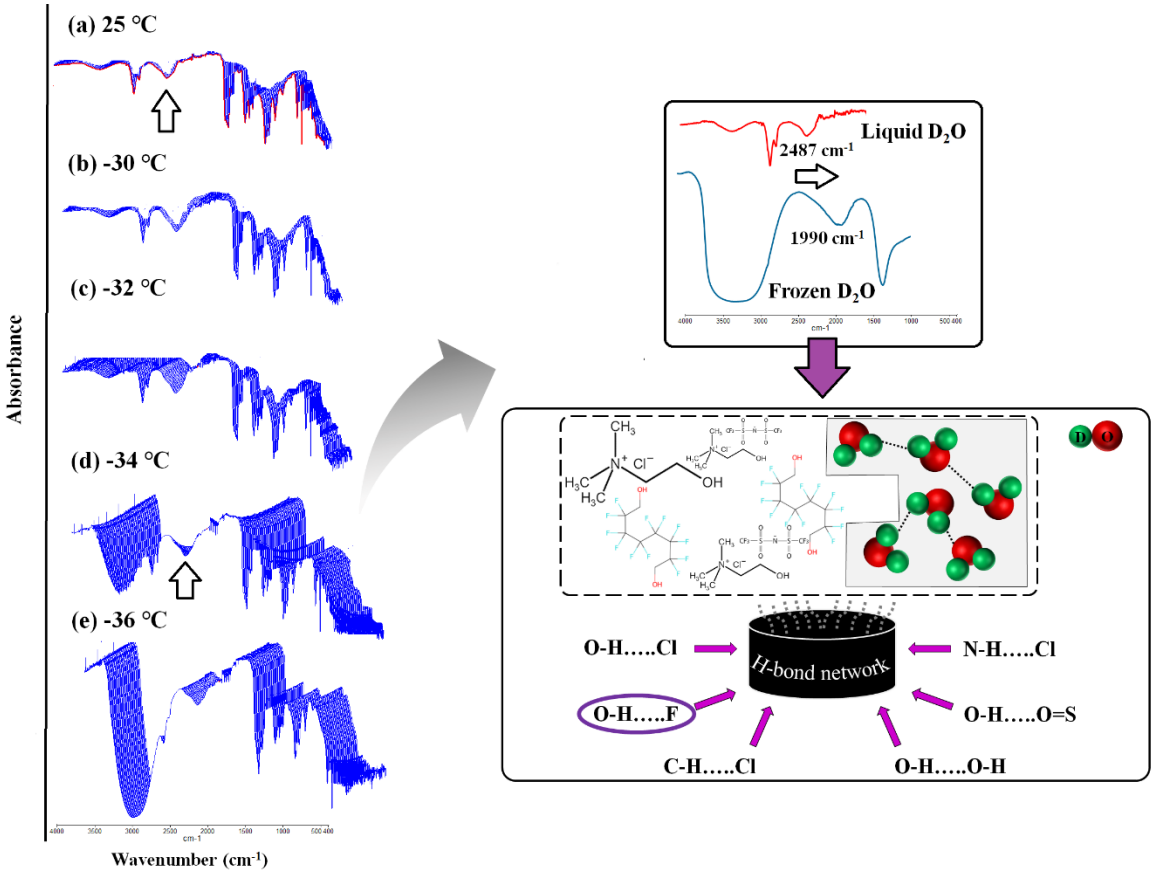

Figure 5-10: ATR-FTIR spectra of the PIL-PFOL/D_2O coating recorded at different temperatures during the cooling procedure.

5.4.1.4 Mechanical properties

The mechanical properties of coatings are intricately linked to the arrangement and density of both intermolecular and intramolecular interactions within the network. Upon evaluating the coatings, we observed a reduced tensile strength and an increased elongation-at-break when we added IL/EG-based DES to PU (Young's modulus = 10.7 MPa ± 0.15, Figure 5-11). These changes reflect the plasticizing effect exerted by IL, which enhances chain mobility within polymer films. Similarly, coatings containing the PFOL-based DESs also exhibited higher elongation, attributed to the plasticizing roles of ILs and DESs [423,424]. Furthermore, the tensile strength of PIL-PFOL, with a Young's modulus of 12.8

MPa ± 0.95, surpassed that of coatings containing EG-based DES (Young's modulus = 7.05 MPa ± 0.24). This difference likely arises from hydrogen bonding facilitating the partial crosslinking between PU chains, thereby restricting their mobility [425,426].

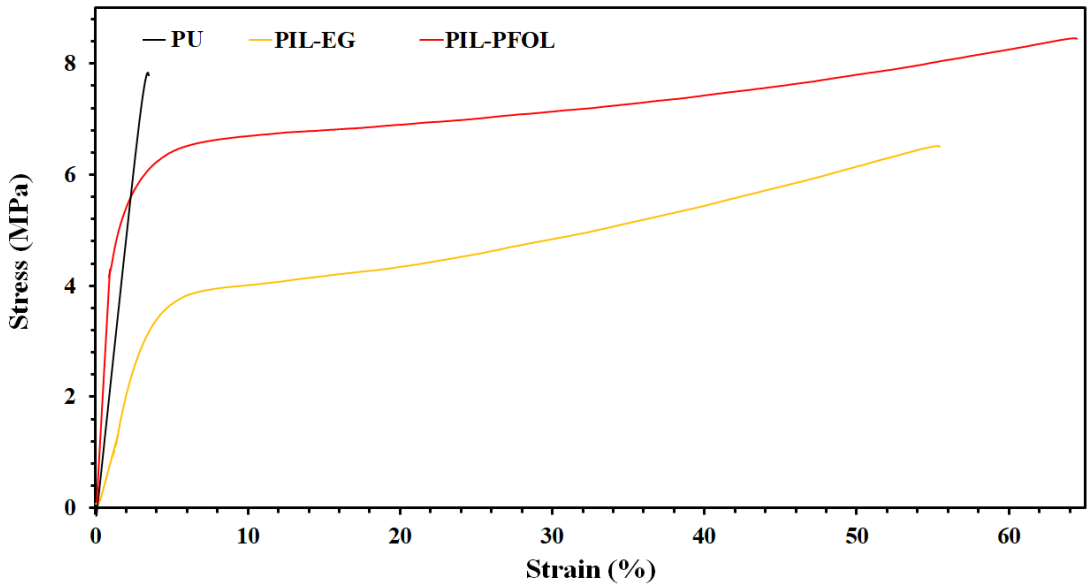

PU-based coatings	PU	PIL-EG	PIL-PFOL
Tensile strength (MPa)	8.5 ± 0.5	6.8 ± 0.2	8.2 ± 0.3
Elongation (%)	5.2 ± 0.1	59.3 ± 1.7	65.7 ± 1.09

Figure 5-11: Mechanical properties of developed coatings containing various DESs, obtained by tensile strength test.

Ice adhesion strength was evaluated over multiple icing/de-icing cycles and under accelerated weathering conditions for the coatings. We applied a push-off test to measure the ice adhesion strength over 20 cycles. The PU coatings showed a consistent performance with minimal variability (Figure 5-12a). Notably, the PIL-PFOL coating exhibited an ice adhesion strength below 20 kPa throughout these cycles.

We then assessed the effect of accelerated weathering conditions on ice adhesion strength after 20 icing/de-icing cycles. PIL-PFOL coatings again demonstrated enhanced resistance to accelerated UV light and high humidity conditions (Figure 5-12). Surface roughness analysis using 3D profilometry indicated increasing roughness for this coating (Sq, root mean square roughness parameter). The inherent plasticizing effect of ILs and DESs reduced surface hardness in the coatings that incorporated these components (Figure 5-12a).

(a)

PU coating	Surface hardness (4° persoz)		Ice adhesion strength (kPa)		
	Before QUV	After QUV	Cycle 0	Cycle 20	After QUV
PU	130.3 ± 4.5	121.9 ± 3.88	320.5 ± 9.6	360.84 ± 6.84	375.4 ± 8.47
PIL-EG	95.64 ± 3.75	92.26 ± 2.92	39.4 ± 5.32	49.3± 5.98	55.1 ± 6.5
PIL-PFOL	115.14 ± 2.33	110.28 ± 3.12	13.7± 7.13	18.1 ± 3.4	20.9 ± 4.01

(b)

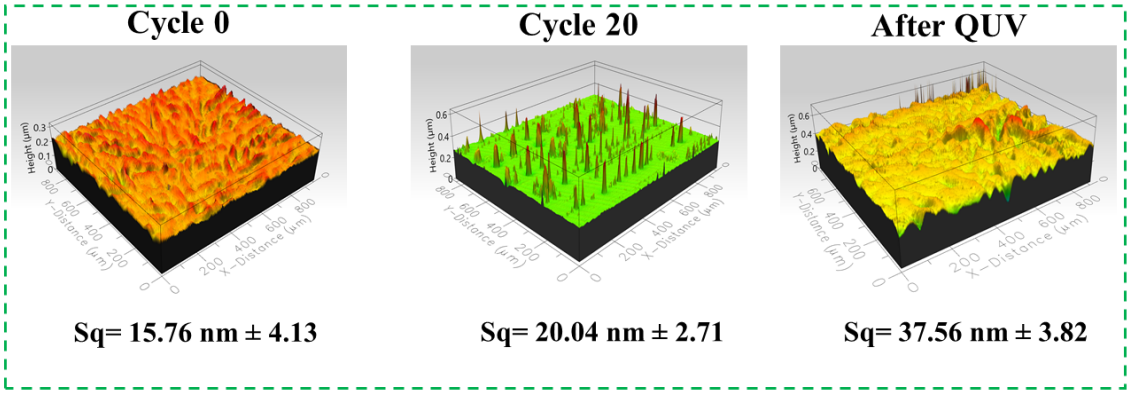

Figure 5-12: (a) Ice adhesion strength and surface hardness of PU coatings exposed to 20 icing/de-icing cycles before and after QUV, as obtained by a push-off test; and (b) 3D profile maps of PIL-PFOL coating samples before and after icing/de-icing cycles.

5.4.1.5 Anti-frosting ability of PU coatings

We subjected the PU coatings to a cold chamber at an air temperature of 0 °C, plate temperature at −20 (± 0.1) °C, and 98% RH during each repeat. A notable shift in the amount of accumulated frost was observed for the PU coatings upon reaching the designated

temperature during the cycles (Figure 5-13a). The DES-containing coatings exhibited a significantly delayed frost formation over the seven cycles. Among all the coatings, the PIL-PFOL sample had the lowest amount of accumulated frost and the highest resistance to frost formation. Additionally, the frost formation pattern on DES-containing coatings became more pointed and localized. In the initial cycles, a bridge-like structure formed on the PU surface during frost formation (Figure 5-13b). Our observations demonstrate the exceptional effectiveness of DESs, particularly PFOL, in enhancing surface resistance to frost formation, marking a substantial advancement in coating technologies [270].

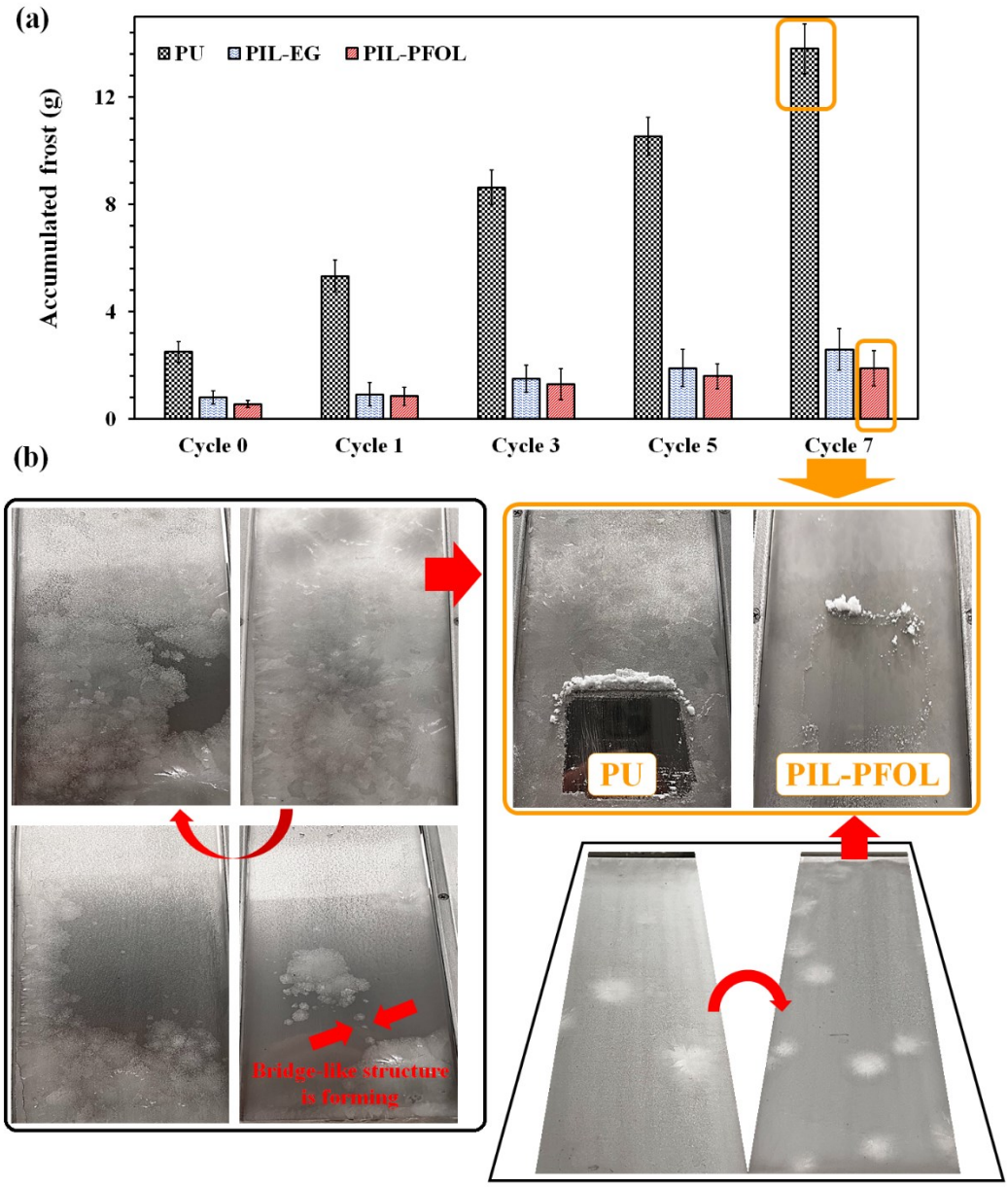

Figure 5-13: (a) The time required for frost formation on coatings during seven frost/defrosting cycles; and (b) corresponding images of the coatings during frost formation.

5.5 Conclusion

Combining multiple ice-responsive materials can enhance the effectiveness of anti-icing surfaces, provided that these materials complement each other without reducing their individual performance. In our study, we combined IL-containing coatings with either EG-

based or PFOL-based DESs, resulting in ice formation temperatures of −24 °C for the PIL-EG system and −35 °C for the PIL-PFOL system. We performed a thorough characterization of the coatings by running SEM, XPS, wettability measurements, and surface roughness analysis, as well as testing hardness, ice adhesion strength against accelerated weather conditions, and tensile strength. Our observations of these surfaces identified the critical role of hydrogen bonding in developing DESs with strong anti-icing properties. After substituting EG with PFOL in the DESs, the coatings exhibited an exceptionally low ice adhesion strength. This improvement is attributed to the formation of a thicker QLL, which acts as a self-lubricating interface, confirmed by solid-state NMR spectroscopy. At nonfreezing temperatures, the PIL-PFOL sample retained more nonfrozen water than PU samples that lacked DES/IL, aligning with our low-temperature ATR-FTIR spectroscopy observations. We identified this increased nonfrozen water presence as the main reason for the delayed ice nucleation and reduced adhesion. DSC demonstrated how this hydrogen-bonding network lowered the melting onset temperature from −0.89 °C for pure water to −30.80 °C for the water/PFOL-based DES. The inherent plasticizing effect of IL and DESs increased the elongation-at-break for modified coatings, whereas the tensile strength of the PIL-PFOL coating remained unchanged to that of PU. Because of the unique thermal characteristics and superior hydrogen bonding of these coatings, particularly for the PIL-PFOL sample, surfaces had minimal frost accumulation and altered frost formation patterns relative to the reference samples. Ultimately, a synergistic hybrid surface, such as the coating presented here, can deepen our understanding of anti-icing solutions and lead to the development of coatings having enhanced icephobic capabilities.

Acknowledgments

The authors acknowledge all support from the Natural Sciences and Engineering Research Council of Canada (NSERC) and Université du Québec à Chicoutimi (UQAC). The authors would also like to express their gratitude to Alexandre Arnold, Department of Chemistry at UQAM, for conducting and helping with SS-NMR spectroscopy. The authors also wish to thank Caroline Blackburn, Shan Yang, and Dr. Jean-Denis Brassard in the Anti-icing materials international laboratory (AMIL-UQAC) for helping with the anti-frosting test. The authors express their sincere gratitude to Pascale Chevallier at Laval University for performing the XPS analysis.

CHAPTER 6

6. CONCLUSION

This Ph.D. thesis tackles the ongoing challenges of ice formation and surface icing across multiple industries by exploring the development of advanced passive anti-icing technologies. Through a comprehensive investigation of ionic liquids (ILs), which have recently emerged as state-of-the-art, ice-responsive materials, this work highlights their unique ability to mitigate frozen surfaces by precisely controlling molecular interactions at the interface. This innovative approach provides unparalleled control over ice formation, positioning ILs as key players in the future of cutting-edge anti-icing technologies. The research journey comprises interconnected chapters that explore the mobility and physicochemical properties of ILs and their contribution to anti-icing capabilities. By examining IL chemistry and its impact on coating performance, the study analyzes key factors affecting ion mobility, including IL properties and matrix hydrophilicity/hydrophobicity. The findings highlight the importance of matrix selection and IL chemistry in advancing coatings for extreme cold environments. Additionally, the potential of deep eutectic solvents as alternative or supplementary agents for efficient ice tackling is emphasized. Subsequent phases involved the synthesis and characterization of choline-based ILs with hydrophilic and hydrophobic anions. The integration of these ILs with

choline-based DESs, which offer diverse hydrogen-bond donors, aims to enhance the system's hydrogen-bonding capabilities and improve the anti-icing properties of the surfaces.

First and foremost, our research focuses on developing innovative anti-icing coatings incorporating novel room temperature ionic liquids (RT-ILs). Using advanced analytical techniques such as ATR-FTIR, XPS, SEM/EDX, and solid-state NMR spectroscopy, we confirmed the presence of these ILs on coating surfaces. These ILs form ionic hydrogen bonds with water molecules, lowering the ice nucleation temperature and creating an unfrozen quasi-interfacial liquid layer (QLL) at low temperatures. This layer facilitates interfacial slippage and reduces ice adhesion strength, enhancing anti-icing properties. Our findings in this phase seek to establish a rational understanding of the relationship between IL mobility, physicochemical properties, and their anti-icing behavior. Key findings reveal the importance of considering various physicochemical characteristics of ILs, including their solubility/miscibility in water, geometric structure, and mobility. The near-surface concentration of ILs is crucial in determining the structure of QLL and their anti-icing performance. The study highlighted that steric hindrance and intramolecular interactions affect IL mobility and the number of effective ions within a matrix. Thus, the miscibility of ILs with the matrix, particularly hydrophobic ILs in hydrophilic matrixes, should be evaluated in detail.

Building on the findings from the initial phase, we further investigated ion mobility by examining the impact of IL percentage, physicochemical properties, and matrix hydrophilicity/hydrophobicity. Using PU and Sylgard 184 as hydrophilic and hydrophobic matrixes, respectively, we found that coatings containing 1-ethyl-3-methylimidazolium bis(trifluoromethanesulfonyl)imide, particularly the PU matrix, exhibited significant

reductions in both ice formation temperature and ice adhesion strength. This improvement was due to the creation of stronger ionic hydrogen-bond networks and thicker QLLs within the PU matrix. Dielectric spectroscopy findings showed stable conductivity at low temperatures as the benchmark of ions mobility, ensuring stable anti-icing performance. Comprehensive analyses of ILs released from non-stoichiometric coatings and their UV absorbance and ionic conductivity highlighted the superior mobility of this IL. Over icing/de-icing cycles and exposure to weathering, coatings containing this IL stabilized their ice adhesion strength, particularly in PU-based coatings. These findings highlight the pivotal role of matrix and IL selection in advancing coatings for extreme cold conditions. Future research could explore aliphatic-based ILs, instead of aromatic and enhance mechanical durability in icing conditions.

Hence, our study in third phase begins with the synthesis and characterization of aliphatic choline-based ILs harboring hydrophilic and hydrophobic anions. We also investigated the anti-icing potential of DESs, focusing on the impact of the HBD component. Choline nitrate and choline TFSI, synthesized as ILs, were mixed with ethylene glycol-based DESs, improving the icephobicity. Altering the HBD component from diol to triol in DESs led to exceptionally low ice formation temperatures and ice adhesion strength, attributed to the thicker QLL acting as a self-lubricating interface. The synergistic effect of combined DESs and ILs improved anti-icing efficacy, with solid-state NMR spectroscopy confirming the formation of thicker QLLs, as well. DSC analysis demonstrated that the hydrogen-bonding network reduced the melting onset temperature to −0.93 °C for water and −30.97 °C for water/glycerol-based DES. These findings underscore the synergistic effect of combining DESs and ILs in enhancing anti-icing efficacy. The plasticizing effect of ILs and DESs, along

with increased rubber-like behavior in tensile strength, significantly lowered the Tg of the coatings, especially when DESs were incorporated. This lower Tg enhances chain mobility and hydrogen bonding at low temperatures, leading to superior anti-icing functionality. The enhanced functionality is further evidenced by the superior anti-frosting capacity of DES-containing coatings.

Similar to the third phase, combining multiple icephobic materials can enhance anti-icing effectiveness. In this phase, we evaluated the effect of hydrophobicity of HBDs, a fluorinated diol as a HBD on the anti-icing properties and compared it with ethylene glycol from the third phase. Mixing EG- or fluorinated diol-based DESs with optimized IL-containing coatings from the third phase resulted in exceptionally low ice adhesion strength and delayed ice nucleation. Comprehensive characterization, including SEM, XPS, wettability measurements, surface roughness analysis, and tensile strength tests, highlighted the critical role of hydrogen bonding in developing DESs with strong anti-icing properties. The inherent plasticizing effect of ILs and DESs increased the elongation at break for modified coatings, while the tensile strength of the coating containing the fluorinated diol remained unchanged compared to PU. Due to the unique thermal characteristics and superior hydrogen bonding of this sample, frost accumulation was minimized, and frost formation patterns were altered compared to references. Hence, a synergistic hybrid surface, like the coating presented in this study, can significantly advance our understanding of anti-icing technologies and contribute to the development of coatings with superior icephobic properties.

In conclusion, this research has made significant milestones in understanding how to create effective anti-icing coatings using ILs. By exploring different types of ILs and their

properties, we've gained valuable insights into their performance in freezing conditions. This study not only opens up new possibilities for tailoring ILs and DESs for specific needs but also offers promising directions for developing advanced passive anti-icing technologies. These advancements have real-world implications for industries dealing with ice formation and surface icing, paving the way for more efficient solutions in the future.

CHPATER 7

7. RECOMMENDATIONS

In this Ph.D. thesis, we report the fabrication of dynamic anti-icing surfaces containing ionic liquids through a comprehensive investigation and optimization of effective parameters. By exploring different types of ILs and their properties within various matrixes, we have gained valuable insights into their performance under freezing conditions. Additionally, our focus shifted towards DESs, an eco-friendly subset of IL analogues, to exploit the outstanding hydrogen-bonding networks through the synergistic combination of DESs and ILs. As the literature shows a limited body of work in this field, several suggestions for future research are worth considering:

i. **Exploration of Diverse ILs:** In this work, we utilized the most commonly used aromatic-based RT-ILs, as per the limited publications in this area. However, the IL world is vast, with significant potential in tunability and hydrophilicity/hydrophobicity. Other types of ILs with subzero or near-room-temperature melting points are promising candidates for further exploration.

ii. **Enhancing IL Stability:** Addressing the challenge of IL depletion or loss during operation, lubricant-absorbent materials could offer a new horizon for increasing the stability of ILs within the polymeric matrix and on the surface. For instance, aerogels or porous particles with controlled pore sizes and surface areas can be optimized for IL adsorption-desorption.

iii. **Encapsulation of ILs:** Encapsulating ILs in various shells, leveraging their unique chemistry and wide selection, could help retain ILs within the matrix while maximizing their other advantageous characteristics during operation.

iv. **Chemical Stabilization of ILs:** Currently, we incorporated ILs physically into the polymeric matrix. Chemically stabilizing ILs within the matrix, such as using polymerizable ILs or poly(ionic liquid)s (PILs), could enhance durability. PILs, with their high electrical conductivity, excellent thermal/mechanical stability, low vapor pressure, and easy processability, offer a versatile platform for green chemistry applications.

v. **Exploring Diverse Matrixes:** In this study, we employed PU and PDMS for fabricating IL-containing coatings. Given the diverse chemistry of ILs, various water- or solvent-based resins could be used to explore their anti-icing properties.

vi. **Improving Mechanical Properties:** Beyond the physicochemical properties of ILs and matrixes, enhanced mechanical properties are a top industry priority during operation and icing/de-icing cycles. Selecting compatible polymeric blends, inorganic absorbents, or micro/nanoparticles could lead to anti-icing coatings with remarkable mechanical robustness and sustainability. Additional tests like microindentation and dynamic mechanical analysis (DMA) could have provided more robust and precise insights into the hardness and crosslinking density of the coatings.

vii. **Broadening DES Chemistry:** Besides ILs, we employed common DESs based on choline chloride as environmentally friendly HBAs. Similar to ILs, the broad chemistry of DESs offers many options to explore their anti-icing or anti-freezing potential, from natural to synthetic variants.

viii. **Combining De-Icing Strategies:** We aimed to develop new dynamic anti-icing coatings using the synergistic effects of two icephobic materials. Other

anti-/de-icing strategies, such as superhydrophobic surfaces, could also be combined with these materials.

ix. **Evaluating Electrochemical Properties:** The electrochemical properties of ILs, DESs, or prepared coatings can be evaluated to understand their potential in electrochemical devices. Assessing the electrical characteristics of the coatings, including potential window, cyclic voltammetry, capacitance, and ionic conductivity, could provide valuable insights. To fully harness their potential, further research should focus on optimizing IL and DES compositions for specific energy storage systems. Investigations into hybrid systems, combining ILs and DESs with advanced nanostructured materials, could lead to breakthroughs in enhancing the performance and sustainability of supercapacitors and batteries.

The increasing demand for high-performance energy storage devices in extreme conditions, such as sub-freezing temperatures, necessitates the development of advanced materials that can maintain efficiency and stability. This research can open up promising oppourtunity in liquid and solid eutectic electrolytes, pioneering green solutions for cold-climate energy storage, to address the persistent challenges posed by battery and supercapacitor performance in harsh environments. Given the growing demand for electric devices and the ongoing challenges with battery performance in harsh environments, this research offer valuable insights into eutectogel-based and eutectic electrolytes designed for sub-freezing conditions, utilizing hydrophobic and hydrophilic deep eutectic solvents.

Furthermore, renewable-source ILs derived from biomass, such as carbohydrate-derived, lignin-derived, and amino acid-based ILs, provide cost-effective and environmentally friendly solutions. Other examples include fatty acid-derived ILs (from plant oils or animal fats), cellulose-derived ILs, and terpene-based ILs, which offer tailored

functionalities for applications such as anti-icing, energy storage, and self-cleaning surfaces. Simplifying application processes can further enhance cost-effectiveness. One-step formulations that combine ILs with binder materials enable direct application, streamlining the process and reducing labor costs. Self-healing materials with IL reservoirs provide an innovative solution, as they can regenerate surface functionality when damaged, extending the coating's lifecycle. By addressing these production, scalability, and application challenges, the adoption of ILs in industrial applications can become more economically feasible and sustainable. These recommendations offer a roadmap for future research, aiming to expand and enhance the effectiveness of anti-icing technologies across various applications.

APPENDIX I

8. SUPPORTING INFORMATION FOR ARTICLE 1

In-depth analysis of the effect of physicochemical properties of ionic liquids on anti-icing behavior of silicon based-coatings

Saba Goharshenas Moghadam*, Ehsan Bakhshandeh, Reza Jafari, Gelareh Momen

Department of Applied Sciences, University of Quebec in Chicoutimi (UQAC), 555, boul. de l'Université, Chicoutimi, Quebec G7H 2B1, Canada

***Corresponding author:** saba.goharshenasmoghadam1@uqac.ca

This article has been accepted in:

Journal of Cold Regions Science and Technology

Evaluation of possible chemical reactions of ILs in either part of Sylgard 184

The strength of the interactions between the independent species is the main characteristic that distinguishes ILs from any other type of liquid. Combination of short and long-range interactions such as hydrogen-bonding, Van der Waals and columbic interactions manifest the importance of possible side chemical reactions in different coatings. Hence, reactivity of each ILs was investigated to monitor possibility of side reactions in each component of Sylgard 184. In order to observe and study probable reactions, mixtures of

each ILs in either part A the base Sylgard 184 or part B the curing agent were prepared and placed at 120 °C for 1 h in the case of gelation. According to Table A-I. 1, because of presence of Pt catalyst in the base Sylgard 184 part A [349], anion of ILB could generate borax, act as a gelator and create film. Since the BF_4^- anion of ILB is sensitive to hydrolysis and oxidization, when exposing catalysts/initiators, ATR-FTIR spectroscopy was employed to study the mixture of ILB and part A [282,307]. According to Figure A-I. 1, the anion of ILB can be oxidized and form borax and release $HF_{(g)}$. FTIR spectra of the mixture roughly indicated that the peaks characteristics of B-O and O-H bonds of $B(OH)_3^-$ were observed at 1440 cm^{-1} and 3500 cm^{-1}, respectively [308].

Table A-I. 1: Evaluation of reactivity of each ILs in either part of Sylgard 184.

Sample	**Reactivity**
ILI + (Sylgard 184) part A	No reaction
ILI + (Sylgard 184) part B	No reaction
ILB + (Sylgard 184) part A	Reaction/film forming
ILB + (Sylgard 184) part B	No reaction

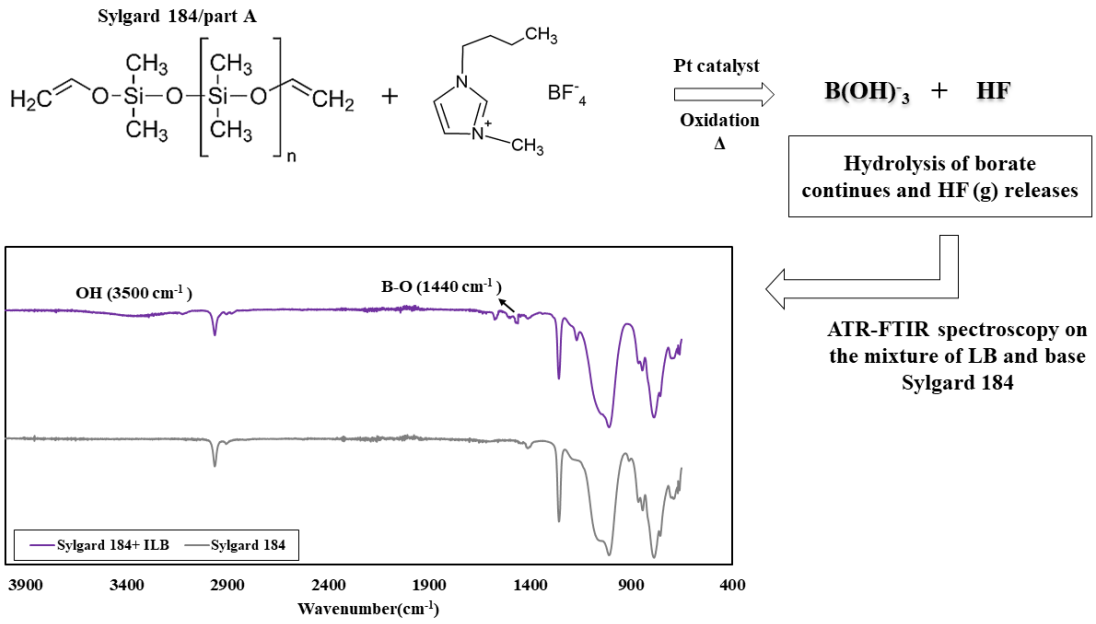

Figure A-I. 1: Proposed schematic reactions between ILB and base Sylgard 184 part A, including FTIR spectra of the mixture.

However, FTIR spectrum of ILs-containing coatings confirms the presence of ILI and cation of ILB on the surface of CILI (ILI + part A + part B) and CILB (ILB + part A + part B) coatings, respectively (Figure A-I. 2).

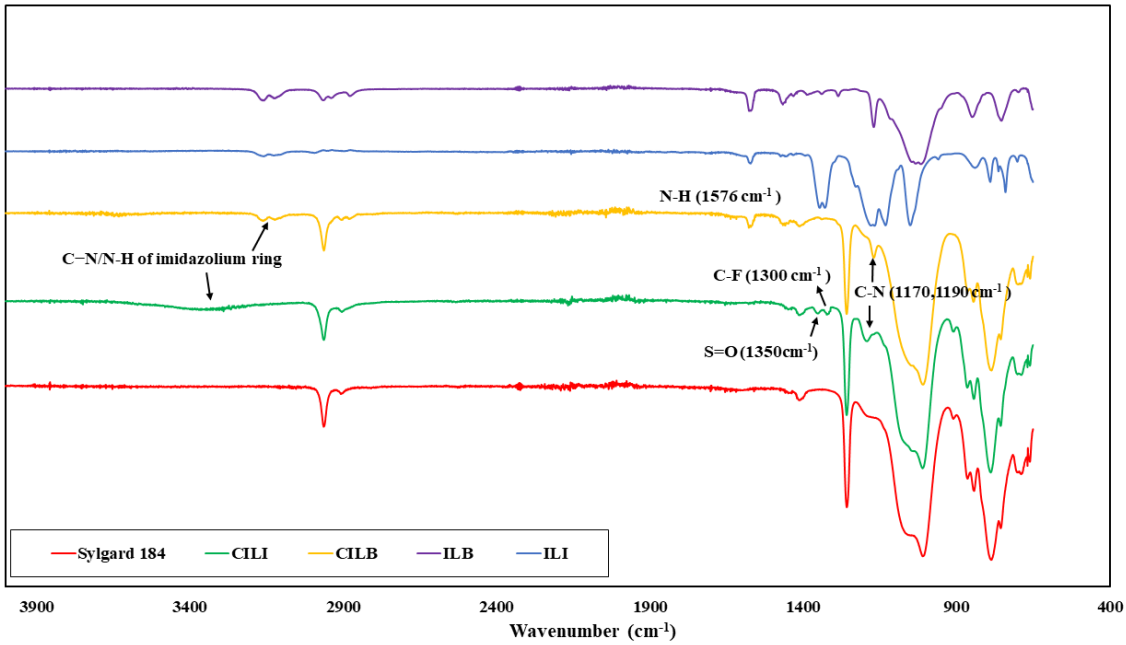

Figure A-I. 2:FT-IR spectra of reference sample lacking ILs, ILs-containing coatings, ILI and ILB.

APPENDIX II

9. SUPPORTING INFORMATION FOR ARTICLE 2

To be or not to be a hydrophobic matrix? the role of coating hydrophobicity on anti-icing behavior and ions mobility of ionic liquids

Saba Goharshenas Moghadam, Gelareh Momen*, Ehsan Bakhshandeh, Reza Jafari

Department of Applied Sciences, University of Quebec in Chicoutimi (UQAC), 555, boul. de l'Université, Chicoutimi, Quebec G7H 2B1, Canada

***Corresponding author:** Gelareh_Momen@uqac.ca

This article has been accepted in:

Chemical Engineering Journal

Materials and methods

Table A-II. 1 indicates chemical structures and melting points of the employed ILs.

Table A-II. 1: Chemical structure of the used ILs in this study.

ILs	Chemical structure	Melting point	Code
1-ethyl-3-methylimidazolium bis(trifluoromethanesulfonyl)imide (**EMIM TFSI**)	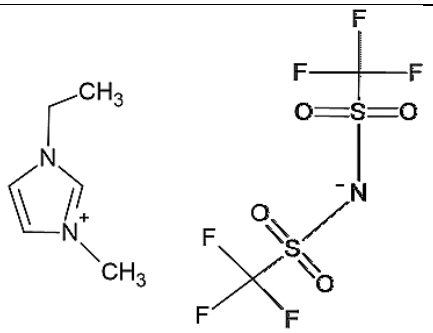	-15 °C	**LI**
1-butyl-3-methylimidazolium tetrafluoroborate (**BMIMBF4**)	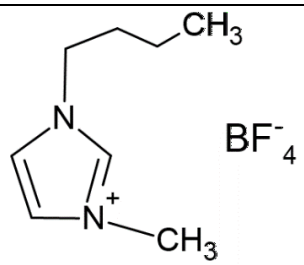	-71 °C	**LB**

Figure A-II. 1 illustrates the experimental setup for the ice nucleation study.

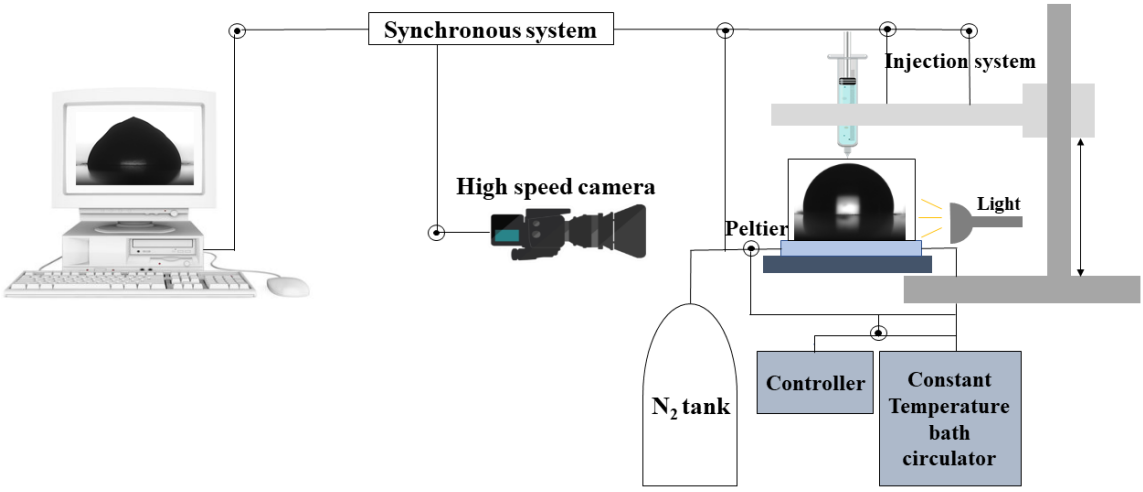

Figure A-II. 1: Schematic of experimental setup for measuring freezing delay time.

Figure A-II. 2a and Figure A-II. 2b depicts schematics of two custom-made experimental setups, namely the push-off and centrifugal adhesion tests, used in our research group to measure ice adhesion strength.

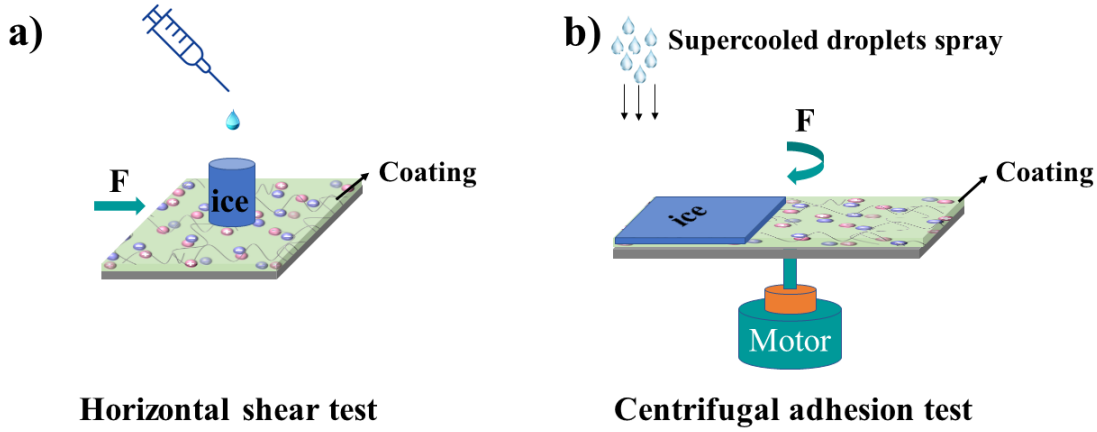

Figure A-II. 2: Schematic of (a) the push-off test and (b) the centrifugal test.

Figure A-II. 3 shows a schematic of the dielectric setup for studying dielectric properties.

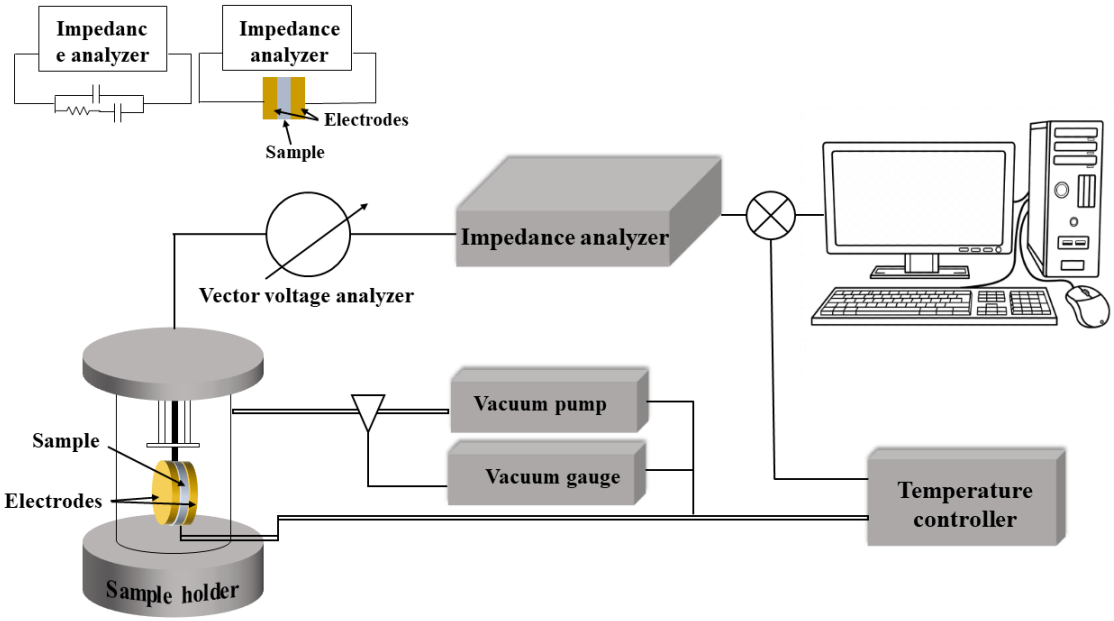

Figure A-II. 3: Schematic of broadband dielectric spectroscopy setup for measuring dielectric properties and conductivity from RT to subzero temperatures.

Results & Discussion

Investigation of probable reactivity of ILs in the used components of coatings

Mobility of ILs in both matrixes is mainly determined by interactions among independent species. ILs in different coatings are prone to side chemical reactions due to a combination of short-range and long-range interactions. Therefore, mixtures of each ILs (10 wt. %) in either part A or part B of both coatings were prepared and placed at 120 °C for 1 h in the case of gelation. As no reactivity between LI and other components was observed, reactivity and sensitivity of LB in each component were investigated to find out why the presence of LB in PU makes opaque coatings. Hence, ATR-FTIR spectroscopy was used to study possible side reactions between LB/polyol component and LB/part A Sylgard 184. Borate can be oxidized to create borax, which can operate as a gelator for a polyol component,

due to its sensitivity to hydrolysis and oxidation in the presence of any initiator or catalyst in some commercial formulations [37,282,307,349]. According to Figure A-II. 4, FTIR spectra of the mixture of LB/part A Sylgard 184 roughly indicated that the peaks characteristics of B-O and O-H bonds of $B(OH)_3^-$ were observed at 1440 cm^{-1} and 3500 cm^{-1}, respectively. Moreover, consumption of hydroxyl groups of polyol and disappearing B-F bond when percentage of LB increased, illustrated that produced borax could act as a crosslinker [308].

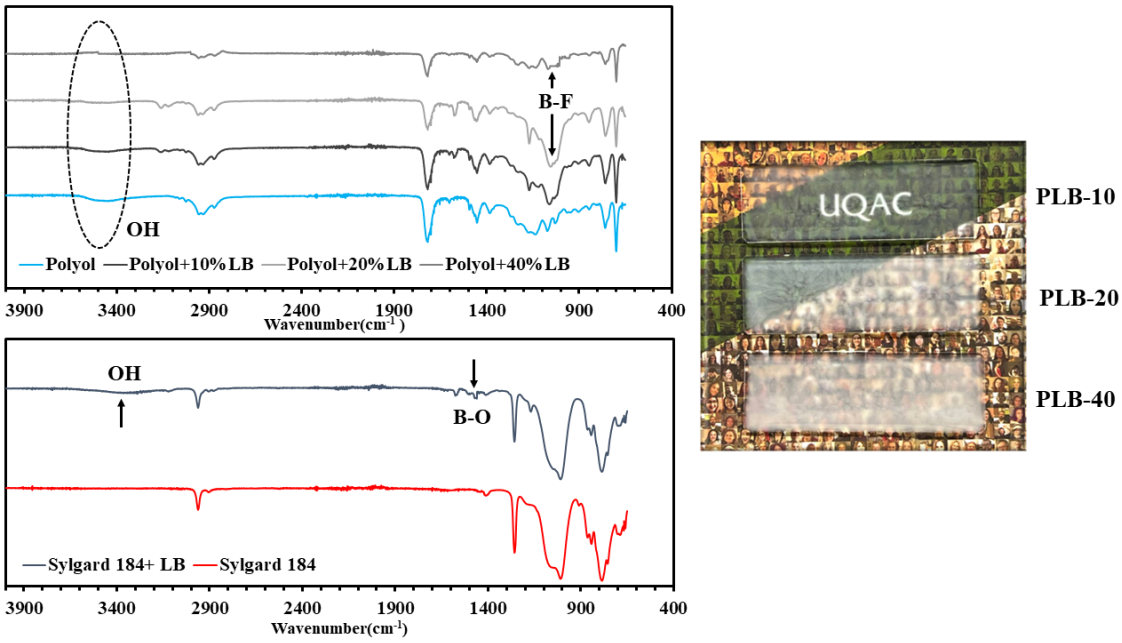

Figure A-II. 4: FTIR spectra of the mixtures of LB/polyol and LB/part A Sylgard 184.

Wetting behavior

The water contact angle (WCA), and sliding angle (SA) of the non-stoichiometric coatings demonstrated in Figure A-II. 5a and Figure A-II. 5b, respectively.

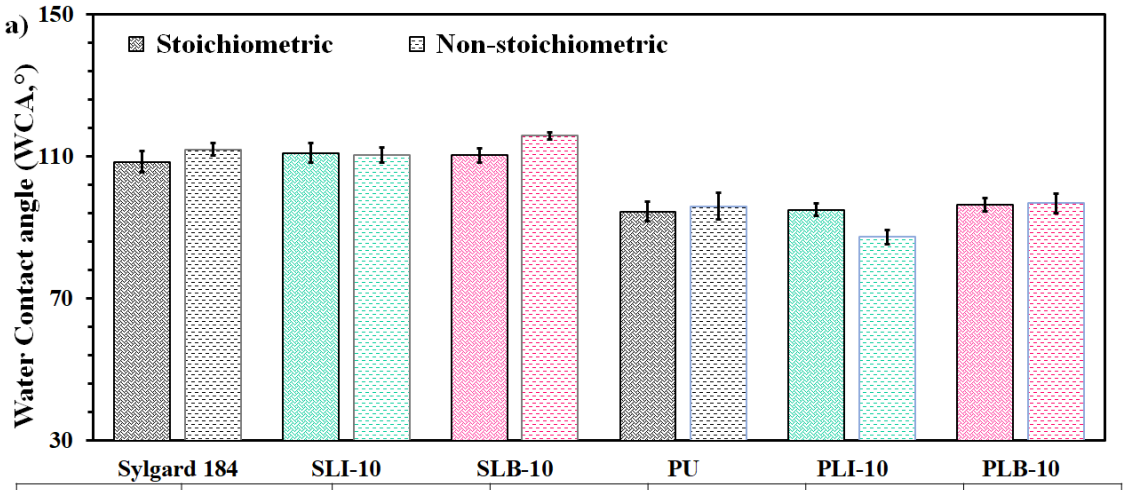

WCA (°)	Sylgard 184	SLI-10	SLB-10	PU	PLI-10	PLB-10
Stoichiometric	108.5±3.05	111±2.73	110.3±1.96	94.4±2.79	94.9±1.76	96.5±1.83
Non-stoichiometric	112±1.7	110.5±2.12	115.9±1.07	96±3.65	87.3±2.06	96.8±2.69

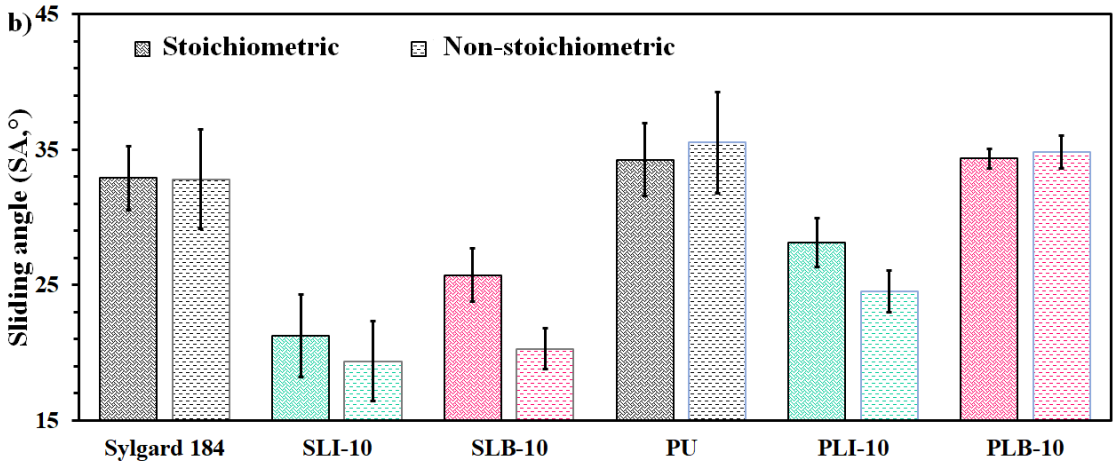

SA (°)	Sylgard 184	SLI-10	SLB-10	PU	PLI-10	PLB-10
Stoichiometric	32.9±2.36	21.2±3.06	25.7±1.97	34.2±2.7	28.1±1.78	34.3±0.7
Non-stoichiometric	32.8±3.66	19.3±2.94	20.2±1.51	35.5±3.75	24.5±1.54	34.8±1.19

Figure A-II. 5: Wetting properties of the non-stoichiometric reference coatings lacking and containing 10 wt.% ILs; (a) WCAs- and (b) SAs.

Dielectric measurements

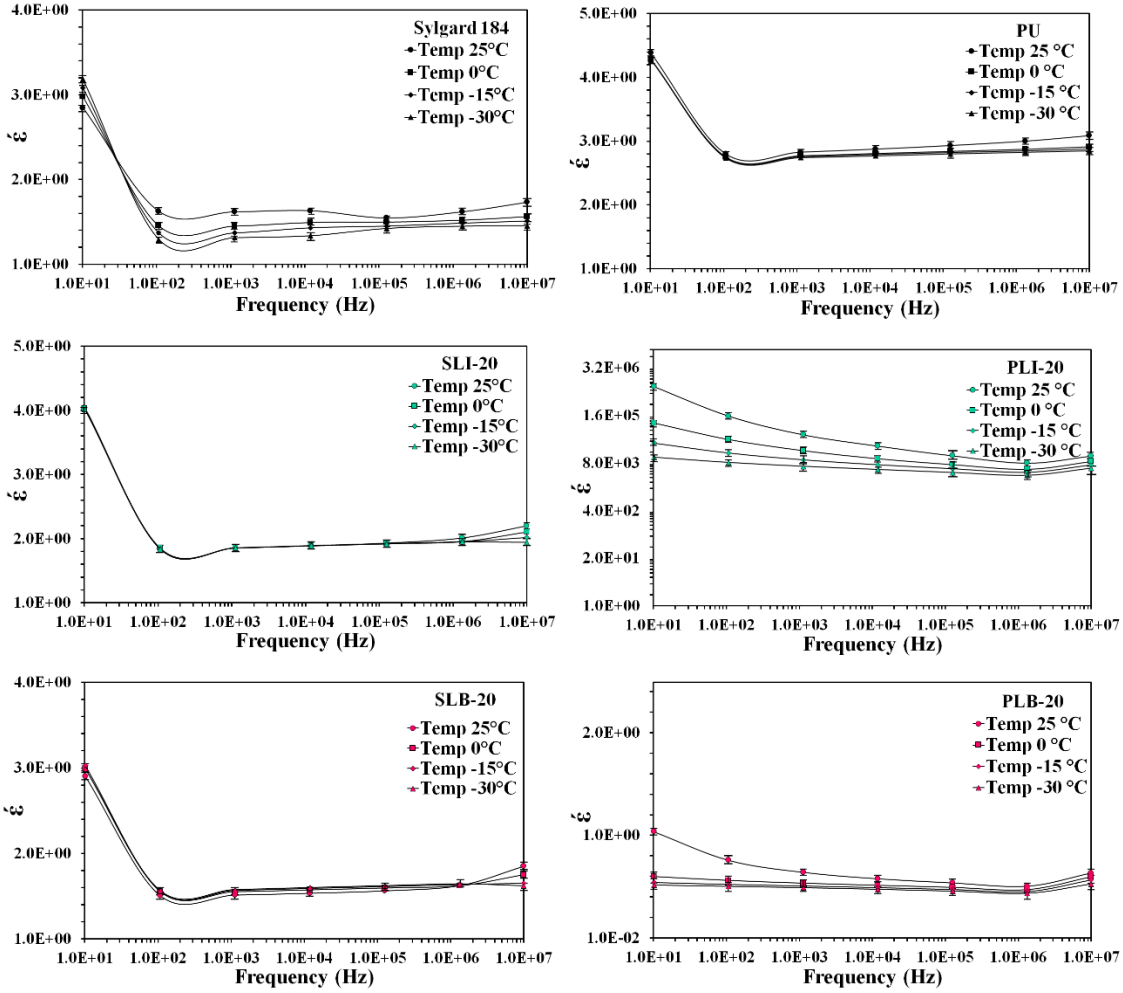

Figure A-II. 6: The variation of dielectric constant with frequencies from 10^1 Hz to 10^7 Hz at different temperatures, for coatings lacking and containing 20 wt.% of ILs.

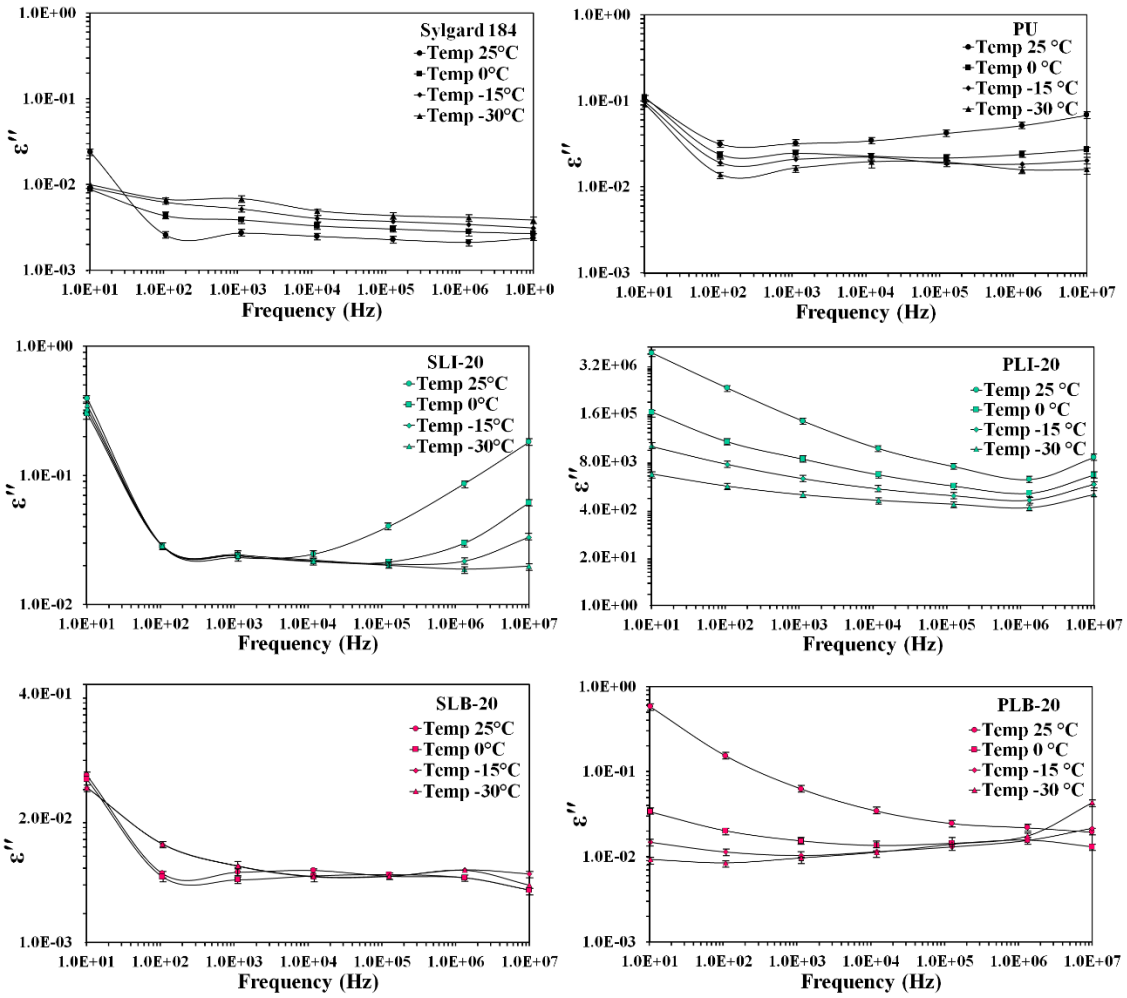

Figure A-II. 7: The variation of dielectric loss factor with frequencies from 10^1 Hz to 10^7 Hz at different temperatures, for coatings lacking and containing 20 wt.% of ILs.

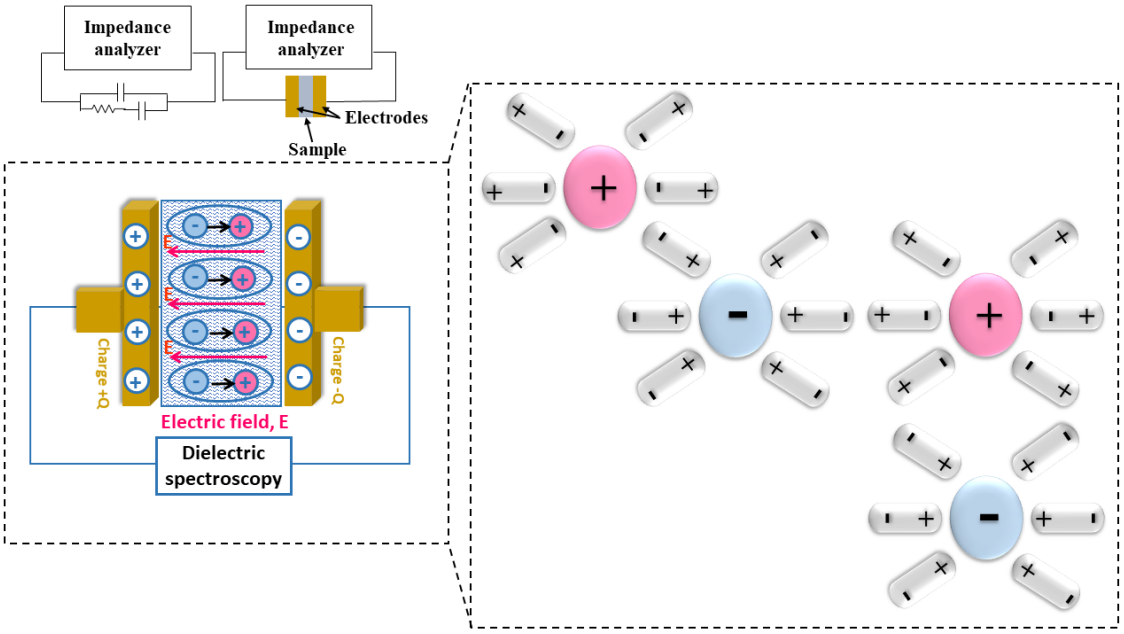

Figure A-II. 8: Schematic of ions screening from their respective surroundings of polarized molecules of atoms.

Surface properties after icing/de-icing cycles and QUV chamber exposure test

Table A-II. 2: Surface hardness, roughness (Sq) and Yellowness index of specimens before and after 20 icing/de-icing cycles and QUV chamber exposure test.

Samples	Surface hardness (4 ° Persoz)		Root mean square height (S_q) (nm)		Yellowness index (YI%)	
	before push-off	after 20 cycles icing/de-icing	before push-off	after 20 cycles icing/de-icing	before QUV	after QUV
			Stoichiometric			
Sylgard 184	61.1 ± 1.7	53.7 ± 1.3	6.358 ± 0.36	10.86 ± 1.68	25.48 ± 1.8	27.09 ± 1.75
SLI-10	44.2 ± 1.32	40.9 ± 1.05	91.23 ± 1.5	139.1 ± 11.98	26.12 ± 1.6	30.56 ± 2.69
SLB-10	36.6 ± 1.35	31.5 ± 2.12	214.64 ± 17.34	397.3 ± 24.98	26.64 ± 2.66	33.98 ± 3.45
PU	129.8 ± 1.83	125.42 ± 1.66	2.584 ± 0.24	3.891 ± 0.26	26.59 ± 0.9	27.51 ± 1.1
PLI-10	96.8 ± 2.72	92.0 ± 1.02	4.062 ± 0.16	15.943 ± 0.13	25.56 ± 1.2	31.55 ± 1.25
PLB-10	94 ± 1.78	90.74 ± 2.45	19.36 ± 2.75	47.31 ± 3.389	26.84 ± 2.61	33.73 ± 2.75
Samples			**Non-stoichiometric**			
Sylgard 184-NS	54.4 ± 1.61	50.16 ± 0.96	6.039 ± 0.279	16.93 ± 1.845	26.73 ± 2.05	28.10 ± 1.66
SLI-10-NS	41.8 ± 1.46	37.9 ± 1.15	94.63 ± 1.93	205.8 ± 15.49	26.73 ± 2.12	32.05 ± 1.9
SLB-10-NS	31.6 ± 2.15	25.36 ± 1.98	238.1 ± 20.69	672.2 ± 26.51	27.05 ± 3.3	35.5 ± 4.1
PU-NS	120.6 ± 2.65	119.13 ± 1.43	3.742 ± 0.19	4.885 ± 0.21	25.39 ± 1.5	30.23 ± 1.05
PLI-10-NS	88.4 ± 1.85	90.34 ± 0.89	6.412 ± 0.19	16.738 ± 0.23	26.71 ± 2.78	32.08 ± 2.16
PLB-10-NS	83.2 ± 1.6	79.28 ± 2.25	28.91 ± 3.26	77.99 ± 3.57	27.26 ± 3.05	34.41 ± 3.81

APPENDIX III

10. SUPPORTING INFORMATION FOR CHAPTER 4

Innovative ice mitigation: Exploring the potential of choline-based deep eutectic solvents and ionic liquids synergies

Materials and methods

Figure A-III. 1a and Figure A-III. 1b depict the schematic of the experimental procedure employed for the synthesis of Ionic Liquids (ILs).

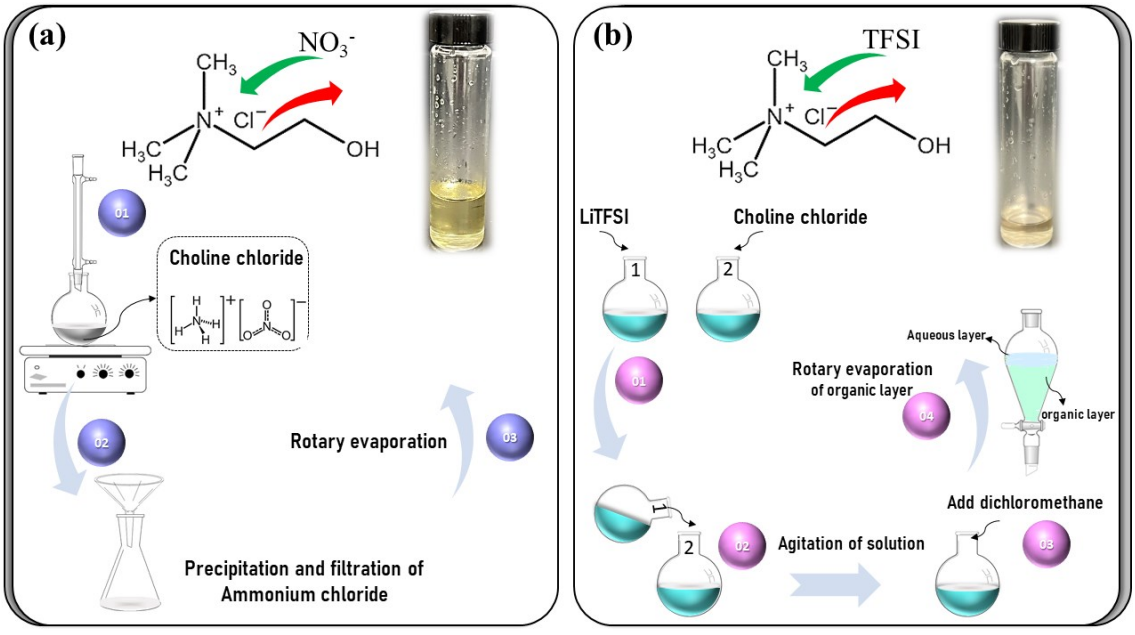

Figure A-III. 1: Schematic illustration of the preparation procedure of choline-based ILs.

Figure A-III. 2 depicts the experimental setup used to measure ice adhesion strength via the push-off test.

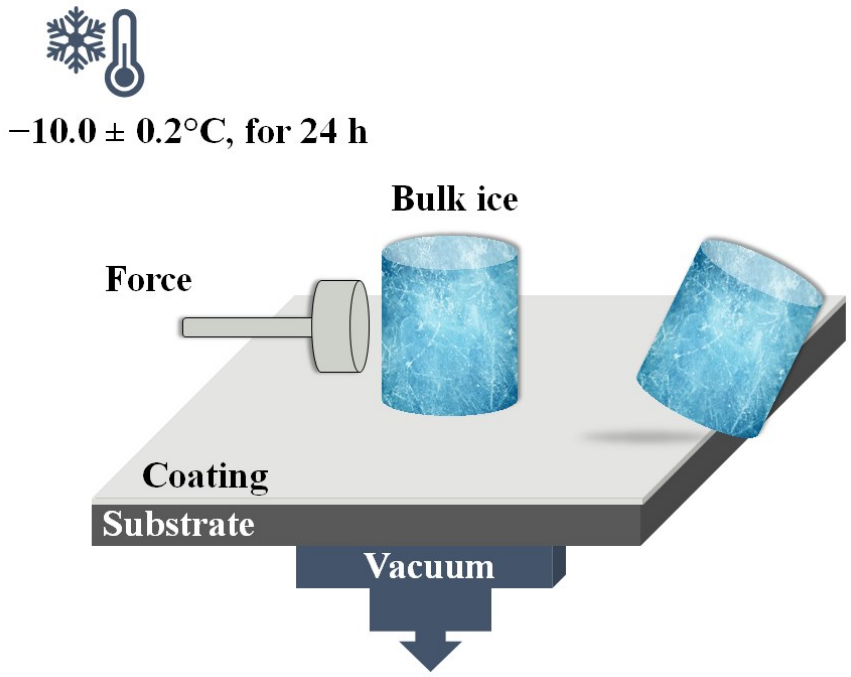

Figure A-III. 2: Schematic diagram of the experimental setup for measuring ice adhesion strength using the push-off test.

Figure A-III. 3 illustrates the experimental setup for the frost formation study.

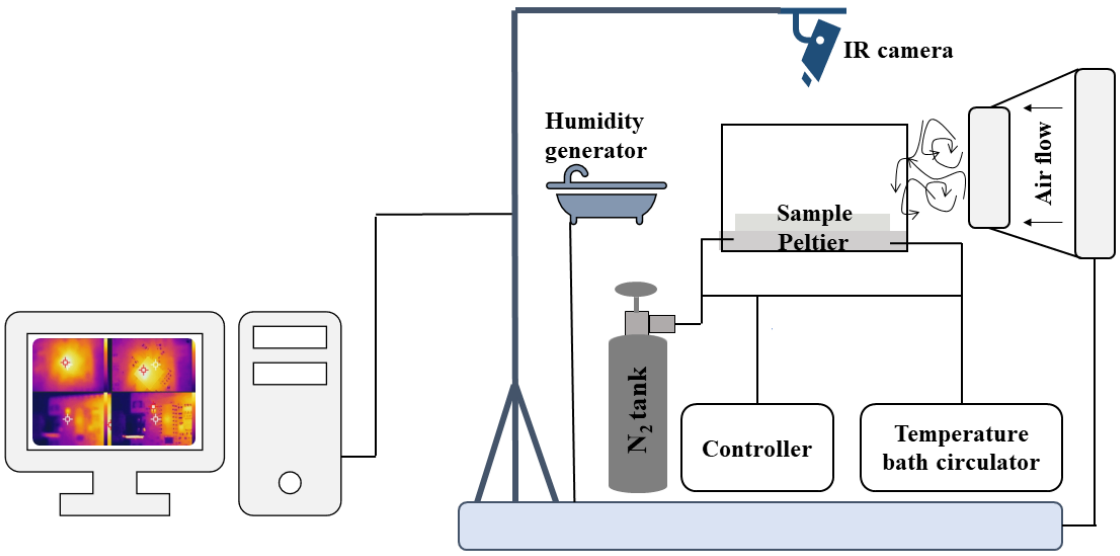

Figure A-III. 3: Schematic illustration of the experimental setup for evaluating anti-frosting capacity of coatings.

Results & Discussion

Ionic liquids synthesis

FT-IR and NMR spectroscopy

Figure A-III. 4a and Figure A-III. 4b present the reactions involved in the synthesis of ILs and the spectra of Choline chloride, the synthesized $ChNO_3$, and ChTFSI, respectively.

FTIR spectroscopy confirmed IL synthesis. Figure A-III. 4a and Figure A-III. 4b illustrate the synthesis reactions for ILs and the spectra of ChCl, the synthesized $ChNO_3$, and ChTFSI, respectively. The synthesized $ChNO_3$ exhibits a vibrational peak at 3306 cm^{-1} (Fig. S3b), corresponding to the O–H tension from the adsorption of choline molecules. Medium peaks observed in the 3017–3034 cm^{-1} range are attributed to C–H stretching vibrations, whereas the strong peak at 1477 cm^{-1} is associated with C–H bending vibrations in the alkanes. Notably, the distinctive vibrational peak for the nitro group (N=O) at 1751 cm^{-1}, the asymmetric stretching of NO_3^- at 1359 cm^{-1}, and the symmetric stretching peak at 831 cm^{-1},

support the occurrence of a nitrate exchange reaction for $ChNO_3$ (Figure A-III. 4a) [445]. Furthermore, a comparison of the ChCl and ChTFSI spectra highlights the occurrence of an anion exchange reaction between chloride (Cl) and bis(trifluoromethanesulfonyl)imide (TFSI). This is evident in the absorption peaks at 1133 and 737, and 1340, 790 cm^{-1}, which are associated with the stretching vibrations of C-F and S=O in the imide group, confirming the successful exchange reaction [446].

Figure A-III. 5a and Figure A-III. 5b display the ^{1}H and ^{13}C-NMR spectra of both ILs. In the ^{13}C NMR spectra, characteristic signals corresponding to $ChNO_3$ and ChTFSI are evident. For instance, in the ^{1}H NMR spectrum of $ChNO_3$ (300 MHz, [$CDCL_3$], δ), peaks are observed at 5.29 (t, 1H, OH, J = 5.0 Hz), 3.76 (m, 2H, CH_2), 3.41 (m, 2H, CH_2), and 3.30 (s, 9H, 3× CH_3) [447]. The ^{13}C NMR spectrum of ChTFSI (75.47 MHz, [$CDCL_3$], δ) displays signals at 118.43 (q, 2 × CF_3, J = 319 Hz), 67.69 (N–CH_2), 56.90 (CH_2), and 54.95 (3 × CH_3), providing insights into the molecular composition of the ILs [446,448].

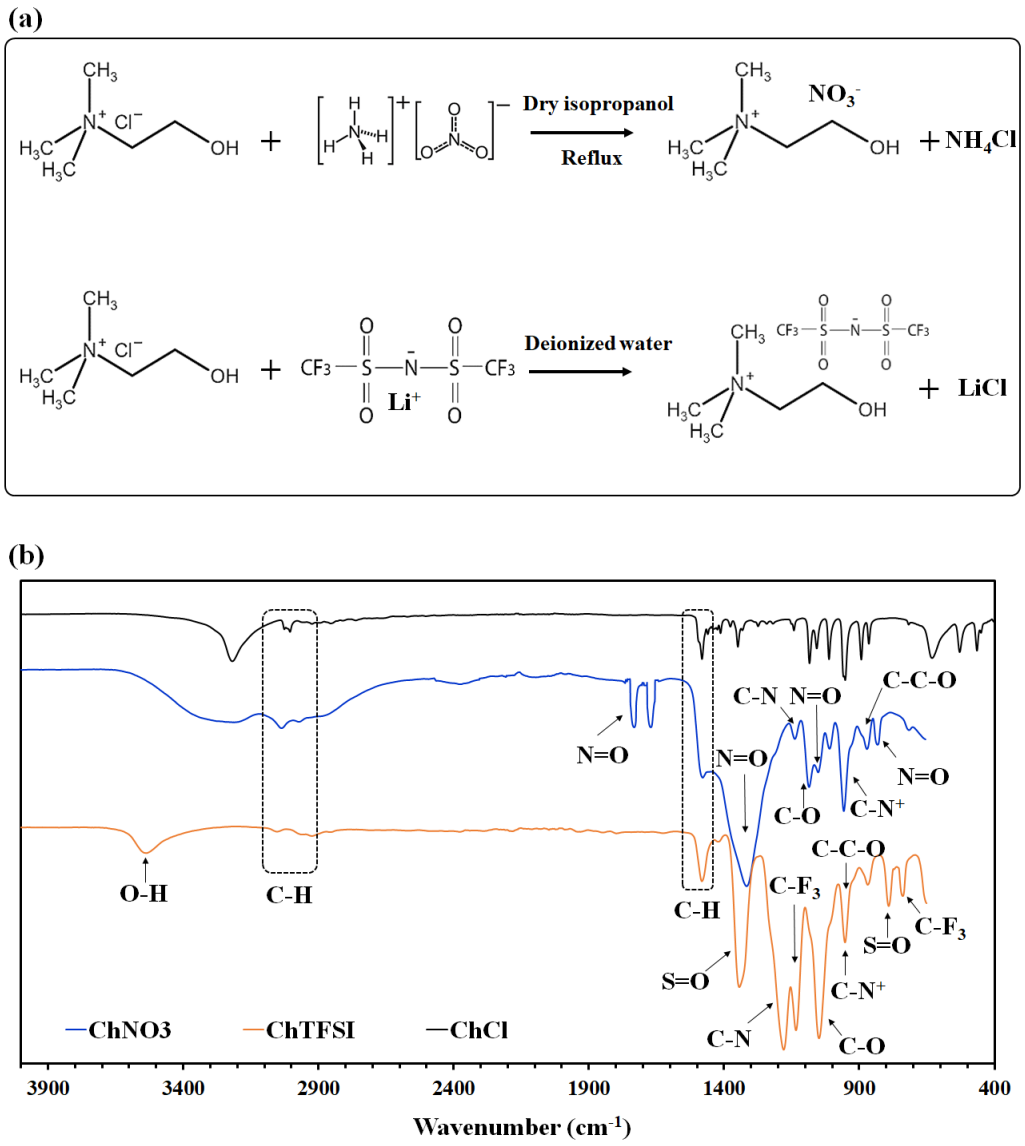

Figure A-III. 4: (a) Reaction procedure for synthesis of choline-based ILs and (b) FT-IR spectrum of ChCl, $ChNO_3$ and ChTFSI.

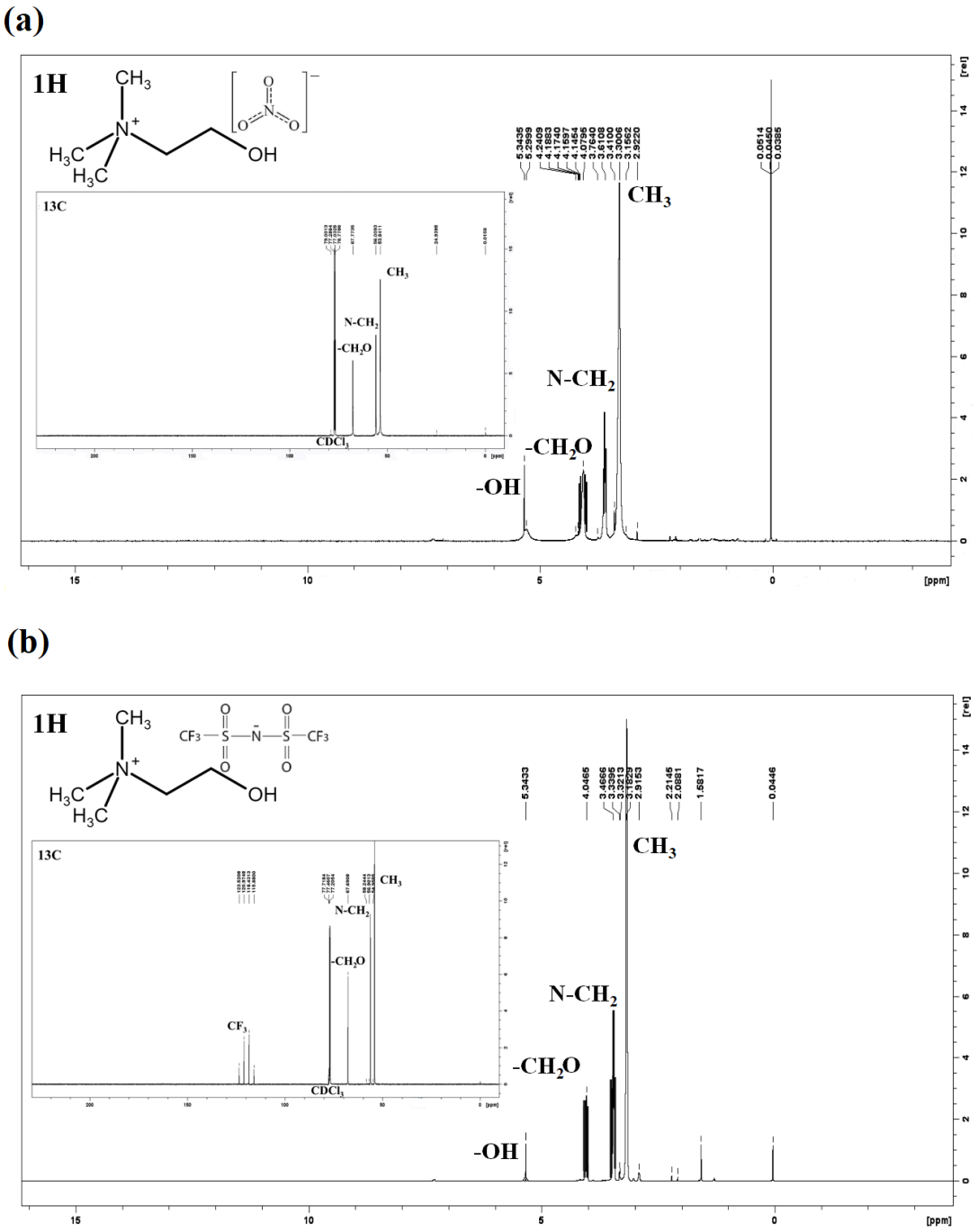

Figure A-III. 5: ^{1}H and ^{13}C NMR spectrum of (a) $ChNO_3$ and (b) ChTFSI.

Synergistic combination of DESs and ILs for anti-icing application

Strategic selection of samples containing ILs to study the effect of DESs on anti-icing performance

To investigate the influence of a widely recognized DES – specifically, a mixture with a ratio of (1) choline chloride to (2) ethylene glycol ((1)Ch:(2)EG) – on the anti-icing performance of PU coatings in conjunction with synthesized choline-based ILs, we meticulously selected optimized samples based on their superior anti-icing properties. Employing the experimental procedure outlined in Figure A-III. 6, PU coatings containing 20 wt.% of $ChNO_3$ and 10 wt.% of ChTFSI were particularly chosen to fabricate a novel series of coating samples in the presence of the DES.

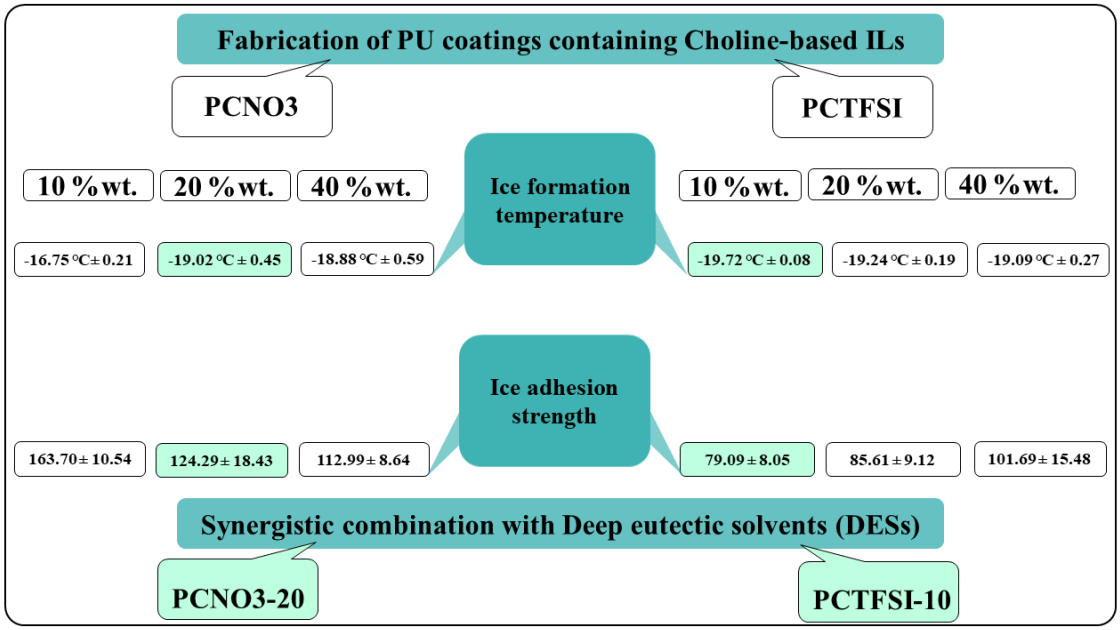

Figure A-III. 6: Diagram illustrating the procedural methodology employed in this research.

REFERENCES

[1] Z. Wang, Recent progress on ultrasonic de-icing technique used for wind power generation, high-voltage transmission line and aircraft, Energy Build. 140 (2017) 42–49. https://doi.org/10.1016/j.enbuild.2017.01.072.

[2] R. Carriveau, A. Edrisy, P. Cadieux, R. Mailloux, Ice Adhesion Issues in Renewable Energy Infrastructure, J. Adhes. Sci. Technol. 26 (2012) 447–461. https://doi.org/10.1163/016942411X574592.

[3] H. Habibi, L. Cheng, H. Zheng, V. Kappatos, C. Selcuk, T.-H. Gan, A dual de-icing system for wind turbine blades combining high-power ultrasonic guided waves and low-frequency forced vibrations, Renew. Energy. 83 (2015) 859–870. https://doi.org/10.1016/j.renene.2015.05.025.

[4] A. Amendola, G. Mingione, On the problem of icing for modern civil aircraft, Air Sp. Eur. 3 (2001) 214–217. https://doi.org/10.1016/S1290-0958(01)90098-X.

[5] M. Lacavalla, P. Marcacci, A. Frigerio, Forecasting and monitoring wet-snow sleeve on overhead power lines in Italy, in: 2015 IEEE Work. Environ. Energy, Struct. Monit. Syst. Proc., IEEE, 2015: pp. 78–83. https://doi.org/10.1109/EESMS.2015.7175856.

[6] C. Armenakis, N. Nirupama, Urban impacts of ice storms: Toronto December 2013, Nat. Hazards. 74 (2014) 1291–1298. https://doi.org/10.1007/s11069-014-1211-7.

[7] G. Hou, K.K. Muraleetharan, V. Panchalogaranjan, P. Moses, A. Javid, H. Al-Dakheeli, R. Bulut, R. Campos, P.S. Harvey, G. Miller, K. Boldes, M. Narayanan, Resilience assessment and enhancement evaluation of power distribution systems subjected to ice storms, Reliab. Eng. Syst. Saf. 230 (2023) 108964. https://doi.org/10.1016/j.ress.2022.108964.

[8] J.W. Busby, K. Baker, M.D. Bazilian, A.Q. Gilbert, E. Grubert, V. Rai, J.D. Rhodes, S. Shidore, C.A. Smith, M.E. Webber, Cascading risks: Understanding the 2021 winter blackout in Texas, Energy Res. Soc. Sci. 77 (2021) 102106. https://doi.org/10.1016/j.erss.2021.102106.

[9] Z. Liu, A. Li, Q. Wang, Y. Chi, L. Zhang, Experimental study on a new type of thermal storage defrosting system for frost-free household refrigerators, Appl. Therm. Eng. 118 (2017) 256–265. https://doi.org/10.1016/j.applthermaleng.2017.02.077.

[10] M. Susoff, K. Siegmann, C. Pfaffenroth, M. Hirayama, Evaluation of icephobic coatings—Screening of different coatings and influence of roughness, Appl. Surf. Sci. 282 (2013) 870–879. https://doi.org/10.1016/j.apsusc.2013.06.073.

[11] T. Rashid, H.A. Khawaja, K. Edvardsen, Review of marine icing and anti-/de-icing systems, J. Mar. Eng. Technol. 15 (2016) 79–87. https://doi.org/10.1080/20464177.2016.1216734.

[12] J.M. Pinar-Pérez, F.P. García Márquez, Managing Costs and Review for Icing Problems, in: Renew. Energies, Springer International Publishing, Cham, 2018: pp. 97–109. https://doi.org/10.1007/978-3-319-45364-4_7.

[13] M.J. Kreder, J. Alvarenga, P. Kim, J. Aizenberg, Design of anti-icing surfaces: smooth, textured or slippery?, Nat. Rev. Mater. 1 (2016) 15003. https://doi.org/10.1038/natrevmats.2015.3.

[14] Z. He, Y. Zhuo, Z. Zhang, J. He, Design of Icephobic Surfaces by Lowering Ice Adhesion Strength: A Mini Review, Coatings. 11 (2021) 1343. https://doi.org/10.3390/coatings11111343.

[15] R. Rekuviene, S. Saeidiharzand, L. Mažeika, V. Samaitis, A. Jankauskas, A.K. Sadaghiani, G. Gharib, Z. Muganlı, A. Koşar, A review on passive and active anti-icing and de-icing technologies, Appl. Therm. Eng. 250 (2024) 123474. https://doi.org/10.1016/j.applthermaleng.2024.123474.

[16] V. Hejazi, K. Sobolev, M. Nosonovsky, From superhydrophobicity to icephobicity: forces and interaction analysis, Sci. Rep. 3 (2013) 2194. https://doi.org/10.1038/srep02194.

[17] D. Chen, M.D. Gelenter, M. Hong, R.E. Cohen, G.H. McKinley, Icephobic Surfaces Induced by Interfacial Nonfrozen Water, ACS Appl. Mater. Interfaces. 9 (2017) 4202–4214. https://doi.org/10.1021/acsami.6b13773.

[18] F. Wang, Y. Zhuo, Z. He, S. Xiao, J. He, Z. Zhang, Dynamic Anti-Icing Surfaces (DAIS), Adv. Sci. 8 (2021). https://doi.org/10.1002/advs.202101163.

[19] Y. Zhuo, S. Xiao, V. Håkonsen, J. He, Z. Zhang, Anti-icing Ionogel Surfaces: Inhibiting Ice Nucleation, Growth, and Adhesion, ACS Mater. Lett. 2 (2020) 616–623. https://doi.org/10.1021/acsmaterialslett.0c00094.

[20] A.M. Emelyanenko, L.B. Boinovich, A.A. Bezdomnikov, E. V. Chulkova, K.A. Emelyanenko, Reinforced Superhydrophobic Coating on Silicone Rubber for Longstanding Anti-Icing Performance in Severe Conditions, ACS Appl. Mater. Interfaces. 9 (2017) 24210–24219. https://doi.org/10.1021/acsami.7b05549.

[21] C. Tao, X. Li, B. Liu, K. Zhang, Y. Zhao, K. Zhu, X. Yuan, Highly icephobic properties on slippery surfaces formed from polysiloxane and fluorinated POSS, Prog. Org. Coatings. 103 (2017) 48–59. https://doi.org/10.1016/j.porgcoat.2016.11.018.

[22] S. Heydarian, R. Jafari, G. Momen, Recent progress in the anti-icing performance of slippery liquid-infused surfaces, Prog. Org. Coatings. 151 (2021) 106096. https://doi.org/10.1016/j.porgcoat.2020.106096.

[23] S.A. Kulinich, S. Farhadi, K. Nose, X.W. Du, Superhydrophobic Surfaces: Are They Really Ice-Repellent?, Langmuir. 27 (2011) 25–29. https://doi.org/10.1021/la104277q.

[24] J.S. Wexler, I. Jacobi, H.A. Stone, Shear-Driven Failure of Liquid-Infused Surfaces, Phys. Rev. Lett. 114 (2015) 168301. https://doi.org/10.1103/PhysRevLett.114.168301.

[25] C. Austen Angell, Y. Ansari, Z. Zhao, Ionic Liquids: Past, present and future, Faraday Discuss. 154 (2012) 9–27. https://doi.org/10.1039/C1FD00112D.

[26] Z. Mossayebi, V.F. Jafari, P.A. Gurr, R. Simons, G.G. Qiao, Reduced Ice Adhesion Using Amphiphilic Poly(Ionic Liquid)-Based Surfaces, ACS Appl. Mater. Interfaces. 15 (2023) 7454–7465. https://doi.org/10.1021/acsami.2c21500.

[27] H. Wang, Y. Wang, Z. Liang, H. Yang, Z. Xu, Endogenous Ionic-Liquid-Infused Coatings by Phase Separation for Anti-Icing and Anti-Bacterial Applications, Adv. Mater. Interfaces. 9 (2022). https://doi.org/10.1002/admi.202102570.

[28] A. Virya, R. Bagchi, K. Lian, Effects of Pore Structure and Carbon Loading on Solid Capacitive Devices at Low Temperatures, J. Electrochem. Soc. 169 (2022) 070522. https://doi.org/10.1149/1945-7111/ac7ef1.

[29] A. Sharma, R. Sharma, R.C. Thakur, L. Singh, An overview of deep eutectic solvents: Alternative for organic electrolytes, aqueous systems & ionic liquids for electrochemical energy storage, J. Energy Chem. 82 (2023) 592–626. https://doi.org/10.1016/j.jechem.2023.03.039.

[30] J. Płotka-Wasylka, M. de la Guardia, V. Andruch, M. Vilková, Deep eutectic solvents vs ionic liquids: Similarities and differences, Microchem. J. 159 (2020) 105539. https://doi.org/10.1016/j.microc.2020.105539.

[31] K.A. Omar, R. Sadeghi, Physicochemical properties of deep eutectic solvents: A review, J. Mol. Liq. 360 (2022) 119524. https://doi.org/10.1016/j.molliq.2022.119524.

[32] S.N. Kuehn KM, Massmann CM, Choline chloride eutectics: Low temperature applications, J. Undergrad. Res. 15 (2017) 5.

[33] C. Lu, C. Wang, J. Wang, Q. Yong, F. Chu, Integration of hydrogen bonding interaction and Schiff-base chemistry toward self-healing, anti-freezing, and conductive elastomer, Chem. Eng. J. 425 (2021) 130652. https://doi.org/10.1016/j.cej.2021.130652.

[34] J. Yang, J. Fan, Z. Liu, B. Zhang, G. Qin, S. Liu, X. Shi, L. Zhu, G. Sun, Q. Chen, Deep Eutectic Solvent-Based Ultra-Stretchable, Anti-Freezing, and Ambient-Stable Supramolecular Ionogel for Wearable Sensor, Macromol. Mater. Eng. 307 (2022). https://doi.org/10.1002/mame.202200248.

[35] C. Lu, X. Wang, Y. Shen, C. Wang, J. Wang, Q. Yong, F. Chu, Liquid-Free, Anti-Freezing, Solvent-Resistant, Cellulose-Derived Ionic Conductive Elastomer for

Stretchable Wearable Electronics and Triboelectric Nanogenerators, Adv. Funct. Mater. 32 (2022). https://doi.org/10.1002/adfm.202207714.

[36] M. Yan, X. Li, H. Lian, A stretchable, compressible and anti-freezing ionic gel based on a natural deep eutectic solvent applied as a strain sensor, J. Appl. Polym. Sci. 139 (2022). https://doi.org/10.1002/app.52607.

[37] S.G. Moghadam, E. Bakhshandeh, R. Jafari, G. Momen, In-depth analysis of the effect of physicochemical properties of ionic liquids on anti-icing behavior of silicon based-coatings, Cold Reg. Sci. Technol. 216 (2023) 104007. https://doi.org/10.1016/j.coldregions.2023.104007.

[38] S. Goharshenas Moghadam, G. Momen, E. Bakhshandeh, R. Jafari, To be or not to be a hydrophobic matrix? the role of coating hydrophobicity on anti-icing behavior and ions mobility of ionic liquids, Chem. Eng. J. 485 (2024) 149696. https://doi.org/10.1016/j.cej.2024.149696.

[39] S. Goharshenas Moghadam, G. Momen, R. Zarrougui, R. Jafari, Innovative ice mitigation: Exploring the potential of choline-based deep eutectic solvents and ionic liquids synergies, Appl. Surf. Sci. 680 (2025) 161300. https://doi.org/10.1016/j.apsusc.2024.161300.

[40] S. Goharshenas moghadam, G. Momen, R. Jafari, Ice-Responsive Coatings: Evaluating the Effect of Hydrogen Bond Donors on Deep Eutectic Solvents/Ionic Liquids Anti-icing Efficiency, Mol. Liq. (2024).

[41] L.L. Shao, L. Yang, C.L. Zhang, Comparison of heat pump performance using fin-and-tube and microchannel heat exchangers under frost conditions, Appl. Energy. 87 (2010) 1187–1197. https://doi.org/10.1016/j.apenergy.2009.08.021.

[42] Y. Sirui, S. Mengjie, G. Runmiao, B. Jiwoong, Z. Xuan, Z. Shiqiang, A review of icing prediction techniques for four typical surfaces in low-temperature natural environments, Appl. Therm. Eng. 241 (2024) 122418. https://doi.org/10.1016/j.applthermaleng.2024.122418.

[43] O. Parent, A. Ilinca, Anti-icing and de-icing techniques for wind turbines: Critical review, Cold Reg. Sci. Technol. 65 (2011) 88–96. https://doi.org/10.1016/j.coldregions.2010.01.005.

[44] O. Fakorede, Z. Feger, H. Ibrahim, A. Ilinca, J. Perron, C. Masson, Ice protection systems for wind turbines in cold climate: characteristics, comparisons and analysis, Renew. Sustain. Energy Rev. 65 (2016) 662–675. https://doi.org/10.1016/j.rser.2016.06.080.

[45] K. Golovin, A. Tuteja, A predictive framework for the design and fabrication of icephobic polymers, Sci. Adv. 3 (2017). https://doi.org/10.1126/sciadv.1701617.

[46] C. Howell, T.L. Vu, C.P. Johnson, X. Hou, O. Ahanotu, J. Alvarenga, D.C. Leslie, O.

Uzun, A. Waterhouse, P. Kim, M. Super, M. Aizenberg, D.E. Ingber, J. Aizenberg, Stability of Surface-Immobilized Lubricant Interfaces under Flow, Chem. Mater. 27 (2015) 1792–1800. https://doi.org/10.1021/cm504652g.

[47] Q. Li, Z. Guo, Fundamentals of icing and common strategies for designing biomimetic anti-icing surfaces, J. Mater. Chem. A. 6 (2018) 13549–13581. https://doi.org/10.1039/C8TA03259A.

[48] X. Zhou, G. Yang, C. Li, J. Wu, Functional microdroplet self-dislodging icephobic surfaces: A review from mechanism to synergic morphology, Appl. Therm. Eng. 215 (2022) 118928. https://doi.org/10.1016/j.applthermaleng.2022.118928.

[49] Y. Shen, X. Wu, J. Tao, C. Zhu, Y. Lai, Z. Chen, Icephobic materials: Fundamentals, performance evaluation, and applications, Prog. Mater. Sci. 103 (2019) 509–557. https://doi.org/10.1016/j.pmatsci.2019.03.004.

[50] Z. Zhang, X.Y. Liu, Control of ice nucleation: freezing and antifreeze strategies, Chem. Soc. Rev. 47 (2018) 7116–7139. https://doi.org/10.1039/C8CS00626A.

[51] T.M. Schutzius, S. Jung, T. Maitra, P. Eberle, C. Antonini, C. Stamatopoulos, D. Poulikakos, Physics of Icing and Rational Design of Surfaces with Extraordinary Icephobicity, Langmuir. 31 (2015) 4807–4821. https://doi.org/10.1021/la502586a.

[52] S. Nath, S.F. Ahmadi, J.B. Boreyko, A Review of Condensation Frosting, Nanoscale Microscale Thermophys. Eng. 21 (2017) 81–101. https://doi.org/10.1080/15567265.2016.1256007.

[53] Y. Zhuo, J. Chen, S. Xiao, T. Li, F. Wang, J. He, Z. Zhang, Gels as emerging anti-icing materials: a mini review, Mater. Horizons. 8 (2021) 3266–3280. https://doi.org/10.1039/D1MH00910A.

[54] M. Nosonovsky, V. Hejazi, Why Superhydrophobic Surfaces Are Not Always Icephobic, ACS Nano. 6 (2012) 8488–8491. https://doi.org/10.1021/nn302138r.

[55] K. Golovin, S.P.R. Kobaku, D.H. Lee, E.T. DiLoreto, J.M. Mabry, A. Tuteja, Designing durable icephobic surfaces, Sci. Adv. 2 (2016). https://doi.org/10.1126/sciadv.1501496.

[56] J.P. Wang, H.C. Yang, C. Te Hsieh, Adsorption of phenol and basic dye on carbon nanotubes/carbon fabric composites from aqueous solution, Sep. Sci. Technol. 46 (2011) 340–348. https://doi.org/10.1080/01496395.2010.508066.

[57] P. Eberle, M.K. Tiwari, T. Maitra, D. Poulikakos, Rational nanostructuring of surfaces for extraordinary icephobicity, Nanoscale. 6 (2014) 4874–4881. https://doi.org/10.1039/C3NR06644D.

[58] M. Zhou, L. Zhang, L. Zhong, M. Chen, L. Zhu, T. Zhang, X. Han, Y. Hou, Y. Zheng, Robust Photothermal Icephobic Surface with Mechanical Durability of Multi-

Bioinspired Structures, Adv. Mater. 36 (2024). https://doi.org/10.1002/adma.202305322.

[59] H. Xiang, Y. Yuan, T. Zhu, X. Dai, C. Zhang, Y. Gai, R. Liao, A novel durable anti-icing slippery surfaces with dendritic porous structure, Mater. Today Phys. 35 (2023) 101137. https://doi.org/10.1016/j.mtphys.2023.101137.

[60] S. Rønneberg, J. He, Z. Zhang, The need for standards in low ice adhesion surface research: a critical review, J. Adhes. Sci. Technol. 34 (2020) 319–347. https://doi.org/10.1080/01694243.2019.1679523.

[61] M.I. Jamil, X. Zhan, F. Chen, D. Cheng, Q. Zhang, Durable and Scalable Candle Soot Icephobic Coating with Nucleation and Fracture Mechanism, ACS Appl. Mater. Interfaces. 11 (2019) 31532–31542. https://doi.org/10.1021/acsami.9b09819.

[62] Z. He, S. Xiao, H. Gao, J. He, Z. Zhang, Multiscale crack initiator promoted super-low ice adhesion surfaces, Soft Matter. 13 (2017) 6562–6568. https://doi.org/10.1039/C7SM01511A.

[63] J. V. Buddingh, G. Liu, Hard Epoxy Coating with Lasting Low Ice Adhesion Strength, ACS Appl. Polym. Mater. 5 (2023) 7485–7496. https://doi.org/10.1021/acsapm.3c01360.

[64] X. Jiang, Y. Lin, X. Xuan, Y. Zhuo, J. Wu, J. He, X. Du, Z. Zhang, T. Li, Stiffening surface lowers ice adhesion strength by stress concentration sites, Colloids Surfaces A Physicochem. Eng. Asp. 666 (2023) 131334. https://doi.org/10.1016/j.colsurfa.2023.131334.

[65] H. Qi, X. Lei, J. Gu, Y. Zhang, X. Gu, G. Zhao, J. Yu, Low modulus of polydimethylsiloxane organogel coatings induced low ice adhesion, Prog. Org. Coatings. 177 (2023) 107435. https://doi.org/10.1016/j.porgcoat.2023.107435.

[66] A. Nistal, B. Sierra-Martín, A. Fernández-Barbero, On the Durability of Icephobic Coatings: A Review, Materials (Basel). 17 (2023) 235. https://doi.org/10.3390/ma17010235.

[67] W. Li, Y. Zhan, S. Yu, Applications of superhydrophobic coatings in anti-icing: Theory, mechanisms, impact factors, challenges and perspectives, Prog. Org. Coatings. 152 (2021) 106117. https://doi.org/10.1016/j.porgcoat.2020.106117.

[68] Y. Zhuo, S. Xiao, A. Amirfazli, J. He, Z. Zhang, Polysiloxane as icephobic materials – The past, present and the future, Chem. Eng. J. 405 (2021) 127088. https://doi.org/10.1016/j.cej.2020.127088.

[69] J.S.N. Utkarsha Umesh Gwalwanshi, and R.G.P. Narayanan Rajagopalan, Icephobic Coatings: Current Trends and Future Perspectives, in: J. Arya, Raj K.Verros, George D.Davim, Paulo (Eds.), Funct. Coatings Innov. Challenges, John Wiley & Sons, 2024: pp. 380–388.

[70] L.A. Wilen, J.S. Wettlaufer, M. Elbaum, M. Schick, Dispersion-force effects in interfacial premelting of ice, Phys. Rev. B. 52 (1995) 12426–12433. https://doi.org/10.1103/PhysRevB.52.12426.

[71] I.A. Ryzhkin, V.F. Petrenko, Physical Mechanisms Responsible for Ice Adhesion, J. Phys. Chem. B. 101 (1997) 6267–6270. https://doi.org/10.1021/jp9632145.

[72] S. Nihonyanagi, S. Yamaguchi, T. Tahara, Water Hydrogen Bond Structure near Highly Charged Interfaces Is Not Like Ice, J. Am. Chem. Soc. 132 (2010) 6867–6869. https://doi.org/10.1021/ja910914g.

[73] S.A. Kulinich, M. Farzaneh, Ice adhesion on super-hydrophobic surfaces, Appl. Surf. Sci. 255 (2009) 8153–8157. https://doi.org/10.1016/j.apsusc.2009.05.033.

[74] J. Schaaf, M. Kauffeld, Ice aluminum debonding with induction heating, J. Adhes. Sci. Technol. 32 (2018) 2111–2127. https://doi.org/10.1080/01694243.2018.1463671.

[75] V. Upadhyay, T. Galhenage, D. Battocchi, D. Webster, Amphiphilic icephobic coatings, Prog. Org. Coatings. 112 (2017) 191–199. https://doi.org/10.1016/j.porgcoat.2017.07.019.

[76] T. Li, P.F. Ibáñez-Ibáñez, V. Håkonsen, J. Wu, K. Xu, Y. Zhuo, S. Luo, J. He, Z. Zhang, Self-Deicing Electrolyte Hydrogel Surfaces with Pa-level Ice Adhesion and Durable Antifreezing/Antifrost Performance, ACS Appl. Mater. Interfaces. 12 (2020) 35572–35578. https://doi.org/10.1021/acsami.0c06912.

[77] S. Heydarian, R. Jafari, G. Momen, Icephobic behavior of a slippery coating containing nanoporous particles as lubricant-loaded carriers, Surfaces and Interfaces. 41 (2023) 103306. https://doi.org/10.1016/j.surfin.2023.103306.

[78] Q. Liu, Y. Yang, M. Huang, Y. Zhou, Y. Liu, X. Liang, Durability of a lubricant-infused Electrospray Silicon Rubber surface as an anti-icing coating, Appl. Surf. Sci. 346 (2015) 68–76. https://doi.org/10.1016/j.apsusc.2015.02.051.

[79] K. Golovin, A. Dhyani, M.D. Thouless, A. Tuteja, Low–interfacial toughness materials for effective large-scale deicing, Science (80-.). 364 (2019) 371–375. https://doi.org/10.1126/science.aav1266.

[80] L. Yang, Y. Li, D. Huan, Y. Yang, J. Wang, C. Zhu, An icephobic coating for aircraft anti-icing system, J. Mater. Sci. 58 (2023) 16322–16335. https://doi.org/10.1007/s10853-023-09055-5.

[81] B. Li, J. Bai, J. He, C. Ding, X. Dai, W. Ci, T. Zhu, R. Liao, Y. Yuan, A Review on Superhydrophobic Surface with Anti-Icing Properties in Overhead Transmission Lines, Coatings. 13 (2023) 301. https://doi.org/10.3390/coatings13020301.

[82] Y. Wang, J. Liu, M. Li, Q. Wang, Q. Chen, The icephobicity comparison of polysiloxane modified hydrophobic and superhydrophobic surfaces under condensing

environments, Appl. Surf. Sci. 385 (2016) 472–480. https://doi.org/10.1016/j.apsusc.2016.05.117.

[83] S. Jung, M. Dorrestijn, D. Raps, A. Das, C.M. Megaridis, D. Poulikakos, Are Superhydrophobic Surfaces Best for Icephobicity?, Langmuir. 27 (2011) 3059–3066. https://doi.org/10.1021/la104762g.

[84] B. Wang, B. Gao, Y. Wan, Comparative study of calcium alginate, ball-milled biochar, and their composites on aqueous methylene blue adsorption, Environ. Sci. Pollut. Res. 26 (2019) 11535–11541. https://doi.org/10.1007/s11356-018-1497-1.

[85] P. Irajizad, A. Al-Bayati, B. Eslami, T. Shafquat, M. Nazari, P. Jafari, V. Kashyap, A. Masoudi, D. Araya, H. Ghasemi, Stress-localized durable icephobic surfaces, Mater. Horizons. 6 (2019) 758–766. https://doi.org/10.1039/C8MH01291A.

[86] X. Sun, V.G. Damle, S. Liu, K. Rykaczewski, Bioinspired Stimuli-Responsive and Antifreeze-Secreting Anti-Icing Coatings, Adv. Mater. Interfaces. 2 (2015). https://doi.org/10.1002/admi.201400479.

[87] H. Zhao, Q. Sun, X. Deng, J. Cui, Earthworm-Inspired Rough Polymer Coatings with Self-Replenishing Lubrication for Adaptive Friction-Reduction and Antifouling Surfaces, Adv. Mater. 30 (2018). https://doi.org/10.1002/adma.201802141.

[88] J. Cui, D. Daniel, A. Grinthal, K. Lin, J. Aizenberg, Dynamic polymer systems with self-regulated secretion for the control of surface properties and material healing, Nat. Mater. 14 (2015) 790–795. https://doi.org/10.1038/nmat4325.

[89] Y. Zhuo, F. Wang, S. Xiao, J. He, Z. Zhang, One-Step Fabrication of Bioinspired Lubricant-Regenerable Icephobic Slippery Liquid-Infused Porous Surfaces, ACS Omega. 3 (2018) 10139–10144. https://doi.org/10.1021/acsomega.8b01148.

[90] Y. Wang, X. Yao, S. Wu, Q. Li, J. Lv, J. Wang, L. Jiang, Bioinspired Solid Organogel Materials with a Regenerable Sacrificial Alkane Surface Layer, Adv. Mater. 29 (2017). https://doi.org/10.1002/adma.201700865.

[91] A. Sandhu, O.J. Walker, A. Nistal, K.L. Choy, A.J. Clancy, Perfluoroalkane wax infused gels for effective, regenerating, anti-icing surfaces, Chem. Commun. 55 (2019) 3215–3218. https://doi.org/10.1039/C8CC09818B.

[92] F. Wang, W. Ding, J. He, Z. Zhang, Phase transition enabled durable anti-icing surfaces and its DIY design, Chem. Eng. J. 360 (2019) 243–249. https://doi.org/10.1016/j.cej.2018.11.224.

[93] W. Cui, T.A. Pakkanen, Fabrication of transparent icephobic surfaces with self-reparability: Effect of structuring and thickness of the lubricant-elastomer layer, Appl. Surf. Sci. 504 (2020) 144061. https://doi.org/10.1016/j.apsusc.2019.144061.

[94] Q. Rao, J. Zhang, X. Zhan, F. Chen, Q. Zhang, UV-driven self-replenishing slippery

surfaces with programmable droplet-guiding pathways, J. Mater. Chem. A. 8 (2020) 2481–2489. https://doi.org/10.1039/C9TA11723G.

[95] A. Masoudi, P. Irajizad, N. Farokhnia, V. Kashyap, H. Ghasemi, Antiscaling Magnetic Slippery Surfaces, ACS Appl. Mater. Interfaces. 9 (2017) 21025–21033. https://doi.org/10.1021/acsami.7b05564.

[96] Y. Ru, R. Fang, Z. Gu, L. Jiang, M. Liu, Reversibly Thermosecreting Organogels with Switchable Lubrication and Anti-Icing Performance, Angew. Chemie. 132 (2020) 11974–11978. https://doi.org/10.1002/ange.202004122.

[97] W. Zheng, L. Teng, Y. Lai, T. Zhu, S. Li, X. Wu, W. Cai, Z. Chen, J. Huang, Magnetic responsive and flexible composite superhydrophobic photothermal film for passive anti-icing/active deicing, Chem. Eng. J. 427 (2022) 130922. https://doi.org/10.1016/j.cej.2021.130922.

[98] P. Irajizad, M. Hasnain, N. Farokhnia, S.M. Sajadi, H. Ghasemi, Magnetic slippery extreme icephobic surfaces, Nat. Commun. 7 (2016) 13395. https://doi.org/10.1038/ncomms13395.

[99] Y. Zhuo, T. Li, F. Wang, V. Håkonsen, S. Xiao, J. He, Z. Zhang, An ultra-durable icephobic coating by a molecular pulley, Soft Matter. 15 (2019) 3607–3611. https://doi.org/10.1039/C9SM00162J.

[100] S. Xiao, B.H. Skallerud, F. Wang, Z. Zhang, J. He, Enabling sequential rupture for lowering atomistic ice adhesion, Nanoscale. 11 (2019) 16262–16269. https://doi.org/10.1039/C9NR00104B.

[101] Z. He, H. Xie, M.I. Jamil, T. Li, Q. Zhang, Electro-/Photo-Thermal Promoted Anti-Icing Materials: A New Strategy Combined with Passive Anti-Icing and Active De-Icing, Adv. Mater. Interfaces. 9 (2022). https://doi.org/10.1002/admi.202200275.

[102] D. Yang, L. Haworth, P. Agrawal, R. Tao, G. McHale, H. Torun, J. Martin, J. Luo, X. Hou, Y. Fu, Dynamic Mitigation Mechanisms of Rime Icing with Propagating Surface Acoustic Waves, Langmuir. 38 (2022) 11314–11323. https://doi.org/10.1021/acs.langmuir.2c01509.

[103] J. Shi, M. Fulford, H. Li, M. Marzook, M. Reisjalali, M. Salvalaglio, C. Molteni, Investigating the quasi-liquid layer on ice surfaces: a comparison of order parameters, Phys. Chem. Chem. Phys. 24 (2022) 12476–12487. https://doi.org/10.1039/D2CP00752E.

[104] F. Wang, S. Xiao, Y. Zhuo, W. Ding, J. He, Z. Zhang, Liquid layer generators for excellent icephobicity at extremely low temperatures, Mater. Horizons. 6 (2019) 2063–2072. https://doi.org/10.1039/C9MH00859D.

[105] R. Rosenberg, Why Is Ice Slippery?, Phys. Today. 58 (2005) 50–54. https://doi.org/10.1063/1.2169444.

[106] G. Malenkov, Liquid water and ices: understanding the structure and physical properties, J. Phys. Condens. Matter. 21 (2009) 283101. https://doi.org/10.1088/0953-8984/21/28/283101.

[107] J. Zhang, J. Huang, K. Huang, J. Zhang, Z. Li, T. Zhao, J. Wu, Egg white coated alginate nanoparticles with electron sprayer for potential anticancer application, Int. J. Pharm. 564 (2019) 188–196. https://doi.org/10.1016/j.ijpharm.2019.04.045.

[108] Y. Marcus, Effect of Ions on the Structure of Water: Structure Making and Breaking, Chem. Rev. 109 (2009) 1346–1370. https://doi.org/10.1021/cr8003828.

[109] S. Chernyy, M. Järn, K. Shimizu, A. Swerin, S.U. Pedersen, K. Daasbjerg, L. Makkonen, P. Claesson, J. Iruthayaraj, Superhydrophilic Polyelectrolyte Brush Layers with Imparted Anti-Icing Properties: Effect of Counter ions, ACS Appl. Mater. Interfaces. 6 (2014) 6487–6496. https://doi.org/10.1021/am500046d.

[110] L. Zhang, Z. Guo, J. Sarma, X. Dai, Passive Removal of Highly Wetting Liquids and Ice on Quasi-Liquid Surfaces, ACS Appl. Mater. Interfaces. 12 (2020) 20084–20095. https://doi.org/10.1021/acsami.0c02014.

[111] R. Dou, J. Chen, Y. Zhang, X. Wang, D. Cui, Y. Song, L. Jiang, J. Wang, Anti-icing Coating with an Aqueous Lubricating Layer, ACS Appl. Mater. Interfaces. 6 (2014) 6998–7003. https://doi.org/10.1021/am501252u.

[112] S. Xiao, J. He, Z. Zhang, Nanoscale deicing by molecular dynamics simulation, Nanoscale. 8 (2016) 14625–14632. https://doi.org/10.1039/C6NR02398C.

[113] V.F. Petrenko, S. Peng, Reduction of ice adhesion to metal by using self-assembling monolayers (SAMs), Can. J. Phys. 81 (2003) 387–393. https://doi.org/10.1139/p03-014.

[114] K.K. Varanasi, T. Deng, J.D. Smith, M. Hsu, N. Bhate, Frost formation and ice adhesion on superhydrophobic surfaces, Appl. Phys. Lett. 97 (2010). https://doi.org/10.1063/1.3524513.

[115] Z. He, Y. Zhuo, J. He, Z. Zhang, Design and preparation of sandwich-like polydimethylsiloxane (PDMS) sponges with super-low ice adhesion, Soft Matter. 14 (2018) 4846–4851. https://doi.org/10.1039/C8SM00820E.

[116] X. Su, H. Li, X. Lai, Z. Yang, Z. Chen, W. Wu, X. Zeng, Vacuum-assisted layer-by-layer superhydrophobic carbon nanotube films with electrothermal and photothermal effects for deicing and controllable manipulation, J. Mater. Chem. A. 6 (2018) 16910–16919. https://doi.org/10.1039/C8TA05273E.

[117] X. Liu, H. Chen, Z. Zhao, Y. Yan, D. Zhang, Slippery liquid-infused porous electric heating coating for anti-icing and de-icing applications, Surf. Coatings Technol. 374 (2019) 889–896. https://doi.org/10.1016/j.surfcoat.2019.06.077.

[118] Y. Wang, J. Xue, Q. Wang, Q. Chen, J. Ding, Verification of Icephobic/Anti-icing Properties of a Superhydrophobic Surface, ACS Appl. Mater. Interfaces. 5 (2013) 3370–3381. https://doi.org/10.1021/am400429q.

[119] A.J. Meuler, J.D. Smith, K.K. Varanasi, J.M. Mabry, G.H. McKinley, R.E. Cohen, Relationships between Water Wettability and Ice Adhesion, ACS Appl. Mater. Interfaces. 2 (2010) 3100–3110. https://doi.org/10.1021/am1006035.

[120] F. Liu, Z. Wang, Q. Pan, Intelligent Icephobic Surface toward Self-Deicing Capability, ACS Sustain. Chem. Eng. 8 (2020) 792–799. https://doi.org/10.1021/acssuschemeng.9b04570.

[121] Y. Wu, L. Dong, X. Shu, Y. Yang, P. Feng, Q. Ran, Recent advancements in photothermal anti-icing/deicing materials, Chem. Eng. J. 469 (2023) 143924. https://doi.org/10.1016/j.cej.2023.143924.

[122] S. Dash, J. de Ruiter, K.K. Varanasi, Photothermal trap utilizing solar illumination for ice mitigation, Sci. Adv. 4 (2018). https://doi.org/10.1126/sciadv.aat0127.

[123] R. Chatterjee, D. Beysens, S. Anand, Delaying Ice and Frost Formation Using Phase-Switching Liquids, Adv. Mater. 31 (2019). https://doi.org/10.1002/adma.201807812.

[124] M. Kuddushi, N.K. Patel, S. Rajput, O.A. El Seoud, J.P. Mata, N.I. Malek, Temperature-Responsive Low Molecular Weight Ionic Liquid Based Gelator: An Approach to Fabricate an Anti-Cancer Drug-Loaded Hybrid Ionogel, ChemSystemsChem. 2 (2020). https://doi.org/10.1002/syst.201900053.

[125] S.J. Craythorne, K. Anderson, F. Lorenzini, C. McCausland, E.F. Smith, P. Licence, A.C. Marr, P.C. Marr, The Co-Entrapment of a Homogeneous Catalyst and an Ionic Liquid by a Sol–gel Method: Recyclable Ionogel Hydrogenation Catalysts, Chem. – A Eur. J. 15 (2009) 7094–7100. https://doi.org/10.1002/chem.200801809.

[126] J.P. Hallett, T. Welton, ChemInform Abstract: Room-Temperature Ionic Liquids: Solvents for Synthesis and Catalysis. Part 2., ChemInform. 42 (2011). https://doi.org/10.1002/chin.201136231.

[127] P. Wasserscheid, W. Keim, Ionic Liquids—New “Solutions” for Transition Metal Catalysis, Angew. Chemie. 39 (2000) 3772–3789. https://doi.org/10.1002/1521-3773(20001103)39:21<3772::AID-ANIE3772>3.0.CO;2-5.

[128] H.L. Chum, V.R. Koch, L.L. Miller, R.A. Osteryoung, Electrochemical scrutiny of organometallic iron complexes and hexamethylbenzene in a room temperature molten salt, J. Am. Chem. Soc. 97 (1975) 3264–3265. https://doi.org/10.1021/ja00844a081.

[129] P. Bonhôte, A.-P. Dias, N. Papageorgiou, K. Kalyanasundaram, M. Grätzel, Hydrophobic, Highly Conductive Ambient-Temperature Molten Salts, Inorg. Chem. 35 (1996) 1168–1178. https://doi.org/10.1021/ic951325x.

[130] D.R. MacFarlane, P. Meakin, J. Sun, N. Amini, M. Forsyth, Pyrrolidinium Imides: A New Family of Molten Salts and Conductive Plastic Crystal Phases, J. Phys. Chem. B. 103 (1999) 4164–4170. https://doi.org/10.1021/jp984145s.

[131] M.J. Earle, K.R. Seddon, Ionic liquids. Green solvents for the future, Pure Appl. Chem. 72 (2000) 1391–1398. https://doi.org/10.1351/pac200072071391.

[132] R. Hayes, G.G. Warr, R. Atkin, Structure and Nanostructure in Ionic Liquids, Chem. Rev. 115 (2015) 6357–6426. https://doi.org/10.1021/cr500411q.

[133] P. Hapiot, C. Lagrost, Electrochemical Reactivity in Room-Temperature Ionic Liquids, Chem. Rev. 108 (2008) 2238–2264. https://doi.org/10.1021/cr0680686.

[134] M. Galiński, A. Lewandowski, I. Stępniak, Ionic liquids as electrolytes, Electrochim. Acta. 51 (2006) 5567–5580. https://doi.org/10.1016/j.electacta.2006.03.016.

[135] D.R. MacFarlane, K.R. Seddon, Ionic Liquids—Progress on the Fundamental Issues, Aust. J. Chem. 60 (2007) 3. https://doi.org/10.1071/CH06478.

[136] T. Tsuda, R. Hagiwara, Chemistry in heterocyclic ammonium fluorohydrogenate room-temperature ionic liquid, J. Fluor. Chem. 129 (2008) 4–13. https://doi.org/10.1016/j.jfluchem.2007.10.004.

[137] H.-H. and R. Ozawa, Structure of Ionic Liquids and Ionic Liquid Compounds: Are Ionic Liquids Genuine Liquids in the Conventional Sense?, in: S.A. RICE (Ed.), Adv. Chem. Phys., John Wiley & Sons, Inc., 2005: pp. 85–105.

[138] T.L. Greaves, C.J. Drummond, Protic Ionic Liquids: Properties and Applications, Chem. Rev. 108 (2008) 206–237. https://doi.org/10.1021/cr068040u.

[139] C.A. Angell, N. Byrne, J.-P. Belieres, Parallel Developments in Aprotic and Protic Ionic Liquids: Physical Chemistry and Applications, Acc. Chem. Res. 40 (2007) 1228–1236. https://doi.org/10.1021/ar7001842.

[140] A.J. Parker, The effects of solvation on the properties of anions in dipolar aprotic solvents, Q. Rev. Chem. Soc. 16 (1962) 163. https://doi.org/10.1039/qr9621600163.

[141] W. Xu, C.A. Angell, Solvent-Free Electrolytes with Aqueous Solution-Like Conductivities, Science (80-.). 302 (2003) 422–425. https://doi.org/10.1126/science.1090287.

[142] L. Chen, G.E. Mullen, M. Le Roch, C.G. Cassity, N. Gouault, H.Y. Fadamiro, R.E. Barletta, R.A. O'Brien, R.E. Sykora, A.C. Stenson, K.N. West, H.E. Horne, J.M. Hendrich, K.R. Xiang, J.H. Davis, On the Formation of a Protic Ionic Liquid in Nature, Angew. Chemie Int. Ed. 53 (2014) 11762–11765. https://doi.org/10.1002/anie.201404402.

[143] A. Noda, M.A.B.H. Susan, K. Kudo, S. Mitsushima, K. Hayamizu, M. Watanabe,

Brønsted Acid−Base Ionic Liquids as Proton-Conducting Nonaqueous Electrolytes, J. Phys. Chem. B. 107 (2003) 4024–4033. https://doi.org/10.1021/jp022347p.

[144] M.S. Miran, T. Yasuda, M.A.B.H. Susan, K. Dokko, M. Watanabe, Binary Protic Ionic Liquid Mixtures as a Proton Conductor: High Fuel Cell Reaction Activity and Facile Proton Transport, J. Phys. Chem. C. 118 (2014) 27631–27639. https://doi.org/10.1021/jp506957y.

[145] J.P. Belieres, C.A. Angell, Protic Ionic Liquids: Preparation, Characterization, and Proton Free Energy Level Representation, J. Phys. Chem. B. 111 (2007) 4926–4937. https://doi.org/10.1021/jp067589u.

[146] J. Estager, J.D. Holbrey, M. Swadźba-Kwaśny, Halometallate ionic liquids – revisited, Chem. Soc. Rev. 43 (2014) 847–886. https://doi.org/10.1039/C3CS60310E.

[147] C.M.G. and M.J. Muldoon, Ionic Liquids in Synthesis, Second, Co, 2007.

[148] M.J.A. Shiddiky, A.A.J. Torriero, Application of ionic liquids in electrochemical sensing systems, Biosens. Bioelectron. 26 (2011) 1775–1787. https://doi.org/10.1016/j.bios.2010.08.064.

[149] H. Liu, Y. Liu, J. Li, Ionic liquids in surface electrochemistry, Phys. Chem. Chem. Phys. 12 (2010) 1685. https://doi.org/10.1039/b921469k.

[150] G. Kaur, H. Kumar, M. Singla, Diverse applications of ionic liquids: A comprehensive review, J. Mol. Liq. 351 (2022) 118556. https://doi.org/10.1016/j.molliq.2022.118556.

[151] K.K. Maniam, S. Paul, Progress in Electrodeposition of Zinc and Zinc Nickel Alloys Using Ionic Liquids, Appl. Sci. 10 (2020) 5321. https://doi.org/10.3390/app10155321.

[152] T. Rüther, A.I. Bhatt, A.S. Best, K.R. Harris, A.F. Hollenkamp, Electrolytes for Lithium (Sodium) Batteries Based on Ionic Liquids: Highlighting the Key Role Played by the Anion, Batter. Supercaps. 3 (2020) 793–827. https://doi.org/10.1002/batt.202000022.

[153] R.A. Abu Talip, W.Z.N. Yahya, M.A. Bustam, Ionic Liquids Roles and Perspectives in Electrolyte for Dye-Sensitized Solar Cells, Sustainability. 12 (2020) 7598. https://doi.org/10.3390/su12187598.

[154] S. Pan, M. Yao, J. Zhang, B. Li, C. Xing, X. Song, P. Su, H. Zhang, Recognition of Ionic Liquids as High-Voltage Electrolytes for Supercapacitors, Front. Chem. 8 (2020). https://doi.org/10.3389/fchem.2020.00261.

[155] Y. Kondo, T. Koyama, S. Sasaki, Tribological Properties of Ionic Liquids, in: Ion. Liq. - New Asp. Futur., InTech, 2013. https://doi.org/10.5772/52595.

[156] O.A. El Seoud, N. Keppeler, N.I. Malek, P.D. Galgano, Ionic Liquid-Based Surfactants: Recent Advances in Their Syntheses, Solution Properties, and

Applications, Polymers (Basel). 13 (2021) 1100. https://doi.org/10.3390/polym13071100.

[157] M.A. Deyab, Understanding the anti-corrosion mechanism and performance of ionic liquids in desalination, petroleum, pickling, de-scaling, and acid cleaning applications, J. Mol. Liq. 309 (2020) 113107. https://doi.org/10.1016/j.molliq.2020.113107.

[158] M.I. Nessim, M.T. Zaky, M.A. Deyab, Three new gemini ionic liquids: Synthesis, characterizations and anticorrosion applications, J. Mol. Liq. 266 (2018) 703–710. https://doi.org/10.1016/j.molliq.2018.07.001.

[159] M. Jain, A. Marfatia, N. Imam, D. Ray, V.K. Aswal, N.Y. Patel, V.H. Raval, S.K. Kailasa, N.I. Malek, Ionic liquid-based catanionic vesicles: A de novo system to judiciously improve the solubility, stability and antimicrobial activity of curcumin, J. Mol. Liq. 341 (2021) 117396. https://doi.org/10.1016/j.molliq.2021.117396.

[160] L. Li, Y. Zhang, Y. Sun, S. Sun, G. Shen, P. Zhao, J. Cui, H. Qiao, Y. Wang, H. Zhou, Manufacturing pure cellulose films by recycling ionic liquids as plasticizers, Green Chem. 22 (2020) 3835–3841. https://doi.org/10.1039/D0GC00046A.

[161] P. V. Bhongale, S.S. Joshi, N.A. Mali, Selective monoalkylation of hydroquinone in the presence of SO3H-functionalized ionic liquids as catalysts, Chem. Pap. 74 (2020) 4461–4471. https://doi.org/10.1007/s11696-020-01230-1.

[162] A.A.M. Elgharbawy, M. Moniruzzaman, M. Goto, Facilitating enzymatic reactions by using ionic liquids: A mini review, Curr. Opin. Green Sustain. Chem. 27 (2021) 100406. https://doi.org/10.1016/j.cogsc.2020.100406.

[163] A.A.C. Toledo Hijo, G.J. Maximo, M.C. Costa, E.A.C. Batista, A.J.A. Meirelles, Applications of Ionic Liquids in the Food and Bioproducts Industries, ACS Sustain. Chem. Eng. 4 (2016) 5347–5369. https://doi.org/10.1021/acssuschemeng.6b00560.

[164] S.K. Zandu, H. Chopra, I. Singh, Ionic Liquids for Therapeutic and Drug Delivery Applications, Curr. Drug Res. Rev. 12 (2020) 26–41. https://doi.org/10.2174/2589977511666191125103338.

[165] A. Krishnan, K.P. Gopinath, D.-V.N. Vo, R. Malolan, V.M. Nagarajan, J. Arun, Ionic liquids, deep eutectic solvents and liquid polymers as green solvents in carbon capture technologies: a review, Environ. Chem. Lett. 18 (2020) 2031–2054. https://doi.org/10.1007/s10311-020-01057-y.

[166] M. Armand, F. Endres, D.R. MacFarlane, H. Ohno, B. Scrosati, Ionic-liquid materials for the electrochemical challenges of the future, in: Mater. Sustain. Energy, Co-Published with Macmillan Publishers Ltd, UK, 2010: pp. 129–137. https://doi.org/10.1142/9789814317665_0020.

[167] N. V. Plechkova, K.R. Seddon, Applications of ionic liquids in the chemical industry, Chem. Soc. Rev. 37 (2008) 123–150. https://doi.org/10.1039/B006677J.

[168] C.P. Mehnert, Supported Ionic Liquid Catalysis, Chem. – A Eur. J. 11 (2005) 50–56. https://doi.org/10.1002/chem.200400683.

[169] A. Riisagera, R. Fehrmanna, M. Haumannb, P. Wasserscheidb, Supported ionic liquids: versatile reaction and separation media, Top. Catal. 40 (2006) 91–102. https://doi.org/10.1007/s11244-006-0111-9.

[170] T. Ueki, M. Watanabe, Macromolecules in Ionic Liquids: Progress, Challenges, and Opportunities, Macromolecules. 41 (2008) 3739–3749. https://doi.org/10.1021/ma800171k.

[171] F. Gayet, L. Viau, F. Leroux, F. Mabille, S. Monge, J.-J. Robin, A. Vioux, Unique Combination of Mechanical Strength, Thermal Stability, and High Ion Conduction in PMMA−Silica Nanocomposites Containing High Loadings of Ionic Liquid, Chem. Mater. 21 (2009) 5575–5577. https://doi.org/10.1021/cm9027918.

[172] J. Le Bideau, L. Viau, A. Vioux, Ionogels, ionic liquid based hybrid materials, Chem. Soc. Rev. 40 (2011) 907–925. https://doi.org/10.1039/C0CS00059K.

[173] R. Göbel, R.J. White, M.-M. Titirici, A. Taubert, Carbon-based ionogels: tuning the properties of the ionic liquid via carbon–ionic liquid interaction, Phys. Chem. Chem. Phys. 14 (2012) 5992. https://doi.org/10.1039/c2cp23929a.

[174] D.M. Correia, L.C. Fernandes, P.M. Martins, C. García-Astrain, C.M. Costa, J. Reguera, S. Lanceros-Méndez, Ionic Liquid–Polymer Composites: A New Platform for Multifunctional Applications, Adv. Funct. Mater. 30 (2020). https://doi.org/10.1002/adfm.201909736.

[175] L.C. Tomé, L. Porcarelli, J.E. Bara, M. Forsyth, D. Mecerreyes, Emerging iongel materials towards applications in energy and bioelectronics, Mater. Horizons. 8 (2021) 3239–3265. https://doi.org/10.1039/D1MH01263K.

[176] R. Tamate, T. Ueki, A.M. Akimoto, R. Yoshida, T. Oyama, H. Kokubo, M. Watanabe, Photocurable ABA triblock copolymer-based ion gels utilizing photodimerization of coumarin, RSC Adv. 8 (2018) 3418–3422. https://doi.org/10.1039/C7RA13181J.

[177] M. Sun, Z. Zeng, L. Peng, Z. Han, C. Yu, S. Cheng, J. Xie, Ultrathin polymer electrolyte film prepared by in situ polymerization for lithium metal batteries, Mater. Today Energy. 21 (2021) 100785. https://doi.org/10.1016/j.mtener.2021.100785.

[178] S. Sultana, K. Ahmed, P.K. Jiwanti, B.Y. Wardhana, M.N.I. Shiblee, Ionic Liquid-Based Gels for Applications in Electrochemical Energy Storage and Conversion Devices: A Review of Recent Progress and Future Prospects, Gels. 8 (2021) 2. https://doi.org/10.3390/gels8010002.

[179] J. Demarteau, A. Fernandez de Añastro, A.S. Shaplov, D. Mecerreyes, Poly(diallyldimethylammonium) based poly(ionic liquid) di- and triblock copolymers by PISA as matrices for ionogel membranes, Polym. Chem. 11 (2020) 1481–1488.

https://doi.org/10.1039/C9PY01552C.

[180] P. Bernardo, J.C. Jansen, F. Bazzarelli, F. Tasselli, A. Fuoco, K. Friess, P. Izák, V. Jarmarová, M. Kačírková, G. Clarizia, Gas transport properties of Pebax®/room temperature ionic liquid gel membranes, Sep. Purif. Technol. 97 (2012) 73–82. https://doi.org/10.1016/j.seppur.2012.02.041.

[181] M.M. Villar-Chavero, J.C. Domínguez, M.V. Alonso, M. Oliet, F. Rodriguez, Chitosan-reinforced cellulosic bionogels: Viscoelastic and antibacterial properties, Carbohydr. Polym. 229 (2020) 115569. https://doi.org/10.1016/j.carbpol.2019.115569.

[182] S. Dai, Y.H. Ju, H.J. Gao, J.S. Lin, S.J. Pennycook, C.E. Barnes, Preparation of silica aerogel using ionic liquids as solvents, Chem. Commun. (2000) 243–244. https://doi.org/10.1039/a907147d.

[183] Z. He, P. Alexandridis, Nanoparticles in ionic liquids: interactions and organization, Phys. Chem. Chem. Phys. 17 (2015) 18238–18261. https://doi.org/10.1039/C5CP01620G.

[184] Q. Lyu, S. Wang, B. Peng, X. Chen, S. Du, M. Li, L. Zhang, J. Zhu, Bioinspired Photonic Ionogels as Interactively Visual Ionic Skin with Optical and Electrical Synergy, Small. 17 (2021). https://doi.org/10.1002/smll.202103271.

[185] S.-Y. Zhang, Q. Zhuang, M. Zhang, H. Wang, Z. Gao, J.-K. Sun, J. Yuan, Poly(ionic liquid) composites, Chem. Soc. Rev. 49 (2020) 1726–1755. https://doi.org/10.1039/C8CS00938D.

[186] A. Muñoz-Bonilla, M. Fernández-García, Poly(ionic liquid)s as antimicrobial materials, Eur. Polym. J. 105 (2018) 135–149. https://doi.org/10.1016/j.eurpolymj.2018.05.027.

[187] W. Qian, J. Texter, F. Yan, Frontiers in poly(ionic liquid)s: syntheses and applications, Chem. Soc. Rev. 46 (2017) 1124–1159. https://doi.org/10.1039/C6CS00620E.

[188] I. Kammakakam, J.E. Bara, E.M. Jackson, Dual Anion–Cation Crosslinked Poly(ionic liquid) Composite Membranes for Enhanced CO 2 Separation, ACS Appl. Polym. Mater. 2 (2020) 5067–5076. https://doi.org/10.1021/acsapm.0c00877.

[189] X. Fan, S. Liu, Z. Jia, J.J. Koh, J.C.C. Yeo, C.-G. Wang, N.E. Surat'man, X.J. Loh, J. Le Bideau, C. He, Z. Li, T.-P. Loh, Ionogels: recent advances in design, material properties and emerging biomedical applications, Chem. Soc. Rev. 52 (2023) 2497–2527. https://doi.org/10.1039/D2CS00652A.

[190] Z. Lei, P. Wu, A highly transparent and ultra-stretchable conductor with stable conductivity during large deformation, Nat. Commun. 10 (2019) 3429. https://doi.org/10.1038/s41467-019-11364-w.

[191] Z. Cao, H. Liu, L. Jiang, Transparent, mechanically robust, and ultrastable ionogels enabled by hydrogen bonding between elastomers and ionic liquids, Mater. Horizons. 7 (2020) 912–918. https://doi.org/10.1039/C9MH01699F.

[192] Y.M. Kim, H.C. Moon, Ionoskins: Nonvolatile, Highly Transparent, Ultrastretchable Ionic Sensory Platforms for Wearable Electronics, Adv. Funct. Mater. 30 (2020). https://doi.org/10.1002/adfm.201907290.

[193] W. Qiu, G. Chen, H. Zhu, Q. Zhang, S. Zhu, Enhanced stretchability and robustness towards flexible ionotronics via double-network structure and ion-dipole interactions, Chem. Eng. J. 434 (2022) 134752. https://doi.org/10.1016/j.cej.2022.134752.

[194] J. Yuan, D. Mecerreyes, M. Antonietti, Poly(ionic liquid)s: An update, Prog. Polym. Sci. 38 (2013) 1009–1036. https://doi.org/10.1016/j.progpolymsci.2013.04.002.

[195] M. Chen, B.T. White, C.R. Kasprzak, T.E. Long, Advances in phosphonium-based ionic liquids and poly(ionic liquid)s as conductive materials, Eur. Polym. J. 108 (2018) 28–37. https://doi.org/10.1016/j.eurpolymj.2018.08.015.

[196] Z. Luo, W. Li, J. Yan, J. Sun, Roles of Ionic Liquids in Adjusting Nature of Ionogels: A Mini Review, Adv. Funct. Mater. 32 (2022). https://doi.org/10.1002/adfm.202203988.

[197] Z. He, C. Wu, M. Hua, S. Wu, D. Wu, X. Zhu, J. Wang, X. He, Bioinspired Multifunctional Anti-icing Hydrogel, Matter. 2 (2020) 723–734. https://doi.org/10.1016/j.matt.2019.12.017.

[198] S. Schöder, H. Reichert, H. Schröder, M. Mezger, J.S. Okasinski, V. Honkimäki, J. Bilgram, H. Dosch, Radiation-Induced Premelting of Ice at Silica Interfaces, Phys. Rev. Lett. 103 (2009) 095502. https://doi.org/10.1103/PhysRevLett.103.095502.

[199] Y. Ding, J. Zhang, X. Zhang, Y. Zhou, S. Wang, H. Liu, L. Jiang, Ionic-Liquid-Gel Surfaces Showing Easy-Sliding and Ultradurable Features, Adv. Mater. Interfaces. 2 (2015). https://doi.org/10.1002/admi.201500177.

[200] W. Yan, T. Li, Y. Zhang, Y. Lin, X. Lan, J. Wu, Thermomechanically Resilient Polyionic Elastomers with Enhanced Anti-Icing Performances, ACS Appl. Mater. Interfaces. 16 (2024) 32693–32701. https://doi.org/10.1021/acsami.4c04501.

[201] Q. Hao, Y. Pang, Y. Zhao, J. Zhang, J. Feng, S. Yao, Mechanism of Delayed Frost Growth on Superhydrophobic Surfaces with Jumping Condensates: More Than Interdrop Freezing, Langmuir. 30 (2014) 15416–15422. https://doi.org/10.1021/la504166x.

[202] S. Jung, M.K. Tiwari, D. Poulikakos, Frost halos from supercooled water droplets, Proc. Natl. Acad. Sci. 109 (2012) 16073–16078. https://doi.org/10.1073/pnas.1206121109.

[203] T.M. Schutzius, S. Jung, T. Maitra, G. Graeber, M. Köhme, D. Poulikakos, Spontaneous droplet trampolining on rigid superhydrophobic surfaces, Nature. 527 (2015) 82–85. https://doi.org/10.1038/nature15738.

[204] S. Jung, M.K. Tiwari, N.V. Doan, D. Poulikakos, Mechanism of supercooled droplet freezing on surfaces, Nat. Commun. 3 (2012) 615. https://doi.org/10.1038/ncomms1630.

[205] G. Graeber, T.M. Schutzius, H. Eghlidi, D. Poulikakos, Spontaneous self-dislodging of freezing water droplets and the role of wettability, Proc. Natl. Acad. Sci. 114 (2017) 11040–11045. https://doi.org/10.1073/pnas.1705952114.

[206] J. Liu, C. Zhu, K. Liu, Y. Jiang, Y. Song, J.S. Francisco, X.C. Zeng, J. Wang, Distinct ice patterns on solid surfaces with various wettabilities, Proc. Natl. Acad. Sci. 114 (2017) 11285–11290. https://doi.org/10.1073/pnas.1712829114.

[207] A. Kirillova, L. Ionov, I. V. Roisman, A. Synytska, Hybrid Hairy Janus Particles for Anti-Icing and De-Icing Surfaces: Synergism of Properties and Effects, Chem. Mater. 28 (2016) 6995–7005. https://doi.org/10.1021/acs.chemmater.6b02765.

[208] S.F. Ahmadi, S. Nath, G.J. Iliff, B.R. Srijanto, C.P. Collier, P. Yue, J.B. Boreyko, Passive Antifrosting Surfaces Using Microscopic Ice Patterns, ACS Appl. Mater. Interfaces. 10 (2018) 32874–32884. https://doi.org/10.1021/acsami.8b11285.

[209] Y. Jin, C. Wu, Y. Yang, J. Wu, Z. He, J. Wang, Inhibiting Condensation Freezing on Patterned Polyelectrolyte Coatings, ACS Nano. 14 (2020) 5000–5007. https://doi.org/10.1021/acsnano.0c01304.

[210] T. Cheng, R. He, Q. Zhang, X. Zhan, F. Chen, Magnetic particle-based super-hydrophobic coatings with excellent anti-icing and thermoresponsive deicing performance, J. Mater. Chem. A. 3 (2015) 21637–21646. https://doi.org/10.1039/C5TA05277G.

[211] S. Wu, Y. Du, Y. Alsaid, D. Wu, M. Hua, Y. Yan, B. Yao, Y. Ma, X. Zhu, X. He, Superhydrophobic photothermal icephobic surfaces based on candle soot, Proc. Natl. Acad. Sci. 117 (2020) 11240–11246. https://doi.org/10.1073/pnas.2001972117.

[212] A.L. DeVries, D.E. Wohlschlag, Freezing Resistance in Some Antarctic Fishes, Science (80-.). 163 (1969) 1073–1075. https://doi.org/10.1126/science.163.3871.1073.

[213] J. Xu, R. Jing, X. Ren, G. Gao, Fish-inspired anti-icing hydrogel sensors with low-temperature adhesion and toughness, J. Mater. Chem. A. 8 (2020) 9373–9381. https://doi.org/10.1039/D0TA02370A.

[214] G. Bai, D. Gao, Z. Liu, X. Zhou, J. Wang, Probing the critical nucleus size for ice formation with graphene oxide nanosheets, Nature. 576 (2019) 437–441. https://doi.org/10.1038/s41586-019-1827-6.

[215] C.I. Biggs, T.L. Bailey, Ben Graham, C. Stubbs, A. Fayter, M.I. Gibson, Polymer mimics of biomacromolecular antifreezes, Nat. Commun. 8 (2017) 1546. https://doi.org/10.1038/s41467-017-01421-7.

[216] R. Drori, C. Li, C. Hu, P. Raiteri, A.L. Rohl, M.D. Ward, B. Kahr, A Supramolecular Ice Growth Inhibitor, J. Am. Chem. Soc. 138 (2016) 13396–13401. https://doi.org/10.1021/jacs.6b08267.

[217] Z. Liu, Z. He, J. Lv, Y. Jin, S. Wu, G. Liu, F. Zhou, J. Wang, Ion-specific ice propagation behavior on polyelectrolyte brush surfaces, RSC Adv. 7 (2017) 840–844. https://doi.org/10.1039/C6RA24847K.

[218] A. Azimi Yancheshme, A. Allahdini, K. Maghsoudi, R. Jafari, G. Momen, Potential anti-icing applications of encapsulated phase change material–embedded coatings; a review, J. Energy Storage. 31 (2020) 101638. https://doi.org/10.1016/j.est.2020.101638.

[219] M. Shamshiri, R. Jafari, G. Momen, A novel hybrid anti-icing surface combining an aqueous self-lubricating coating and phase-change materials, Prog. Org. Coatings. 177 (2023) 107414. https://doi.org/10.1016/j.porgcoat.2023.107414.

[220] P.T. Anastas, J.C. Warner, Green Chemistry, Theory and Practice, Oxford University PressOxford, 2000. https://doi.org/10.1093/oso/9780198506980.001.0001.

[221] A.P. Abbott, G. Capper, D.L. Davies, R.K. Rasheed, V. Tambyrajah, Novel solvent properties of choline chloride/urea mixtures, Chem. Commun. (2003) 70–71. https://doi.org/10.1039/b210714g.

[222] A.P. Abbott, D. Boothby, G. Capper, D.L. Davies, R.K. Rasheed, Deep Eutectic Solvents Formed between Choline Chloride and Carboxylic Acids: Versatile Alternatives to Ionic Liquids, J. Am. Chem. Soc. 126 (2004) 9142–9147. https://doi.org/10.1021/ja048266j.

[223] A.P. Abbott, G. Capper, S. Gray, Design of Improved Deep Eutectic Solvents Using Hole Theory, ChemPhysChem. 7 (2006) 803–806. https://doi.org/10.1002/cphc.200500489.

[224] F.S. Mjalli, O.U. Ahmed, Characteristics and intermolecular interaction of eutectic binary mixtures: Reline and Glyceline, Korean J. Chem. Eng. 33 (2016) 337–343. https://doi.org/10.1007/s11814-015-0134-7.

[225] B.B. Hansen, S. Spittle, B. Chen, D. Poe, Y. Zhang, J.M. Klein, A. Horton, L. Adhikari, T. Zelovich, B.W. Doherty, B. Gurkan, E.J. Maginn, A. Ragauskas, M. Dadmun, T.A. Zawodzinski, G.A. Baker, M.E. Tuckerman, R.F. Savinell, J.R. Sangoro, Deep Eutectic Solvents: A Review of Fundamentals and Applications, Chem. Rev. 121 (2021) 1232–1285. https://doi.org/10.1021/acs.chemrev.0c00385.

[226] E.L. Smith, A.P. Abbott, K.S. Ryder, Deep Eutectic Solvents (DESs) and Their

Applications, Chem. Rev. 114 (2014) 11060–11082. https://doi.org/10.1021/cr300162p.

[227] Q. Zhang, K. De Oliveira Vigier, S. Royer, F. Jérôme, Deep eutectic solvents: syntheses, properties and applications, Chem. Soc. Rev. 41 (2012) 7108. https://doi.org/10.1039/c2cs35178a.

[228] S.L. Perkins, P. Painter, C.M. Colina, Experimental and Computational Studies of Choline Chloride-Based Deep Eutectic Solvents, J. Chem. Eng. Data. 59 (2014) 3652–3662. https://doi.org/10.1021/je500520h.

[229] R. Stefanovic, M. Ludwig, G.B. Webber, R. Atkin, A.J. Page, Nanostructure, hydrogen bonding and rheology in choline chloride deep eutectic solvents as a function of the hydrogen bond donor, Phys. Chem. Chem. Phys. 19 (2017) 3297–3306. https://doi.org/10.1039/C6CP07932F.

[230] T. Zhekenov, N. Toksanbayev, Z. Kazakbayeva, D. Shah, F.S. Mjalli, Formation of type III Deep Eutectic Solvents and effect of water on their intermolecular interactions, Fluid Phase Equilib. 441 (2017) 43–48. https://doi.org/10.1016/j.fluid.2017.01.022.

[231] S. Zahn, Deep eutectic solvents: similia similibus solvuntur?, Phys. Chem. Chem. Phys. 19 (2017) 4041–4047. https://doi.org/10.1039/C6CP08017K.

[232] A.P. Abbott, J.C. Barron, K.S. Ryder, D. Wilson, Eutectic-Based Ionic Liquids with Metal-Containing Anions and Cations, Chem. – A Eur. J. 13 (2007) 6495–6501. https://doi.org/10.1002/chem.200601738.

[233] L.I.N. Tomé, V. Baião, W. da Silva, C.M.A. Brett, Deep eutectic solvents for the production and application of new materials, Appl. Mater. Today. 10 (2018) 30–50. https://doi.org/10.1016/j.apmt.2017.11.005.

[234] Y.H. Choi, J. van Spronsen, Y. Dai, M. Verberne, F. Hollmann, I.W.C.E. Arends, G.-J. Witkamp, R. Verpoorte, Are Natural Deep Eutectic Solvents the Missing Link in Understanding Cellular Metabolism and Physiology?, Plant Physiol. 156 (2011) 1701–1705. https://doi.org/10.1104/pp.111.178426.

[235] Y. Dai, G.J. Witkamp, R. Verpoorte, Y.H. Choi, Natural Deep Eutectic Solvents as a New Extraction Media for Phenolic Metabolites in Carthamus tinctorius L., Anal. Chem. 85 (2013) 6272–6278. https://doi.org/10.1021/ac400432p.

[236] Y. Dai, R. Verpoorte, Y.H. Choi, Natural deep eutectic solvents providing enhanced stability of natural colorants from safflower (Carthamus tinctorius), Food Chem. 159 (2014) 116–121. https://doi.org/10.1016/j.foodchem.2014.02.155.

[237] M. Espino, M. de los Ángeles Fernández, F.J.V. Gomez, M.F. Silva, Natural designer solvents for greening analytical chemistry, TrAC Trends Anal. Chem. 76 (2016) 126–136. https://doi.org/10.1016/j.trac.2015.11.006.

[238] N. Li, Y. Wang, K. Xu, Y. Huang, Q. Wen, X. Ding, Development of green betaine-based deep eutectic solvent aqueous two-phase system for the extraction of protein, Talanta. 152 (2016) 23–32. https://doi.org/10.1016/j.talanta.2016.01.042.

[239] I.M. Aroso, R. Craveiro, Â. Rocha, M. Dionísio, S. Barreiros, R.L. Reis, A. Paiva, A.R.C. Duarte, Design of controlled release systems for THEDES—Therapeutic deep eutectic solvents, using supercritical fluid technology, Int. J. Pharm. 492 (2015) 73–79. https://doi.org/10.1016/j.ijpharm.2015.06.038.

[240] I.M. Aroso, J.C. Silva, F. Mano, A.S.D. Ferreira, M. Dionísio, I. Sá-Nogueira, S. Barreiros, R.L. Reis, A. Paiva, A.R.C. Duarte, Dissolution enhancement of active pharmaceutical ingredients by therapeutic deep eutectic systems, Eur. J. Pharm. Biopharm. 98 (2016) 57–66. https://doi.org/10.1016/j.ejpb.2015.11.002.

[241] H.G. Morrison, C.C. Sun, S. Neervannan, Characterization of thermal behavior of deep eutectic solvents and their potential as drug solubilization vehicles, Int. J. Pharm. 378 (2009) 136–139. https://doi.org/10.1016/j.ijpharm.2009.05.039.

[242] R.K. Ibrahim, M. Hayyan, M.A. AlSaadi, S. Ibrahim, A. Hayyan, M.A. Hashim, Physical properties of ethylene glycol-based deep eutectic solvents, J. Mol. Liq. 276 (2019) 794–800. https://doi.org/10.1016/j.molliq.2018.12.032.

[243] M.S. Sitze, E.R. Schreiter, E. V. Patterson, R.G. Freeman, Ionic Liquids Based on FeCl 3 and FeCl 2 . Raman Scattering and ab Initio Calculations, Inorg. Chem. 40 (2001) 2298–2304. https://doi.org/10.1021/ic001042r.

[244] J.Z. Yang, Y. Jin, W.G. Xu, Q.G. Zhang, S.L. Zang, Studies on mixture of ionic liquid EMIGaCl4 and EMIC, Fluid Phase Equilib. 227 (2005) 41–46. https://doi.org/10.1016/j.fluid.2004.10.026.

[245] X. Li, K.H. Row, Development of deep eutectic solvents applied in extraction and separation, J. Sep. Sci. 39 (2016) 3505–3520. https://doi.org/10.1002/jssc.201600633.

[246] B. Kudłak, K. Owczarek, J. Namieśnik, Selected issues related to the toxicity of ionic liquids and deep eutectic solvents—a review, Environ. Sci. Pollut. Res. 22 (2015) 11975–11992. https://doi.org/10.1007/s11356-015-4794-y.

[247] Y.P. Mbous, M. Hayyan, A. Hayyan, W.F. Wong, M.A. Hashim, C.Y. Looi, Applications of deep eutectic solvents in biotechnology and bioengineering—Promises and challenges, Biotechnol. Adv. 35 (2017) 105–134. https://doi.org/10.1016/j.biotechadv.2016.11.006.

[248] Z. Chen, M. Ludwig, G.G. Warr, R. Atkin, Effect of cation alkyl chain length on surface forces and physical properties in deep eutectic solvents, J. Colloid Interface Sci. 494 (2017) 373–379. https://doi.org/10.1016/j.jcis.2017.01.109.

[249] Z. Chen, T.L. Greaves, G.G. Warr, R. Atkin, Mixing cations with different alkyl chain lengths markedly depresses the melting point in deep eutectic solvents formed from

alkylammonium bromide salts and urea, Chem. Commun. 53 (2017) 2375–2377. https://doi.org/10.1039/C7CC00201G.

[250] M.G. Montalbán, C.L. Bolívar, F.G. Díaz Baños, G. Víllora, Effect of Temperature, Anion, and Alkyl Chain Length on the Density and Refractive Index of 1-Alkyl-3-methylimidazolium-Based Ionic Liquids, J. Chem. Eng. Data. 60 (2015) 1986–1996. https://doi.org/10.1021/je501091q.

[251] A. Yadav, S. Pandey, Densities and Viscosities of (Choline Chloride + Urea) Deep Eutectic Solvent and Its Aqueous Mixtures in the Temperature Range 293.15 K to 363.15 K, J. Chem. Eng. Data. 59 (2014) 2221–2229. https://doi.org/10.1021/je5001796.

[252] A.P. Abbott, R.C. Harris, K.S. Ryder, Application of Hole Theory to Define Ionic Liquids by their Transport Properties, J. Phys. Chem. B. 111 (2007) 4910–4913. https://doi.org/10.1021/jp0671998.

[253] Y. Chen, W. Chen, L. Fu, Y. Yang, Y. Wang, X. Hu, F. Wang, T. Mu, Surface Tension of 50 Deep Eutectic Solvents: Effect of Hydrogen-Bonding Donors, Hydrogen-Bonding Acceptors, Other Solvents, and Temperature, Ind. Eng. Chem. Res. 58 (2019) 12741–12750. https://doi.org/10.1021/acs.iecr.9b00867.

[254] P. Makoś, A. Przyjazny, G. Boczkaj, Hydrophobic deep eutectic solvents as “green” extraction media for polycyclic aromatic hydrocarbons in aqueous samples, J. Chromatogr. A. 1570 (2018) 28–37. https://doi.org/10.1016/j.chroma.2018.07.070.

[255] M.A.A. Rocha, C.M.S.S. Neves, M.G. Freire, O. Russina, A. Triolo, J.A.P. Coutinho, L.M.N.B.F. Santos, Alkylimidazolium Based Ionic Liquids: Impact of Cation Symmetry on Their Nanoscale Structural Organization, J. Phys. Chem. B. 117 (2013) 10889–10897. https://doi.org/10.1021/jp406374a.

[256] A. Paiva, R. Craveiro, I. Aroso, M. Martins, R.L. Reis, A.R.C. Duarte, Natural Deep Eutectic Solvents – Solvents for the 21st Century, ACS Sustain. Chem. Eng. 2 (2014) 1063–1071. https://doi.org/10.1021/sc500096j.

[257] C. Florindo, F.S. Oliveira, L.P.N. Rebelo, A.M. Fernandes, I.M. Marrucho, Insights into the Synthesis and Properties of Deep Eutectic Solvents Based on Cholinium Chloride and Carboxylic Acids, ACS Sustain. Chem. Eng. 2 (2014) 2416–2425. https://doi.org/10.1021/sc500439w.

[258] S.P. Kelley, A. Narita, J.D. Holbrey, K.D. Green, W.M. Reichert, R.D. Rogers, Understanding the Effects of Ionicity in Salts, Solvates, Co-Crystals, Ionic Co-Crystals, and Ionic Liquids, Rather than Nomenclature, Is Critical to Understanding Their Behavior, Cryst. Growth Des. 13 (2013) 965–975. https://doi.org/10.1021/cg4000439.

[259] B.D. Ribeiro, C. Florindo, L.C. Iff, M.A.Z. Coelho, I.M. Marrucho, Menthol-based Eutectic Mixtures: Hydrophobic Low Viscosity Solvents, ACS Sustain. Chem. Eng. 3

(2015) 2469–2477. https://doi.org/10.1021/acssuschemeng.5b00532.

[260] Q.B. Cheng, L.W. Zhang, Highly Efficient Enzymatic Preparation of Daidzein in Deep Eutectic Solvents, Molecules. 22 (2017) 186. https://doi.org/10.3390/molecules22010186.

[261] L. Zhang, J. Huang, H. Guo, L. Ge, Z. Tian, M. Zhang, J. Wang, G. He, T. Liu, J. Hofkens, D.J.L. Brett, F. Lai, Tuning Ion Transport at the Anode-Electrolyte Interface via a Sulfonate-Rich Ion-Exchange Layer for Durable Zinc-Iodine Batteries, Adv. Energy Mater. 13 (2023). https://doi.org/10.1002/aenm.202203790.

[262] M. Chen, W. Zhu, H. Guo, Z. Tian, L. Zhang, J. Wang, T. Liu, F. Lai, J. Huang, Tightly confined iodine in surface-oxidized carbon matrix toward dual-mechanism zinc-iodine batteries, Energy Storage Mater. 59 (2023) 102760. https://doi.org/10.1016/j.ensm.2023.03.038.

[263] Y. Liu, Y. Liu, X. Wu, Pre-intercalation Strategies to Layered Vanadium-based Electrode Materials for Aqueous Zinc Batteries, Batter. Supercaps. 6 (2023). https://doi.org/10.1002/batt.202200461.

[264] Y. Liu, Y. Liu, X. Wu, Y.-R. Cho, High performance aqueous zinc battery enabled by potassium ion stabilization, J. Colloid Interface Sci. 628 (2022) 33–40. https://doi.org/10.1016/j.jcis.2022.08.046.

[265] W. Li, X. Jing, K. Jiang, D. Wang, Observation of Structural Decomposition of Na 3 V 2 (PO 4) 3 and Na 3 V 2 (PO 4) 2 F 3 as Cathodes for Aqueous Zn-Ion Batteries, ACS Appl. Energy Mater. 4 (2021) 2797–2807. https://doi.org/10.1021/acsaem.1c00067.

[266] H. Bao, H. Guo, X. Zhang, Z. Tian, J. Huang, T. Liu, F. Lai, Anti-Freezing Electrolytes in Aqueous Multivalent Metal-Ion Batteries: Progress, Challenges, and Optimization Strategies, Chem. Rec. 24 (2024). https://doi.org/10.1002/tcr.202300212.

[267] J. Wu, Q. Liang, X. Yu, Q. Lü, L. Ma, X. Qin, G. Chen, B. Li, Deep Eutectic Solvents for Boosting Electrochemical Energy Storage and Conversion: A Review and Perspective, Adv. Funct. Mater. 31 (2021). https://doi.org/10.1002/adfm.202011102.

[268] C. Zhang, L. Zhang, G. Yu, Eutectic Electrolytes as a Promising Platform for Next-Generation Electrochemical Energy Storage, Acc. Chem. Res. 53 (2020) 1648–1659. https://doi.org/10.1021/acs.accounts.0c00360.

[269] W. Viola, T.L. Andrew, An Aqueous Eutectic Electrolyte for Low-Cost, Safe Energy Storage with an Operational Temperature Range of 150 °C, from −70 to 80 °C, J. Phys. Chem. C. 125 (2021) 246–251. https://doi.org/10.1021/acs.jpcc.0c09676.

[270] Y. Tian, D.-W. Sun, L. Xu, T.-H. Fan, Z. Zhu, Bio-inspired eutectogels enabled by binary natural deep eutectic solvents (NADESs): Interfacial anti-frosting, freezing-tolerance, and mechanisms, Food Hydrocoll. 128 (2022) 107568.

https://doi.org/10.1016/j.foodhyd.2022.107568.

[271] J. Li, C. Wang, Y. Xing, Y. Wang, L. Wang, C. Shao, W. Jiang, X. Ji, G. Yang, J. Chen, G. Lyu, “Deep Eutectic Solvent-in-Water” Hydrogels Enable High-Performance Flexible Strain Sensors for Electronic Skin with a Wide Operating Temperature Range, ACS Sustain. Chem. Eng. 11 (2023) 10578–10589. https://doi.org/10.1021/acssuschemeng.3c02734.

[272] Y. Yan, C. He, L. Zhang, H. Dong, X. Zhang, Freeze-resistant, rapidly polymerizable, ionic conductive hydrogel induced by Deep Eutectic Solvent (DES) after lignocellulose pretreatment for flexible sensors, Int. J. Biol. Macromol. 224 (2023) 143–155. https://doi.org/10.1016/j.ijbiomac.2022.10.111.

[273] G. Ge, K. Mandal, R. Haghniaz, M. Li, X. Xiao, L. Carlson, V. Jucaud, M.R. Dokmeci, G.W. Ho, A. Khademhosseini, Deep Eutectic Solvents-Based Ionogels with Ultrafast Gelation and High Adhesion in Harsh Environments, Adv. Funct. Mater. 33 (2023). https://doi.org/10.1002/adfm.202207388.

[274] L. Hu, S. Gao, L. Zhao, L. Dai, D. Zhang, C. Wang, X. Fang, F. Chu, Highly Conductive, Anti-Freezing Hemicellulose-Based Hydrogels Prepared via Deep Eutectic Solvents and Their Applications, Gels. 9 (2023) 725. https://doi.org/10.3390/gels9090725.

[275] H. Cheng, K. Yang, Y. Zhang, S. Liao, M. Du, J. Li, N. Ma, M. Xue, X. Zhang, Y. Wang, A Novel Ionic Conductive Polyurethane Based on Deep Eutectic Solvent Continuing Traditional Merits, ACS Appl. Mater. Interfaces. 14 (2022) 52402–52410. https://doi.org/10.1021/acsami.2c15356.

[276] X. Li, M. Yan, J. Xiao, H. Lian, Ultrafast fabrication of deep eutectic solvent flexible ionic gel with high-transmittance, freeze-resistant and conductivity by frontal polymerization, J. Colloid Interface Sci. 650 (2023) 1382–1392. https://doi.org/10.1016/j.jcis.2023.07.038.

[277] N. Li, L. Qiu, X. Ji, W. Chen, Engineering Ionic Dough with a Deep Eutectic Solvent: From a Traditional Dough Figurine to Flexible Electronics, Chem. Mater. 35 (2023) 7814–7824. https://doi.org/10.1021/acs.chemmater.3c01761.

[278] R. Li, T. Fan, G. Chen, K. Zhang, B. Su, J. Tian, M. He, Autonomous Self-Healing, Antifreezing, and Transparent Conductive Elastomers, Chem. Mater. 32 (2020) 874–881. https://doi.org/10.1021/acs.chemmater.9b04592.

[279] Z. He, Y. Zhuo, F. Wang, J. He, Z. Zhang, Design and preparation of icephobic PDMS-based coatings by introducing an aqueous lubricating layer and macro-crack initiators at the ice-substrate interface, Prog. Org. Coatings. 147 (2020) 105737. https://doi.org/10.1016/j.porgcoat.2020.105737.

[280] L. Wang, Q. Gong, S. Zhan, L. Jiang, Y. Zheng, Robust Anti-Icing Performance of a Flexible Superhydrophobic Surface, Adv. Mater. 28 (2016) 7729–7735.

https://doi.org/10.1002/adma.201602480.

[281] Z. Azimi Dijvejin, M.C. Jain, R. Kozak, M.H. Zarifi, K. Golovin, Smart low interfacial toughness coatings for on-demand de-icing without melting, Nat. Commun. 13 (2022) 5119. https://doi.org/10.1038/s41467-022-32852-6.

[282] S. Zhang, J. Zhang, Y. Zhang, Y. Deng, Nanoconfined Ionic Liquids, Chem. Rev. 117 (2017) 6755–6833. https://doi.org/10.1021/acs.chemrev.6b00509.

[283] K. Dong, S. Zhang, Hydrogen Bonds: A Structural Insight into Ionic Liquids, Chem. – A Eur. J. 18 (2012) 2748–2761. https://doi.org/10.1002/chem.201101645.

[284] F. Javed, F. Ullah, M.R. Zakaria, H.M. Akil, An approach to classification and hi-tech applications of room-temperature ionic liquids (RTILs): A review, J. Mol. Liq. 271 (2018) 403–420. https://doi.org/10.1016/j.molliq.2018.09.005.

[285] Y. Shen, X. Wei, Y. Wang, Y. Shen, L. Li, Y. Huang, K.K. Ostrikov, C.Q. Sun, Energy absorbancy and freezing-temperature tunability of NaCl solutions during ice formation, J. Mol. Liq. 344 (2021) 117928. https://doi.org/10.1016/j.molliq.2021.117928.

[286] J. Wu, L. Mu, X. Feng, X. Lu, R. Larsson, Y. Shi, Poly(alkylimidazolium bis(trifluoromethylsulfonyl)imide)-Based Polymerized Ionic Liquids: A Potential High-Performance Lubricating Grease, Adv. Mater. Interfaces. 6 (2019). https://doi.org/10.1002/admi.201801796.

[287] M. Kazancioglu, R. Lehman, M. Hara, Inorganic silicate polymers made directly from silica using ionic liquid as ionic plasticizer: Monovalent-only system, Mater. Today Commun. 24 (2020) 101058. https://doi.org/10.1016/j.mtcomm.2020.101058.

[288] L. Chen, C. Zhao, X. Duan, J. Zhou, M. Liu, Finely Tuning the Lower Critical Solution Temperature of Ionogels by Regulating the Polarity of Polymer Networks and Ionic Liquids, CCS Chem. 4 (2022) 1386–1396. https://doi.org/10.31635/ccschem.021.202100855.

[289] P.C. Marr, A.C. Marr, Ionic liquid gel materials: applications in green and sustainable chemistry, Green Chem. 18 (2016) 105–128. https://doi.org/10.1039/C5GC02277K.

[290] W. Huang, J. Huang, Z. Guo, W. Liu, Icephobic/anti-icing properties of superhydrophobic surfaces, Adv. Colloid Interface Sci. 304 (2022) 102658. https://doi.org/10.1016/j.cis.2022.102658.

[291] A.T. Mulroney, M.C. Gupta, Ice adhesion properties of periodic surface microtextured optically transparent superhydrophobic polydimethylsiloxane, Cold Reg. Sci. Technol. 198 (2022) 103540. https://doi.org/10.1016/j.coldregions.2022.103540.

[292] Z. Zhang, L. Ma, Y. Liu, J. Ren, H. Hu, An experimental study of rain erosion effects on a hydro-/ice-phobic coating pertinent to Unmanned-Arial-System (UAS) inflight

icing mitigation, Cold Reg. Sci. Technol. 181 (2021) 103196. https://doi.org/10.1016/j.coldregions.2020.103196.

[293] A. Azimi Yancheshme, G. Momen, R. Jafari Aminabadi, Mechanisms of ice formation and propagation on superhydrophobic surfaces: A review, Adv. Colloid Interface Sci. 279 (2020) 102155. https://doi.org/10.1016/j.cis.2020.102155.

[294] S. Heydarian, K. Maghsoudi, R. Jafari, H. Gauthier, G. Momen, Fabrication of liquid-infused textured surfaces (LITS): The effect of surface textures on anti-icing properties and durability, Mater. Today Commun. 32 (2022) 103935. https://doi.org/10.1016/j.mtcomm.2022.103935.

[295] Y.H. Yeong, A. Milionis, E. Loth, J. Sokhey, Self-lubricating icephobic elastomer coating (SLIC) for ultralow ice adhesion with enhanced durability, Cold Reg. Sci. Technol. 148 (2018) 29–37. https://doi.org/10.1016/j.coldregions.2018.01.005.

[296] Y. Wang, J. Zhang, H. Dodiuk, S. Kenig, J.A. Ratto, C. Barry, S. Turkoglu, J. Mead, The effect of superhydrophobic coating composition on the topography and ice adhesion, Cold Reg. Sci. Technol. 201 (2022) 103623. https://doi.org/10.1016/j.coldregions.2022.103623.

[297] M. Yang, W. Liu, L. Liang, C. Jiang, C. Liu, Y. Xie, H. Shi, F. Zhang, K. Pi, A mild strategy to construct superhydrophobic cotton with dual self-cleaning and oil–water separation abilities based on TiO2 and POSS via thiol-ene click reaction, Cellulose. 27 (2020) 2847–2857. https://doi.org/10.1007/s10570-019-02963-3.

[298] Z. He, W.J. Xie, Z. Liu, G. Liu, Z. Wang, Y.Q. Gao, J. Wang, Tuning ice nucleation with counterions on polyelectrolyte brush surfaces, Sci. Adv. 2 (2016). https://doi.org/10.1126/sciadv.1600345.

[299] B. Liang, G. Zhang, Z. Zhong, Y. Huang, Z. Su, Superhydrophilic Anti-Icing Coatings Based on Polyzwitterion Brushes, Langmuir. 35 (2019) 1294–1301. https://doi.org/10.1021/acs.langmuir.8b01009.

[300] M. Shamshiri, R. Jafari, G. Momen, Potential use of smart coatings for icephobic applications: A review, Surf. Coatings Technol. 424 (2021) 127656. https://doi.org/10.1016/j.surfcoat.2021.127656.

[301] C. Urata, R. Hönes, T. Sato, H. Kakiuchida, Y. Matsuo, A. Hozumi, Textured Organogel Films Showing Unusual Thermoresponsive Dewetting, Icephobic, and Optical Properties, Adv. Mater. Interfaces. 6 (2019). https://doi.org/10.1002/admi.201801358.

[302] T. Li, K. Xu, L. Shi, J. Wu, J. He, Z. Zhang, Dual-ionic hydrogels with ultralong anti-dehydration lifespan and superior anti-icing performance, Appl. Mater. Today. 26 (2022) 101367. https://doi.org/10.1016/j.apmt.2022.101367.

[303] Y. Ren, J. Guo, Z. Liu, Z. Sun, Y. Wu, L. Liu, F. Yan, Ionic liquid–based click-

ionogels, Sci. Adv. 5 (2019). https://doi.org/10.1126/sciadv.aax0648.

[304] N.R. Dhumal, K. Noack, J. Kiefer, H.J. Kim, Molecular Structure and Interactions in the Ionic Liquid 1-Ethyl-3-methylimidazolium Bis(Trifluoromethylsulfonyl)imide, J. Phys. Chem. A. 118 (2014) 2547–2557. https://doi.org/10.1021/jp502124y.

[305] F. Shi, Y. Deng, Abnormal FT-IR and FTRaman spectra of ionic liquids confined in nano-porous silica gel, Spectrochim. Acta Part A Mol. Biomol. Spectrosc. 62 (2005) 239–244. https://doi.org/10.1016/j.saa.2004.12.031.

[306] D.Y. AYDIN, M. GÜRÜ, F. AKKURT, Investigation of synthesis parameters of antimony fluoroborate and its usability as a flame retardant for cellulosic fabrics, Cellul. Chem. Technol. 55 (2021) 893–900. https://doi.org/10.35812/CelluloseChemTechnol.2021.55.75.

[307] S. Werner, M. Haumann, P. Wasserscheid, Ionic Liquids in Chemical Engineering, Annu. Rev. Chem. Biomol. Eng. 1 (2010) 203–230. https://doi.org/10.1146/annurev-chembioeng-073009-100915.

[308] R. V. Gadhave, V. S.K., P. V. Dhawale, P.T. Gadekar, Effect of boric acid on poly vinyl alcohol- tannin blend and its application as water-based wood adhesive, Des. Monomers Polym. 23 (2020) 188–196. https://doi.org/10.1080/15685551.2020.1826124.

[309] Y.L. Verma, R.K. Singh, Conformational States of Ionic Liquid 1-Ethyl-3-methylimidazolium Bis(trifluoromethylsulfonyl)imide in Bulk and Confined Silica Nanopores Probed by Crystallization Kinetics Study, J. Phys. Chem. C. 119 (2015) 24381–24392. https://doi.org/10.1021/acs.jpcc.5b06672.

[310] I.J. Villar-Garcia, E.F. Smith, A.W. Taylor, F. Qiu, K.R.J. Lovelock, R.G. Jones, P. Licence, Charging of ionic liquid surfaces under X-ray irradiation: the measurement of absolute binding energies by XPS, Phys. Chem. Chem. Phys. 13 (2011) 2797–2808. https://doi.org/10.1039/C0CP01587C.

[311] M. Reinmöller, A. Ulbrich, T. Ikari, J. Preiß, O. Höfft, F. Endres, S. Krischok, W.J.D. Beenken, Theoretical reconstruction and elementwise analysis of photoelectron spectra for imidazolium-based ionic liquids, Phys. Chem. Chem. Phys. 13 (2011) 19526. https://doi.org/10.1039/c1cp22152c.

[312] V. Lockett, R. Sedev, C. Bassell, J. Ralston, Angle-resolved X-ray photoelectron spectroscopy of the surface of imidazolium ionic liquids, Phys. Chem. Chem. Phys. 10 (2008) 1330. https://doi.org/10.1039/b713584j.

[313] C. Kolbeck, M. Killian, F. Maier, N. Paape, P. Wasserscheid, H.-P. Steinrück, Surface Characterization of Functionalized Imidazolium-Based Ionic Liquids, Langmuir. 24 (2008) 9500–9507. https://doi.org/10.1021/la801261h.

[314] D.S. Silvester, T.L. Broder, L. Aldous, C. Hardacre, A. Crossley, R.G. Compton,

Using XPS to determine solute solubility in room temperature ionic liquids, Analyst. 132 (2007) 196. https://doi.org/10.1039/b700212b.

[315] T. Huhtamäki, X. Tian, J.T. Korhonen, R.H.A. Ras, Surface-wetting characterization using contact-angle measurements, Nat. Protoc. 13 (2018) 1521–1538. https://doi.org/10.1038/s41596-018-0003-z.

[316] R.L. Gardas, R. Ge, N. Ab Manan, D.W. Rooney, C. Hardacre, Interfacial tensions of imidazolium-based ionic liquids with water and n-alkanes, Fluid Phase Equilib. 294 (2010) 139–147. https://doi.org/10.1016/j.fluid.2010.02.022.

[317] H.U. Sajid, R. Kiran, Improving the wettability of structural steels by employing ionic liquids, J. Mol. Liq. 324 (2021) 115137. https://doi.org/10.1016/j.molliq.2020.115137.

[318] C. Kolbeck, J. Lehmann, K.R.J. Lovelock, T. Cremer, N. Paape, P. Wasserscheid, A.P. Fröba, F. Maier, H.-P. Steinrück, Density and Surface Tension of Ionic Liquids, J. Phys. Chem. B. 114 (2010) 17025–17036. https://doi.org/10.1021/jp1068413.

[319] K. Shimizu, B.S.J. Heller, F. Maier, H.-P. Steinrück, J.N. Canongia Lopes, Probing the Surface Tension of Ionic Liquids Using the Langmuir Principle, Langmuir. 34 (2018) 4408–4416. https://doi.org/10.1021/acs.langmuir.7b04237.

[320] G. Law, P.R. Watson, Surface Tension Measurements of N -Alkylimidazolium Ionic Liquids, Langmuir. 17 (2001) 6138–6141. https://doi.org/10.1021/la010629v.

[321] I.M. Gindri, D.A. Siddiqui, C.P. Frizzo, M.A.P. Martins, D.C. Rodrigues, Improvement of tribological and anti-corrosive performance of titanium surfaces coated with dicationic imidazolium-based ionic liquids, RSC Adv. 6 (2016) 78795–78802. https://doi.org/10.1039/C6RA13961B.

[322] X. Dai, N. Sun, S.O. Nielsen, B.B. Stogin, J. Wang, S. Yang, T.-S. Wong, Hydrophilic directional slippery rough surfaces for water harvesting, Sci. Adv. 4 (2018). https://doi.org/10.1126/sciadv.aaq0919.

[323] K. Dong, S. Zhang, J. Wang, Understanding the hydrogen bonds in ionic liquids and their roles in properties and reactions, Chem. Commun. 52 (2016) 6744–6764. https://doi.org/10.1039/C5CC10120D.

[324] M. Klähn, C. Stüber, A. Seduraman, P. Wu, What Determines the Miscibility of Ionic Liquids with Water? Identification of the Underlying Factors to Enable a Straightforward Prediction, J. Phys. Chem. B. 114 (2010) 2856–2868. https://doi.org/10.1021/jp1000557.

[325] J.L. Anthony, E.J. Maginn, J.F. Brennecke, Solution Thermodynamics of Imidazolium-Based Ionic Liquids and Water, J. Phys. Chem. B. 105 (2001) 10942–10949. https://doi.org/10.1021/jp0112368.

[326] M. Freemantle, Chapter 5-Ionic Liquids as Designer solvents, in: An Introd. to Ion.

Liq., Royal Society of Chemistry, 2010: pp. 41–53.

[327] D. MacFarlane, M. Kar, J. Pringle, Fundamentals of Ionic Liquids From Chemistry to Applications, First edit, WILEY-VCH Verlag GmbH & Co. KGaA, Weinheim, 2017.

[328] I. Njoroge, B.W. Bout, M.W. Matson, P.E. Laibinis, G.K. Jennings, Co-Poly(ionic liquid) Films via Anion Exchange for the Continuous Tunability of Ion Transport and Wettability, ACS Omega. 3 (2018) 16158–16164. https://doi.org/10.1021/acsomega.8b02165.

[329] M. Shamshiri, R. Jafari, G. Momen, Icephobic properties of aqueous self-lubricating coatings containing PEG-PDMS copolymers, Prog. Org. Coatings. 161 (2021) 106466. https://doi.org/10.1016/j.porgcoat.2021.106466.

[330] R.S. Hebbar, A.M. Isloor, A.F. Ismail, Contact Angle Measurements, in: Membr. Charact., Elsevier, 2017: pp. 219–255. https://doi.org/10.1016/B978-0-444-63776-5.00012-7.

[331] S.A. Kulinich, M. Farzaneh, How Wetting Hysteresis Influences Ice Adhesion Strength on Superhydrophobic Surfaces, Langmuir. 25 (2009) 8854–8856. https://doi.org/10.1021/la901439c.

[332] M.G. Freire, P.J. Carvalho, R.L. Gardas, I.M. Marrucho, L.M.N.B.F. Santos, J.A.P. Coutinho, Mutual Solubilities of Water and the [Cnmim][Tf2N] Hydrophobic Ionic Liquids, J. Phys. Chem. B. 112 (2008) 1604–1610. https://doi.org/10.1021/jp7097203.

[333] Y. Farnam, H.S. Esmaeeli, P.D. Zavattieri, J. Haddock, J. Weiss, Incorporating phase change materials in concrete pavement to melt snow and ice, Cem. Concr. Compos. 84 (2017) 134–145. https://doi.org/10.1016/j.cemconcomp.2017.09.002.

[334] D.F. Miranda, C. Urata, B. Masheder, G.J. Dunderdale, M. Yagihashi, A. Hozumi, Physically and chemically stable ionic liquid-infused textured surfaces showing excellent dynamic omniphobicity, APL Mater. 2 (2014). https://doi.org/10.1063/1.4876636.

[335] P.W. Wilson, W. Lu, H. Xu, P. Kim, M.J. Kreder, J. Alvarenga, J. Aizenberg, Inhibition of ice nucleation by slippery liquid-infused porous surfaces (SLIPS), Phys. Chem. Chem. Phys. 15 (2013) 581–585. https://doi.org/10.1039/C2CP43586A.

[336] P.Wilson, A.Heneghan, A.D.Haymet, Ice nucleation in nature: supercooling point (SCP) measurements and the role of heterogeneous nucleation, Cryobiology. 46 (2003) 88–98. https://doi.org/10.1016/S0011-2240(02)00182-7.

[337] M. Bešter-Rogač, M. V. Fedotova, S.E. Kruchinin, M. Klähn, Mobility and association of ions in aqueous solutions: the case of imidazolium based ionic liquids, Phys. Chem. Chem. Phys. 18 (2016) 28594–28605. https://doi.org/10.1039/C6CP05010G.

[338] H. Ohno, Functional Design of Ionic Liquids, Bull. Chem. Soc. Jpn. 79 (2006) 1665–1680. https://doi.org/10.1246/bcsj.79.1665.

[339] S. Katayama, S. Fujiwara, NMR Study of the freezing/thawing mechanism of water in polyacrylamide gel, J. Phys. Chem. 84 (1980) 2320–2325. https://doi.org/10.1021/j100455a022.

[340] A. Amirfazli, C. Antonini, CHAPTER 11. Fundamentals of Anti-Icing Surfaces, in: Non-Wettable Surfaces Theory, Prep. Appl., 2016: pp. 319–346. https://doi.org/10.1039/9781782623953-00319.

[341] Z. He, L. Zheng, Z. Liu, S. Jin, C. Li, J. Wang, Inhibition of Heterogeneous Ice Nucleation by Bioinspired Coatings of Polyampholytes, ACS Appl. Mater. Interfaces. 9 (2017) 30092–30099. https://doi.org/10.1021/acsami.7b10014.

[342] J. Chen, Y. Wang, B. Leibauer, T. Seki, K. Meister, Y. Nagata, M. Bonn, Tuning Ice Nucleation by Mussel-Adhesive Inspired Polyelectrolytes: The Role of Hydrogen Bonding, CCS Chem. 4 (2022) 2890–2990. https://doi.org/10.31635/ccschem.022.202202087.

[343] F. Chen, D. Zhou, J. Wang, T. Li, X. Zhou, T. Gan, S. Handschuh-Wang, X. Zhou, Rational Fabrication of Anti-Freezing, Non-Drying Tough Organohydrogels by One-Pot Solvent Displacement, Angew. Chemie. 130 (2018) 6678–6681. https://doi.org/10.1002/ange.201803366.

[344] V.I. Kvlividze, V.F. Kiselev, A.B. Kurzaev, L.A. Ushakova, The mobile water phase on ice surfaces, Surf. Sci. 44 (1974) 60–68. https://doi.org/10.1016/0039-6028(74)90093-4.

[345] J. Dupont, P.A.Z. Suarez, Physico-chemical processes in imidazolium ionic liquids, Phys. Chem. Chem. Phys. 8 (2006) 2441. https://doi.org/10.1039/b602046a.

[346] T. Köddermann, C. Wertz, A. Heintz, R. Ludwig, Ion-Pair Formation in the Ionic Liquid 1-Ethyl-3-methylimidazolium Bis(triflyl)imide as a Function of Temperature and Concentration, ChemPhysChem. 7 (2006) 1944–1949. https://doi.org/10.1002/cphc.200600034.

[347] J. Hao, T. Zemb, Self-assembled structures and chemical reactions in room-temperature ionic liquids, Curr. Opin. Colloid Interface Sci. 12 (2007) 129–137. https://doi.org/10.1016/j.cocis.2006.11.004.

[348] B. Wang, L. Qin, T. Mu, Z. Xue, G. Gao, Are Ionic Liquids Chemically Stable?, Chem. Rev. 117 (2017) 7113–7131. https://doi.org/10.1021/acs.chemrev.6b00594.

[349] L. Vast, L. Carpentier, F. Lallemand, J.-F. Colomer, G. Van Tendeloo, A. Fonseca, J.B. Nagy, Z. Mekhalif, J. Delhalle, Multiwalled carbon nanotubes functionalized with 7-octenyltrichlorosilane and n-octyltrichlorosilane: dispersion in Sylgard®184 silicone and Young's modulus, J. Mater. Sci. 44 (2009) 3476–3482.

https://doi.org/10.1007/s10853-009-3464-1.

[350] S. MF, Additions to and substitutions at C-C[pi]-Bonds, in: M.G. Knochel P (Ed.), Compr. Org. Synth., Second Edi, Elsevier, 1991: pp. 342–392.

[351] S. Rabbani, E. Bakhshandeh, R. Jafari, G. Momen, Superhydrophobic and icephobic polyurethane coatings: Fundamentals, progress, challenges and opportunities, Prog. Org. Coatings. 165 (2022) 106715. https://doi.org/10.1016/j.porgcoat.2022.106715.

[352] S. Li, J. Qin, M. He, R. Paoli, Fast Evaluation of Aircraft Icing Severity Using Machine Learning Based on XGBoost, Aerospace. 7 (2020) 36. https://doi.org/10.3390/aerospace7040036.

[353] P. Guo, Y. Zheng, M. Wen, C. Song, Y. Lin, L. Jiang, Icephobic/Anti-Icing Properties of Micro/Nanostructured Surfaces, Adv. Mater. 24 (2012) 2642–2648. https://doi.org/10.1002/adma.201104412.

[354] Z. Tian, P. Fan, D. Zhu, L. Wang, H. Zhao, C. Chen, R. Peng, D. Li, H. Zhang, M. Zhong, Anti-ice-pinning superhydrophobic surfaces for extremely low ice adhesion, Chem. Eng. J. 473 (2023) 145382. https://doi.org/10.1016/j.cej.2023.145382.

[355] S. Jiang, Y. Diao, H. Yang, Recent advances of bio-inspired anti-icing surfaces, Adv. Colloid Interface Sci. 308 (2022) 102756. https://doi.org/10.1016/j.cis.2022.102756.

[356] Z. Cheng, W. Feng, Y. Zhang, L. Sun, Y. Liu, L. Chen, C. Wang, A Highly Robust Amphibious Soft Robot with Imperceptibility Based on a Water-Stable and Self-Healing Ionic Conductor, Adv. Mater. 35 (2023). https://doi.org/10.1002/adma.202301005.

[357] J. Ji, N. Liu, Y. Tian, H. Zhai, S. Zhao, G. Liu, Y. Wei, L. Feng, Ultralong Inhibition of heterogeneous ice nucleation by robust Anti-Freezing coating with Self-Lubricating ionic salts layer, Chem. Eng. J. 474 (2023) 145537. https://doi.org/10.1016/j.cej.2023.145537.

[358] B. Wu, X. Cui, H. Jiang, N. Wu, C. Peng, Z. Hu, X. Liang, Y. Yan, J. Huang, D. Li, A superhydrophobic coating harvesting mechanical robustness, passive anti-icing and active de-icing performances, J. Colloid Interface Sci. 590 (2021) 301–310. https://doi.org/10.1016/j.jcis.2021.01.054.

[359] Q. Rao, Y. Lu, L. Song, Y. Hou, X. Zhan, Q. Zhang, Highly Efficient Self-Repairing Slippery Liquid-Infused Surface with Promising Anti-Icing and Anti-Fouling Performance, ACS Appl. Mater. Interfaces. 13 (2021) 40032–40041. https://doi.org/10.1021/acsami.1c09491.

[360] M. Shamshiri, R. Jafari, G. Momen, An intelligent icephobic coating based on encapsulated phase change materials (PCM), Colloids Surfaces A Physicochem. Eng. Asp. 655 (2022) 130157. https://doi.org/10.1016/j.colsurfa.2022.130157.

[361] S.K. Singh, A.W. Savoy, Ionic liquids synthesis and applications: An overview, J. Mol. Liq. 297 (2020) 112038. https://doi.org/10.1016/j.molliq.2019.112038.

[362] T. Torimoto, T. Tsuda, K. Okazaki, S. Kuwabata, New Frontiers in Materials Science Opened by Ionic Liquids, Adv. Mater. 22 (2010) 1196–1221. https://doi.org/10.1002/adma.200902184.

[363] P. Zhang, Z. Xue, C. Wang, J. Sun, F. Shao, X. Zou, B. Li, M. Qi, Y. Jing, Y. Jia, Mechanisms of ionic liquids on the enhancement of interfacial transport of lithium ions in crown ether system, J. Clean. Prod. 366 (2022) 132782. https://doi.org/10.1016/j.jclepro.2022.132782.

[364] J. Huang, H. Zhang, X. Yuan, Y. Sha, J. Li, T. Dong, Y. Song, S. Zhang, Regulating robust interphase using a functional ionic liquid additive with bi-electrode affinity to stabilize the high-voltage lithium-rich lithium metals batteries, Chem. Eng. J. 464 (2023) 142578. https://doi.org/10.1016/j.cej.2023.142578.

[365] D. Yu, Z. Ma, Z. Liu, X. Jiang, H.A. Younus, X. Wang, S. Zhang, Optimizing interfacial wetting by ionic liquid for high performance solid-state lithium metal batteries operated at ambient temperature, Chem. Eng. J. 457 (2023) 141043. https://doi.org/10.1016/j.cej.2022.141043.

[366] Y.L. Kobzar, K. Fatyeyeva, Ionic liquids as green and sustainable steel corrosion inhibitors: Recent developments, Chem. Eng. J. 425 (2021) 131480. https://doi.org/10.1016/j.cej.2021.131480.

[367] W. Jiang, X. Li, G. Gao, F. Wu, C. Luo, L. Zhang, Advances in applications of ionic liquids for phase change CO2 capture, Chem. Eng. J. 445 (2022) 136767. https://doi.org/10.1016/j.cej.2022.136767.

[368] Y. Zhao, N. Yang, X. Chu, F. Sun, M.U. Ali, Y. Zhang, B. Yang, Y. Cai, M. Liu, N. Gasparini, J. Zheng, C. Zhang, C. Guo, H. Meng, Wide-Humidity Range Applicable, Anti-Freezing, and Healable Zwitterionic Hydrogels for Ion-Leakage-Free Iontronic Sensors, Adv. Mater. 35 (2023). https://doi.org/10.1002/adma.202211617.

[369] A. Aldhaleai, P.A. Tsai, Dynamic Wetting of Ionic Liquid Drops on Hydrophobic Microstructures, Langmuir. 38 (2022) 16073–16083. https://doi.org/10.1021/acs.langmuir.2c02694.

[370] J. Kozakiewicz, J. Przybylski, B. Hamankiewicz, K. Sylwestrzak, J. Trzaskowska, M. Krajewski, M. Ratyński, W. Sarna, A. Czerwiński, UV-Cured Poly(Siloxane-Urethane)-Based Polymer Composite Materials for Lithium Ion Batteries—The Effect of Modification with Ionic Liquids, Materials (Basel). 13 (2020) 4978. https://doi.org/10.3390/ma13214978.

[371] K. Konieczna, K. Yavir, M. Kermani, A. Mielewczyk-Gryń, A. Kloskowski, The new silica-based coated SPME fiber as universal support for the confinement of ionic liquid as an extraction medium, Sep. Purif. Technol. 252 (2020) 117411.

https://doi.org/10.1016/j.seppur.2020.117411.

[372] Ehsan Kianfar, Sajjad Mafi, Ionic Liquids: Properties, Application, and Synthesis, Fine Chem. Eng. (2020) 22–31. https://doi.org/10.37256/fce.212021693.

[373] G. McHale, N. Afify, S. Armstrong, G.G. Wells, R. Ledesma-Aguilar, The Liquid Young's Law on SLIPS: Liquid–Liquid Interfacial Tensions and Zisman Plots, Langmuir. 38 (2022) 10032–10042. https://doi.org/10.1021/acs.langmuir.2c01470.

[374] K.C. Kao, Dielectric Phenomena in Solids With Emphasis on Physical Concepts of Electronic Processes, Elsevier, 2004.

[375] F.-C. Chiu, A Review on Conduction Mechanisms in Dielectric Films, Adv. Mater. Sci. Eng. 2014 (2014) 1–18. https://doi.org/10.1155/2014/578168.

[376] V.M. Mohan, W. Qiu, J. Shen, W. Chen, Electrical properties of poly(vinyl alcohol) (PVA) based on LiFePO4 complex polymer electrolyte films, J. Polym. Res. 17 (2010) 143–150. https://doi.org/10.1007/s10965-009-9300-0.

[377] H. Erdemi, A. Baykal, E. Karaoğlu, M.S. Toprak, Synthesis and conductivity studies of piperidine-4-carboxylic acid functionalized Fe3O4 nanoparticles, Mater. Res. Bull. 47 (2012) 2193–2199. https://doi.org/10.1016/j.materresbull.2012.06.006.

[378] A. Baykal, H. Erdemi, M. Amir, Temperature and Frequency Dependence on Electrical Properties of Fe3O4@ Caffeic Acid Nanocomposite, J. Inorg. Organomet. Polym. Mater. 26 (2016) 190–196. https://doi.org/10.1007/s10904-015-0296-0.

[379] M. Yılmazoğlu, F. Bayıroğlu, H. Erdemi, U. Abaci, H.Y. Guney, Dielectric properties of sulfonated poly(ether ether ketone) (SPEEK) electrolytes with 1-ethyl-3-methylimidazolium tetrafluoroborate salt: Ionic liquid-based conduction pathways, Colloids Surfaces A Physicochem. Eng. Asp. 611 (2021) 125825. https://doi.org/10.1016/j.colsurfa.2020.125825.

[380] V.M. Mohan, W. Qiu, J. Shen, W. Chen, Electrical properties of poly(vinyl alcohol) (PVA) based on LiFePO 4 complex polymer electrolyte films, J. Polym. Res. 17 (2010) 143–150. https://doi.org/10.1007/s10965-009-9300-0.

[381] M. Shukla, S. Sah, A Comparative Study of Piperidinium and Imidazolium Based Ionic Liquids: Thermal, Spectroscopic and Theoretical Studies, in: Ion. Liq. - New Asp. Futur., InTech, 2013. https://doi.org/10.5772/51797.

[382] I. Tanabe, Y. Kurawaki, Y. Morisawa, Y. Ozaki, Electronic absorption spectra of imidazolium-based ionic liquids studied by far-ultraviolet spectroscopy and quantum chemical calculations, Phys. Chem. Chem. Phys. 18 (2016) 22526–22530. https://doi.org/10.1039/C6CP02930B.

[383] N.A. Noorhisham, D. Amri, A.H. Mohamed, N. Yahaya, N.M. Ahmad, S. Mohamad, S. Kamaruzaman, H. Osman, Characterisation techniques for analysis of imidazolium-

based ionic liquids and application in polymer preparation: A review, J. Mol. Liq. 326 (2021) 115340. https://doi.org/10.1016/j.molliq.2021.115340.

[384] L. Makkonen, Ice Adhesion —Theory, Measurements and Countermeasures, J. Adhes. Sci. Technol. 26 (2012) 413–445. https://doi.org/10.1163/016942411X574583.

[385] J. Sarma, L. Zhang, Z. Guo, X. Dai, Sustainable icephobicity on durable quasi-liquid surface, Chem. Eng. J. 431 (2022) 133475. https://doi.org/10.1016/j.cej.2021.133475.

[386] E. Bakhshandeh, S. Sobhani, R. Jafari, G. Momen, New insights into tailoring physicochemical properties for optimizing the anti-icing behavior of polyurethane coatings, J. Appl. Polym. Sci. 140 (2023). https://doi.org/10.1002/app.54610.

[387] A. Ahmad, N. Mansor, H. Mahmood, T. Iqbal, M. Moniruzzaman, Effect of ionic liquids on thermomechanical properties of polyetheretherketone-multiwalled carbon nanotubes nanocomposites, J. Appl. Polym. Sci. 139 (2022). https://doi.org/10.1002/app.51788.

[388] F. Ren, J. Wang, F. Xie, K. Zan, S. Wang, S. Wang, Applications of ionic liquids in starch chemistry: a review, Green Chem. 22 (2020) 2162–2183. https://doi.org/10.1039/C9GC03738A.

[389] B.L. Gadilohar, G.S. Shankarling, Choline based ionic liquids and their applications in organic transformation, J. Mol. Liq. 227 (2017) 234–261. https://doi.org/10.1016/j.molliq.2016.11.136.

[390] A. Pandey, Bhawna, D. Dhingra, S. Pandey, Hydrogen Bond Donor/Acceptor Cosolvent-Modified Choline Chloride-Based Deep Eutectic Solvents, J. Phys. Chem. B. 121 (2017) 4202–4212. https://doi.org/10.1021/acs.jpcb.7b01724.

[391] J.J. Buzolic, H. Li, Z.M. Aman, G.G. Warr, R. Atkin, Self-assembled nanostructure induced in deep eutectic solvents via an amphiphilic hydrogen bond donor, J. Colloid Interface Sci. 616 (2022) 121–128. https://doi.org/10.1016/j.jcis.2022.02.029.

[392] B. Socas-Rodríguez, Á. Santana-Mayor, A. V. Herrera-Herrera, M.Á. Rodríguez-Delgado, Deep eutectic solvents, in: Green Sustain. Process Chem. Environ. Eng. Sci., Elsevier, 2020: pp. 123–177. https://doi.org/10.1016/B978-0-12-817386-2.00005-6.

[393] R. Gupta, M. Yadav, R. Gaur, G. Arora, P. Yadav, R.K. Sharma, Magnetically supported ionic liquids: a sustainable catalytic route for organic transformations, Mater. Horizons. 7 (2020) 3097–3130. https://doi.org/10.1039/D0MH01088J.

[394] A.S. Khan, T.H. Ibrahim, N.A. Jabbar, M.I. Khamis, P. Nancarrow, F.S. Mjalli, Ionic liquids and deep eutectic solvents for the recovery of phenolic compounds: effect of ionic liquids structure and process parameters, RSC Adv. 11 (2021) 12398–12422. https://doi.org/10.1039/D0RA10560K.

[395] Z. Yuan, H. Liu, W.F. Yong, Q. She, J. Esteban, Status and advances of deep eutectic

solvents for metal separation and recovery, Green Chem. 24 (2022) 1895–1929. https://doi.org/10.1039/D1GC03851F.

[396] I.M. Pateli, D. Thompson, S.S.M. Alabdullah, A.P. Abbott, G.R.T. Jenkin, J.M. Hartley, The effect of pH and hydrogen bond donor on the dissolution of metal oxides in deep eutectic solvents, Green Chem. 22 (2020) 5476–5486. https://doi.org/10.1039/D0GC02023K.

[397] H. Yang, L. Ying, Y. Wang, A. Farooq, P. Wang, Z. Wang, Versatile, durable conductive networks assembled from MXene and sericin-modified carbon nanotube on polylactic acid textile micro-etched via deep eutectic solvent, J. Colloid Interface Sci. 658 (2024) 648–659. https://doi.org/10.1016/j.jcis.2023.11.187.

[398] A. Gertrudes, R. Craveiro, Z. Eltayari, R.L. Reis, A. Paiva, A.R.C. Duarte, How Do Animals Survive Extreme Temperature Amplitudes? The Role of Natural Deep Eutectic Solvents, ACS Sustain. Chem. Eng. 5 (2017) 9542–9553. https://doi.org/10.1021/acssuschemeng.7b01707.

[399] A.M. de Castro, D. Prasavath, J. V. Bevilaqua, C.A.M. Portugal, L.A. Neves, J.G. Crespo, Role of water on deep eutectic solvents (DES) properties and gas transport performance in biocatalytic supported DES membranes, Sep. Purif. Technol. 255 (2021) 117763. https://doi.org/10.1016/j.seppur.2020.117763.

[400] R. Liu, C. Qiao, Q. Liu, L. Liu, J. Yao, Fabrication and Properties of Anti-freezing Gelatin Hydrogels Based on a Deep Eutectic Solvent, ACS Appl. Polym. Mater. 5 (2023) 4546–4553. https://doi.org/10.1021/acsapm.3c00634.

[401] X. Lin, X. Wang, H. Cui, P. Rao, Y. Meng, G. Ouyang, H. Guo, Hydrogels with ultra-highly additive adjustable toughness under quasi-isochoric conditions, Mater. Horizons. 10 (2023) 993–1004. https://doi.org/10.1039/D2MH01451C.

[402] R. Chatterjee, R.U. Thanjukutty, C. Carducci, A. Neogi, S. Chakraborty, V.P.B.R. Bapu, S. Banik, S.K.R.S. Sankaranarayanan, S. Anand, Adhesion of impure ice on surfaces, Mater. Horizons. 11 (2024) 419–427. https://doi.org/10.1039/D3MH01440A.

[403] Y. Jian, S. Handschuh-Wang, J. Zhang, W. Lu, X. Zhou, T. Chen, Biomimetic anti-freezing polymeric hydrogels: keeping soft-wet materials active in cold environments, Mater. Horizons. 8 (2021) 351–369. https://doi.org/10.1039/D0MH01029D.

[404] D. Yang, R. Bao, A.T. Clare, K.-S. Choi, X. Hou, Phase change surfaces with porous metallic structures for long-term anti/de-icing application, J. Colloid Interface Sci. 660 (2024) 136–146. https://doi.org/10.1016/j.jcis.2024.01.091.

[405] D.R. Nutt, J.C. Smith, Dual Function of the Hydration Layer around an Antifreeze Protein Revealed by Atomistic Molecular Dynamics Simulations, J. Am. Chem. Soc. 130 (2008) 13066–13073. https://doi.org/10.1021/ja8034027.

[406] K. Liu, C. Wang, J. Ma, G. Shi, X. Yao, H. Fang, Y. Song, J. Wang, Janus effect of

antifreeze proteins on ice nucleation, Proc. Natl. Acad. Sci. 113 (2016) 14739–14744. https://doi.org/10.1073/pnas.1614379114.

[407] A. Hudait, Y. Qiu, N. Odendahl, V. Molinero, Hydrogen-Bonding and Hydrophobic Groups Contribute Equally to the Binding of Hyperactive Antifreeze and Ice-Nucleating Proteins to Ice, J. Am. Chem. Soc. 141 (2019) 7887–7898. https://doi.org/10.1021/jacs.9b02248.

[408] S. Deville, C. Viazzi, C. Guizard, Ice-Structuring Mechanism for Zirconium Acetate, Langmuir. 28 (2012) 14892–14898. https://doi.org/10.1021/la302275d.

[409] Y. Fu, M. Zhang, H. Qu, K. Liu, Z. Zhang, Y. Yang, B. Li, F. Liu, L. Wang, Insights into supramolecular assembly formation of pyridine tetrazolium and aromatic acid assisted via hydrogen-bonding, J. Mol. Struct. 1206 (2020) 127697. https://doi.org/10.1016/j.molstruc.2020.127697.

[410] Z. Naseem, R.A. Shehzad, A. Ihsan, J. Iqbal, M. Zahid, A. Pervaiz, G. Sarwari, Theoretical investigation of supramolecular hydrogen-bonded choline chloride-based deep eutectic solvents using density functional theory, Chem. Phys. Lett. 769 (2021) 138427. https://doi.org/10.1016/j.cplett.2021.138427.

[411] C.R. Ashworth, R.P. Matthews, T. Welton, P.A. Hunt, Doubly ionic hydrogen bond interactions within the choline chloride–urea deep eutectic solvent, Phys. Chem. Chem. Phys. 18 (2016) 18145–18160. https://doi.org/10.1039/C6CP02815B.

[412] G. García, M. Atilhan, S. Aparicio, An approach for the rationalization of melting temperature for deep eutectic solvents from DFT, Chem. Phys. Lett. 634 (2015) 151–155. https://doi.org/10.1016/j.cplett.2015.06.017.

[413] P. Kalhor, J. Xu, H. Ashraf, B. Cao, Z.-W. Yu, Structural Properties and Hydrogen-Bonding Interactions in Binary Mixtures Containing a Deep-Eutectic Solvent and Acetonitrile, J. Phys. Chem. B. 124 (2020) 1229–1239. https://doi.org/10.1021/acs.jpcb.9b10751.

[414] K. Saiswani, A. Narvekar, D. Jahagirdar, R. Jain, P. Dandekar, Choline chloride:glycerol deep eutectic solvents assist in the permeation of daptomycin across Caco-2 cells mimicking intestinal bilayer, J. Mol. Liq. 383 (2023) 122051. https://doi.org/10.1016/j.molliq.2023.122051.

[415] N. Parsana, O. El Seoud, A. Al-Ghamdi, N. Kasoju, N. Malek, Deep Eutectic Solvent and Poly (Vinyl Alcohol) Based Self-healable, Injectable and Adhesive „Eutectogel": An Emerging Drug Delivery Vehicle, ChemistrySelect. 9 (2024). https://doi.org/10.1002/slct.202304157.

[416] L. Saiz, J.A. Padró, E. Guàrdia, Structure of liquid ethylene glycol: A molecular dynamics simulation study with different force fields, J. Chem. Phys. 114 (2001) 3187–3199. https://doi.org/10.1063/1.1340605.

[417] J.J. Towey, A.K. Soper, L. Dougan, The structure of glycerol in the liquid state: a neutron diffraction study, Phys. Chem. Chem. Phys. 13 (2011) 9397. https://doi.org/10.1039/c0cp02136a.

[418] C. Tao, S. Bai, X. Li, C. Li, L. Ren, Y. Zhao, X. Yuan, Formation of zwitterionic coatings with an aqueous lubricating layer for antifogging/anti-icing applications, Prog. Org. Coatings. 115 (2018) 56–64. https://doi.org/10.1016/j.porgcoat.2017.11.002.

[419] K. Jafari, M.H. Fatemi, P. Estellé, Deep eutectic solvents (DESs): A short overview of the thermophysical properties and current use as base fluid for heat transfer nanofluids, J. Mol. Liq. 321 (2021) 114752. https://doi.org/10.1016/j.molliq.2020.114752.

[420] L. Meredith, A. Elbourne, T.L. Greaves, G. Bryant, S.J. Bryant, Physico-chemical characterisation of glycerol- and ethylene glycol-based deep eutectic solvents, J. Mol. Liq. 394 (2024) 123777. https://doi.org/10.1016/j.molliq.2023.123777.

[421] H. Peyrovedin, R. Haghbakhsh, A.R.C. Duarte, A. Shariati, Deep Eutectic Solvents as Phase Change Materials in Solar Thermal Power Plants: Energy and Exergy Analyses, Molecules. 27 (2022) 1427. https://doi.org/10.3390/molecules27041427.

[422] C. Florindo, L. Romero, I. Rintoul, L.C. Branco, I.M. Marrucho, From Phase Change Materials to Green Solvents: Hydrophobic Low Viscous Fatty Acid–Based Deep Eutectic Solvents, ACS Sustain. Chem. Eng. 6 (2018) 3888–3895. https://doi.org/10.1021/acssuschemeng.7b04235.

[423] E. Veroutis, S. Merz, R.A. Eichel, J. Granwehr, Intra- and inter-molecular interactions in choline-based ionic liquids studied by 1D and 2D NMR, J. Mol. Liq. 322 (2021) 114934. https://doi.org/10.1016/j.molliq.2020.114934.

[424] M. Andonegi, D. Correia, N. Pereira, M. Salado, C.M. Costa, S. Lanceros-Mendez, K. de la Caba, P. Guerrero, Sustainable Collagen Blends with Different Ionic Liquids for Resistive Touch Sensing Applications, ACS Sustain. Chem. Eng. 11 (2023) 5986–5998. https://doi.org/10.1021/acssuschemeng.3c00052.

[425] M. Zdanowicz, R. Jędrzejewski, R. Pilawka, Deep eutectic solvents as simultaneous plasticizing and crosslinking agents for starch, Int. J. Biol. Macromol. 129 (2019) 1040–1046. https://doi.org/10.1016/j.ijbiomac.2019.02.103.

[426] E.A. Recker, D. Hardy, G.I. Anderson, A. Mirjafari, D. V. Wagle, Covalently linked hydrogen bond donors: The other side of molecular frustration in deep eutectic solvents, J. Chem. Phys. 155 (2021). https://doi.org/10.1063/5.0058165.

[427] S. Jiang, S. Wang, G. Peng, C. Qiao, J. Yao, Structural Characterization and Properties of Deep Eutectic Solvents Plasticized Chitosan Films, J. Macromol. Sci. Part B. 63 (2024) 461–477. https://doi.org/10.1080/00222348.2023.2271785.

[428] J. Liang, R.D. Ludescher, Effects of glycerol on the molecular mobility and hydrogen bond network in starch matrix, Carbohydr. Polym. 115 (2015) 401–407. https://doi.org/10.1016/j.carbpol.2014.08.105.

[429] B.Z. Newby, M.K. Chaudhury, H.R. Brown, Macroscopic Evidence of the Effect of Interfacial Slippage on Adhesion, Science (80-.). 269 (1995) 1407–1409. https://doi.org/10.1126/science.269.5229.1407.

[430] S. Zhang, F. Gao, Z. Jiang, Q. He, J. Lu, Y. Hou, X. Zhan, Q. Zhang, Bioinspired durable interpenetrating network anti-icing coatings enabled by binders and hydrophobic-ion specific synergies, Chem. Eng. J. 479 (2024) 147836. https://doi.org/10.1016/j.cej.2023.147836.

[431] L. Li, S. Khodakarami, X. Yan, K. Fazle Rabbi, A.A. Gunay, A. Stillwell, N. Miljkovic, Enabling Renewable Energy Technologies in Harsh Climates with Ultra-Efficient Electro-Thermal Desnowing, Defrosting, and Deicing, Adv. Funct. Mater. 32 (2022). https://doi.org/10.1002/adfm.202201521.

[432] M. Vijay, D. Jena, Intelligent adaptive observer-based optimal control of overhead transmission line de-icing robot manipulator, Adv. Robot. 30 (2016) 1215–1227. https://doi.org/10.1080/01691864.2016.1207562.

[433] X. Wu, Y. Pan, Z. Han, Y. Shen, Does Anti-Condensation coatings guarantee Anti-Icing Properties?, Appl. Surf. Sci. 649 (2024) 159101. https://doi.org/10.1016/j.apsusc.2023.159101.

[434] M.P. Goertz, X.-Y. Zhu, J.E. Houston, Exploring the Liquid-like Layer on the Ice Surface, Langmuir. 25 (2009) 6905–6908. https://doi.org/10.1021/la9001994.

[435] S. Takagi, Approximate thermodynamics of the liquid-like layer on an ice sphere based on an interpretation of the wetting parameter, J. Colloid Interface Sci. 137 (1990) 446–455. https://doi.org/10.1016/0021-9797(90)90419-O.

[436] T. Kling, F. Kling, D. Donadio, Structure and Dynamics of the Quasi-Liquid Layer at the Surface of Ice from Molecular Simulations, J. Phys. Chem. C. 122 (2018) 24780–24787. https://doi.org/10.1021/acs.jpcc.8b07724.

[437] J. Zhao, G. Wu, P. Wang, T. Wang, Z. Li, L. Chen, Mussel-inspired construction of multifunctional cotton fabric with superhydrophobicity, conductivity and antibacterial activity, Cellulose. 26 (2019) 6979–6993. https://doi.org/10.1007/s10570-019-02553-3.

[438] S.A. Tolba, W. Xia, Molecular insights into the hydration of zwitterionic polymers, Mol. Syst. Des. Eng. 8 (2023) 1040–1048. https://doi.org/10.1039/D3ME00020F.

[439] S. Tian, R. Li, X. Liu, J. Wang, J. Yu, S. Xu, Y. Tian, J. Yang, L. Zhang, Inhibition of Defect-Induced Ice Nucleation, Propagation, and Adhesion by Bioinspired Self-Healing Anti-Icing Coatings, Research. 6 (2023).

https://doi.org/10.34133/research.0140.

[440] M. Shamshiri, G. Momen, R. Jafari, Icephobic coatings beyond boundaries: Layered integration of phase change materials beneath a PEG-PDMS copolymer–containing coating to enhance anti-icing performance, Prog. Org. Coatings. 189 (2024) 108324. https://doi.org/10.1016/j.porgcoat.2024.108324.

[441] R. V. Khose, M.P. Bondarde, S. Some, Novel bio-inspired deep eutectic solvent and graphene functionalized deep eutectic solvent as an efficient flame retardant material for cotton fabric, Cellulose. 28 (2021) 11199–11208. https://doi.org/10.1007/s10570-021-04216-8.

[442] P. Kim, C. Weeraratna, S. Nemšák, N. Dias, A.K. Lemmens, K.R. Wilson, M. Ahmed, Interfacial Nanostructure and Hydrogen Bond Networks of Choline Chloride and Glycerol Mixtures Probed with X-ray and Vibrational Spectroscopies, J. Phys. Chem. Lett. 15 (2024) 3002–3010. https://doi.org/10.1021/acs.jpclett.4c00052.

[443] Y. Uda, S. Zepeda, F. Kaneko, Y. Matsuura, Y. Furukawa, Adsorption-Induced Conformational Changes of Antifreeze Glycoproteins at the Ice/Water Interface, J. Phys. Chem. B. 111 (2007) 14355–14361. https://doi.org/10.1021/jp075429s.

[444] M. Koochaki, G. Momen, S. Lavoie, R. Jafari, Enhancing Icephobic Coatings: Exploring the Potential of Dopamine-Modified Epoxy Resin Inspired by Mussel Catechol Groups, Biomimetics. 9 (2024) 349. https://doi.org/10.3390/biomimetics9060349.

[445] M. Jafari, A. Heydari, Using choline nitrate as solvent and oxidant in direct oxidation of organic halides and alcohols to aldehyde and its derivatives, J. Mol. Struct. 1264 (2022) 133267. https://doi.org/10.1016/j.molstruc.2022.133267.

[446] B. Onghena, J. Jacobs, L. Van Meervelt, K. Binnemans, Homogeneous liquid–liquid extraction of neodymium(<scp>iii</scp>) by choline hexafluoroacetylacetonate in the ionic liquid choline bis(trifluoromethylsulfonyl)imide, Dalt. Trans. 43 (2014) 11566–11578. https://doi.org/10.1039/C4DT01340A.

[447] I.G. Cruz-Reyes, J.A. Mendoza-Pérez, R. Ruiz-Guerrero, D.Y. Medina-Velázquez, L.G. Zepeda-Vallejo, Á. de J. Morales-Ramírez, Kinetics of Zn–C Battery Leaching with Choline Chloride/Urea Natural Deep Eutectic Solvents, Recycling. 7 (2022) 86. https://doi.org/10.3390/recycling7060086.

[448] K. Fujii, Y. Soejima, Y. Kyoshoin, S. Fukuda, R. Kanzaki, Y. Umebayashi, T. Yamaguchi, S. Ishiguro, T. Takamuku, Liquid Structure of Room-Temperature Ionic Liquid, 1-Ethyl-3-methylimidazolium Bis-(trifluoromethanesulfonyl) Imide, J. Phys. Chem. B. 112 (2008) 4329–4336. https://doi.org/10.1021/jp7105499.